HYBRID AIR BEARINGS FOR HIGH SPEED TURBO MACHINERY

By

Guang Pu

A thesis submitted to

The University of Birmingham

for the degree of

DOCTOR OF PHILOSOPHY

School of Mechanical Engineering

The University of Birmingham

December 2015

ABSTRACT

This PhD project is set out to develop a type of hybrid journal air bearings with reduced reliance on the supply of compressed air for mobile turbomachinery applications. The research work covers hydrostatic and hybrid journal air bearings with non-compliant clearance boundaries. The approach adopted combined numerical analysis based on CFD and experimental verification of the designs.

The research can be divided into three sections. In the first section, numerical approaches to model hydrostatic and hybrid journal air bearings with a fixed clearance boundary were developed based on finite difference method (FDM) and finite volume method (FVM) respectively. The computational time of the iterative process was reduced using the Newton's method and successive relaxation. The rotor used for dynamic analysis was modelled using finite element method based on the Timoshenko beam theory with gyroscopic effect. The governing equation of motion for a general rotor-bearing system with a constant rotational speed was provided. This section also includes a discussion on the analytical methods to predict the performance of a rotor bearing system with both linear perturbation analysis and non-linear transient analysis.

In the second section, theoretical and experimental studies were performed on hydrostatic journal air bearings. Performance of the bearings was investigated in non-rotational and rotational conditions. The analysis on stability and natural frequencies of rotor bearing system was performed using the linear bearing model in two cases. In the first case (**CASE I**), the system consists of a rotor and two journal bearings without viscoelastic support outside the bearing sleeve, while in the second case (**CASE II**), the same rotor-bearing system has

viscoelastic support. A test rig was designed and manufactured based on the system configuration in **CASE II.** The unbalance responses of the rotor in the test rig were predicted using non-linear transient analysis and measured experimentally at two sensor positions from 50k rpm to 100k rpm in rotor speed. The experimental and prediction results were compared and discussed.

In the third section, theoretical and experimental study were performed on hybrid journal air bearings. The proposed hybrid journal air bearings combine hydrostatic air bearings with orifice restrictors and herringbone grooved hydrodynamic air bearings. The design allows the rotor to be lifted by compressed air during stop and low speed sessions. When the speed of the rotor is sufficiently high, the rotor can be fully self-suspended. A novel herringbone groove design has been proposed to improve bearing reaction forces at given static equilibrium positions. The influence of some design parameters on the dynamic performance of hybrid air bearings are then investigated. The analysis on natural frequencies and stability of the rotor supported by the hybrid air bearings were performed in the same cases as in previous section. The unbalance responses of the rotor bearing system in **CASE II** were predicted using non-linear transient analysis and measured experimentally in two working conditions from 50k rpm to 120k rpm rotor speed at the two sensor positions. In the first condition, the compressed air supply pressure (P_S) is maintained at bar. The responses of the rotor showed a synchronous component (unbalance excitation). In the second working condition, the bearings are fully self-acting with no external compressed air supply. The responses of the rotor showed a synchronous component (unbalance excitation) and a clear sub-synchronous component around 820Hz (self-excited whirl).

Through the theoretical and experimental investigations of the hybrid journal air bearings, the objectives of the project have been implemented and the aims have been met. The hybrid air bearings have been fitted to a rotor from a turbocharger for a 2Litres diesel engine. The feature of the hybrid air bearing has been proven working in experiments by cutting off compressed air when the rotational speed is sufficiently high. A novel type of herringbone grooves has been developed for hybrid journal air bearings for improved performance.

Dedicated to my family

ACKNOWLEDGEMENTS

Above all, I would like to express great appreciation to my research supervisor, Professor Kyle Jiang for his guidance, idea and support on the research work during this PhD project. The way in which he approaches research and work inspires me. I am very grateful for his efforts in improving my communication and presentation skills.

I would like to thank Professor Damien Walmsley at School of Dentistry in the University of Birmingham for kindly providing high resolution laser vibrometer. I owe my sincere thanks to Vahid Nasrikkahi, Pavel Pencheve and Tahseen Jwad in laser machining process. Without them, the innovative idea cannot be put in practice. I should also thank the members of the Nanotechnology Group, for being kind and supportive and my collogues Muhao, Jianyi, Yang, Changzhao, Haichun, Tianshi, Sagar, Jason, Susan, Guanxiong for sharing their knowledge and expertise throughout the completion of this work. I would like to thank my parents for their support throughout my graduate study journey. They are always being there as a sounding board. Finally, I would also like to thank my wife, Xiaoxu Zou, for her greatest tenderness and unswerving support during my difficult times.

LIST OF PUBLICATIONS AND ACHIEVEMENTS

List of publications:

- Yunluo Yu, Guang Pu, and Kyle Jiang, Modelling and analysis of the static characteristics and dynamic responses of herringbone-grooved thrust bearings, to be presented in The 3rd International Conference on Mechanical Engineering and Automation Science (ICMEAS 201), O ctober, 201
- Yunluo Yu, Guang Pu, and Kyle Jiang, Numerical modelling and analysis of hydrostatic thrust air bearings for high loading capacities and low air consumption, to be presented in The 3rd International Conference on Mechanical Engineering and Automation Science (ICMEAS 201) , O ctober, 201

Patent:

Kyle Jiang and Guang Pu, Improvements in or Relating to Gas Bearings, International patent WO201 0606 9A 1, 13 April, 201

Grant Awarded:

July 2015, Innovate UK Project 10 05 (P roof of Concept), 'Hiperturbo', £100,000, for the development of a high performance turbocharger with the proposed hybrid air bearings.

Competition Awards:

The air bearings developed in the project were installed into a turbocharger for a reduced turbo lag and increased speed. We were invited to take part in the following competitions and received prizes.

- “A High performance Turbocharger”, The Second prize, the International New Energy and Intelligent Vehicle Competition of CIEC (Suzhou region), Suzhou, China, October 2016

- “A High performance Turbocharger”, The third prize, The final of the International New Energy and Intelligent Vehicle Competition of CIEC, Beijing Diaoyutai State Guest Houses, Beijing, January 201

TABLE OF CONTENTS

LIST OF TABLES

LIST OF FIGURES

NOMENCLATURE

α	Surface correcting coefficient
α_g	Ratio of groove width to total width (groove plus ridge)
β_g	Angle of herringbone grooves, degree
γ	Deformation ratio of the O-ring
γ_g	Fraction of bearing length occupied by grooves
ε	Eccentricity ratio, *e/c*
ζ	Bearing length to diameter ratio
η	Viscosity of fluid, $p_a \cdot s$
θ	Circumferential coordinate
$\Delta\theta$	Distance between two points in θ direction
θ_{xi}, θ_{yi}	Rotational displacement of i^{th} Node under right hand rule
λ	A complex root of the equation
λ_m	Mean free molecular path of air and atmospheric pressure
λ_g	Groove width
v_0	Characteristic speeds in z direction, $v_0 = u_0 \frac{h_0}{l_0}$
ξ	Coordinate along the circumferential direction
ρ	Density of the fluid, kg/m^3
ρ_0	Local density in the fluid film, kg/m^3
τ	Dimensionless time, $\frac{\omega t}{2}$
ω	Rotational speed, *rad/s*

ω_{sr}	Relaxation factor
ω_w	Angular frequency of the journal orbit (whirling frequency), *rad/s*
Γ	Projected boundaries of the controlled volume
Λ	Compressibility number or bearing number
Ω	Whirling frequency ratio or perturbation frequency ratio
∇	Differential operator
c	Radial clearance, μm
A_r	Restricted area, m^2
b_0	Characteristic lengths in z direction
b_s	Damping coefficients of the support
C_d	Discharge coefficient of orifices
C_{corf}	Correction coefficient
d_0	Orifice diameter, *mm*
dl	Unit length of each cell boundary at a controlled volume in FVM
$d_{i,j}$	Damping coefficients, *Ns/m*
d_{poc}	Pocket diameter, *mm*
$d_{xx}, d_{xy}, d_{yx}, d_{yy}$	Equivalent damping coefficients at a static equilibrium position, *Nm/s*
D	Diameter, *mm*
D_{kn}	Inverse Knudsen number
e	Eccentricity, μm
f_p	Excitation frequency

F_{X0brg} , F_{Y0brg}	Bearing forces in the Δx_j And Δy_j Directions at the static equilibrium position
$\boldsymbol{g}$	Body accelerations (per unit mass) acting on the continuum
G_{num}	Number of herringbone grooves
h	Air film thickness, μm
h_0	Characteristic film thickness, μm
H_d	Local clearance at the downstream of an orifice at the entrance to air film
h_g	Maximum depth of herringbone grooves, μm
H_u	Local film clearance upstream at the volume under the orifice
H	Dimensionless film thickness, h/c
H_g	Maximum groove depth ratio, h_g/c
$i - 1/2$	Interpolation values of *P* at the boundary of two adjacent controlled volume in FVM
ID	Inner diameter, *mm*
$Img()$	Imaginary part of a complex number
I_D	Lumped diametral moment of inertia
I_P	Polar moment of inertia
$j - 1/2$	Interpolation values of *H* at the boundary of two adjacent controlled volume in FVM
$k_{i,j}$	Stiffness coefficients, *N/m*
K_d	Entrance loss coefficient
K_n	Knudsen number

$k_{xx}, k_{xy}, k_{yx}, k_{yy}$	Equivalent stiffness coefficients at a static equilibrium position, *N/m*
$K_{xx}, K_{xy}, K_{yx}, K_{yy}$, $D_{xx}, D_{xy}, D_{yx}, D_{yy}$	Dimensionless form of stiffness and damping coefficients at a static equilibrium position
l	Length of the bearing, *mm*
l_0	Characteristic lengths in ξ direction
$\vec{n}$	Outward unit vector normal to the boundaries of each cell at a controlled volume in FVM
$\boldsymbol{N_{ori}}$	Number of orifices
OD	Outer diameter, *mm*
p	Pressure in the air film, bar
$\bar{p}$	Flow pressure, *bar*
p_0	Flow pressure at the downstream of an orifice, *bar*
p_a	Ambient pressure，1*bar*
P_{avg}	Average pressure, *bar*
p_c	Local static pressure at the pocket edge, *bar*
P_d	Flow pressure downstream at the entrance, *bar*
p_{dyn}	Dynamic pressure, *bar*
p_s	Flow pressure at the upstream of an orifice, *bar*
P_u	Flow pressure upstream at the volume under the restrictor
P	Dimensionless pressure, p/p_a
P_s	Supply pressure, *bar*
q	Displacement vector in governing equation of motion

Q_p	Slip flow corrector for Poiseuille flow
Q_c	Slip flow corrector for Couette flow
$\mathcal{R}(\Delta\theta^2)$	Lagrange remainder
$Re()$	Real part of a complex number
R_{spec}	Gas constant
r_0	Bearing radius, *mm*
t	Time, *s*
T	Temperature in Kelvin, *K*
$\boldsymbol{u}$	Flow velocity, *m/s*
$\overline{u}$	Averaged velocity, *m/s*
u_0	Characteristic speeds in ξ direction, journal surface speed in journal bearings
W	Lumped mass
x_i, y_i	Translational displacement of i^{th} Node
x_{J0} , y_{J0}	Static equilibrium position of the journal centre
$\Delta x_J, \Delta y_J$	Displacement of the journal centre in the *x* and *y* directions
$\Delta\dot{x}_J,\ \Delta\dot{y}_J$	Velocity of the journal centre in the *x* and *y* directions
$X_{J1},\ Y_{J1}$	Dimensionless amplitude of the displacement in the Δx_j And Δy_j Directions
z	Coordinate along the axial direction
Z	Dimensionless axial coordinate
$\dot{m}_{ori}$	Flow rate through an orifice, kg/s
$\dfrac{\dot{m}_{ori}}{\partial\xi\partial z}$	Flux term or flow rate per unit area

$\frac{\partial P}{\partial X_J}, \frac{\partial P}{\partial Y_J}$	Changes of dimensionless pressure introduced by the displacement of the journal centre
$\frac{\partial P}{\partial \dot{X}_J}, \frac{\partial P}{\partial \dot{Y}_J}$	Changes of dimensionless pressure introduced by the velocity of the journal centre
$[\mathbf{0}]$	Null matrix
$[\mathbf{I}]$	Unit matrix
$\boldsymbol{C}$	Damping
$[\boldsymbol{C_s}]$	Structural damping matrix
$[\boldsymbol{C_b}]$	Bearing's damping matrix
$[\boldsymbol{C_v}]$	Structure Damping matrix of the bearing sleeve
$[\boldsymbol{F}]$	Force vector
$[\boldsymbol{F_{brg}}]$	The bearing force vector
$[\boldsymbol{F_g}]$	Static gravitational force vector
$[\boldsymbol{F_{ub}}]$	Synchronous unbalance excitation force vector
$[\boldsymbol{G}]$	Gyroscopic matrix
$[\boldsymbol{CG_{sys\_1}}]$	System damping and gyroscopic matrix
$\boldsymbol{J}$	System characteristic matrix
$\boldsymbol{K}$	Stiffness
$[\boldsymbol{K_s}]$	Structural stiffness matrix derived from strain energy
$[\boldsymbol{K_b}]$	Bearings' stiffness matrix
$[\boldsymbol{K_v}]$	Stiffness matrix of the bearing sleeve
$[\boldsymbol{K_{sys\_1}}]$	System stiffness matrix
$\boldsymbol{M}$	System mass and inertia

$[\boldsymbol{M}]$	Mass and inertia matrix
$[\boldsymbol{M_s}]$	Shaft structure mass and inertia matrix
$[\boldsymbol{M_v}]$	Bearing sleeve mass and inertia matrix

CHAPTER 1: INTRODUCTION

This thesis presents a study on the development of hybrid air bearings with a fixed clearance boundary for micro turbomachinery. The research was driven by the needs of high speed and mobile turbomachinery and stationary compressed air source cannot be used, such as turbochargers and micro gas turbine engines.

This chapter introduce the research conducted in this project. A brief background of air bearings is presented. The aim, objectives and contributions to the knowledge of the field are then introduced, followed by a summary of the thesis organisation.

1.1 Background

Air bearings are bearings that use a thin air film to provide exceedingly low friction between surfaces. They can provide oil-free and frictionless precision motions. They are widely applied in precision and high-speed machines, including high speed spindles, turbo expander/generators etc. Air bearings can be classified as either 'hydrostatic', 'hydrodynamic' or 'hybrid'. Hydrostatic air bearings rely on external compressed air source to form the air films and lift the rotor of the machine during their operation. This makes them not suitable for portable devices. Hydrodynamic air bearings require high relative speeds between surfaces to lift loading, but have a dry friction issue at low speed. Hybrid air bearing are externally pressurized but with enhanced features used in self-acting bearings.

In this study, a hybrid journal air bearing is proposed. It is designed as a combination of a hydrostatic bearing with orifice restrictors and a hydrodynamic bearing with herringbone grooved journal. The hybrid bearings work as hydrostatic air bearings to lift the rotor by compressed air at low speeds, which occur at the start and the end of a rotation session. When the rotational speed goes over a threshold, the bearings will be self-acting to form air films and lift the rotor. The supply of compressed air can be then switched off to reduce air consumption. As either the start or stop session usually takes a few seconds, the proposed hybrid air bearings only need a very small compressed air source to support them. In applications such as turbochargers and micro gas turbine engines, an air reservoir could be sufficient to supply air for the bearings to start. The reservoir can be refilled with the air from the compressor of these machines. Therefore, the proposed hybrid air bearings have the potential to reduce the reliance of compressed air and be applied in turbomachinery.

1.2 Aim and objectives

The aim of this PhD project is to develop a type of hybrid journal air bearings with reduced reliance on the supply of compressed air for mobile turbo machinery applications, typically including turbochargers and micro gas turbine engines used as range extenders for electric vehicles. This research will study the proposed hybrid air bearing theoretically and experimentally.

Three challenges are posed for this research. The first is the modelling of hybrid journal air bearings and the rotor structure they support, to enable the performance of the rotor bearing system to be predicted. The second is to apply the proposed hybrid air bearings to a rotor of a micro turbomachine and prove the bearings work in both hydrostatic and hydrodynamic modes. The third is to verify the accuracy of the rotor bearing model with experiments.

The objectives of the research to achieve the research aim mentioned above are set out below:

1. Review the state of the art of the research relating to air bearings and their applications in high-speed turbomachinery.

2. Develop numerical approaches to model journal air bearings and verify the validity of the methodology used by comparing some predicted performance with references.

3. Use appropriate methodology to model the rotor bearing system. The rotor is modelled as linear using finite element method based on Timoshenko beam theory with gyroscopic effect.

4. Perform theoretical studies using the developed model on rotor bearing system with hydrostatic journal air bearings. Verify numerical analytical methodology by comparing predicted performance with experimental ones.

5. Perform theoretical studies using the developed model on the proposed hybrid journal air bearings. Design hybrid air bearings for the developed test rig. Verify the predicted performance of the system with experiments.

1.3 Contributions

By accomplishing the aim and objectives, this research has three novel contributions to air bearing knowledge and applications:

1. A type of hybrid journal air bearing has been developed for applications in micro turbomachinery. The hybrid air bearings have been fitted to a rotor from a turbocharger for 2Litres diesel engines. The feature of the hybrid air bearing has been proven to work in experiments by cutting off compressed air when the rotational speed is sufficiently high.

2. A novel type of herringbone grooves has been developed for hybrid air bearings in the project for improved performance. The grooves are also applicable to hydrodynamic air bearings.

3. The proposed hybrid journal air bearing design (combinations of hydrostatic air bearings with orifice restrictors and herringbone grooved self-acting bearings) is modelled using finite volume method. The bearing model is used in the non-linear transient rotor dynamic analysis and can give adequate predictions of the unbalance response of a non-symmetric rotor bearing system. The literature survey prior to this project shows the research work on the same type of hybrid journal air bearings is limited to using narrow groove theory and linear perturbation analysis.

1.4 The outline of the Thesis

This thesis consists of six chapters. Chapter 1 is the introduction of the research topics covered by this thesis. The aim of the project, objectives and thesis outline are included.

Chapter 2 gives a comprehensive literature review summarising the previous published work in the core areas relevant to this thesis. This chapter starts with research works on hydrostatic air bearings with focus on the modelling of the bearing, mainly the restrictor system. This is then followed by reviews of hydrodynamic air bearings. Literatures reviewed in this area is focused on herringbone grooved self-act bearings. Literatures of foil air bearings and tilt pad air bearings are included but not reviewed in depth. Previous research works on hybrid air bearings are reviewed and followed by a list of areas in which the present thesis proposes to improve on. At the end, the appropriate numerical techniques in modelling air bearings and rotor bearing system are introduced.

Chapter 3 begins by introducing the theories of fluid dynamics relevant to modelling of air bearings. A numerical model based on finite difference method is developed for hydrostatic journal air bearings. A numerical mode based on finite volume method is developed for hybrid journal air bearings. Several numerical techniques are applied to provide a reliable and stable iteration process. Next, the methodology used to model rotor bearing system is introduced. The rotor used in this project is then modelled with some verifications on its dynamic properties using impact hammer tests. At the end, the analysis methods used to predict the performance of rotor bearing system are discussed under two approaches: linear perturbation analysis and non-linear transient analysis.

Chapter 4 presents the theoretical and experimental studies on hydrostatic journal air bearings with orifice restrictors. It begins with a comparison of different flow models for orifice restrictors and how they are improved in this thesis. Following on, the effects of orifice diameters, radial clearances and supply pressures on bearing's performance are investigated under non-rotational and rotational conditions. The analysis on stability and natural frequencies of rotor bearing system are performed using linear bearing models on two cases, namely **CASE I & II** respectively. Then a test rig is designed according to the system configuration in **CASE II**. The unbalance responses of the rotor in the test rig are predicted using non-linear transient analysis and measured experimentally.

Chapter 5 is focused on the investigation of hybrid journal air bearings with orifice restrictors and herringbone grooved journal. It starts with setting the numerical model for the hybrid journal air bearing. A modified groove profile with cosine spline is then proposed as an enhancement. The influences of some design parameters on performance of hybrid journal air bearings are then investigated under rotational condition. The analysis on stability and natural frequencies of rotor bearing system supported by hybrid journal air bearings are performed on the two cases used in Chapter 4. Finally, experimental investigations on unbalance responses are carried out on hybrid journal air bearings using the developed test rig under two working conditions: with compressed air supply and without. The unbalance responses under these two conditions are also predicted using non-linear transient analysis. The experimental and prediction results are compared and discussed.

Chapter 6 concludes the research work in this PhD project. The major research conclusions are drawn. Future research work on hybrid air bearings and their applications is suggested.

CHAPTER 2: LITERATURE REVIEW

2.1 Introduction

This chapter gives a comprehensive review on the techniques relevant to the air bearings research project. Firstly, literatures of hydrostatic, hydrodynamic and hybrid journal air bearings are reviewed. Secondly, numerical techniques used in modelling of air bearings are introduced. Finally, literatures on modelling and stability analysis of rotor bearing system are discussed.

Air bearings use a thin film of pressurized air to support load and provide exceedingly low friction. Properties of this thin air film are governed by the compressible Reynolds Equation. Air bearings have been developed for over 50 years. Early studies on air bearings were completely based on experiments and engineering practice. The results were used to design air bearings in an empirical method [1-3]. More recent literatures on air bearings tends to use numerical approaches to solve the compressible Reynolds Equation and predict the dynamic performance of the air bearings. Experiments are generally included as verifications to the numerical approaches. The review of the air bearing technology in this section will be focused on hydrostatic air bearings, hydrodynamic air bearings and hybrid air bearings. Foil air bearings are briefly reviewed within the hydrodynamic air bearings to cover an important category of air bearings. However, as this thesis is focused on developing a type of hybrid air bearings with a fixed clearance boundary, foil bearings have compliant clearance boundaries and is outside the scope of this project. They will not be reviewed in depth, so as the tilt pad air bearings.

2.2 Hydrostatic air bearings

In hydrostatic air bearings, a thin air film is maintained between two opposing surfaces using externally pressurized air. These bearings can lift an object at zero rotational speed. The pressurized air continuously flows into bearing clearance through restrictors and escapes into the atmosphere at the two ends of the bearing. Three types of restrictors can be used in hydrostatic air bearings: capillary compensators, orifices, and porous media. The latter two are commonly used because of their compact structures and advantages in installation. Figure 2.1 shows some typical restrictor designs used in hydrostatic air bearings.

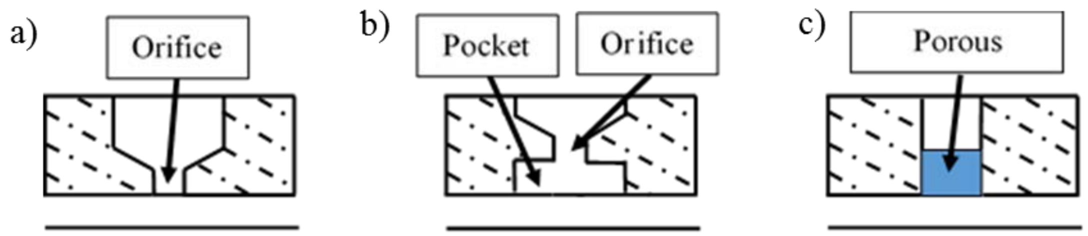

Figure 2.1 a) Orifice restrictors b) Orifice restrictors with pocket c) Porous material restrictors

The mechanism of hydrostatic air bearings makes their performance highly depend on the restrictor configurations. A major research area of hydrostatic air bearings is the bearings' performance with different restrictor configurations. It is studied both theoretically and experimentally by many researchers. An important part of these research work is the modelling of flow properties through restrictors used in the bearings. Numerical studies on hydrostatic air bearings with orifice restrictors normally using a separation of variable method [4] to calculate the overall flow rate through an orifice. One approach is to set up physical equations which accurately describe the edge loss effect by introducing correction factors [1]. The other approach is based on the CFD to simulate the flow velocity field. Numerical studies on hydrostatic air bearings with porous restrictors adopted Darcy's law [5] to model the porous media. The 3D Cauchy's law is commonly applied with finite volume method to calculate pressure drop and the across flow rate through the media. Other related methods require investigation of micro structures in porous materials [6]. Experimental work on hydrostatic air bearings involves two parts: (1) Measurements of steady state pressure distribution in air film using thrust bearings. This allows the model of restrictors and bearings to be verified; (2) Measurements of stability on the rotor dynamics.

In this section, literatures of hydrostatic air bearings with orifice restrictors are reviewed first with focus on the modelling of the restrictors. Researches on hydrostatic air bearings with porous media are discussed afterwards. The mathematical modes of them provided by different researchers are shown with comments on their limitations.

2.2.1 Modelling of orifice restrictors of hydrostatic bearings

An early study on hydrostatic air bearings with orifice restrictors from E. G. Pink [ ] reported an effect of orifices in air bearings known as 'entrance loss'. When the flow enters the bearing clearance, the flow velocity is increased and results in a significant conversion of static pressure into kinetic energy within air film. E. G. Pink provided an accurate mathematic model to take which took this effect into account. He also reported that there would be a recovery on static pressure downstream of the restrictors. The entrance loss effect and pressure recovery in [ ] are shown in Figure 2.2. Bearing reaction forces to static load of hydrostatic air bearings predicted using Pink's model in [ ] showed a good agreement with experimental data. However, a main limitation of his work is that the measurements and predictions were made only at non-rotational condition.

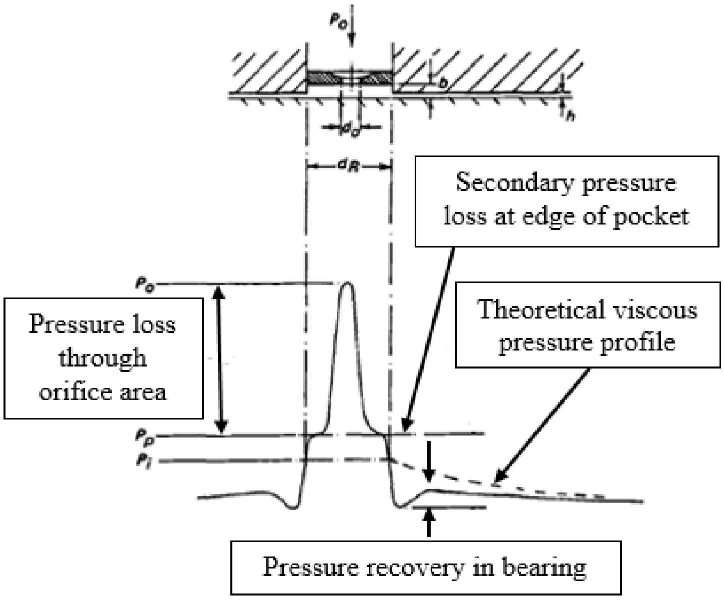

Figure 2.2 Pink's model of flow through orifice restrictors [ ]

Investigations on hydrostatic bearings with orifice restrictors were extended with the help of CFD. Flow properties through orifice restrictors were investigated and modelled with the bearing numerically. Masaaki Miyatake [8] studied the effect of micron-level (30um to 50um diameter) orifices in hydrostatic air thrust bearings and showed an increase in the load capacity under the same mass flow rate. G. Belforte and T. Raparelli [9] improved the studies on the entrance loss effect by means of performing a series of CFD analysis on bearings with plain orifice restrictors. They used an experimental method to identify the discharge coefficient experimentally [10]. The results were compared with theoretical predictions. Figure 2.3 shows the measurement method and test bench used in [10]. Figure 2.4 shows a comparison of the results between their numerical and experimental work. G. Belforte and T. Raparelli also concluded that the radius around an orifice restrictor in the thrust bearings where pressure recovery occurred could be approximated by the following relation:

$$r_i = \frac{d_0}{2} + 40 * \mathrm{h} \qquad \textit{Equation 2.1}$$

where r_i is the radius around an orifice and h the average air film thickness.

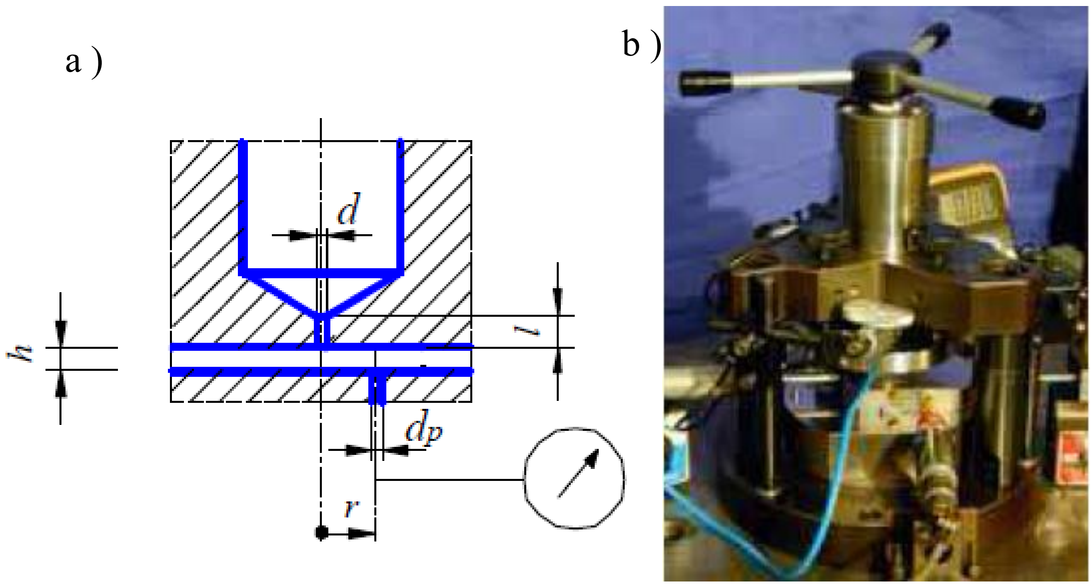

Figure 2.3 a) The pressure in the thrust bearings was measured with an off-set, r, from the location of an orifice; and b) The test bench[, 8]

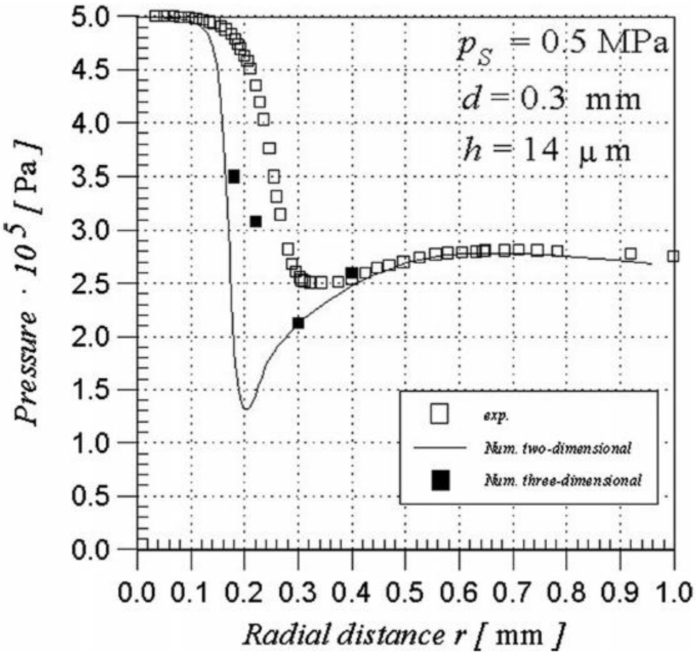

Figure 2.4 Comparison of the pressure distribution around an orifice between CFD and experimental results, G. Belforte and T. Raparelli [9, 10]

The above studies were mainly performed on hydrostatic thrust air bearings. The results proved that CFD could be employed as a reliable tool to investigate the performance of orifice restrictors. There were also plenty of works on flow properties of orifice restrictors in hydrostatic journal air bearings based on CFD, i.e. the influence of the discharge coefficient [11], and taking dynamic flow effects into account [12]. A few of them involved a similar measurement as presented in [10]. It should also be noted that the manufacturing errors of orifice restrictors had a significant influence on bearing reaction forces in both journal and thrust bearings. This influence was summarized in K. J. Stout's work [13].

The work presented in this thesis adopted the plain orifice as restrictors. The mathematical model used is based on the results in [, 9] and [10]. Other correction factors in [11-13] were also considered to further improve the accuracy of the model in predicting the performance of the bearing. The improved model and Equations will be explained in Chapter 3.

2.2.2 Modelling of porous media restrictors of hydrostatic bearings

Porous materials have been applied to hydrostatic air bearings for a long time. Among all different types of restrictors, porous material restrictors provide the most uniform pressure distribution, which results in high bearing reaction forces and stiffness. Porous hydrostatic air bearings are convenient to manufacture and can be machined into complex geometries, as the pores inside the material serve as built-in restrictors.

The literature from the 19 0s laid down the fundamentals for analyzing externally pressurized porous bearings with assumptions that flow in porous materials was one dimensional and incompressible. These early works were reviewed by Sneck in 1968 [14] and then updated by Majumda[15] in 19 6. Later, other corrections, such as compressible and slip flow, were included to improve the accuracy of predictions. Mori [16] extended the theory by introducing the method of equivalent clearance, which allowed for the two-dimensional flow to be accounted. One of the commonly adopted 3D models to predict the flow in the porous material for hydrostatic air bearings was developed by Majumdar [1 , 18]. Based on this theory, Rao [19-21] studied the rotational performance of porous hydrostatic journal air bearings. The equivalent stiffness and damping coefficients were calculated and the results were compared with previous solutions, showing better accuracy. He also suggested that if the thickness of the porous material was small compared with the radius of the bearing, the flow direction could be considered as radial only.

All above literatures have not addressed tangential velocity slip effect at the porous-fluid film interface. K. C. Singh [22] and his co-workers developed a method to predict the steady-state performance of an annular thrust bearing based on the Beavers-Joseph slip velocity conditions which took the tilt and anisotropy of the porous materials into account. In Singh's report, there were three important conclusions: the slip effect was less predominant if the flow film was uniform; it was more significant in materials with lower permeability and slip coefficient; and it became more dominant at higher radius to film thickness ratio.

Kwan [23] summarized most of the previous work and carried out a series of experiments and measurements based on hot isostatically pressed porous alumina. In his work, several specimens with different porosities ranging from 0.1 to 0.4 were tested. The results showed that the slip coefficient was widely spread according to open porosity, but had a good agreement with the Beaver-Joseph model when porosity was less than 0.15. In a later publication by Kwan [24] and his co-worker, a simplified method for the correction of the velocity slip effect is proposed. They compared the flow rate of air passed through two solid surfaces and that through one porous surface in the experiments. As the results implied the flow passage in the presence of a porous surface was higher, an equivalent clearance could be applied to flow rate Equations. They also explained that this equivalent clearance differed from measurements of either porous surface roughness or pore size. The exact relationship between equivalent clearance and micro structure of porous materials was not given and could only be acquired through experiments.

There were also some reports to compare the performance of different types of restrictors. Mohamed Fourka [25] compared plain orifice, orifice with pocket and porous medium in hydrostatic thrust air bearings. The results showed that the highest bearing reaction force to static load was achieved by bearings with porous media. Pocket bearings had higher stiffness but it decreased sharply as film thickness increased. In comparison, porous air bearings had a wide range of settlement and better stability. Another advantage of using porous inserts was that there would not be any local pressure loss at the entrance to the bearing surface [26]. Plain orifice bearings could also achieve high bearing reaction forces and stiffness but at the cost of high air consumption. The author suggested the design of the restrictor system should be a compromise among load capacity, stiffness and air consumption based on the application of the bearings.

To improve the stability of porous hydrostatic journal air bearings and prevent ‘pneumatic hammer’ caused by the internal cavities in the porous material, porous materials with surface-restricted layers caught the interests of researchers in recent years. Kwan also studied porous hydrostatic thrust air bearings with a two-layered structure [23]. Each layer of the porous bulk had a different permeability. The porous bearings with a similar structure were studied by a group of researchers in Japan [2 -30]. They discovered that there existed a surface-restrict layer after grinding of porous metals. This surface-restrict layer had lower permeability than the porous material itself. The report from Togo [2] showed one of the benefits of having this layer: the threshold of instability of journal bearings was improved significantly at high speeds in the experiments. The prediction from numerical studies carried out by other researchers [28-30] showed good agreement with experimental data. Additionally, these studies also implied that surface-restrict layers not only increased load capacity but also reduced friction. However, it was impossible to measure the permeability of surface-restricted layers. Yuta Otsu [31] introduced a surface restriction ratio to relate it to the permeability of porous material. By comparing flow rate passed through a porous medium with and without a surface-restrict layer, Yuta also showed that the thickness of the surface-restricted layer had little influence on the characteristics of bearings.

For the purpose of reducing the size of porous air bearings, the shape of compressed air supply area (the channel from which compressed air are fed to porous material) was investigated by Yoshimoto [30] to avoid deformation of thin porous media. He compared the performance of hydrostatic thrust air bearings with annular groove to supply air with those using a full circile to supply air and concluded that static stiffness was mainly influenced by the outer diameter of the supply area and a surface-restricted layer could reduce the effect of the supply area on bearing's characteristics.

2.3 Hydrodynamic air bearings

Hydrodynamic air bearings are also known as 'self-acting air bearings'. Unlike hydrostatic air bearings, a thin pressurized air film in these bearings is generated from the relative motion between two opposing surfaces instead of relying on external pressurized gas source. In conventional hydrodynamic air bearings, the boundary of air film is non-compliant and the pressure in the air film is built up when air is dragged into physical wedges between the two bearing surfaces. Some sub-structures can be applied on bearing surfaces to enhance the performance, for example, spiral grooved journal and multiple lope bearing sleeve. Figure 2.5 indicates the mechanism of pressure build-up in a plain journal bearing.

Another well-known type of hydrodynamic air bearings are foil air bearings. The core of a foil bearing is a compliant, spring like foil lining which supports the rotor at zero speed. Once spin speed of the rotor is fast enough, the foil and the rotor are separated by a thin air film generated from the rotation via viscosity effect. This flexible clearance boundary makes foil air bearings clearly distinguished from their hydrodynamic relevants.

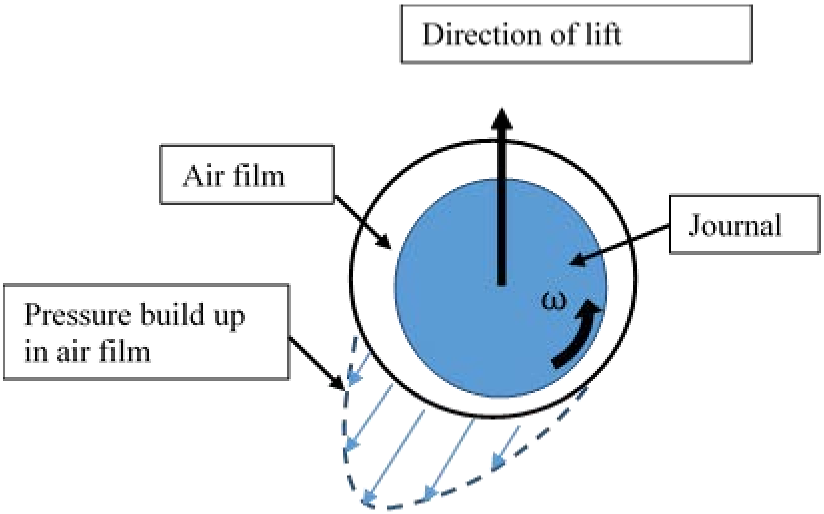

Figure 2.5 Formation of air film in hydrodynamic journal air bearings, ω is rotating direction of journal

Literature found so far on conventional hydrodynamic air bearings is focused on spiral grooved or herringbone grooved air bearings, which related most to the research work in this project. Literature on foil air bearings is also included in this section to cover the knowledge.

2.3.1 Herringbone grooved hydrodynamic air bearings

Conventional hydrodynamic air bearings usually use some sort of surface structures to facilitate the pressure built-up. These surface structures are machined permanently either onto the stationary bearing sleeves or the rotating components. Some typical designs are known as multilobe bearings and spiral grooved bearings. The latter are also known as herringbone grooved bearings, which are widely used because of their excellent stability and load capacity compared with others. The review of conventional hydrodynamic air bearings is focused on herringbone grooved bearings in this section.

The working principle of herringbone bearings is developed from step sliders. It makes use of the pressure surge caused by sudden reduction in fluid film thickness. A herringbone grooved air bearing has a number of groove-ridge pairs, which makes the overall pressure profile into a saw teeth shape. Grooves can either be engraved fully or partially on the surface with a certain angle inclined to the axial direction. These bearings are normally light loaded and need to operate at high speeds (several ten thousand to several hundred thousand rpm) with extremely low radial clearance ranging from 2 to 10μm. In practice, such small clearance demands a high precision manufacturing process. On the other hand, there is no need for an external gas source, which simplifies bearing systems and makes the machine portable. Hydrodynamic air bearings are normally applied in oil-free turbo-machinery and instrumentation, such as optical scanner.

The development of hydrodynamic herringbone bearings started around 1965. Early work was focused on the prediction of the bearings' characteristics using the narrow groove theory (NGT) [32, 33]. In such analysis, several assumptions are made. First, it is assumed that the herringbone bearings have an infinite number of grooves with infinitesimal width. In this case, the pressure profile in the air film becomes smooth. Secondly, deflection used to analyse rotational performance should stay within small amplitude, for example, within 0.2 eccentricity ratio. These assumptions limit the use of NGT to herringbone air bearings with large groove number. Later in 1969, Cunningham[34] compared the empirical formulae for herringbone journal bearings in experiments for six different rotors and concluded that load capacity was over predicted at low groove number and the altitude angle was smaller. After that time, research work on the herringbone bearings was transferred into numerical analysis based on the finite difference method (FDM), finite volume method (FVM) and finite element method (FEM). Bonneau [35] used a finite element method with the Petrov-Galerkin weighted discrete scheme to analyze herringbone journal bearings with 4 to 16 grooves. The method produced a relatively accurate prediction on the load-deflection relation. Although the finite element method had advantages in handling complex geometries, the process required a long computational time and was complex in coding. The finite difference method and finite volume method were used by other researchers in attempting to find a fast and accurate solution to a problem. Kobayashi [36] carried out a numerical analysis of herringbone journal bearings based on a finite difference scheme in a skewered coordinate system. The prediction in load capacity had a good agreement with Cunningham's experiment when the rotor speed was 38k rpm. However, the predicted loading capacity was lower than reality for a rotor speed at 60k rpm and higher for a rotor speed less than 20k rpm. It should be noted that in [36], Kobayashi considered the differences between having a grooved journal and having a grooved sleeve in numerical analysis. Kobayashi also presented a non-linear bearing model using semi-implicit Crank-Nicoson algorism [3] , which had advantages in generating convergent numerical solutions over others.

Another important research stream in the study of herringbone bearings is the optimization in the design of bearings' geometry. In [36], Cunningham noted that groove depth had a significant influence on the load capacity of the bearings. Gad [38] and his co-workers investigated the influence of the groove profile by introducing the bevelled-step groove design. Oil lubricated herringbone bearings with this groove profile showed an increase in load capacity and lower friction torque compared to a rectangular groove profile. Although, the groove geometry in Gad's publication was based on oil-lubricated herringbone bearings, the results still serve as a reference for gas-lubricated herringbone bearings and a further improvement of the performance can be achieved by modifying the groove profile.

There are other attempts to optimize the gas-lubricated herringbone bearings. In Ikeda [39] and his co-workers' research, a hydrodynamic air bearing with non-uniform herringbone grooves was proposed for high speed spindles. The grooves were designed to grow narrower towards the centre along axial direction with curved pitch as shown in Figure 2.6. The numerical model was based on the finite volume method under the boundary-fitted coordinate mesh. Their results showed a 23% increase in the critical speed and had good agreement with experimental data. Schiffmann [40] suggested a groove design with variable width, depth and local pitch at four different locations in the grooved region along the axial direction, as shown in Figure 2. . The enhanced groove design increased the clearance to diameter ratio up to 80% while maintaining the same stability margin. A table of the optimum groove parameters for different bearing length to diameter ratios and compressibility numbers was summarized as guidelines for designs. Schiffmann's bearing model was based on the narrow groove theory.

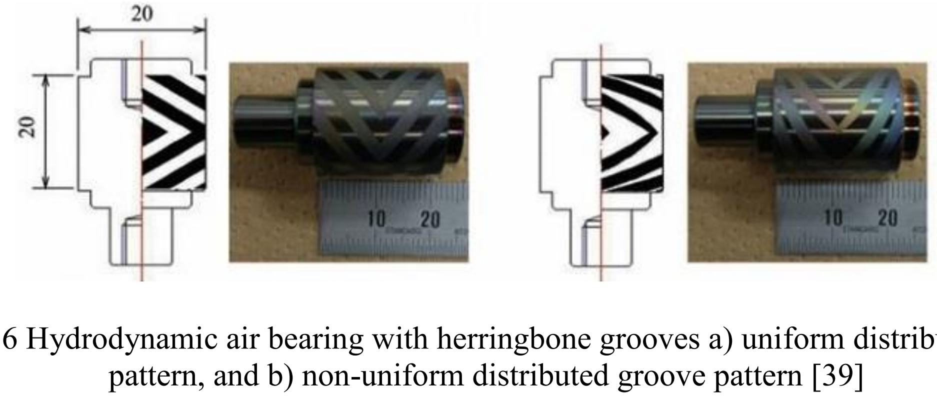

Figure 2.6 Hydrodynamic air bearing with herringbone grooves a) uniform distributed groove pattern, and b) non-uniform distributed groove pattern [39]

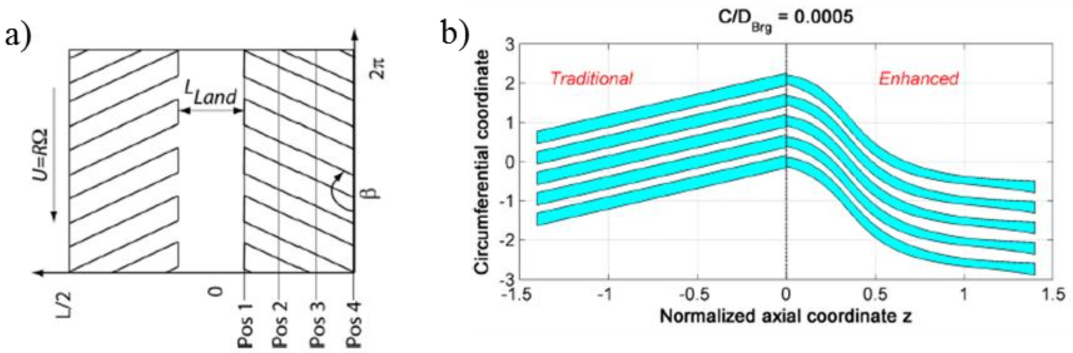

Figure 2. a) Position of the interpolation points for the enhanced groove geometry b) Traditional groove shape and the enhanced groove shape [40]

Although the optimization strategies in [39, 40] showed improvement on the performance of herringbone air bearings, neither of them considered the effect of the optimization on the groove profile. As suggested in [39], the original proposed groove geometry should also be shallower towards the centre along axial direction, but it cannot be achieved because of the limitation of fabrication. Additionally, the grooves were manufactured on stationary parts in their experiments, where the effects of rotating groove were not involved. In Schiffmann's work [40], the bearing model based on the narrow groove theory restricted their results to herringbone air bearings with large groove numbers. In project, the conventional rectangular groove profile was optimized into a curved profile of cosine waves and machined using an advanced laser system. The detail of the proposed novel groove design was discussed in Chapter 4.

The effect of using viscoelastic support on the stability of herringbone air bearings was also discussed by some researchers [41-43]. In these works, the supporting structure were illustrated as a spring and damper element in parallel with their equivalent stiffness and damping coefficient defined as Equations 2.2 and 2.3. Tomioka and Miyanaga [41] showed that the stability of the system could be effectively improved when the stiffness of the support was close to that of herringbone air bearings. In their case, the ideal damping coefficient of the support was between 0.2 and 0.6. They also found that the viscoelastic support system could have worse stability than the rigid support system if the damping coefficient of the support was less than 0.1 [42]. Experiments were also provided to verify the predictions. The empirical equations to describe the dynamic properties of O-rings were concluded as shown in Equations 2.2 and 2.3 [43].

$$k_s = k' \exp\left(k'' f_p\right)$$ *Equation 2.2*

$$b_s = b' + \frac{1}{\exp\left(b'' f_p\right)}$$ *Equation 2.3*

where k_s and b_s are the stiffness and damping coefficients of the support, k', k'', b', b'' the dynamic properties of the O-rings determined by the least square method from experimental data, and f_p the excitation frequency.

The analysis of stability in Tomioka and Miyanaga's work was performed using both linear perturbation method and non-linear transient method. The two methods had good agreement with each other. However, their rotor model was based on a symmetric rigid rotor supported by two identical herringbone bearings without considering gyroscopic effects. The bearing model was still based on NGT. The research presented in this has extended their study to a non-symmetric rotor system with herringbone grooves fabricated on the rotor. The gyroscopic effects were also considered in the rotor model used. The model of rotor used in this project is introduced in Chapter 3. Because the viscoelastic support in present work was formed by nitrile rubber O-rings, Equations 2.2 and 2.3 are used as references.

2.3.2 Foil air bearings

A foil bearing is made of elastic metal with one end foils fixed on a stationary sleeve. A foil air bearing is made of elastic metal foils fixed on a stationary sleeve. The journal of the shaft is supported by these spring-loaded foil linings. Once the rotating speed of the journal is sufficiently high, the foils deform and are pushed away from the shaft by the increasing pressure within the air film. To avoid wear, the shaft must accelerate to a 'lift-off' speed quickly and work at high speeds to maintain the air pressure and keep the foils away from the shaft.

The development of foil air bearings started from the 1960s and they were first put into commercial applications on air cycle machines for airliners [44]. The application of foil bearings then expanded into different kinds of oil-free turbo machinery, such as turbo blowers and turbo generators. The advantages of foil air bearings over other types of hydrodynamic air bearings are their compliant clearance boundary, which provides excellent resistance to thermal expansion, high coulomb damping characteristic and shock load stability [44]. Figure 2.8 illustrates two types of foil air bearings: a multi-leaf foil air bearing and a bump foil air bearing.

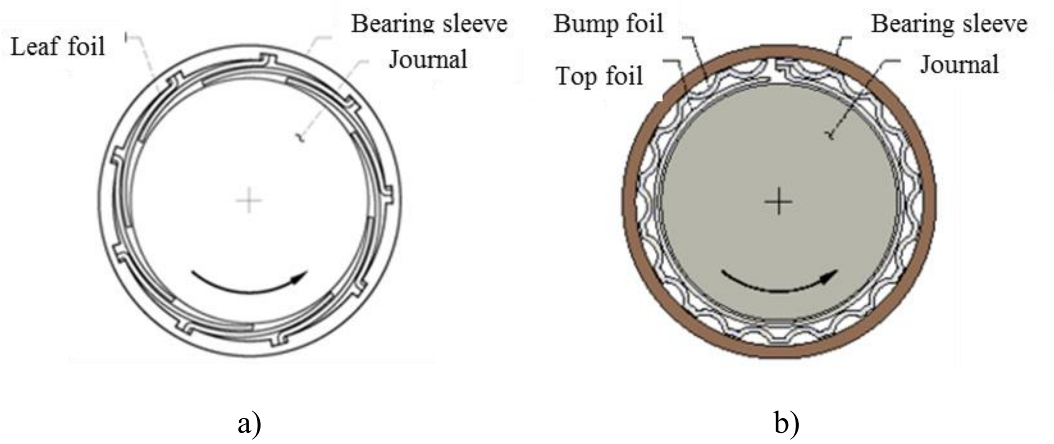

Figure 2.8 Two designs of foil air bearings [44] a) Schematic of a multi-leaf foil journal bearings, and b) Schematic of bump foil journal bearings

Unlike other air bearings, the numerical model of a foil air bearing requires interactive between air film and the compliance foil lining. An early numerical model was introduced by Heshmat [45] in which the top foil was assumed to be ideal without sag between the bumps but with membrane stress. The pressure in the air film was still governed by the Reynolds Equation while the pressure dependent clearance was considered. In later work, it was a general practice to neglect the deflection of the foil structure in axial direction [46]. Foil air bearings were investigated using both theoretical analysis and experiments in [4 -49].

Besides the foil air bearing showed in Figure 2.8, there were also studies on other types of foil bearings. San Andrés [50] compared foil air bearings using metal mesh wire with bump type foil air bearings and showed that the former offered larger damping to dissipate mechanical energy. Feng [51] analysed the performance of a novel hybrid bump-metal mesh foil bearing. Studies of foil air bearing applied in micro-turbo machinery also draw the attention of the author. Most rotors used in turbo machinery are non-symmetric, performance of foil air bearings in these applications was investigated together with finite element rotor dynamic model [52]. Lee, Park and Sim carried a series of researches into foil bearings for turbocharger applications [53-55]. The rotor dynamic performance of lobed foil air bearings was studied and tested to evaluate the effects of mechanical preload and bearing clearance [55]. The results reveal that a decrease in radial clearance or an introduction of mechanical preload could improve the performance of foil air bearings. They also carried out a feasibility study of a foil air bearing supported turbocharger for a two-litre diesel engine [53]. In their latest work [54], the rotor dynamic performance of the turbocharger with foil air bearings was compared to that supported by floating ring bearings. The tests showed that the turbocharger equipped with foil air bearings provided 20% higher rotational speed and showed improvements in rotor dynamic performance. Although the finite element based rotor model was used in [53-55], the foil air bearings were modelled as a linear system using perturbation method, in which bearing forces were represented by equivalent stiffness and damping coefficients.

In the case that foil air bearings are modelled as non-linear as reported in [56-58], a non-simultaneous routine was generally adopted to solve the bearing model and the system governing equations of motion. This is also the case in non-linear transient analysis of conventional air bearings. However, this routine does not reflect the simultaneously interaction among rotor, air film and the foil structure. It is also inherently time consuming in computations as solutions require sufficiently small time steps to achieve required accuracy. To overcome the issue, Bonello and Pham [59, 60] proposed a novel algorithm which enables to achieve the solution of the whole system simultaneously. The proposed method was cross-verified between different transformations (finite difference transformation and mesh free Galerkin Reduction) of the Reynolds Equation. They also proved that the novel Galerkin Reduction significantly reduced the computational time. This simultaneous routine was then applied on stability analysis of a turbocharger with foil air bearings in [60]. The simultaneous routine can also be helpful in the non-linear rotor dynamic analysis on other types of air bearings.

2.3.3 Tilt pad air bearings

Pivot pad air bearings, also known as tilt pad bearings, are originally designed as oil-lubricated hydrodynamic bearings for high-speed turbo machinery. The first hydrodynamic pivot pad bearing was invented by Kingsbury [61]. In the 1960s, with the increasing demand for oil-free turbo machinery, researchers started to investigate the possibility of using gas-lubricated pivot pad bearings and investigated their performance characteristics. Pivot pad air bearings are normally made of four or five individual pads which are supported by a pivot at the back, as depicted in Figure 2.9. These pads can wobble about the pivot. This feature allows a better stability compared with the conventional hydrodynamic air bearings under varying working conditions. The difficulty in predicting the flow properties for pivot pad bearings was the complexity of geometry. For example, a single pad will provide three degrees of freedom about pitch, roll and yaw axes. Timothy [62] and his co-workers summarized the detailed theoretical development of pivot pad bearings, up until very recent developments, in their review article. Unlike other types of hydrodynamic air bearings, the recent research works on the pivot pad bearings involved identification of the pad transfer function. The new approach helped develop more accurate models in predicting the rotational performance. Early work was reported by Wilkes and Childs [63]. However, the complex structure of pivot pad bearings and the assembly technique made it difficult to fit them in micro turbo machinery.

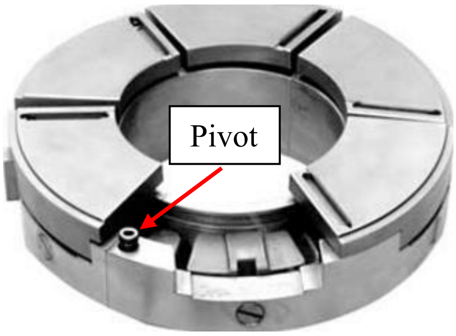

Figure 2.9 Pivot at the back of a pad in a tilt pad air bearing

2.4 Hybrid air bearings

The term ‘gas-lubricated hybrid journal bearing’ was first reported by Lund [64]. However, in his definition, it was an externally pressurized gas journal bearing including hydrodynamic effect caused by the rotating journal. The hybrid bearing concept has been extended to describe an air bearing which works in either hydrostatic or hydrodynamic depending on the rotational speed of the rotor. This kind of hybrid bearings can lift at low rotational speeds with externally compressed air and fully self-act without external air supply when rotational speed is sufficiently high.

Researches on hybrid air bearings can be found in both conventional and compliant air bearings, for example hybrid foil air bearings. Because the research in this thesis is only concerned with non-compliant air bearings, the work on hybrid foil air bearings, such as investigated in [65, 66], is not discussed here.

Ives and Rowe [6] reported hybrid journal bearings combined with hydrostatic and hydrodynamic bearings. Their effort showed that this combination did allow the bearing to support load at a wide range of speeds, including zero speed. Other researchers also reported works based on different combinations of the gas-lubricated bearings. Osbourne and San Andrés [68] reported a design of gas-lubricated journal bearings based on the combination of three lobe bearings and hydrostatic air bearings with orifices. The experimental results showed an increase in critical speed and threshold whirl frequency ratio (whirling frequency over journal rotating frequency), which allowed for a higher stable operation, compared with that of purely hydrostatic/hydrodynamic air bearing designs. The results also indicated that by increasing supply pressure, better stability could be achieved. In another report published by Osbourne and San Andrés later [69], predictions of rotor dynamic performance on a test rotor were discussed. The predicted stable operation speed was somehow much lower than that observed from the test. They suggested that the current physical models of lubrication and orifice flow need to be modified for hybrid bearings to fit the experimental observations. Zhu and San Andrés [0] also developed flexure pivot hydrostatic gas bearings which were a type of hybrid bearing in actually. The design was modified from four-pad pivot pad bearings by adding an inclined inject nozzle at the spare space between each pad, Figure 2.10. The results demonstrated an enhanced performance compared with the original four pads' design. In a later publication by San Andrés [1] , the effect of supply pressure in hybrid bearings in [0] on the vibration while crossing system critical speeds was investigated. It was found that the use of external pressurization stiffened the bearings and increased the rotor-bearing system critical speeds. However, the damping ratio of the system decreased accordingly, which made the system more sensible to imbalance when crossing critical speeds. Additionally, the experiments in [1] showed no external pressurization would be necessary for operation beyond the critical speeds of the rotor-bearing system. In particular, the critical speeds during coast down could be fully eliminated over an extended operating speed range by manually control the external supply pressure.

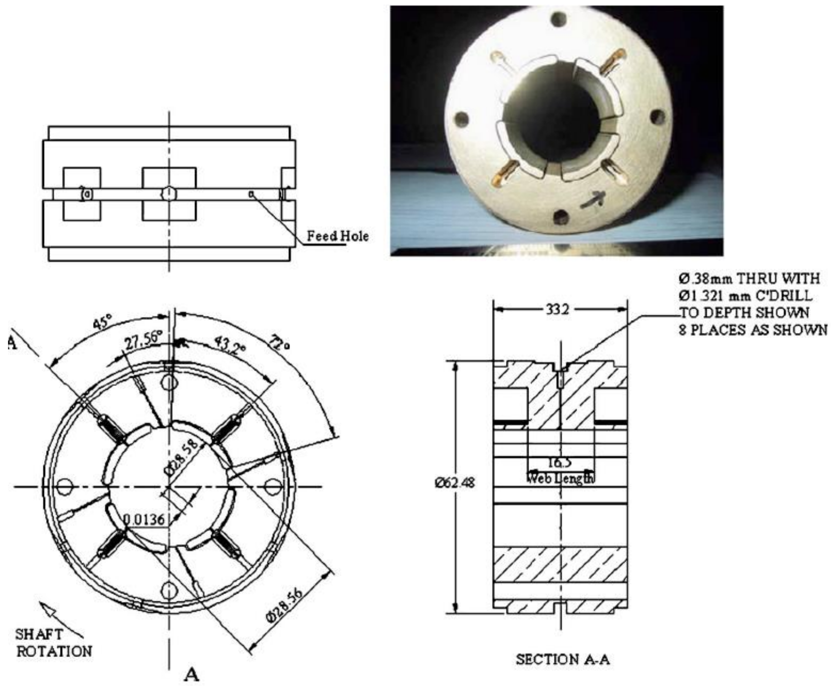

Figure 2.10 Flexure pivot hybrid gas bearings designed by Zhu and San Andrés [0]

The advantages of hybrid air bearings demonstrated in [68- 1] inspired the author to further investigate into this area and provide hybrid air bearings with compact structures for micro turbo machinery. The hybrid air bearings proposed in the thesis is a combination of hydrostatic air bearings with plain orifice restrictors and hydrodynamic air bearings with herringbone grooves fabricated on the surface of the rotor. The herringbone grooves are also enhanced by a novel groove profile investigated in this research. Figure 2.11 gives a demonstration of the proposed hybrid air bearings. The most similar researches to the present work was made by

Stanev [2] and Zhang [3] . They both used the same combination proposed here, referring to Figure 2.11. According to their investigations, this type of hybrid air bearings showed improvement on non-rotational and rotational performance. Zhang's work [3] was more focused on the application in power MEMS with the gas rarefaction effects considered. Although the influence of restrictor location and fabrication defects were discussed, it was for the thrust bearings only and less interested in for the applications discussed in this thesis. In Stanev's work [2] , the performance of the hybrid journal air bearing was investigated. It was noticed that the stability of this hybrid bearing was increased significantly for a compressibility number over 10 compared with that of the hydrostatic air bearings and was lower for a compressibility number between 3 and . Stanev concluded that improvement on stiffness and stability of the bearings could be substantial for hybrid journal bearings in this configuration operating at a compressibility number over 30. However, there were some limitations on the work in [2] . Firstly, Stanev's hybrid air bearing model was based on the narrow groove theory which limits the model to bearings with large groove number. There was a need for precision models of the proposed hybrid air bearings using other numerical techniques, for example, finite difference/volume/element method. Secondly, the parametric studies on the performance, especially the stability analysis of rotor bearing system was based on the linear perturbation method, in which bearing forces were linearized and represented by equivalent stiffness and damping coefficients. In the approach in [2] , the analysis was only applied to a symmetric and rigid rotor supported on two identical bearings. No modelling of rotor was involved. Also, the steady-state amplitude of the self-excited whirl of the bearings could not be predicted using the linear rotor bearing model. Thus, the rotor dynamic behaviour of a non-symmetric rotor supported by such hybrid air bearings was not fully explained and it would be of great potential for turbo machinery applications.

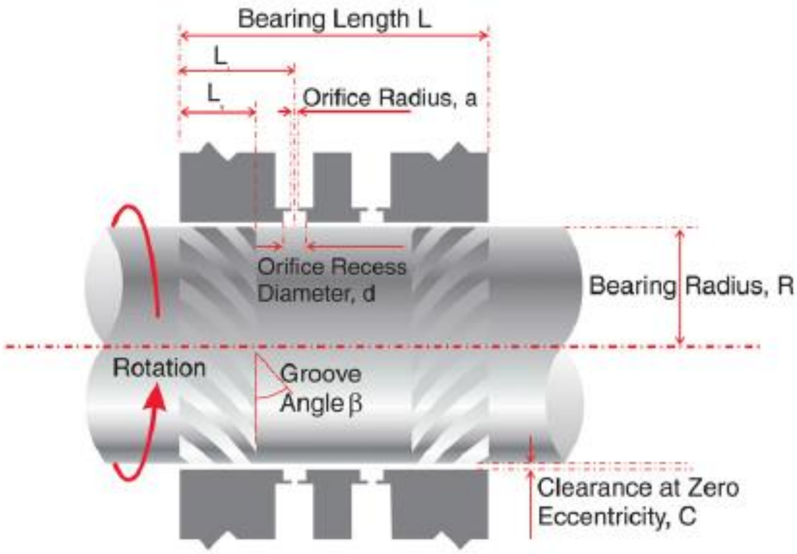

Figure 2.11 Grooved hybrid air bearings designed by P. Stanev, F. P. Wardle, J. Corbett[2]

With reference to the limitations in Stanev's work and the optimization on herringbone grooved air bearings in [38-40], the work presented in this thesis extends the studies on the proposed hybrid air bearings in following aspects:

1) A numerical model based on finite volume method is provided for the hybrid air bearings which is suitable for any groove number and took the effects of rotating grooves into account.

2) A novel profile of herringbone groove pattern in air bearings is fabricated to enhance the hybrid air bearings. Its positive effects on the performance are investigated and confirmed.

3) Both linear perturbation method and non-linear transient method are performed to study the rotational performance of hybrid air bearings and the rotor dynamic configuration they support. The former is used in theoretical studies of bearings to understand the influence of different design parameters and give predictions on the stability and natural frequencies of rotor bearing system. The latter is applied with finite element rotor dynamic model of a non-symmetric rotor to predict unbalance responses and compare with experimental measurements.

In an attempt to apply the proposed hybrid air bearings to turbomachinery, external dampers are used outside stationary bearing sleeves. The benefits of this arrangement were not only investigated by the authors in [41-43] but also by Ertas [4] and Delgado [5] . The latter two used metal wire mesh as external dampers in parallel with compliant hybrid air bearings. One improvement by using this arrangement was the elimination of self-excited whirl as the results shown in Figure 2.12 [4] . The use of external dampers could also help reduce the sensitivity of the rotor-bearing to imbalance while crossing the critical speeds of the system as addressed in [1] for hybrid air bearings.

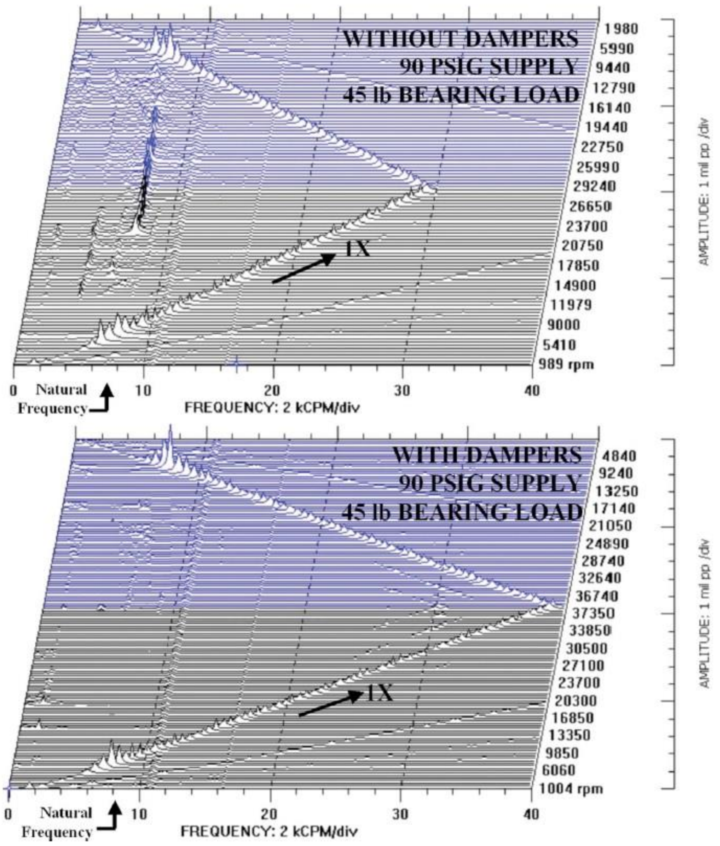

Figure 2.12 The elimination of self-excited whirl by introducing mesh metal wire damper in parallel with a hybrid compliant air bearing [4]

2.5 Numerical techniques in modelling of air bearings

tasks in this project. The nature of the work is to solve the Reynolds Equation numerically. As a second order partial differential equation, there are three discrete schemes which can be used: the finite difference method (FDM), the finite element method (FEM) and the finite volume method (FVM). In this area, NASA has provided several numerical approaches which are commonly used nowadays. Florin suggested that by applying Newton's method, it could reduce the computational time significantly. Newton's method was also proven to have better numerical stability in getting converged solutions [6] . Wang [- 9] carried out a series of studies on numerical methods which can be applied to solving a compressible Reynolds Equation. These works included comparisons of different methods with respect to computational time and numerical stability, the applications of Newton's method, successive relaxation and the G-S method. He also suggested different stopping criterion in the iterative process and analysed the truncation error of numerical approaches. The above literature was all based on FDM and they have good agreement with experimental results for hydrostatic air bearings and plain journal bearings. In the analysis of herringbone bearings, FDM is limited by the complex surface patterns. In this case, FEM is considered as an alternative approach. Challenges in the FEM approach were the interpolation of shape functions at each node in the discrete scheme. Faria [80] suggested a higher order shape function based on index function which showed relatively good accuracy. FVM was also suggested by some researchers. The FVM scheme for air bearing modelling can be derived by integrating the Reynolds Equation using the Green's theorem in a controlled volume surrounding a point in the air film. This approach showed advantages in dealing with film discontinuities and some pocket restrictor configurations [81].

The modelling of the proposed hybrid air bearings in this thesis is based on the FVM scheme. Some numerical techniques used in the FDM scheme is also adopted to improve the computational speed and numerical stability.

2.6 Modelling of rotor bearing system and stability analysis

In this project, the rotor supported by hybrid air bearings is non-symmetric and has built-on components such as a turbine and a compressor, as shown in Figure 2.13. A well accepted method to model such a rotor is using finite element method based on the Timoshenko beam theory with gyroscopic effect [82]. In this method, the rotor is modelled as linear. The shaft elements are formed of two nodes with four degrees of freedom (4-DOF) on each. The built-on components were modelled as lumped masses and moment of inertia. Figure 2.14 shows a typical shaft element used in the model and its coordinate system. This linear rotor model can be combined with either linear or non-linear bearing models to give predictions on the performance of the system.

Figure 2.13 A rotor to be supported by the proposed hybrid air bearings

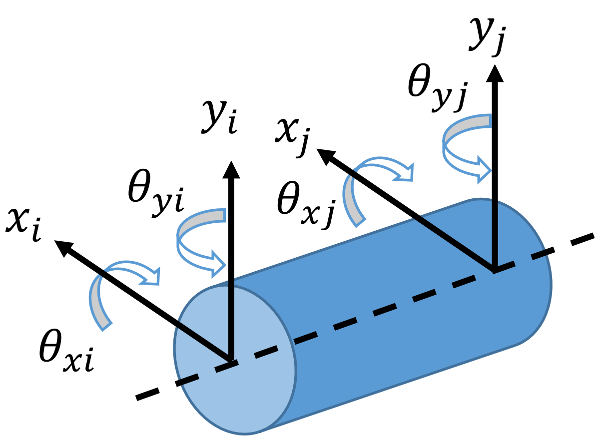

Figure 2.14 A 4-DOF model of shaft element and global coordinates used in Timoshenko beam theory

The general governing equations of motion for a modelled rotor bearing system with constant rotational speed, ω, are shown in Equation 2.4 [83]. The techniques of adding non-linear bearing model and external damper were described in [84] for several situations. They were used as references for modelling rotor bearings system in this project.

$$\boldsymbol{M}\ddot{q} + \boldsymbol{K}q + (\boldsymbol{C} + \omega\boldsymbol{G})\dot{q} = F \qquad \textit{Equation 2.4}$$

$$q = \left[\dots\ x_i\ y_i\ \theta_{xi}\ \theta_{yi}\ \dots\right]^T \qquad \textit{Equation 2.5}$$

where q is the system displacement vector to be solved, x_i, y_i the translational displacement of i^{th} node, θ_{xi}, θ_{yi} the rotational displacement of i^{th} node under right hand rule, $\boldsymbol{M}$, $\boldsymbol{K}$, $\boldsymbol{C}$, $\boldsymbol{G}$ the system mass and inertia, stiffness, damping and gyroscopic matrices, ω the rotational speed and F the force vector that contains all forces/moments, including unbalance excitations, shaft bow forces, gravitational and/or static loads and all nonlinear interconnection forces.

One important topic in the studies of air bearings is the stability of the rotor bearing system, which refers to the stability of static equilibrium position (SEP) of a journal to small perturbations. Two approaches can be used to analyse the stability of a rotor bearing system: the linear perturbation analysis and the non-linear transient analysis. In the linear perturbation analysis, the centre of journal is assumed to whirlr around the SEP under a given frequency with small amplitude. Bearing forces are linearized and represented by equivalent stiffness and damping coefficients. The stability of the linearized system can then be evaluated by omitting the force vector in Equation 2.4 and examining the eigenvalues [60, 85] . However, the linear model cannot predict the steady-state amplitude of the self-excited whirl. In the non-linear transient analysis, the bearing is modelled as non-linear. The bearing forces are no longer approximated by the equivalent stiffness and damping coefficients but forces applied to the rotor. This approach allows the steady-state amplitude of the self-excited whirl to be predicted [86].

In this thesis, the both approaches are employed. The linear perturbation analysis is used to study the influence of design parameters on rotational performance of hybrid air bearings and give predictions on the stability and natural frequencies of rotor bearing system theoretically. The non-linear transient analysis is used to predict unbalance responses of rotor bearing system and compare with those observed from experiments.

2.7 Summary

This chapter outlines the aspects relevant to the proposed hybrid air bearings and techniques used in modelling and analysis of rotor bearing system. The literature survey on hybrid air bearings has highlighted the necessity and novelty of the research presented within this thesis.

Literature reviewed on hydrostatic air bearings was focused on works that involve modelling of the bearing, especially the restrictor system and its interactions with air film. The orifice restrictors are usually modelled using empirical equations with correction on the entrance loss effect. Modelling of porous media restrictors is commonly based on 3D Cauchy's law.

In conventional hydrodynamic air bearings, spiral or herringbone grooved bearings are often used because of their excellent stability compared to others. Numerical models of herringbone grooved bearings are usually based on one of the following approaches: NGT, FDM, FEM and FVM. Research works also show that the performance of this type of air bearing can be improved using optimized groove geometry and viscoelastic supports. Hydrodynamic air bearing with compliant bearing boundaries, such as foil bearings and tilt pad bearings are reviewed to cover the relevant knowledge.

Hybrid air bearings combine the features of hydrostatic and hydrodynamic air bearings. Different combinations are possible in this category, for example, hybrid herringbone grooved bearings and hybrid pivot pad bearings. The relevant literatures of hybrid air bearings show that progress has been made in improving the load capacity and stability. By means of adjusting the supply air pressure, hybrid air bearings can also change the system’s critical speeds.

Modelling of air bearings requires the Reynolds Equation to be solved numerically. Newton’s method and successive relaxation techniques are commonly applied with several mesh based algorisms to provide the solution.

Flexible rotors used in rotor dynamic analysis are modelled using finite element method based on the Timoshenko beam theory with gyroscopic effect. The governing equation of motion for a rotor bearing system can either be used in a linear analysis approach or a non-linear approach to give predictions on the stability information of the system.

CHAPTER 3: NUMERICAL ANALYSIS OF AIR BEARINGS

3.1 Introduction

This chapter introduces the theories used for analysing the performance of air bearings and the development of numerical air bearing models to be used in the study as presented in the following chapters. The bearing models are derived for gas-lubricated journal bearings with non-compliant boundaries. Truncation errors are provided for analysing the accuracy of the bearing models. Both linear perturbation analysis and non-linear transient analysis are explained in order to investigate the stability and unbalance responses of gas-lubricated journal bearings. The rotor used in this project is modelled using finite element method based on Timoshenko beam theory.

This chapter starts with an introduction to the theories of fluid dynamics relevant to gas-lubricated bearings, including the effects of slip flow. Next, air bearing models are developed with assumptions and numerical techniques. The proposed numerical approach is then used to analyse hydrostatic journal air bearings with pocketed orifice restrictors for verification. The validity and accuracy of the rotor model is investigated using an impact hammer on a free-free rotor condition. Then, the linear perturbation analysis and its limitations are discussed. Afterwards, non-linear transient analysis is carried out based on a non-simultaneous routine. Finally, a summary is provided at the end of the chapter.

3.2 Modelling of gas-lubricated journal bearings with non-compliant boundaries

In General, gas-lubricated bearings can be modelled using the compressible Reynolds Equation. In the study, the Reynolds Equation is solved numerically by means of finite difference methods (FDM) and finite volume method (FVM). Other flow effects can be considered by adding boundary conditions before solving the Reynold Equation.

3.2.1 Discrete scheme of Reynolds Equation

The performance of a journal air bearing largely depends on five important parameters: the pressure (p), the rotational speed (ω), the air film thickness (h), the bearing radius (r_0) and the length of the bearing (l). Their relationships are described in the Reynolds Equation, as shown in Equation 3.3. The Reynolds Equation is derived from the Navier-Stokes Equations, Equation 3.1, and mass continuity Equation, Equation 3.2. It represents the momentum conservation as a simplified form of the Navier-Stokes Equations and mass conservation by satisfying the mass continuity of the gas.

$$\frac{\partial \boldsymbol{u}}{\partial t} + \boldsymbol{u} \cdot \nabla \boldsymbol{u} = -\frac{1}{\rho} \nabla \bar{p} + \eta \nabla^2 \boldsymbol{u} + \frac{1}{3} \eta \nabla (\nabla \cdot \boldsymbol{u}) + \boldsymbol{g} \qquad \textit{Equation 3.1}$$

$$\frac{\partial \rho}{\partial t} + \nabla \cdot (\rho \boldsymbol{u}) = 0 \qquad \textit{Equation 3.2}$$

where ρ is the density of the fluid, $\boldsymbol{u}$ the flow velocity, ∇ the differential operator, $\bar{p}$ the flow pressure, η the viscosity of fluid, and $\boldsymbol{g}$ the body accelerations (per unit mass) acting on the continuum.

The Reynolds Equation for journal air bearings is given as Equation 3.3. It is convenient to unwrap journal bearings from a radial symmetry plane by means of spreading the circular surface of the journal flat.

$$\frac{\partial}{\partial \xi}\left(\frac{ph^3}{12\eta}\frac{\partial p}{\partial \xi}\right) + \frac{\partial}{\partial \mathrm{z}}\left(\frac{ph^3}{12\eta}\frac{\partial p}{\partial z}\right) = \overline{u}\frac{\partial (ph)}{\partial \xi} + \frac{\partial (ph)}{\partial t} \qquad \textit{Equation 3.3}$$

where ξ is the coordinate along the circumferential direction, *z* the coordinate along the axial direction, p the pressure in the air film, h the local thickness of the air film. η the dynamic viscosity of air, $\overline{u}$ an averaged velocity of the rotating journal and stationary sleeve, and *t* the time.

The Reynolds Equation is a second order partial differential equation (PDE) which does not have an analytical solution, but can be solved by using numerical approaches. In practice, it is convenient to normalize the parameters and rewrite Equation 3.3 into its dimensionless form, as shown in Equation 3.5.

Normalized parameters are:

$$\theta = \frac{\xi}{r_0}, \mathrm{Z} = \frac{z}{r_0}, P = \frac{p}{p_a}, H = \frac{h}{C}, \overline{u} = \frac{\omega r_0}{2}, \tau = \frac{\omega \mathrm{t}}{2} \qquad \textit{Equation 3.4}$$

where C is for the radial clearance, p_a the ambient pressure and r_0 the radius of the journal bearing.

The dimensionless form of Equation 3.3 is:

$$\frac{\partial}{\partial\theta}\left(PH^3\frac{\partial P}{\partial\theta}\right) + \frac{\partial}{\partial Z}\left(PH^3\frac{\partial P}{\partial Z}\right) = \Lambda\frac{\partial(PH)}{\partial\theta} + \Lambda\frac{\partial(PH)}{\partial\tau},$$
$$\Lambda = \frac{6\eta\omega {r_0}^2}{p_a {h_0}^2} \qquad \textit{Equation 3.5}$$

where Λ is known as the compressibility number or bearing number. Most of the performance characteristics of air bearings can be determined with respect to Λ.

In this study, the performance of air bearings was investigated using the FDM for hydrostatic bearings and the FVM for hydrodynamic and hybrid bearings. A discretizing scheme is needed in both numerical methods. In this research, the five-point central difference scheme is adopted.

The scheme is derived from the Taylor series expansion with second order accuracy. If there are five discrete points in the air film, as shown in Figure 3.1, the pressure at point (i, j) can be expressed using the Taylor expansion.

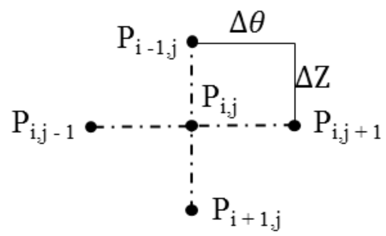

Figure 3.1 Five-point discrete scheme

$$P(i, j+1) = P(i, j) + \Delta\theta \frac{\partial P}{\partial \theta} + \frac{\Delta\theta^2}{2!} \frac{\partial^2 P}{\partial \theta^2} + \frac{\Delta\theta^3}{3!} \frac{\partial^3 P}{\partial \theta^3} \cdots \qquad \textit{Equation 3.6}$$

$$P(i, j-1) = P(i, j) - \Delta\theta \frac{\partial P}{\partial \theta} + \frac{\Delta\theta^2}{2!} \frac{\partial^2 P}{\partial \theta^2} - \frac{\Delta\theta^3}{3!} \frac{\partial^3 P}{\partial \theta^3} \cdots \qquad \textit{Equation 3.7}$$

Subtracting Equation 3. f rom Equation 3.6 and dividing the result by $\Delta\theta$ lead to Equation 3.8:

$$\frac{\partial P}{\partial \theta} = \frac{P(i, j+1) - P(i, j-1)}{2\Delta\theta} + \mathcal{R}(\Delta\theta^2) \qquad \textit{Equation 3.8}$$

where $\Delta\theta$ is the distance between two points in θ direction and $\mathcal{R}(\Delta\theta^2)$ the Lagrange remainder. It determines the accuracy of the discrete scheme and is a function of $\Delta\theta$. The same discrete scheme can be applied to other partial difference terms.

$$\frac{\partial P}{\partial \mathrm{Z}} = \frac{P(i+1,j) - P(i-1,j)}{2\Delta \mathrm{Z}} + \mathcal{R}(\Delta \mathrm{Z}^2) \qquad \textit{Equation 3.9}$$

$$\frac{\partial^2 P}{\partial \theta^2} = \frac{P(i,j+1) + P(i,j-1) - P(i,j)}{\Delta\theta^2} + \mathcal{R}(\Delta\theta^2) \qquad \textit{Equation 3.10}$$

$$\frac{\partial^2 P}{\partial \mathrm{Z}^2} = \frac{P(i+1,j) + P(i-1,j) - P(i,j)}{\Delta \mathrm{Z}^2} + \mathcal{R}(\Delta \mathrm{Z}^2) \qquad \textit{Equation 3.11}$$

The five-point central difference scheme is adopted because of its accuracy and numerical stability in iterative computations [8].

3.2.2 Assumptions and challenges in modelling air bearings

Before starting the development of bearing models, some general assumptions need to be made to simplify the problem. They are as follows:

- In an air film, the inertia effect is neglected [88].

- No turbulence flow is considered in the proposed bearing models.
- The air properties are assumed to follow the ideal gas law.
- The viscosity of air is considered as a constant.
- The pressure within the air film does not vary along the depth of the air film.

The above assumptions are applied to all bearing models proposed in this thesis.

From [88], the Reynolds Numbers are defined in the field of fluid film lubrication as:

$$R_\xi = \frac{intertia}{viscous} = \frac{\rho_0 u_0 {h_0}^2}{\eta_0 l_0} \qquad \textit{Equation 3.12}$$

$$R_z = \frac{intertia}{viscous} = \frac{\rho_0 v_0 {h_0}^2}{\eta_0 b_0} \qquad \textit{Equation 3.13}$$

where ρ_0 is the local density in the fluid film, h_0 the characteristic film thickness. l_0 and b_0 are the characteristic lengths in ξ and z direction, u_0 and v_0 are the characteristic speeds in ξ, z direction. u_0 normally refers to the journal surface speed in journal bearings and $v_0 = u_0 \frac{h_0}{l_0}$. η_0 is the absolute viscosity. All parameters are in SI units.

One challenge in the development of simulation models for air bearings is that the numerical solution to the Reynolds Equation may become unstable and diverge during iterative computations if many bearing design parameters are involved. For example, when three design parameters need to be considered for a plain journal bearing, which are the radius r_0, the length

l and the radial clearance c, the discrete Reynolds Equation will yield a converged solution under all reasonable conditions. However, for a hydrostatic journal air bearing with orifice restrictors, if three additional design parameters are involved, i.e. supply pressure P_s, orifice diameter d_0 and number of orifices, the discrete Reynolds Equation may not yield a converged solution at some conditions, when the supply pressure is high. This can be resolved using other numerical techniques, such as the Newton's method introduced in Section 3.2.4

The other sources of divergence are the high compressibility number and eccentricities. High values of these two indicate the pressure distribution within the air film will change rapidly at the physical wedge and cause divergence. This can be overcome by using fine mesh locally to smoothen the pressure profile.

In addition, the Green's theorem, Newton's method and successive relaxation are applied to the modelling and computations of the air bearings. With all the analysis and measures taken, repeated simulation practice shows that the proposed model has good numerical stability for a wide range of design and working parameters, while maintaining a reasonable computational time.

3.2.3 Mesh and boundary conditions

The mesh grid used for the bearing models is based on the five-point central difference scheme. As shown in Figure 3.2, the surface of the journal bearing is unwrapped flat from a radial symmetric plane. The unwrapped surface is meshed with a uniform grid under the following principles:

- The locations of the restrictors coincide with the grid nodes for hydrostatic journal air bearings;
- The locations of the restrictors and the apexes of herringbone grooves both coincide with the grid nodes for hybrid/hydrodynamic journal air bearings;
- The coordinate system is placed on the stationary component;
- There are M nodes in Z direction and N nodes in θ direction as indicated in Figure 3.2.

The boundary conditions applied to all journal bearing models are periodic boundary and ambient pressure boundary. Other boundary conditions, such as orifice boundary and slip flow boundary, are added by modifying the Reynolds Equation at specific nodes in the mesh. The flow continuity boundaries at the edges of herringbone grooves in hydrodynamic/hybrid journal air bearing are self-satisfied by using the FVM approach.

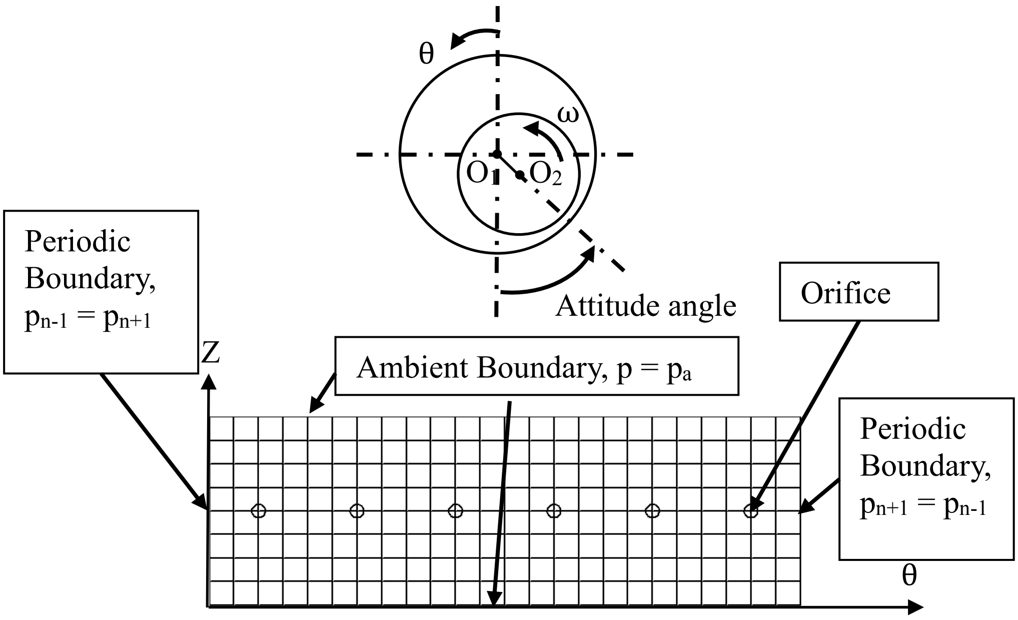

Figure 3.2 Mesh and boundary conditions for static air journal bearings

The orifice boundary is added to the nodes aligned with restrictors. The Reynolds Equation (Equation 3.3) at these nodes is modified as Equation 3.14. The term, $\frac{\dot{m}_{ori}}{\partial\xi\partial z}$ represents the flux which is caused by the orifice restrictors.

$$\frac{\partial}{\partial\xi}\left(\frac{ph^3}{12\eta}\frac{\partial p}{\partial\xi}\right)+\frac{\partial}{\partial z}\left(\frac{ph^3}{12\eta}\frac{\partial p}{\partial z}\right)+\frac{\dot{m}_{ori}}{\partial\xi\partial z}=\overline{u}\frac{\partial(ph)}{\partial\xi}+\frac{\partial(ph)}{\partial t} \qquad \textit{Equation 3.14}$$

where $\dot{m}_{ori}$ is the flow rate through an orifice. It can be calculated by solving Equations 3.15 and 3.16. $\dot{m}_{ori}$ refers to the flow rate in a 'choking' condition. $\frac{\dot{m}_{ori}}{\partial\xi\partial z}$ is the flux term or flow rate per unit area. The both can be expressed as follows.

$$\dot{m}_{ori}=Cd*Ar*p_{s*}\left\{\frac{2\gamma}{\gamma-1}R_{spec}T\left[\left(\frac{p_0}{p_s}\right)^{\frac{2}{\gamma}}-\left(\frac{p_0}{p_s}\right)^{\frac{\gamma+1}{\gamma}}\right]\right\}^{\frac{1}{2}},\frac{p_0}{p_s}>\left[\frac{2}{\gamma+1}\right]^{\frac{\gamma}{\gamma-1}}$$

Equation 3.15

$$\dot{m}_{ori}=Cd*Ar*p_s*\left[\frac{2\gamma}{\gamma+1}\right]^{\frac{1}{2}}\left[\frac{2}{\gamma+1}\right]^{\frac{1}{\gamma-1}},\frac{p_0}{p_s}\leq\left[\frac{2}{\gamma+1}\right]^{\frac{\gamma}{\gamma-1}} \qquad \textit{Equation 3.16}$$

where R_{spec} is the gas constant, T the temperature in Kelvin, p_0 the flow pressure at the downstream of an orifice, p_s the flow pressure at the upstream of an orifice and will be given at fixed value depends on the actual pressure used in the bearing, and γ the specific heat ratio of air. In most conditions, γ equals to 1.4. C_d is the coefficient of discharge. It is a factor relating the actual mass flow rate to the theoretical mass flow rate for an orifice. A_r is the restricted area. For application to air bearings, A_r can be calculated as $\pi {d_0}^2$ or $\pi d_0 h$ whichever is smaller. h is the local air film thickness.

In fluid dynamics, the fluid velocity at a solid boundary can be treated either as non-slip condition or slip condition. The non-slip condition assumes that the fluid velocity at all fluid-solid boundaries equals to that of the solid boundaries. On the other hand, the slip flow condition assumes that the fluid has a non-zero velocity, relative to the solid boundaries. In the air bearing models, these two conditions refer to the air velocity at the journal surface and stationary sleeve surface. In most of the cases, the no-slip boundary will be employed at the fluid-solid boundaries. The Reynolds Equation (Equation 3.3) can then be used straightforwardly. If the slip boundary is applied, the Reynolds Equation needs to be modified accordingly.

Here the slip flow condition is determined by the Knudsen number, Equation 3.1 , which is defined as the ratio of the mean free molecular path to characteristic dimension. The characteristic dimension for air bearing applications is the radial clearance. When the Knudsen number, K_n, is greater than 0.01, the dimensionless first order slip flow correctors, D_{kn} and Q_p, are added to the Reynolds Equation (Equation 3.5) for the Poiseuille and Couette flow terms to satisfy the slip flow boundary.

$$K_n = \frac{\lambda_m p_a}{ph} \qquad \textit{Equation 3.17}$$

$$D_{kn} = \frac{\sqrt{\pi}}{2K_n} = \frac{\sqrt{\pi}ph}{2\lambda_m p_a}$$ *Equation 3.18*

where D_{kn} is the inverse Knudsen number, and $\lambda_m = 0.064\mu m$ the mean free molecular path of air at 21 degrees and atmospheric pressure. If Q_p is the slip flow corrector for Poiseuille flow and Q_c is the slip flow corrector for Couette flow, they can be expressed as:

$$Q_p = \frac{\alpha\sqrt{\pi}}{2} + \frac{D}{6}$$ *Equation 3.19*

$$Q_c = \frac{D}{6}$$ *Equation 3.20*

where $\alpha = (2 - \sigma)/\sigma$ is the surface correcting coefficient and $\sigma = 0.8$ for practical surfaces [89].

By substituting Equation 3.19 and Equation 3.20 into Equation 3.5, the dimensionless Reynolds Equation with slip flow boundary can be generated as Equation 3.21. This equation will serve as the governing equation in FDM and FVM when slip flow boundary condition is considered.

$$\frac{\partial}{\partial \theta}\left(Q_p P H^3 \frac{\partial P}{\partial \theta}\right) + \frac{\partial}{\partial Z}\left(Q_p P H^3 \frac{\partial P}{\partial Z}\right) = \Lambda \frac{\partial (Q_c P H)}{\partial \theta} + 2\Lambda \frac{\partial (PH)}{\partial \tau}$$

Equation 3.21

3.2.4 FDM, FVM, iterative strategies and numerical techniques

In simulation of hydrostatic journal air bearings, the FDM is adopted in iterative computations. In simulation of hydrodynamic and hybrid journal air bearings, the FVM is adopted in iterative computations.

In the FDM approach, the Reynolds Equation with orifice boundary conditions (Equation 3.14) is discretized straightforwardly using Equations 3.8 to 3.11. The discrete equation has both first and second order partial differentiation of P. It is then solved numerically using the algorithm shown in Figure 3.3.

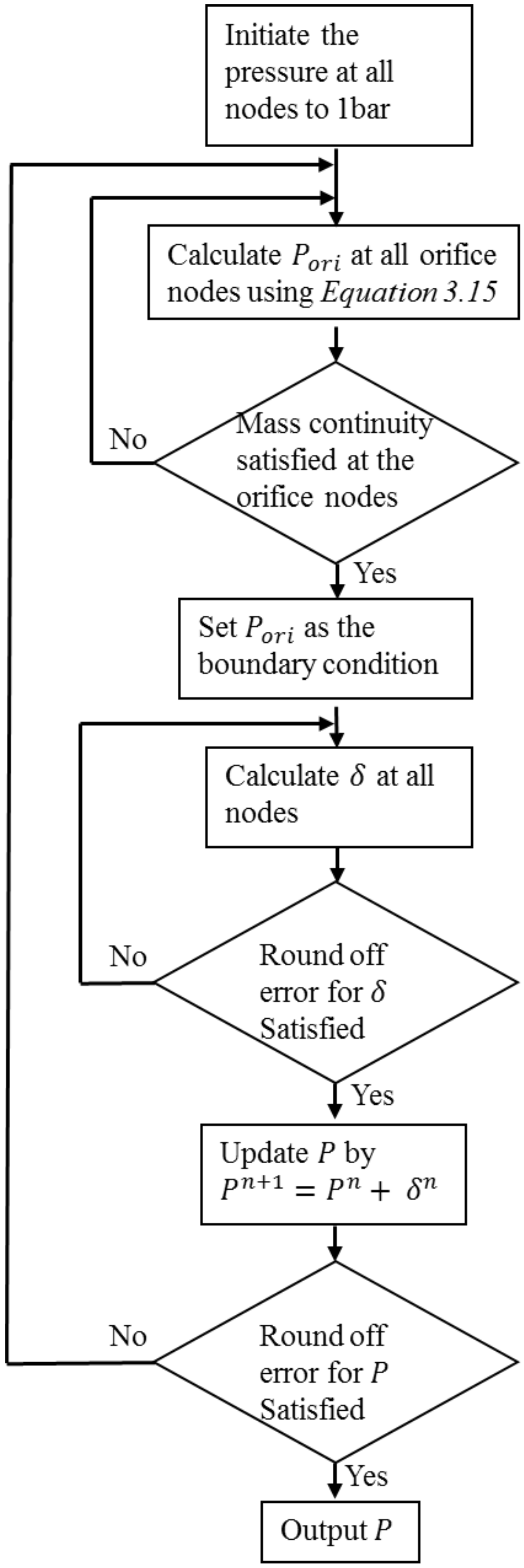

Figure 3.3 A flow diagram of the FDM approach

In order to improve the numerical stability and convergence rate of the iterative process, Newton's method is adopted [90]. It is a general algorithm for linearizing second order partial differential equations, and is often combined with a successive relaxation method for either good numerical stability, or fast converging rate. The linearization procedure is demonstrated below.

In Newton's method, f is defined as a function of P:

$$f(P) = \frac{\partial}{\partial\theta}\left(PH^3\frac{\partial P}{\partial\theta}\right) + \frac{\partial}{\partial Z}\left(PH^3\frac{\partial P}{\partial Z}\right) - \Lambda\frac{\partial(PH)}{\partial\theta} \qquad \text{Equation 3.22}$$

In reference with Newton's method, the following expression stands:

$$f(P^n) + f'(P^n)(P^{n+1} - P^n) = 0 \qquad \text{Equation 3.23}$$

where the superscript n and $n+1$ denote the n^{th} and $(n+1)^{th}$ iterative step.

By means of introducing parameter, $\delta^n = P^{n+1} - P^n$, and apply Taylor expansion to $f(P^n)$ within the interval $[P^n, P^n + \delta^n]$, there exists some point in this interval, denoted by $P^n + \beta\delta^n$ for some $\beta \in [0,1]$, such that:

$$f(P^n + \beta\delta^n) = f(P^n) + \delta^n\beta f'(P^n) + R((\delta\beta)^2)$$ *Equation 3.24*

And:

$$\frac{df(P^n + \beta\delta^n)}{d\beta}|_{\beta=0} = \delta^n f'(P^n) = -f(P^n)$$ *Equation 3.25*

Expressing the term $f(P^n + \beta\delta^n)$ with Equation 3.22 and making differential with respect to β, one can get the following equation:

$$\frac{df(P^n + \beta\delta^n)}{d\beta}|_{\beta=0}$$
$$= 2\left[\frac{\partial}{\partial\theta}\left(H^3\delta^n\frac{\partial P^n}{\partial\theta} + H^3P^n\frac{\partial\delta^n}{\partial\theta}\right) + \frac{\partial}{\partial Z}\left(H^3\delta^n\frac{\partial P^n}{\partial Z} + H^3P^n\frac{\partial\delta^n}{\partial Z}\right)\right] - \Lambda\frac{\partial(\delta^n H)}{\partial\theta}$$

Equation 3.26

Substituting expressions of $\frac{df(P^n+\beta\delta^n)}{d\beta}|_{\beta=0}$ and $f(P^n)$ into Equation 3.25, the equation to be solved at n^{th} iterative step is transformed into:

$$2\left[\frac{\partial}{\partial\theta}\left(H^3\delta^n\frac{\partial P^n}{\partial\theta}+H^3P^n\frac{\partial\delta^n}{\partial\theta}\right)+\frac{\partial}{\partial \mathrm{Z}}\left(H^3\delta^n\frac{\partial P^n}{\partial \mathrm{Z}}+H^3P^n\frac{\partial\delta^n}{\partial \mathrm{Z}}\right)\right]-\Lambda\frac{\partial(\delta^nH)}{\partial\theta}$$
$$=-\frac{\partial}{\partial\theta}\left(P^nH^3\frac{\partial P^n}{\partial\theta}\right)-\frac{\partial}{\partial \mathrm{Z}}\left(P^nH^3\frac{\partial P^n}{\partial \mathrm{Z}}\right)+\Lambda\frac{\partial(P^nH)}{\partial\theta}$$

Equation 3.27

Applying central difference equations for δ, Equation 3.2 can be expressed as a linear algebraic equation with respect to δ:

$$a_{i,j}\delta_{i,j}+b_{i,j}\delta_{i,j-1}+c_{i,j}\delta_{i,j+1}+d_{i,j}\delta_{i-1,j}+e_{i,j}\delta_{i+1,j}+Con_{i,j}=0$$

Equation 3.28

where (i,j) denotes the point at i[th] row and j[th] column in the mesh. $a_{i,j}, b_{i,j}, c_{i,j}, d, e_{i,j}, Con_{i,j}$ are the terms related with H, P, θ, Z only and they are listed in Appendix A.

The introduced parameter $\delta_{i,j}$ can be found with a successive relaxation method.

$$\delta_{i,j}{}^{n+1}=\delta_{i,j}{}^{n}+\omega_{sr}\left[\frac{b_{i,j}\delta_{i,j-1}+c_{i,j}\delta_{i,j+1}+d_{i,j}\delta_{i-1,j}+e_{i,j}\delta_{i+1,j}+Con_{i,j}}{a_{i,j}}\right]$$

Equation 3.29

where ω_{sr} is the relaxation factor ranging from 0 to 2. For $1<\omega_{sr}<2$, the method is known as successive over-relaxation, and can increase the convergence rate. On the other hand, the method becomes successive under relaxation and can make a non-convergence case converged. The optimized relaxation factor can be pre-determined with respect to the grid size in the discrete scheme [91].

Although a linear system, represented by Equation 3.28 can be solved quickly in most numerical tools, there are some limitations of this procedure. Firstly, in Equation 3.24 and Equation 3.25, β is set as 0. This may not be true when small clearances are involved in the simulation. In Cheng's report [92], Newton's method failed to converge at $6\mu m$ bearing radial clearance with 0.1 eccentricity ratio. Additional numerical treatments, such as the rate cutting method or pre-conditioned conjugate gradient method (PCG), are required to make the computations converge. Secondly, the flux term in Equation 3.14 for nodes with orifice restrictors disturbs the stability of convergence. The pressure at the nodes of an orifice needs to be calculated in a separate process first to balance the flow rate into and out of the boundary around the point. This pressure is then used as an initial boundary condition to calculate the pressure distribution at other nodes. Thirdly, the above procedure is not suitable for fluid problems with fluid film discontinuity which will be the case of hydrodynamic and hybrid bearings investigated in this project.

The aforementioned limitations with the FDM approach can be resolved by adopting the numerical approach based on finite volume method (FVM). The hydrodynamic and hybrid journal air bearings in this research adopt the herringbone groove surface patterns, as shown in Figure 3.4 a). At the edges of a groove, there is a sudden change in the air film thickness and results fluid film discontinuity issues presented in Figure 3.4 b). If FDM is used, additional boundary conditions need to be applied to all groove edges to ensure the continuity of mass flow, which makes the computations complex. In this case, the FVM can serve as a useful tool to overcome the problem with FDM and simplify the process. The flow chart of the FVM approach is shown in Figure 3.5.

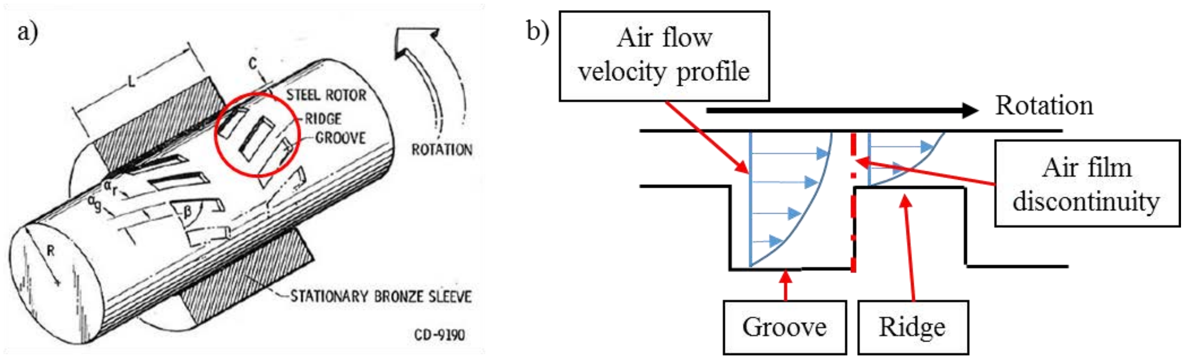

Figure 3.4 a) A conventional herringbone grooved journal from [93] b) A cross-section view in axial direction of grooves in the circled area from a). The air film discontinuity is marked at the interface of one groove-ridge pair.

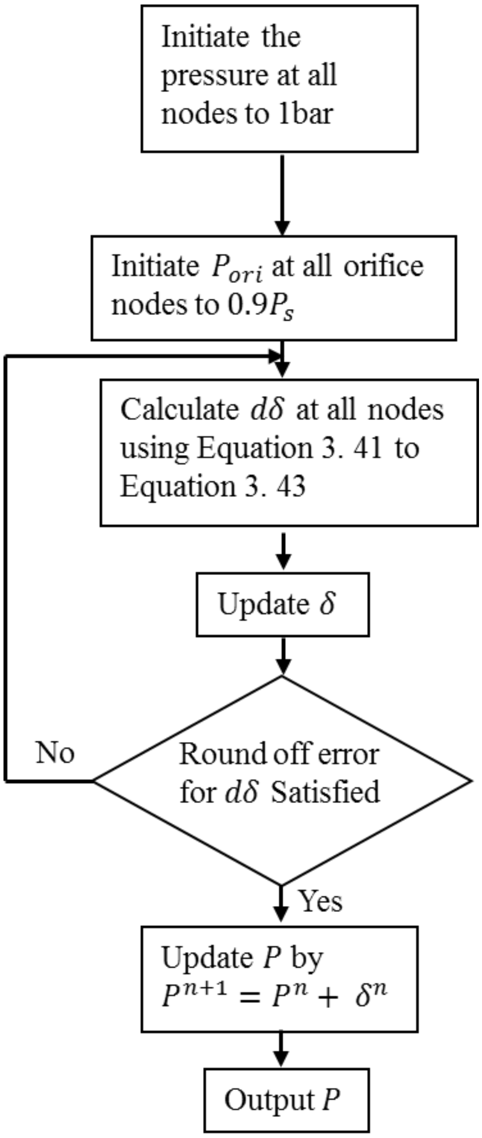

Figure 3.5 A flow diagram of the FDM approach

The FVM approach is similar to the FDM except that it calculates flow properties in a controlled volume surrounding each node. The divergence terms in the Reynolds Equation need to be converted to surface integrals using divergence theorem. The controlled volume surrounding a node of the mesh can be illustrated as Figure 3. 6 a). The Reynolds Equation (Equation 3.5) can be integrated using Green's Theorem along the boundaries of the controlled volume and lead to

Equation 3.31. The projected area of the controlled volume on the meshed surface can be divided into four cells, as in Figure 3. 6 b), for the ease of computations.

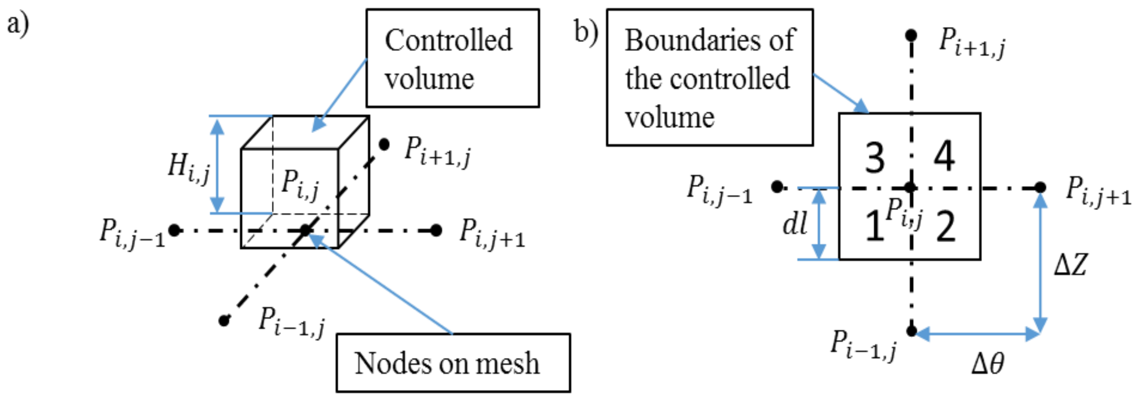

Figure 3. 6 a) Controlled volume surrounding a node in FVM approach b) Projected view of the controlled volume on the meshed surface

Equation 3.30 is the transformation of the Reynolds Equation used in the FVM approach. The physical meaning of Equation 3.30 is that the net inlet flow rate through all boundaries equal to the accumulating rate of the mass in the controlled volume. It is assumed that the pressure and clearance vary linearly in the controlled volume. The integrals of the divergence terms in Equation 3.30 can then be expressed numerically using the discrete form for each cell boundary. Equation 3.31 and Equation 3.32 give an example of these integrals along the left and bottom boundaries of Cell 1. Similar expression can be derived for other cells in the same manner, and they are listed in Appendix B. Equation 3.30 is rewritten as Equation 3.33 for the convenience of computations.

$$\oint_{\Gamma} [\frac{\partial}{\partial \theta}\left(PH^3\frac{\partial P}{\partial \theta} - \Lambda PH\right) + \frac{\partial}{\partial Z}\left(PH^3\frac{\partial P}{\partial Z}\right)]\vec{n} * dl = \iint \Lambda\frac{\partial(PH)}{\partial \tau}\partial\theta\partial Z$$

Equation 3.30

where Γ denotes the projected boundaries of the controlled volume used in FVM. $\vec{n}$ is the outward unit vector normal to the boundaries of each cell. dl is the unit length of each cell boundary.

$$\overline{Q_{\theta 1}} = [-P_{i,j-1/2}H_{i-,j-1/2}{}^3\frac{P_{i,j} - P_{i,j-1}}{\Delta\theta} + \Lambda P_{i,j-\frac{1}{2}}H_{i-,j-\frac{1}{2}}]\frac{\Delta Z}{2}$$

Equation 3.31

$$\overline{Q_{Z1}} = -P_{i-1/2,j}H_{i-,j-1/2}{}^3\frac{P_{i,j} - P_{i-1,j}}{\Delta Z}\frac{\Delta\theta}{2}$$ *Equation 3.32*

$$\sum_{k=1}^{4}(Q_{\theta k} + Q_{Zk}) = \iint \Lambda\frac{\partial(PH)}{\partial \tau}\partial\theta\partial Z$$ *Equation 3.33*

where the subscripts $i-$ and $j-1/2$ denote the interpolation values of P and H. Subscripts $\theta 1$ and $Z1$ denote the integrals for the left boundary and bottom boundary of Cell 1 respectively.

The discrete formula of Equation 3.33 can be reordered into a polynomial form with respect to terms including $P_{i,j}, P_{i-1,j}, P_{i+1,j}, P_{i,j-1}, P_{i,j+1}$:

$$A_{i,j}{P_{i,j}}^2 + B_{i,j}P_{i,j} + C1_{i,j}{P_{i,j-1}}^2 + C2_{i,j}{P_{i,j+1}}^2 + D1_{i,j}{P_{i-1,j}}^2 + D2_{i,j}{P_{i,j+1}}^2 + E1_{i,j}P_{i,j-1} + E2_{i,j}P_{i,j+1} = \iint \Lambda \frac{\partial(PH)}{\partial \tau} \partial\theta \partial Z$$

Equation 3.34

where $A_{i,j}, B_{i,j}, C1_{i,j}, C2_{i,j}, D1_{i,j}, D2_{i,j}, E1_{i,j}, E2_{i,j}$ are constant coefficients that do not contain P in each iteration step. The mathematic expressions of these coefficients are listed in Appendix B.

Newton's method and successive relaxation method can still be applied with minor modifications on the discrete formula. It is assumed that $P_{i,j}$ is the only variable in one iterative step. The following function with respect to $P_{i,j}$ can be formed:

$$f(P_{i,j} + \delta_{i,j}) = A_{i,j}(P_{i,j} + \delta_{i,j})^2 + B_{i,j}(P_{i,j} + \delta_{i,j}) + C1_{i,j}(P_{i,j-1} + \delta_{i,j-1})^2 + C2_{i,j}(P_{i,j+1} + \delta_{i,j+1})^2 + D1_{i,j}(P_{i-1,j} + \delta_{i-1,j})^2 + D2_{i,j}(P_{i+1,j} + \delta_{i+1,j})^2 + E1_{i,j}(P_{i,j-1} + \delta_{i,j-1}) + E2_{i,j}(P_{i,j+1} + \delta_{i,j+1})$$

Equation 3.35

$$f'(P_{i,j} + \delta_{i,j}) = \frac{df(P_{i,j} + \delta_{i,j})}{d(P_{i,j} + \delta_{i,j})} = 2A_{i,j}(P_{i,j} + \delta_{i,j}) + B_{i,j}$$

Equation 3.36

Apply Newton's method in Equation 3.23.

$$d\delta = \frac{f(P_{i,j} + \delta_{i,j})}{f'(P_{i,j} + \delta_{i,j})}$$

Equation 3.37

$$\delta_{i,j}{}^{n+1} = \delta_{i,j}{}^{n} - \omega_{sr} d\delta^{n}$$

Equation 3.38

In each iterative step, $\delta_{i,j}$ is updated by Equation 3.3 until $d\delta$ reaches a preset difference range; $(P_{i,j} + \delta_{i,j})$ is then output as the pressure distribution within the air film.

3.2.5 Validation of the bearing model in the static equilibrium analysis

The proposed numerical approach was first verified by comparing the static equilibrium position with the experiment results reported by Pink [ ].

The bearing used in [ ] is a hydrostatic journal air bearing shown in Figure 3. . The compensation system used is orifice restrictors with pockets. There are two rows of restrictors located symmetrically, and each row had eight restrictors. The dimensions of the bearing are listed in Table 3.1. The CFD simulation was carried out on a 29×97 grid, Figure 3.8. The pressure distribution and bearing force at different eccentricities are shown in Figure 3.9 and Figure 3.10 The predicted dimensionless bearing force agrees well with the experiment results. The maximum error is less than 5%.

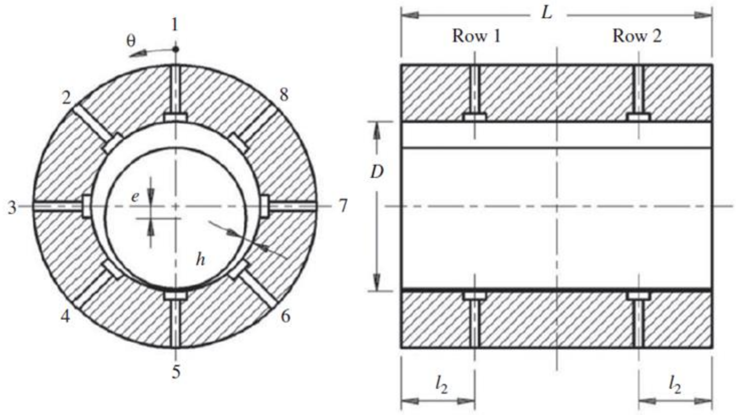

Figure 3. Schematic drawings of hydrostatic journal air bearings with equally distributing pocketed orifice restrictors [ ]

Table 3.1 Bearing parameters of the hydrostatic journal air bearings to be analysed

Diameter, D (mm)	Length, L (mm)	Clearance , c	Orifice Diameter, d_0	Pocket Diameter, d_{poc}	Supply Pressure, P_s
85.2	85.2	18μm	0.2mm	2.6mm	.8bar
Number of restrictors	Row of restrictors	Location of the restrictors to the edge of the bearing, a			
8 per row	2	$l_1 = l_2 = 0.25L$			

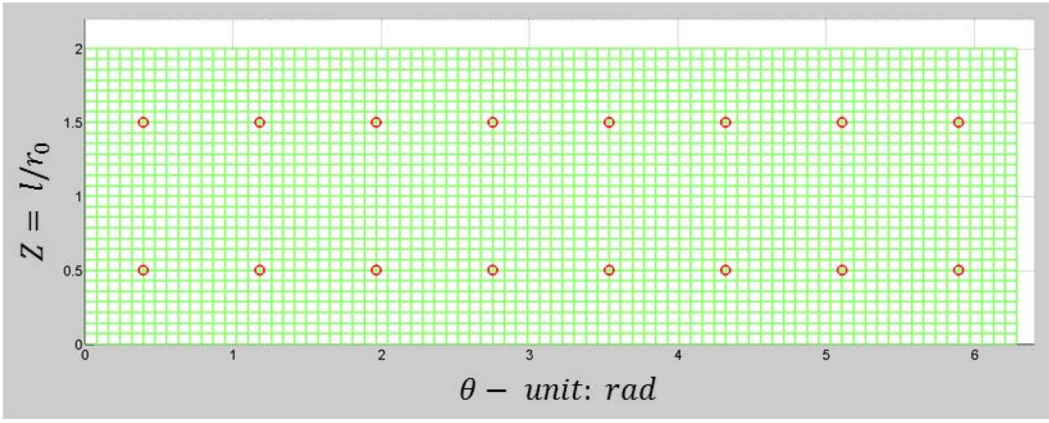

Figure 3.8 Mesh for the static air journal bearing

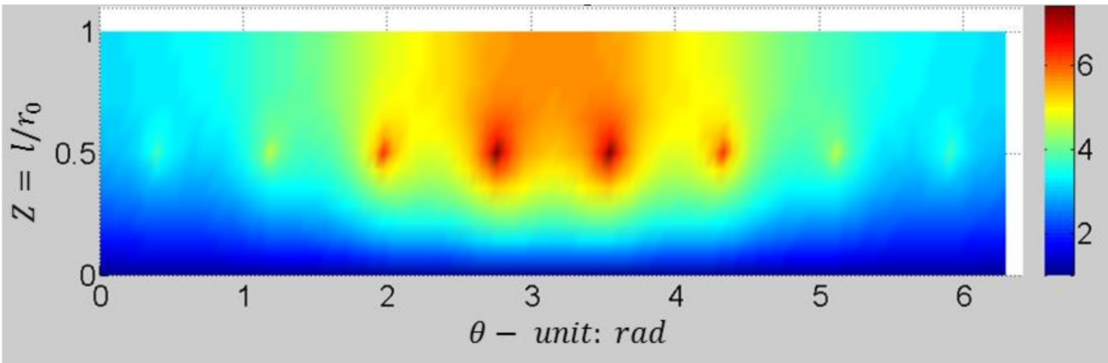

Figure 3.9 Pressure distribution from the bottom boundary to the axial symmetry plan, eccentricity ratio, 0.4

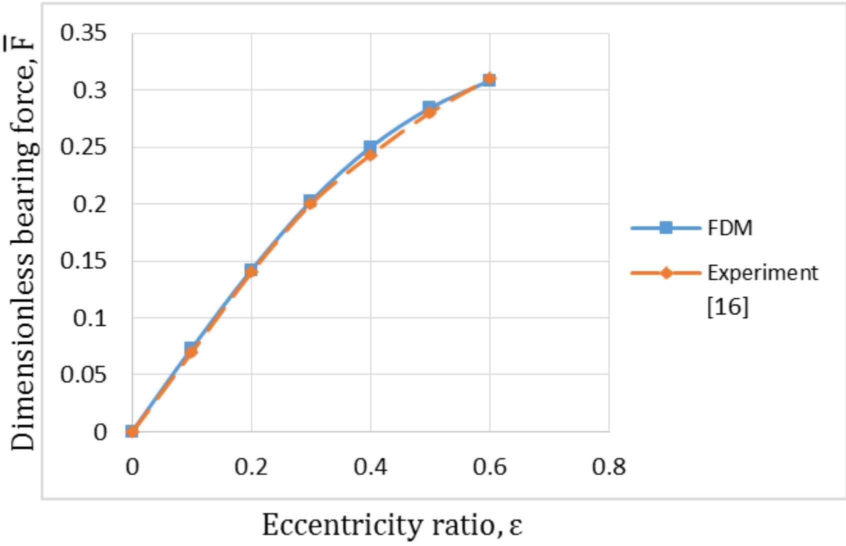

Figure 3.10 Dimensionless bearing force VS. Eccentricity ratio, $\bar{F} = \frac{F_{brg}}{(p_s - p_a)2r_0 l}$, F_{brg} is the bearing force in newton.

3.2.6 Analysis of truncation errors

In the above numerical analysis, there are two types of errors. One is round-off error, which terminates the iterative process once it is satisfied. The round-off error does not accumulate and is normally pre-set in the order of 1e-6.

The other error is the truncation error, which comes from the Lagrange remainder derived from the Taylor's expansion used in the finite difference scheme for the Reynolds Equation. It is related with the grid size. The difference between a true solution and a converged numerical solution mostly depends on the truncation error. The following procedure has been adopted to analysis the truncation error [9] .

In the proposed simulation model, the average pressure (P_{avg}) is defined by integrating the pressure of the air film and dividing by the bearing area. It is used to analyse the truncation error. The true solution can be expressed as:

$$P_{avg}TS = P_{avg}NS + ErrTE$$ *Equation 3.39*

ErrTE is the truncation error term and can be rewritten as:

$$ErrTE = \frac{m^r\left(P_{avg}(\Delta x) - P_{avg}\left(\frac{\Delta x}{m}\right)\right)}{\Delta x^r(m^r - 1)}$$ *Equation 3.40*

where r is the order of the iterative method. It can be determined by carrying out three iterative processes on different grid sizes, for example applying Δx, $\frac{\Delta x}{m}$ and $\frac{\Delta x}{m^2}$ to Equation 3.40.

$$r = log_m \frac{(P_{avg}NS(\Delta x) - P_{avg}NS\left(\frac{\Delta x}{m}\right))}{(P_{avg}NS\left(\frac{\Delta x}{m}\right) - P_{avg}NS\left(\frac{\Delta x}{m^2}\right))}$$ *Equation 3.41*

The truncation error analysis was applied to simulations in section 3.2.5. The results yielded an error level of 8%. The same method can be applied to all other simulation models used in this thesis. The peak pressure can also be used to evaluate the truncation error.

3.3 Modelling of rotor

In this project, air bearings will be designed to support the rotor used in a turbocharger for a 2-liter diesel engine. The shaft diameter is increased to 20mm over a length of 20mm at two journal bearing locations to accommodate the size of air bearings used in this project, as shown in Figure 3.11 a). The rotor is referred as R-1. The rotor contains add-on elements, such as shaft extensions, compressor and turbine. The mechanical structure of these rotors is modelled using a finite element method (FEM) based on the Timoshenko Beam Theory to describe their dynamic properties [82, 84]. The rotor model will be coupled with bearing models to give predictions on the vibrational information of the system in Chapters 4 and 5, which is then compared with the experimental data for verification.

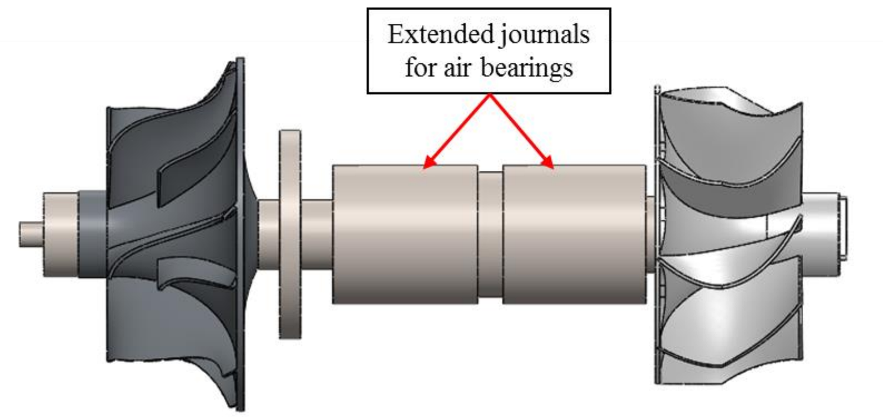

a) Rotor R-1

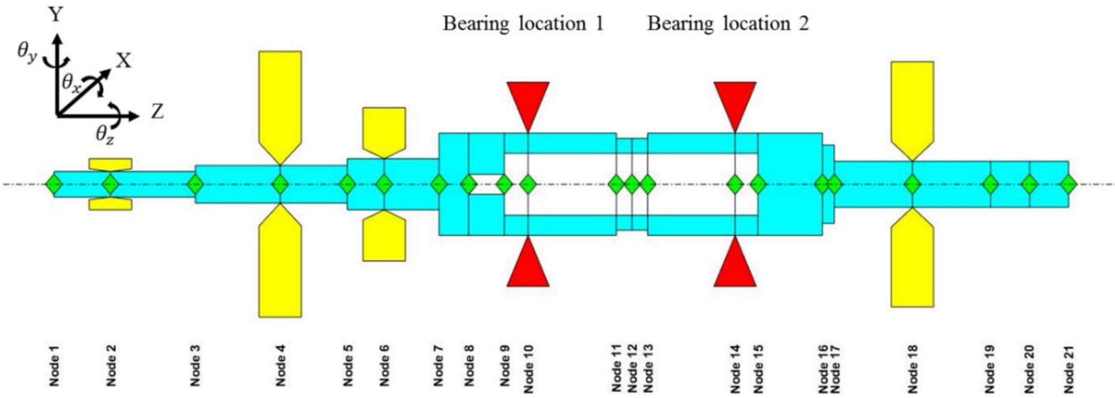

b) Model of R-1

Figure 3.11 The rotors used in this project and their finite element models. a) Rotor R-1 - a rotor for turbochargers and b) Finite element model of rotor R-1 and the global coordinate system.

3.3.1 Finite element rotor model and impact tests

The finite element model of rotor R-1 composes of a set of finite rotor segments with 8-DOF, as introduced in Section 2.3.4. The schematic drawing of the model is illustrated as Figure 3.11 b). Rotor R-1 has a length of 118.3mm and a total mass of 230.9 grams. Its model is defined by 20 elements and 21 nodes. The Inconel turbine of R-1 is represented as a disc with the same mass and moment of inertia of the turbine wheel. The aluminium compressor is modelled as one disc on the steel shaft retaining the same mass and the moment of inertia. Table 3.2 describes detailed finite element model information of the rotor, including element length (*L*), outer diameter (*OD*), inner diameter (*ID*), lumped mass (*W*), lumped diametral moment of inertia (*I_D*) and polar moment of inertia (*I_P*). Figure 3.12 shows the first four free-free undamped modes at zero speed of the rotors, predicated by the finite element models.

Table 3.2 Finite element model of rotor R-1

Node	*L(mm)*	*OD(mm)*	*ID(mm)*	*W(g)*	*I_D(g*mm^2)*	*I_P(g*mm^2)*
1	6.67	2.50	0	0	0	0
2	10.00	2.50	0	2.84	31.80	48.33
3	10.00	3.70	0	0	0	0
4	7.91	3.70	0	26.04	3637.91	5563.02
5	4.34	5.00	0	0	0	0
6	6.46	5.00	0	15.08	953.79	1884.96
7	3.50	10.00	0	0	0	0
8	4.20	10.00	1.94	0	0	0
9	2.80	10.00	6.06	0	0	0
10	10.40	10.00	6.06	0	0	0
11	1.85	9.00	6.06	0	0	0
12	1.85	9.00	6.06	0	0	0
13	10.30	10.00	6.06	0	0	0
14	2.70	10.00	6.06	0	0	0
15	7.60	10.00	0	0	0	0
16	1.40	7.65	0	0	0	0
17	9.20	4.50	0	0	0	0
18	9.20	4.50	0	56.00	3514.14	7669.08
19	4.60	4.50	0	0	0	0
20	4.60	4.50	0	0	0	0
21	0	4.50	0	0	0	0

To verify the validity of the rotor model, impact hammer tests have been performed to find the undamped natural frequencies of the flexible rotor. Figure 3.13 illustrates the bode plots generated from the impact hammer tests on free-free rotor. The associated natural frequencies of the first two flexible modes are listed in Table 3.3 and compared with the predictions from rotor models. It can be seen that the predictions on the natural frequencies have good agreements with experimental observations. The proposed rotor model is equivalent to the rotor used in experiments in dynamics.

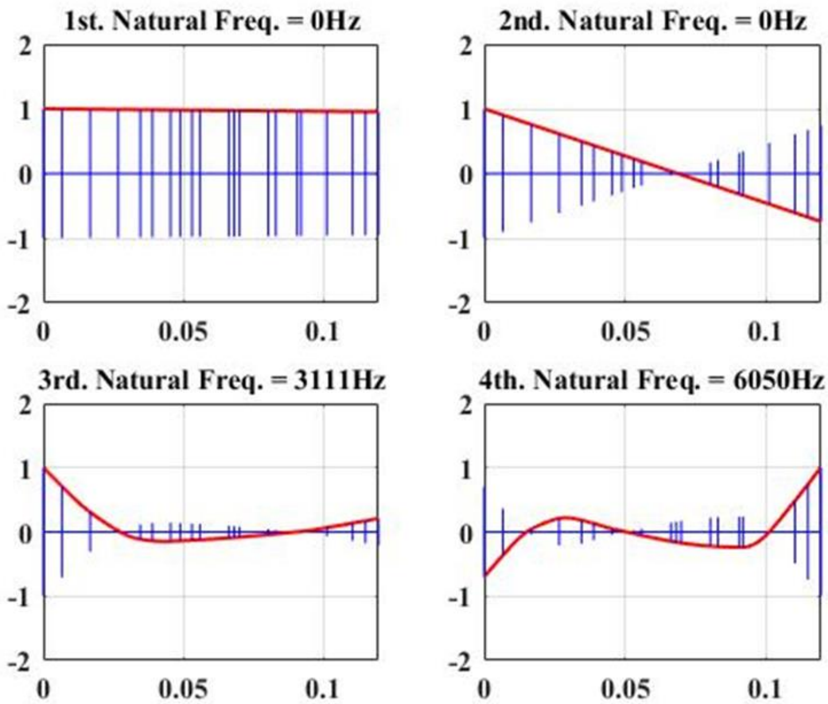

Figure 3.12. The first four Free-free undamped modes of R-1 at zero speed

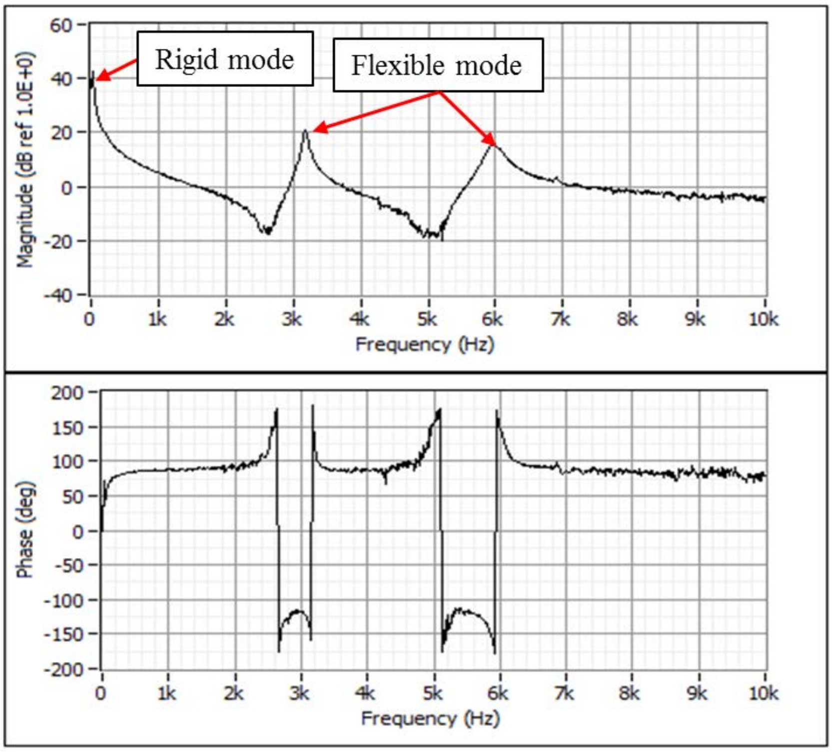

Figure 3.13 Bode plots of impact hammer tests on free-free rotor R-1 at zero speed

Table 3.3 A comparison of Eigen-frequencies from the rotor model and impact hammer tests

Eigen-frequencies of flexible modes			
Rotor	Prediction from FEM model	Impact hammer tests	Error
R-1	3111Hz	31 0Hz	1.8%
	6050Hz	5950Hz	1.6%

The gyroscopic effect will result in the natural frequencies splitting along with rotational speeds into forward and backward whirl. To demonstrate this effect, R-1 is assumed to be supported on undamped isotropic supports of stiffness $k_{xx} = k_{yy} = 1.7e^{7}\mathrm{N/m}$. Results are presented in the Campbell diagram shown in Figure 3.14.

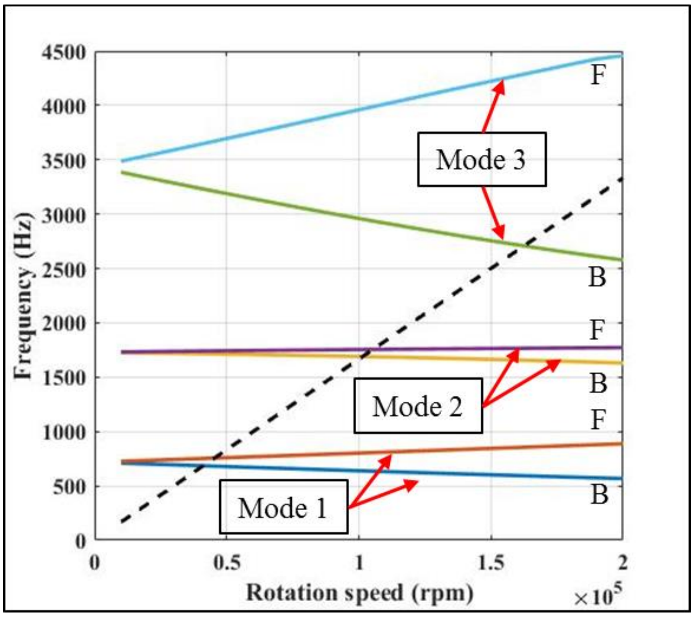

a) Campbell diagram of R-1

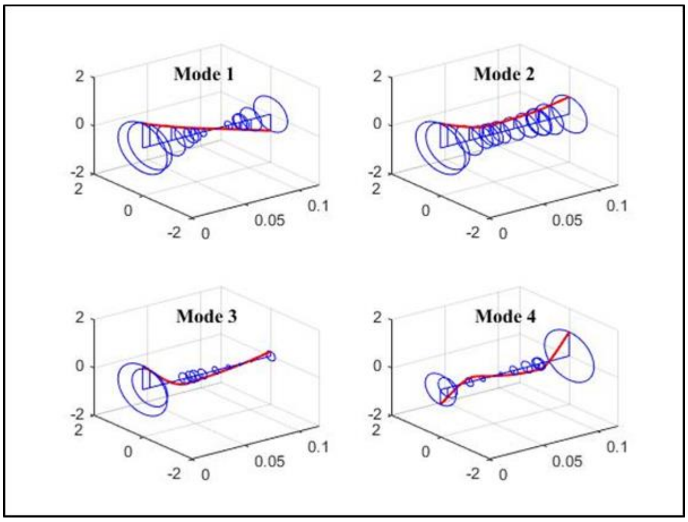

b) Mode shape plotted at 1.6 Hz

Figure 3.14 Campbell diagram and mode shape of rotor R-1 with undamped isotropic support. The dash line in Campbell diagram is the synchronous line, ‘F’ refers to forward mode and ‘B’ refers to backward mode.

3.3.2 Governing Equations of rotor dynamic system

The governing equation of motion for a general rotor-bearing system, with rotor modelled as in Section 3.3.1 and a constant rotational speed, ω, is [84]:

$$[\boldsymbol{M}]\{\ddot{q}\} + [\boldsymbol{K_s}]\{q\} + ([\boldsymbol{C_s}] + \omega[\boldsymbol{G}])\{\dot{q}\} = [\boldsymbol{F_{brg}}] + [\boldsymbol{F_g}] + [\boldsymbol{F_u}]$$

Equation 3.42

$$q = [\ldots\ x_i\ y_i\ \theta_{xi}\ \theta_{yi}\ \ldots]^T$$

Equation 3.43

where q is the system displacement vector to be solved, x_i, y_i the translational displacement of i^{th} node and θ_{xi}, θ_{yi} the rotational displacement of i^{th} node under right hand rule. $[\boldsymbol{M}]$ is the mass and inertia matrix, $[\boldsymbol{K_s}]$ the structural stiffness matrix derived from strain energy, $[\boldsymbol{C_s}]$ the structural damping matrix, $[\boldsymbol{G}]$ the gyroscopic matrix, $[\boldsymbol{F_{brg}}]$ the bearing force vector, $[\boldsymbol{F_g}]$ the static gravitational force vector, and $[\boldsymbol{F_{ub}}]$ the synchronous unbalance excitation force vector.

The expressions of the element matrices are given in Appendix C. The global matrices $[\boldsymbol{M}]$, $[\boldsymbol{K_s}]$, $[\boldsymbol{C_s}]$ and $[\boldsymbol{G}]$ are assembled using the element matrices with the method described in [84]. This governing equation will be applied to both linear and non-linear rotor dynamic analysis in this project.

3.4 Linear perturbation analysis

The concept of linear perturbation analysis was first suggested by Lund [94], who applied the procedure on both gas and oil bearings. In this analysis, bearing forces were linearized using Taylor's expansion and expressed using stiffness and damping coefficients with respect to a static equilibrium configuration. Figure 3.15 shows a static equilibrium configuration of journal bearings and the coordinate system used for performing perturbation analysis. In the figure, the stationary bearing sleeve is represented by the outer circle with its centre at O_1. The shaded circle represents the rotating journal whose centre is O_2. Bearing forces are indicated by blue arrows in horizontal and vertical directions. Static load is indicated by red arrow. In this case, O_2 is placed coinciding with the static equilibrium position. The dash circle is the trajectory of O_2 with small perturbations. Δx_j and Δy_j are the displacement coordinates of O_2 relative to the static equilibrium position.

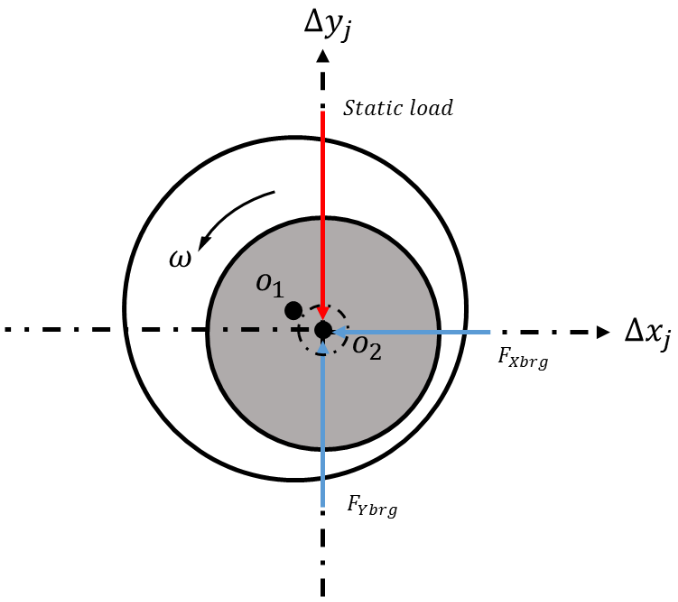

Figure 3.15 Static equilibrium configuration and coordinate system of linear perturbation analysis.

3.4.1 Linearization of bearing forces with perturbation method

In the linear perturbation analysis, it is assumed that the geometrical centre of the journal orbits near a static equilibrium position with infinity small amplitude as shown in Figure 3.16, and the motion of the journal is in a harmonic form.

With the assumptions, variation of air film thickness and pressure in the Reynolds Equation (Equation 3.5) is expressed by Equation 3.44 and3.45.

$$H(\theta, Z, X_J, Y_J) = H_0(\theta, Z, X_{J0}, Y_{J0}) + \Delta X_J sin\theta - \Delta Y_J cos\theta$$

Equation 3.44

$$P(\theta, Z, X_J, Y_J) = P_0(\theta, Z, X_{J0}, Y_{J0}) + \Delta X_J \frac{\partial P}{\partial \Delta X_J} + \Delta \dot{X}_J \frac{\partial P}{\partial \Delta \dot{X}_J} + + \Delta Y_J \frac{\partial P}{\partial \Delta Y_J} + \Delta \dot{Y}_J \frac{\partial P}{\partial \Delta \dot{Y}_J}$$

Equation 3.45

The normalized parameters in the above equations are:

$$X_{J0} = \frac{x_{J0}}{c}, Y_J = \frac{y_{J0}}{c}, \Delta X_J = \frac{\Delta x_J}{c}, \Delta Y_J = \frac{\Delta y_J}{c}, \Delta \dot{X}_J = \frac{\Delta \dot{x}_J}{\omega c}, \Delta \dot{Y}_J = \frac{\Delta \dot{y}_J}{\omega c}$$

Equation 3.46

where H_0 and P_0 are the dimensionless air film thickness and pressure at the static equilibrium position respectively, x_{J0} and y_{J0} the static equilibrium position of the journal centre, Δx_J and Δy_J the displacement of the journal centre in the *x* and *y* directions, $\Delta\dot{x}_J$ and $\Delta\dot{y}_J$ the velocity of the journal centre in the *x* and *y* directions, c the radial clearance of the bearing, ω the rotation speed of the rotor, $\frac{\partial P}{\partial X_J}$ and $\frac{\partial P}{\partial Y_J}$ the changes of dimensionless pressure introduced by the displacement of the journal centre and $\frac{\partial P}{\partial \dot{X}_J}$ and $\frac{\partial P}{\partial \dot{Y}_J}$ the changes of dimensionless pressure introduced by the velocity of the journal centre.

The displacement of the journal centre is assumed as follows:

$$\Delta X_J = X_{J1}e^{st}, \qquad \Delta\dot{X}_J = s\Delta X_J, \qquad \Delta\ddot{X}_J = s^2\Delta X_J \qquad \textit{Equation 3.47}$$

$$\Delta Y_J = Y_{J1}e^{st}, \quad \Delta\dot{Y}_J = s\Delta Y_J, \qquad \Delta\ddot{Y}_J = s^2\Delta Y_J \qquad \textit{Equation 3.48}$$

where X_{J1} and Y_{J1} are the dimensionless amplitude of the displacement in the Δx_j and Δy_j directions. ω_w is the angular frequency of the journal orbit. $s = \lambda + i\omega_w$ and $i = \sqrt{-1}$.

Equation 3.45 can be simplified by using Equations 3.4 a nd 3.48.

$$P(\theta, Z, X_J, Y_J) = P_0(\theta, Z, X_{J0}, Y_{J0}) + \Delta X_J P_1 + \Delta Y_J P_2 \qquad \textit{Equation 3.49}$$

$$P_1 = \frac{\partial P}{\partial \Delta X_J} + s\frac{\partial P}{\partial \Delta \dot{X}_J}, P_2 = \frac{\partial P}{\partial \Delta Y_J} + s\frac{\partial P}{\partial \Delta \dot{Y}_J} \qquad \text{Equation 3.50}$$

Substituting Equation 3.44 and Equation 3.49 to the Reynolds Equation (Equation 3.5), and neglecting terms at the order of ΔX_J and ΔY_J, one can get the zeroth-order and first-order lubrication equations, Equations 3.51 and 3.52, respectively.

The zeroth-order lubrication equation can be written as follows, which stands for pressure at a static equilibrium position:

$$\frac{\partial}{\partial \theta}\left(P_0 {H_0}^3 \frac{\partial P_0}{\partial \theta}\right) + \frac{\partial}{\partial Z}\left(P_0 {H_0}^3 \frac{\partial P_0}{\partial Z}\right) = \Lambda \frac{\partial (P_0 H_0)}{\partial \theta} \qquad \text{Equation 3.51}$$

The first-order lubrication equation can be written as follows, which describes the pressure changes because of the whirl of the journal:

$$\begin{aligned} &\frac{\partial}{\partial \theta}\left(P_0 {H_0}^3 \frac{\partial P_j}{\partial \theta} + 3P_0 {H_0}^2 H_j \frac{\partial P_0}{\partial \theta} + {H_0}^3 P_j \frac{\partial P_0}{\partial \theta}\right) \\ &+ \frac{\partial}{\partial Z}\left(P_0 {H_0}^3 \frac{\partial P_j}{\partial Z} + 3P_0 {H_0}^2 H_j \frac{\partial P_0}{\partial Z} + {H_0}^3 P_j \frac{\partial P_0}{\partial Z}\right) \\ &= \Lambda \frac{\partial}{\partial \theta}(P_0 H_i + P_i H_0) + \frac{s}{\omega} \cdot 2\Lambda\left(P_0 H_j + P_j H_0\right) \end{aligned} \qquad \text{Equation 3.52}$$

$$j = 1, 2$$

where $H_1 = sin\theta$ and $H_2 = -cos\theta$. ω is the rotation speed of the rotor.

By solving Equations 3.51 and 3.52, the bearing forces can be represented using equivalent stiffness and damping coefficients. These coefficients can be obtained by means of calculating the pressure changes P_1 and P_2 from Equation 3.52. The stiffness and damping coefficients can then be expressed as Equation 3.53 to Equation 3.60.

$$K_{xx} = \frac{k_{xx}c}{p_a l d_0} = -\int_0^{2\pi}\int_0^L Re(P1)\sin(\theta)\,dZd\theta$$ *Equation 3.53*

$$K_{xy} = \frac{k_{xy}c}{p_a l d_0} = -\int_0^{2\pi}\int_0^L Re(P1)\cos(\theta)\,dZd\theta$$ *Equation 3.54*

$$K_{yx} = \frac{k_{yx}c}{p_a l d_0} = -\int_0^{2\pi}\int_0^L Re(P2)\sin(\theta)\,dZd\theta$$ *Equation 3.55*

$$K_{yy} = \frac{k_{yy}c}{p_a l d_0} = -\int_0^{2\pi}\int_0^L Re(P2)\cos(\theta)\,dZd\theta$$ *Equation 3.56*

$$D_{xx} = \frac{d_{xx}c\omega_w}{p_a l d_0} = -\int_0^{2\pi}\int_0^L Img(P1)\sin(\theta)\,dZd\theta$$ *Equation 3.57*

$$D_{xy} = \frac{d_{xy}c\omega_w}{p_a l d_0} = -\int_0^{2\pi}\int_0^L Img(P1)\cos(\theta)\,dZd\theta$$ *Equation 3.58*

$$D_{yx} = \frac{d_{yx}c\omega_w}{p_a l d_0} = -\int_0^{2\pi}\int_0^L Img(P2)\sin(\theta)\,dZd\theta$$ *Equation 3.59*

$$D_{yy} = \frac{d_{yy} c \omega_w}{p_a l d_0} = -\int_0^{2\pi} \int_0^L Img(P2) \cos(\theta)\, dZ d\theta \qquad \textit{Equation 3.60}$$

where $k_{xx}, k_{xy}, k_{yx}, k_{yy}$ are the stiffness coefficients of the air film, $d_{xx}, d_{xy}, d_{yx}, d_{yy}$ the damping coefficients of the air film, $K_{xx}, K_{xy}, K_{yx}, K_{yy}, D_{xx}, D_{xy}, D_{yx}, D_{yy}$ their dimensionless form, c the radial clearance of the bearing, l the length of the bearing, d_0 the diameter of the bearing, p_a the ambient pressure, ω_w the angular frequency of whirling, and $L = 2l/d_0$, the dimensionless bearing length. $Re()$ represents the real part of a complex number. $Img()$ represents the imaginary part of a complex number.

In the coordinate system shown in Figure 3.15, the bearing forces in the *x* and *y* directions can be represented in a matrix regarding a static equilibrium position as follows:

$$\begin{bmatrix} F_{Xbrg} \\ F_{Ybrg} \end{bmatrix} = \begin{bmatrix} F_{X0brg} \\ F_{Y0brg} \end{bmatrix} - \begin{bmatrix} k_{xx} & k_{xy} \\ k_{yx} & k_{yy} \end{bmatrix} \begin{bmatrix} \Delta x_J \\ \Delta y_J \end{bmatrix} - \begin{bmatrix} d_{xx} & d_{xy} \\ d_{yx} & d_{yy} \end{bmatrix} \begin{bmatrix} \Delta \dot{x}_J \\ \Delta \dot{y}_J \end{bmatrix} \qquad \textit{Equation 3.61}$$

where F_{X0brg} and F_{Y0brg} are the bearing forces in the Δx_j and Δy_j directions at the static equilibrium position.

3.4.2 Static equilibrium stability analysis

In a static equilibrium stability analysis (SESA), the static gravitational force vector is counteracted by the static forces (F_{X0brg}, F_{Y0brg}) given by the bearing force linearization [85]. The unbalance force vector is also omitted from the equation. The governing equation (Equation 3.42) can be reformed as:

$$[\boldsymbol{M}]\{\ddot{q}\} + ([\boldsymbol{K_s}] + [\boldsymbol{K_b}])\{q\} + ([\boldsymbol{C_s}] + [\boldsymbol{C_b}] + \boldsymbol{\omega}[\boldsymbol{G}])\{\dot{q}\} = 0$$

Equation 3.62

where $[\boldsymbol{K_b}]$ and $[\boldsymbol{C_b}]$ is the linearized bearing stiffness and damping matrices. They contain the stiffness and damping coefficients of bearing extracted from linear perturbation analysis.

With the assumptions that the perturbation is in harmonic form, the displacement vector $\{q\}$ can be found as follows:

$$\{q\} = \{q_0\}e^{\lambda t}$$

Equation 3.63

where λ is a complex root of the equation.

For general use, it is convenient to reform the second order equation, Equation 3.62 using state space method into first order form. Substituting Equation 3.63 and:

$$\{u\} = \left\{\begin{matrix} q \\ \dot{q} \end{matrix}\right\}$$ *Equation 3.64*

into Equation 3.62 with after some manipulation leads to the Equation 3.65,

$$\begin{bmatrix} [0] & [\mathrm{I}] \\ -[\boldsymbol{M_s}]^{-1}[\boldsymbol{K_{sys}}] & -[\boldsymbol{M_s}]^{-\mathbf{1}}[\boldsymbol{CG_{sys}}] \end{bmatrix}\{u_0\} = \lambda[I]\{u_0\}$$ *Equation 3.65*

where [0] and [I] are null and unit matrices. $[\boldsymbol{K_{sys}}] = [\boldsymbol{K_s}] + [\boldsymbol{K_b}]$ and $[\boldsymbol{CG_{sys}}] = [\boldsymbol{C_s}] + [\boldsymbol{C_b}] + \boldsymbol{\omega}[\boldsymbol{G}]$. $\boldsymbol{J} = \begin{bmatrix} [0] & [\mathrm{I}] \\ -[\boldsymbol{M_s}]^{-1}[\boldsymbol{K_{sys}}] & -[\boldsymbol{M_s}]^{-\mathbf{1}}[\boldsymbol{CG_{sys}}] \end{bmatrix}$ is the system characteristic matrix.

Equation 3.65 is in the form of a standard eigenvalue problem. The eigenvalues of the augmented system appear in complex conjugate pairs, as do their respective eigenvectors. On solution of Equation 3.65, the eigenvalues are found in the form of:

$$\lambda_i = s_i + \sqrt{-1} * \omega_i$$ *Equation 3.66*

where i denotes the i^{th} eigenvalue. The imaginary part, ω_i, is the whirl speed. For assurance of stability, all the real parts, s_i, must be negative.

The stability of the system can be investigated by means of examining the leading eigenvalue [60], λ_L (i.e. the one whose real part is nearest to $+\infty$), of the system characteristic matrix $\boldsymbol{J}$. If the real part of λ_L is negative, the system is stable. Otherwise, the system is unstable and ω_L gives corresponding whirl speed.

In the project, SESA were performed on rotor bearing systems based on R-1. Because there is no additional static load, the gravitational force of the rotor will determine the static equilibrium positions of the both journal bearings at a given rotational speed. According to the axial locations of rotor centre of gravity and the two journal bearings, the equivalent gravitational force applied is 1.04N at bearing location 1 and 1.2N at bearing location 2 with reference to R-1 model. At each bearing location, the static equilibrium position is calculated by letting $F_{X0brg} = 0$ and F_{y0brg} equals to the equivalent gravitational force.

3.4.3 Limitations of the proposed linear perturbation analysis

The limitations of the linear perturbation analysis used in this project can be summarized as below:

1. The orbit of the journal centre is assumed to follow a harmonic motion.

2. As the linear bearing model is applied, the computations cannot find the steady state amplitude of the self-excited whirl, or the so-called limited cycle.

These limitations can be overcome using non-linear transient analysis, which is introduced next

3.5 Non-linear transient analysis

Non-linear transient analysis can analyse the orbit of the journal without assumptions of small harmonic vibrations to the journal behaviours. Bearing forces in the analysis are no longer approximated by stiffness and damping coefficients. This analysis requires the governing equations of the rotor dynamic system, coupled with non-linear bearing models, to be solved as functions of time. Non-linear transient analysis can be used to study the stability and unbalance responses of the rotor bearing system. In this section, the non-linear transient analysis used in the study is introduced.

3.5.1 Bearing models in non-linear transient analysis

The bearing models of both the FDM and the FVM approaches consider time as an independent variable. The time dependent differential term, $\Lambda\frac{\partial(PH)}{\partial\tau}$, in the Reynolds Equation (Equation 3.5) needs to be treated numerically in the non-linear transient analysis, so that it can be coupled with the equations of motion of the rotor-bearing system. Here, it is expressed using two finite difference schemes with respect to time.

For bearing models based on the FDM approach, an implicit difference scheme is applied to generate a discrete form of the time dependent term in the Reynolds Equation as Equation 3.6 , and the algorithm is shown in Figure 3.16 a).

$$\left[\frac{\partial}{\partial \theta}\left(PH^3\frac{\partial P}{\partial \theta} - \Lambda PH\right) + \frac{\partial}{\partial Z}\left(PH^3\frac{\partial P}{\partial Z}\right)\right]_{i,j}^{n} = \Lambda\frac{(P_{i,j}H_{i,j})^n - (P_{i,j}H_{i,j})^{n-1}}{\Delta\tau}$$

Equation 3.67

where *n* denotes the values at current time step t_n and (*n* - *1*) the values at previous time step t_{n-1}

For bearing models based on the FVM approach, the Crank-Nicolson semi-implicit scheme is applied to transform Equation 3.32 into Equation 3.68. The algorithm is shown in Figure 3.16 b). This scheme is always numerically stable and suitable for unsteady gas-bearing problems [3] .

$$\sum_{k=1}^{4}(\overline{Q_{\theta k}} + \overline{Q_{Zk}}) = \frac{\Lambda\Delta\theta\Delta Z}{4}\frac{P_{i,j}{}^{(n)}\sum_k^4 H_{i,j,k}{}^{(n)} - P_{i,j}{}^{(n-1)}\sum_k^4 H_{i,j,k}{}^{(n-1)}}{\Delta\tau}$$

Equation 3.68

where the subscript k corresponds to each of the cell numbers shown in Figure 3.   used in the FVM approach. The definitions of $\overline{Q_{\theta k}}$ and $\overline{Q_{Zk}}$ are:

$$\overline{Q_{\theta k}} = \frac{1}{2}\left({Q_{\theta k}}^{(n)} + {Q_{\theta k}}^{(n-1)}\right) \; and \; \overline{Q_{Zk}} = \frac{1}{2}\left({Q_{Zk}}^{(n)} + {Q_{Zk}}^{(n-1)}\right)$$

Equation 3.69

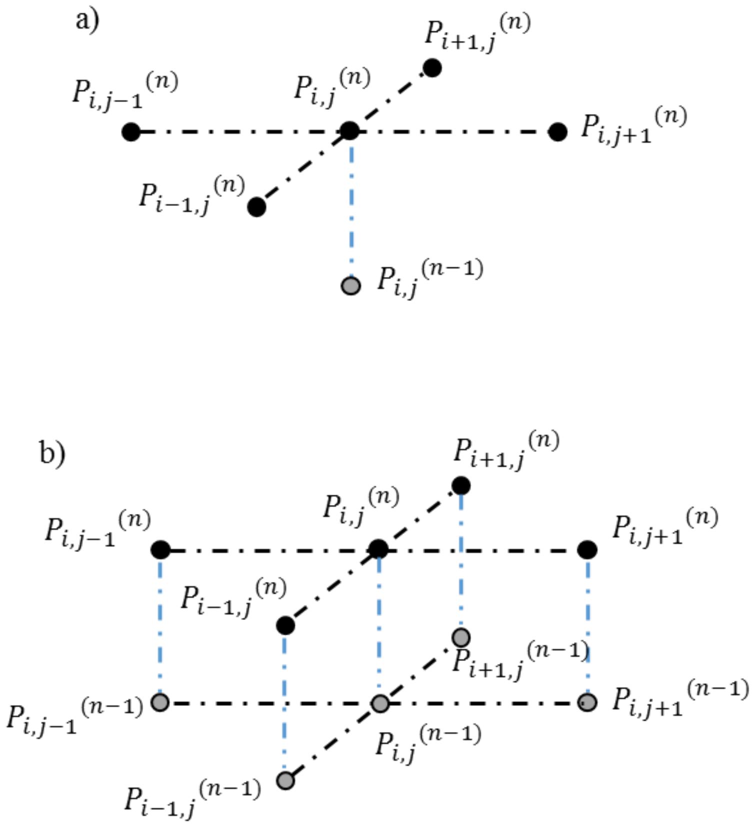

Figure 3.16 The algorithm of time dependent finite difference scheme. a) Algorithm of the implicit scheme in the FDM approach. b) Algorithm of the Crank-Nicolson semi-implicit scheme in the FVM approach

3.5.2 Non-linear transient stability analysis

In non-linear transient stability analysis, the governing equation (Equation 3.42) can be used directly. It needs to be solved with the non-linear bearing model as function of time. The solution can be found by adopting a non-simultaneous iterative process to couple the bearing models with governing equation of motion for the rotor bearing system [42, 56]. This process involves the following steps:

1) To initiate the iterative process, the displacement of R-1 model at time step t_{n-1} will be given with zero velocities. The pressure in the air film is pre-set as ambient.

2) By using the displacement and velocity of bearing locations at the previous time step t_{n-1}, the Reynolds Equation in bearing models is solved to yield the bearing forces for time step t_n, ${F_{Xbrg}}^{(n)}$ and ${F_{Ybrg}}^{(n)}$.

3) The bearing forces are then treated as algebraic and applied to the governing equation of motion. The latter is solved as state equations using Matlab ODE (e.g. ode23/ode23s) solvers. The solution gives the displacement and velocity states of all nodes in R-1 model at time step t_n, including those of the bearing locations.

4) Repeat step 2 to 3 until a pre-set maximum simulation time is reached.

The above non-simultaneous routine will be used in Chapter 4 and 5 to give predictions on the rotor bearing system responses to unbalance excitation at various constant rotor speeds. The rotor responses at each speed will be calculated with appropriated initial conditions set by MATLAB ODE (ode23/ode23s) solvers for the first 00 shaft revolutions. The steady state of the simulation is assumed to be achieved in the last 100 revolutions, from which the response data are collected and analysed.

The stability of the system can be identified by means of examining the time history of journal trajectory: In the absence of unbalance excitation ($[\boldsymbol{F_{ub}}]$ is null), if the static equilibrium position (SEP) of the bearing is stable, free perturbation decays and a converged trajectory can be observed. Otherwise, the growth of free perturbation is contained within a limit cycle and the trajectory gives the steady state amplitude of self-excited whirl. The whirl speed of the limit cycle can be analysed by performing Fast Fourier Transform (FFT) of the time history. In the presence of unbalanced forces (unbalance excitation), a stable SEP shows an orbit with frequency that is equal to the rotational speed. On the other hand, an unstable SEP with unbalanced excitation will lead to an orbit with a non-synchronous component of self-excited whirl and a synchronous component driven by unbalanced forces.

3.5.3 The conditions for the proposed non-linear transient analysis

There are some restrictions on the conducted transient analysis using the rotor model in junction with non-linear bearing models. They are listed as follows:

1) The non-linear transient analysis is based on the constant rotational speed;

2) Non-linear bearing models are coupled with the rotor model by applying the bearing force vector into the governing equations of motion for the system under a non-simultaneous routine. In reality, they react to each other simultaneously. Sufficiently small-time steps need to be maintained in the integration of the rotor ODE;

3) The mass, stiffness, damping and gyroscopic matrices represent the dynamic properties of the rotor. Non-linear bearings and viscoelastic-support are modelled individually. The gyroscopic effects are considered as a function of rotational speed;

4) The rotor is assumed to be axial symmetric and modelled with a Timoshenko beam element. Only the lateral motions are considered.

3.6 Summary

This chapter gives theories and numerical techniques adopted in the study of air bearings and the rotor dynamic configuration. In this area, hydrostatic journal air bearings are modelled using the finite difference method. Hydrodynamic and hybrid journal air bearings are modelled using the finite volume method. Various boundary conditions applied to the bearing models are explained. A static equilibrium analysis was performed using the proposed bearing model of hydrostatic air bearings. The results were compared with experimental data from [16] and showed good agreement. Rotor R-1 used in the project were modelled using finite element method based on Timoshenko beam theory. The rotor model was verified by means of performing impact tests on free-free rotor. The techniques to identify the stability of rotor bearing system are provided as linear perturbation analysis and non-linear transient analysis.

The both analytical approaches will be applied in Chapters 4 and 5 to estimate vibrational performance of the rotor bearing system. The conditions of these analysis are stated.

CHAPTER 4: HYDROSTATIC JOURNAL AIR BEARINGS

4.1 Introduction

In this chapter, non-rotational and rotational performance of hydrostatic journal air bearings are investigated. The performance is first analysed using the numerical approach presented in Chapter 3. The predicted rotational performance is then compared with experimental ones for verification of the proposed numerical approaches.

In section 4.2, modelling of hydrostatic journal air bearings is introduced with a focus on refining restrictor boundary conditions to improve the accuracy of the model.

In section 4.3, the model of hydrostatic journal air bearings is used to study the non-rotational performance. The influence of some design parameters on bearing reaction forces to static load are studied for the optimal design.

Section 4.4 presents theoretical studies on the rotational performance of hydrostatic journal air bearings using linear perturbation analysis. The influence of bearing design parameters on equivalent bearing stiffness and damping coefficients is investigated. The analysed coefficients are then used to build up a linear bearing model and combined with the rotor model (R-1) to give predictions on the stability and natural frequencies of the system.

Section 4.5 describes a non-linear transient analysis (NTA) to predict unbalance responses of practical rotor-bearing systems, which is then verified by experiments. The model and techniques used in the NTA for hydrostatic journal air bearings are explained at the first place. Experiments on rotational performance is performed with R-1 rotor in a speed range from 50k to 100k rpm. Experimental data are compared with prediction from NTA at the end.

For the convenience of reading, the nomenclatures of the design parameters of hydrostatic journal air bearings are presented below. Table 4.1 lists the range of these parameters used in this chapter.

- r_0, radius of the bearing, mm
- l, length of the bearing, mm
- c, radial clearance, µm
- P_s, supply pressure (absolute), bar
- d_0, orifice diameter, mm
- N_{ori}, number of orifices

Table 4.1 Design parameters of the hydrostatic journal air bearing

Radius of the bearings, $\boldsymbol{r_0}$ (mm)	Length to diameter ratio, $\boldsymbol{l/2r_0}$	Radial clearance, $\boldsymbol{c}$ µm	Orifice diameter, $\boldsymbol{d_0}$ (µm)	Supply Pressure, $\boldsymbol{p_s}$ (bar)	Number of orifices, $\boldsymbol{N_{ori}}$
4 & 10	0.5 to 2	5 to 10	50 to 300	3 to 7.5	4 to 8

4.2 Modelling of hydrostatic journal air bearings

Hydrostatic journal air bearings are modelled based on the methods presented in Chapter 3. The Reynold's Equation is solved numerically using finite difference method. The bearings are considered symmetric about the middle lines of the axial length and the both ends are open to atmosphere. Finite difference (FD) grid only needs to cover half of the bearing length. Orifices are used as restrictors and the centre of each orifice coincides with a node in the FD grid. Figure 4.1 a) shows a typical grid and the boundary conditions. The red circles represent the orifice restrictors which are coincided with grid nodes.

Since orifice flow model is applied as a boundary condition, accuracy of the bearing model will largely rely on it in addition to the grid size. It is necessary to investigate flow properties through the orifice restrictors in air bearings and develop accurate flow models. This section will focus on the development of a refined orifice flow model to be used as boundary conditions.

a)

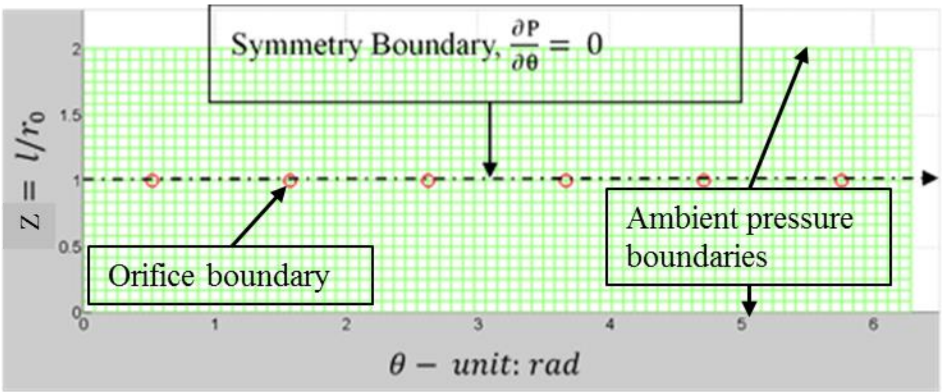

b)

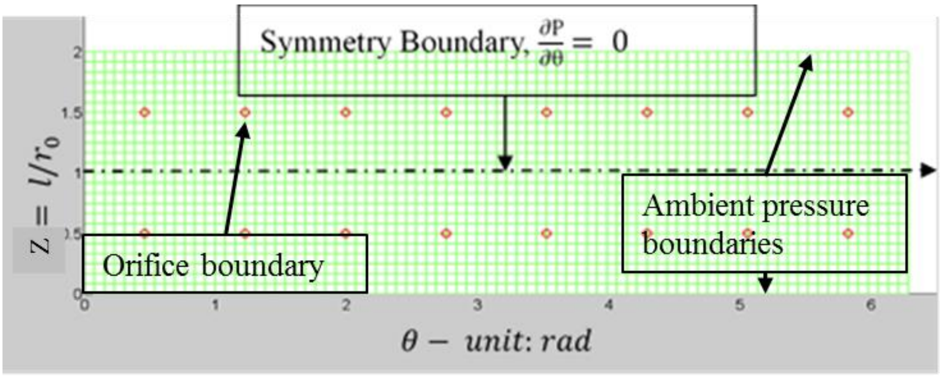

Figure 4.1 Mesh of bearing surface in FDM a) Grid and boundary conditions for single-row restrictor system; b) Grid and boundary conditions for double-row restrictor system

4.2.1 Orifice flow model in hydrostatic journal air bearings

A commonly used orifice flow model is a set of empirical equations which stand for normal and choked flow conditions such as Equations 3.15 and 3.16 introduced in Chapter 3. However, they are not suitable to be directly applied to modelling of hydrostatic journal air bearings. This is because of an effect known as entrance loss. Such effect is a result of a rapid increase in dynamic pressure locally around an orifice when air flow is pressurized into bearing clearance [3].

A well accepted orifice flow model with consideration of the entrance loss effect was provided by Pink [3]. In his model, a correction coefficient C_{corf} was used to adjust overall flow rate through an orifice restrictor in hydrostatic journal air bearings. The corrected flow rate can be formulated for normal and choking conditions respectively as Equations 4.1 and 4.2.

$$\frac{dm}{dt} = C_{orf} * Cd * \frac{\pi {d_0}^2}{4\left(1 + {\delta_l}^2\right)^{\frac{1}{2}}} * p_{s*} \left\{ \frac{2\gamma}{\gamma - 1} RT \left[\left(\frac{p_0}{p_s}\right)^{\frac{2}{\gamma}} - \left(\frac{p_0}{p_s}\right)^{\frac{\gamma+1}{\gamma}} \right] \right\}^{\frac{1}{2}},$$

$$\frac{p_0}{p_s} > \left[\frac{2}{\gamma + 1}\right]^{\frac{\gamma}{\gamma - 1}} \qquad \textit{Equation 4.1}$$

$$\dot{m}_{ori} = C_{orf} * Cd * Ar * p_s * \left[\frac{2\gamma}{\gamma + 1}\right]^{\frac{1}{2}} \left[\frac{2}{\gamma + 1}\right]^{\frac{1}{\gamma - 1}}, \frac{p_0}{p_s} \leq \left[\frac{2}{\gamma + 1}\right]^{\frac{\gamma}{\gamma - 1}}$$

Equation 4.2

$$C_{orf} = \left[\frac{1 + {\delta_l}^2}{1 + K_d {\delta_l}^2 Cd^2}\right]^{\frac{1}{2}} \qquad \textit{Equation 4.3}$$

$$\delta_l = \frac{\pi {d_0}^2}{4\pi d_r h} \qquad \textit{Equation 4.4}$$

where K_d is the entrance loss coefficient introduced by Vohr [95]. It relates static pressure in the pockets, static pressure at the edges of pockets, and dynamic pressure:

$$p_p - p_c = K_d * p_{dyn} \qquad \textit{Equation 4.5}$$

where p_c is the local static pressure at the pocket edge and p_{dyn} the dynamic pressure. From Vohr's experimental work [95], K_d is a function of the Reynolds number defined for air bearings [88], Re:

$$K_d = 0.15 + 0.000225R_e, \qquad if\ 0 < R_e < 2000 \qquad \textit{Equation 4.6}$$

Or

$$K_d = 0.6, \qquad if\ 2000 < R_e \qquad \textit{Equation 4.7}$$

R_e is given by:

$$R_e = \frac{dm}{dt} * \frac{2}{\pi\mu d_r} \qquad \textit{Equation 4.8}$$

For un-choked orifice flow, C_d should be considered as a variable with respect to orifice diameter and the pressure drops.

By taking the effect of the orifice diameter into account, C_d can be written as:

$$C_d{}^* = 0.52 + 2.1 * d_0 - 3 * d_0{}^2 \qquad \textit{Equation 4.9}$$

By taking the effect of the pressure drop into account, C_d can be written as:

$$C_d = \frac{C_d{}^*}{1.174 - 0.327 * \frac{p_0}{p_s}}, \qquad if\ \frac{p_0}{p_s} > \left[\frac{2}{\gamma + 1}\right]^{\frac{\gamma}{\gamma - 1}} \qquad \textit{Equation 4.10}$$

where d_0 is the orifice diameter. Under 'choking' conditions, C_d is regarded as a constant equal to 0.8.

In this project, Pink's orifice flow model was initially applied directly to the bearing model. However, numerical study showed that this orifice flow model tended to underestimate bearing forces in static equilibrium analysis when the grid size was smaller than the pocket diameter, or when it was applied to a plain orifice in comparison with experimental data from other research work. Table 4.2 shows the results obtained by using Pink's flow model on different grid sizes and comparisons between predicted bearing forces at zero rotation speed for a hydrostatic journal air bearing with parameters from Table 4.1. It can be seen bearing reaction force to static load dropped 6% to 8.8% when a fine grid size is applied.

Table 4.2 Comparison of the dimensionless bearing reaction forces on different grid sizes and the experiments, the eccentricity ratio is 0.4 and 0.8

Dimensionless pocket diameter, d_{poc}/r_0 = 0.061							
	Coarse Grid, 29x97, $\Delta\theta = 0.065, \Delta Y = 0.0714$		Fine Grid, 49x177 $\Delta\theta = 0.0357, \Delta Y = 0.0417$				
$\boldsymbol{\varepsilon}$	Pink's flow model		Pink's flow model		Modified orifice flow model		Experiment
	$\overline{W}$	Difference	$\overline{W}$	Difference	$\overline{W}$	Difference	$\overline{W}$
0.4	0.2499	1.2%	0.2322	6.0%	0.2448	0.8%	0.247
0.8	0.3350	1.8%	0.3109	8.8%	0.3582	5.0%	0.341

One possible cause for this issue is that the local pressure drop and pressure recovery only occur at a radius around the pocket or plain orifice. G. Belforte and T. Raparelli [9] summarized the radius where pressure recovery occurs with CFD and experiments for hydrostatic thrust air bearings. The radius can be expressed as Equation 4.11.

$$r_i = \frac{d_0}{2} + 40 * h \qquad \textit{Equation 4.11}$$

where r_i is the radius around an orifice.

When the grid size is smaller than the radius of the pocket or the orifice, Pink's flow model underestimated the pressure at the orifice nodes. An alternative flow model was then developed and introduced in section 4.2.2 for fine grid size. The discrete effect of mass flow is considered.

4.2.2 Modified orifice flow model

The modified orifice flow model is based on the mass continuity equation. It is considered as the flow rate through an orifice into the volume under a restrictor equals to that into the bearing clearance, Figure 4.2 a). Equations 4.1 and 4.2 are adopted to describe the flow rate through an orifice while C_d is considered as a variable calculated by Equation 4.10. P_u is the average pressure in the volume under an orifice restrictor. The flow rate at the entrance to bearing clearance is hereby given as:

$$Q(P_d, P_u, H_d, H_u) = \Gamma_s * P_u * \left\{\frac{2\gamma}{\gamma - 1} RT\left[\left(\frac{P_d}{P_u}\right)^{\frac{2}{\gamma}} - \left(\frac{P_d}{P_u}\right)^{\frac{\gamma+1}{\gamma}}\right]\right\}^{\frac{1}{2}}, \frac{P_d}{P_u} > \left[\frac{2}{\gamma + 1}\right]^{\frac{\gamma}{\gamma-1}}$$

Equation 4.12

$$Q(P_d, P_u, H_d, H_u) = \Gamma_s * P_u * \left[\frac{2\gamma}{\gamma + 1}\right]^{\frac{1}{2}} \left[\frac{2}{\gamma + 1}\right]^{\frac{1}{\gamma-1}}, \frac{p_d}{p_u} \leq \left[\frac{2}{\gamma + 1}\right]^{\frac{\gamma}{\gamma-1}}$$ *Equation 4.13*

$$\Gamma_s = \frac{12\eta\sqrt{R_{spec}T}C_d\pi d_{poc}}{p_a c^2} * \frac{(H_d + H_u)}{2}$$ *Equation 4.14*

$$C_d = 0.9093 - 0.0751\frac{P_d}{P_u}$$ *Equation 4.15*

where P_d and H_d are flow pressure and local clearance downstream at the entrance and P_u and H_u the flow pressure and local film clearance upstream at the volume under the restrictor.

The empirical formula Equation 4.15, provided by Neves [11], can be used to calculate C_d for un-choked flow to account for the entrance loss effect. For a choking condition, C_d is regarded as a constant and equal to 0.8.

For a grid configuration as shown in Figure 4.2 b), the flow properties at the restrictor nodes are described by the algebraic formula as in Equation 4.16, instead of the Reynolds Equation. $P_{i,j}$ is the pressure at the restrictor nodes. $P_{i-1,j}$, $P_{i+1,j}$, $P_{i,j-1}$ and $P_{i,j+1}$ are the pressure at the four adjacent points. Q_k(k = 1, 2, 3, 4) is the flow rate into the bearing clearance through a quarter of the orifice edge and can be calculated using Equations 4.12 and 4.13. The algebraic formula can be written as:

$$\begin{aligned} Q_{ori}\left(P_{i,j}, P_s, H_{i,j}\right) &= \sum_{k=1}^{4} Q_k(P_d, P_u, H_d, H_u) \\ Q_1(P_d, P_u, H_d, H_u) &= Q_1\left(P_{i-1,j}, P_{i,j}, H_{i-1,j}, H_{i,j}\right) \\ Q_2(P_d, P_u, H_d, H_u) &= Q_2\left(P_{i+1,j}, P_{i,j}, H_{i+1,j}, H_{i,j}\right) \\ Q_3(P_d, P_u, H_d, H_u) &= Q_3\left(P_{i,j-1}, P_{i,j}, H_{i,j-1}, H_{i,j}\right) \\ Q_4(P_d, P_u, H_d, H_u) &= Q_4\left(P_{i,j+1}, P_{i,j}, H_{i,j+1}, H_{i,j}\right) \end{aligned} \qquad \text{Equation 4.16}$$

a) b)

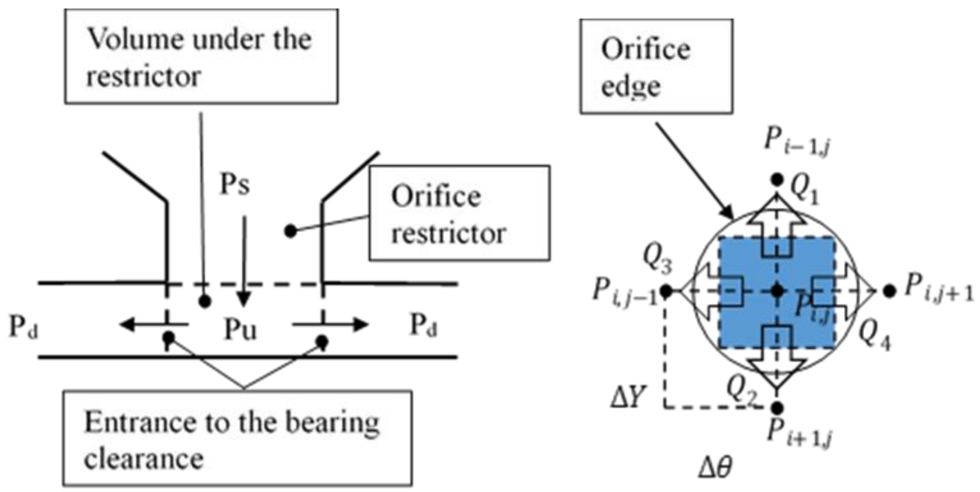

Figure 4.2 Modified orifice flow model. a) Pressure and flow direction under an orifice restrictor b) Flow into the bearing clearance through the edge of an orifice restrictor for a grid size where $\Delta\theta = \Delta Y = d_{poc}/2r_0$

4.3 Non-rotational performance of hydrostatic journal air bearings

In this section, model of hydrostatic journal air bearings is used to study the non-rotational performance. The influence of design parameters on bearing reaction forces to static load and compressed air consumptions at given static equilibrium configurations is investigated. The optimization of design parameters is for achieving maximum bearing reaction force while reducing compressed air consumptions.

4.3.1 Effect of eccentricity on the flow rate

For all types of hydrostatic journal air bearings, bearing reaction forces increase directly with eccentricity as shown in Figure 3.10. At non-rotational configuration, the attitude angle, which is defined as angle between line of journal centre and housing centre to bearing reaction force, is zero for symmetrical orifice arrangements such as in Figure 4.1. Before investigating the effect of other design parameters, it is necessary to understand how flow rate varies with eccentricity. Local film thickness under each orifice restrictor is different from others due to the eccentricity and will change accordingly. The flow rate of hydrostatic journal air bearings with the geometry listed in Table 4.3 is analysed to investigate the effect of eccentricity.

Table 4.3 Design parameters of hydrostatic journal air bearings used to investigate the effect of eccentricity on flow rate

Radius of the bearings, $\boldsymbol{r_0}$ (mm)	Length to diameter ratio, $\boldsymbol{l/2r_0}$	Orifice diameter, $\boldsymbol{d_0}$ (μm)	Number of orifices per row, $\boldsymbol{N_{ori}}$	Radial clearance, $\boldsymbol{c}$ (μm)	Supply Pressure, $\boldsymbol{P_s}$ (bar)
4	1	300	6	5, 10, 15	4, 6

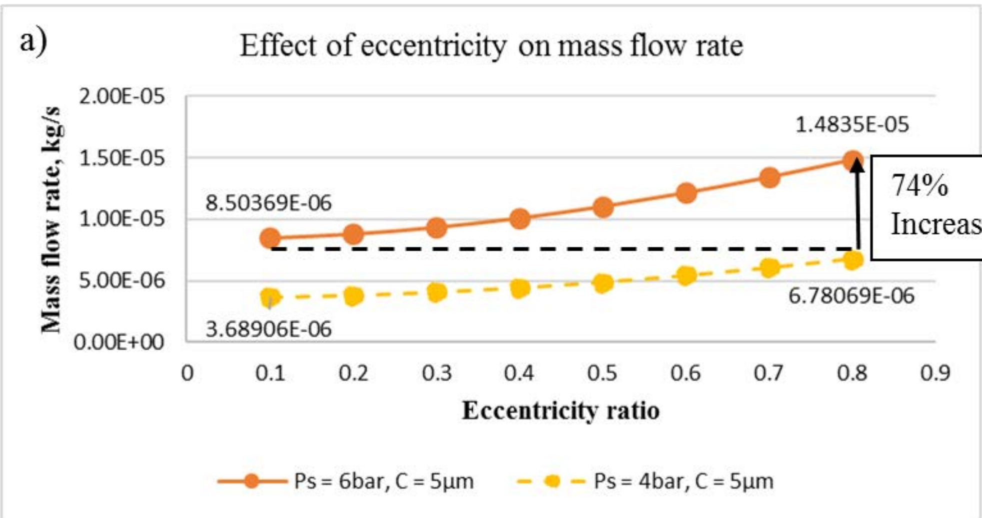

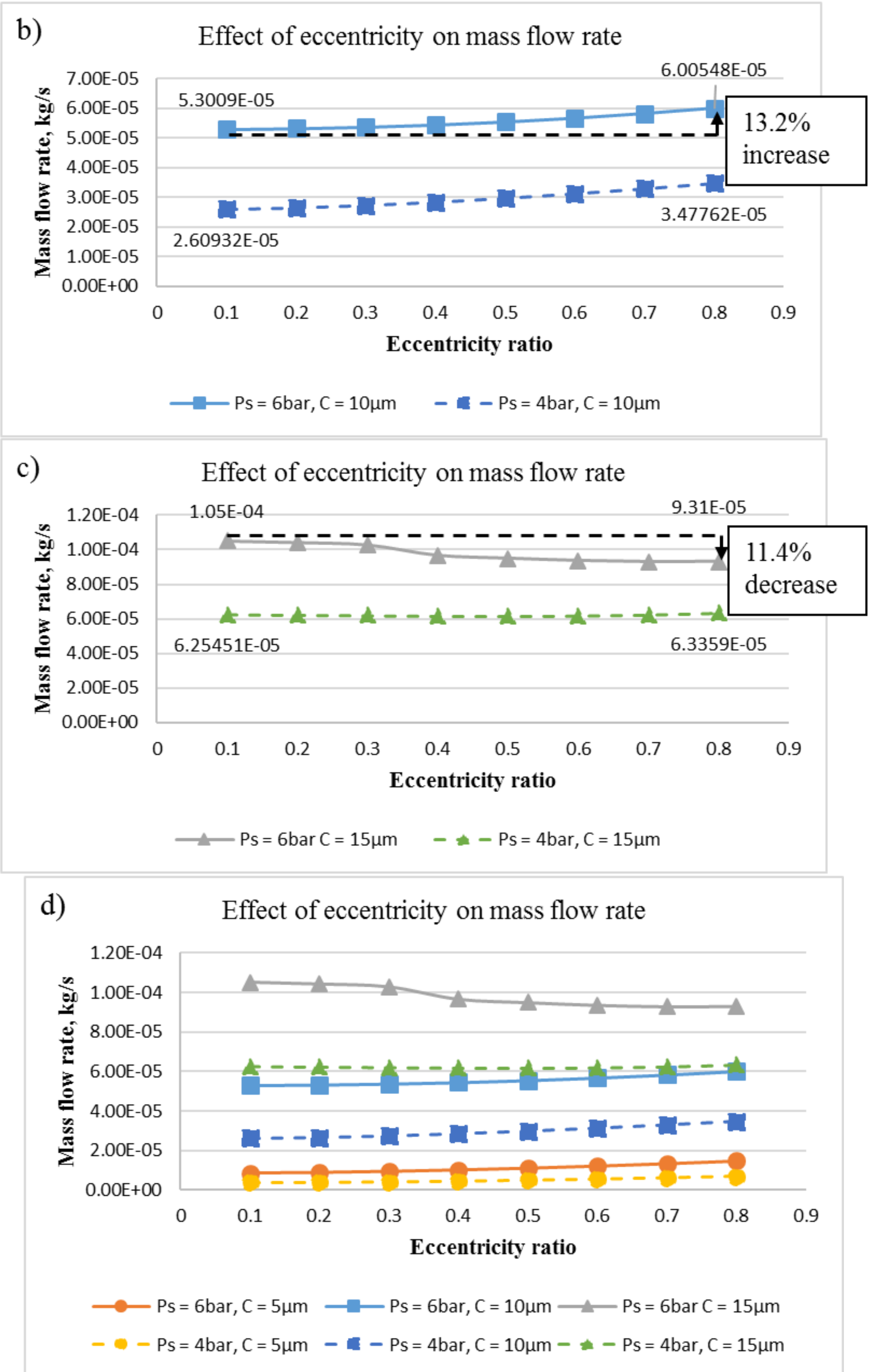

Figure 4.3 Effect of eccentricity on mass flow rate of static air journal bearings for different supply pressure and radial clearance combinations

Figure 4.3 shows the variation of mass flow rate with eccentricity at different supply pressures and radial clearances. In Figure 4.3 a) to c), the radial clearance increases from 5 μm to 15 μm at two supply pressures. The percentage of the mass flow rate variation reduces from 74% down to around 10%. With a larger radial clearance, the effect of eccentricity on mass flow rate becomes less significant. In Figure 4.3 d), it can be found that mass flow rate increases with the supply pressure and radial clearance.

4.3.2 Optimization of radial clearance, orifice diameter and supply pressure

Hydrostatic journal air bearings with low air consumption while maintaining reasonable bearing reaction forces to static load reduce the demand on air supplies and enable the applications of hydrostatic air bearings to be expanded. The influence of radial clearance, the diameter of orifice restrictors and the effect of supply pressure on the bearing reaction forces and mass flow rate are investigated in this section to find optimized combinations.

Figure 4.4 shows that the bearing reaction force has a parabolic relationship with the radial clearance. The optimized radial clearance at which maximum bearing reaction forces to static load varies with the supply pressure. The optimized radial clearance becomes smaller when higher supply pressure is used. On the other hand, both supply pressure and radial clearance have a linear effect on mass flow rate, Figure 4.5. This is because the restricted area is the annular region at the edge of orifice restrictors.

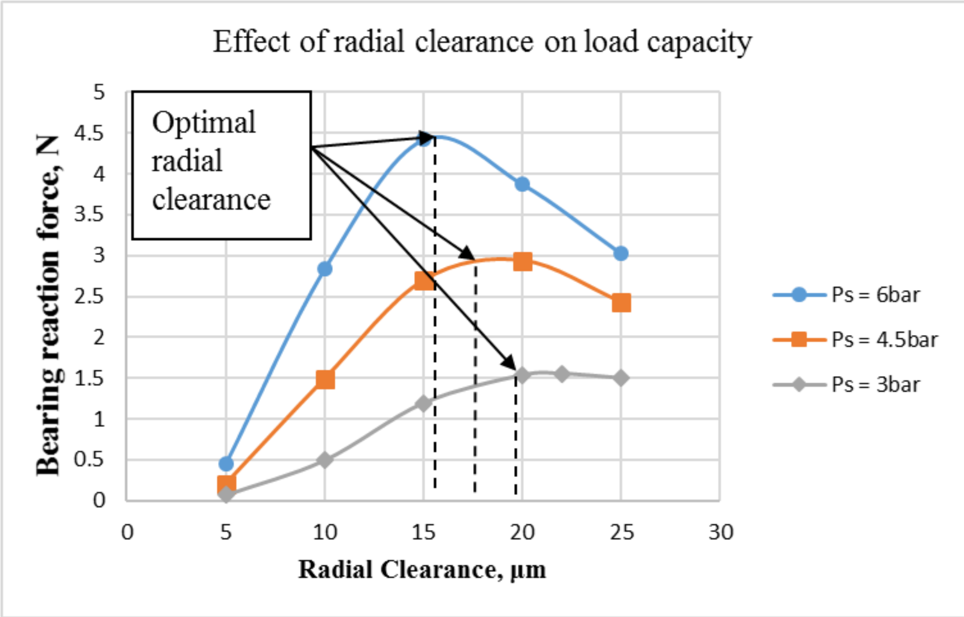

Figure 4.4 The effect of radial clearance on bearing reaction forces for hydrostatic journal air bearings with 8mm diameter, a length to radius ratio of 1, and a single row of orifice restrictors at a 0.4 eccentricity ratio

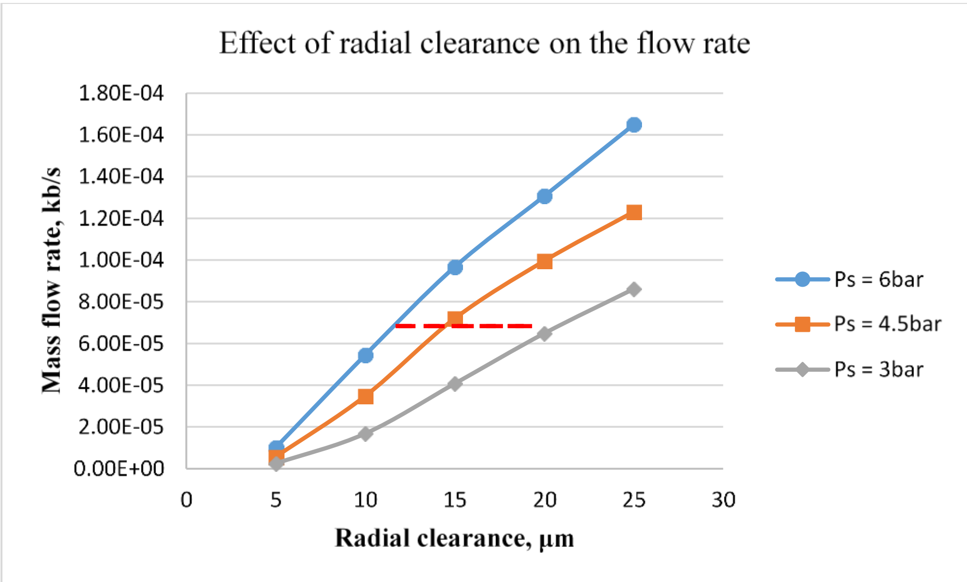

Figure 4.5 The effect of radial clearance on flow rate at different supply pressures for hydrostatic journal air bearings with 8mm diameter, a length to radius ratio of 1, and a single row of orifice restrictors at a 0.4 eccentricity ratio

It should be noticed that when the mass flow rate of the supplied air is limited at a certain level, as the dashed line indicated in Figure 4.5. The radial clearance at this condition for each supply pressure in Figure 4.5 can be used to calculate bearing reaction forces using Figure 4.4. It can be found that bearing reaction forces are improved by using high supply pressure and low radial clearance. For example, bearings with 6 bar supply pressure and 12µm clearance have up to 40% higher bearing forces compared to bearings with 4.5bar supply pressure and 15µm clearance, Figure 4.4. However, the air consumption of the former is much lower as shown in Figure 4.6.

In general, the bearing reaction forces always increase with supply pressure at the cost of air consumption, as shown in Figure 4. and Figure 4.8. The increasing rate of bearing reaction forces drops rapidly while the increasing rate of mass flow does not vary a lot. The efficiency of improving bearing reaction forces to static load by using higher supply pressure is less significant.

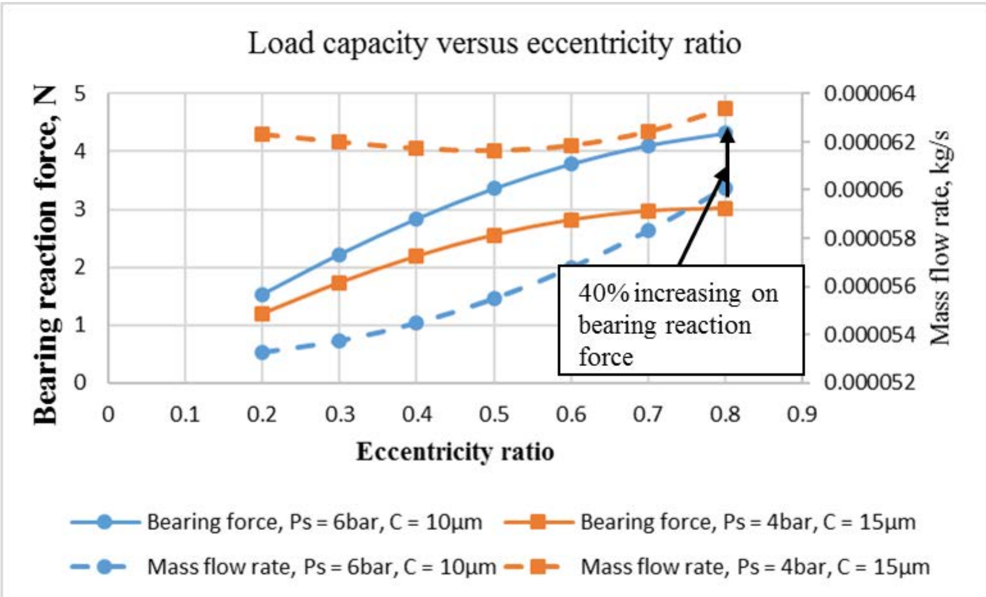

Figure 4.6 Bearing reaction forces in relation with mass flow rate of hydrostatic journal air bearings

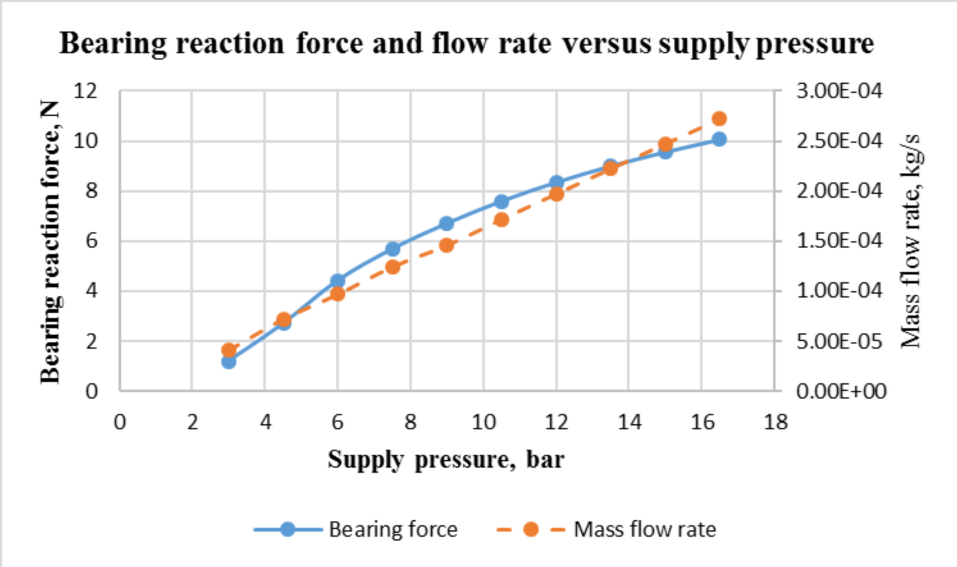

Figure 4. Effect of supply pressure on bearing reaction forces versus mass flow rate. Journal bearings with 15 μm radial clearance, 8 mm diameter, length to radius ratio as 1, single row orifice restrictors

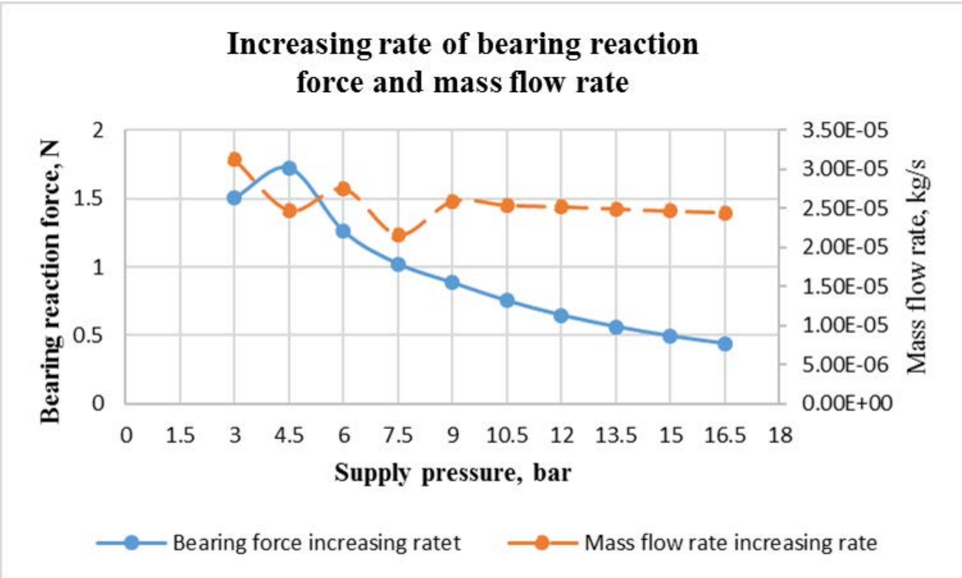

Figure 4.8 Increasing rate of bearing reaction forces versus mass flow rate

The effect of orifice diameters on bearing reaction forces and mass flow rate was investigated. The study was carried out on hydrostatic journal air bearings with 3 bar supply pressure and 0.4 eccentricity ratio. The dimensions of the bearings were the same as listed in Table 4.3. The results are plotted in Figure 4.9 and Figure 4.10. The optimal radial clearance is defined as the radial clearance where maximum bearing reaction forces are achieved. The optimal radial clearances for some given orifice diameters have been found from tests and are listed in Table 4.4. It is observed from tests that the optimal radial clearance decreases with the reduction of orifice diameters. Figure 4.9 shows that curves of bearing reaction forces become sharp as a result of reduced orifice diameter. For example, for an orifice diameter of 100 μm, the bearing reaction forces can decrease by 3% from the maximum in zone A, then drop rapidly once the bearing radial clearance moves away from it. However, for an orifice diameter of 300 μm, the reduction of bearing reaction forces is maintained at less than 3% in a much wider range B. In other words, the latter has a higher tolerance of manufacturing errors. In Figure 4.10, the relationships between the maximum bearing reaction forces and the associated mass flow rate are plotted. It can be found that the variation of the maximum bearing reaction forces is less than 1%, but the mass flow rate increases seven times when orifice diameter increases from 100 μm to 300 μm.

Table 4.4 Optimal radial clearance at different orifice diameters

	Orifice diameter (μm)				
	300	250	200	150	100
Optimal radial clearance (μm)	22	20	17	14	11

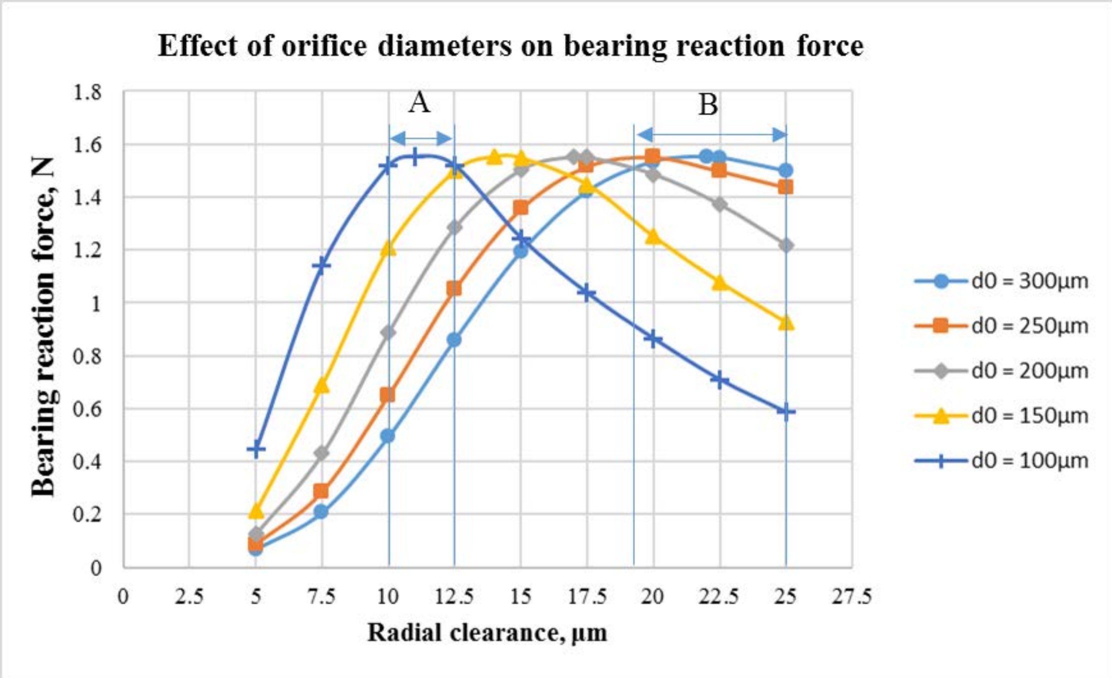

Figure 4.9 Effect of orifice diameters on bearing reaction forces to static load

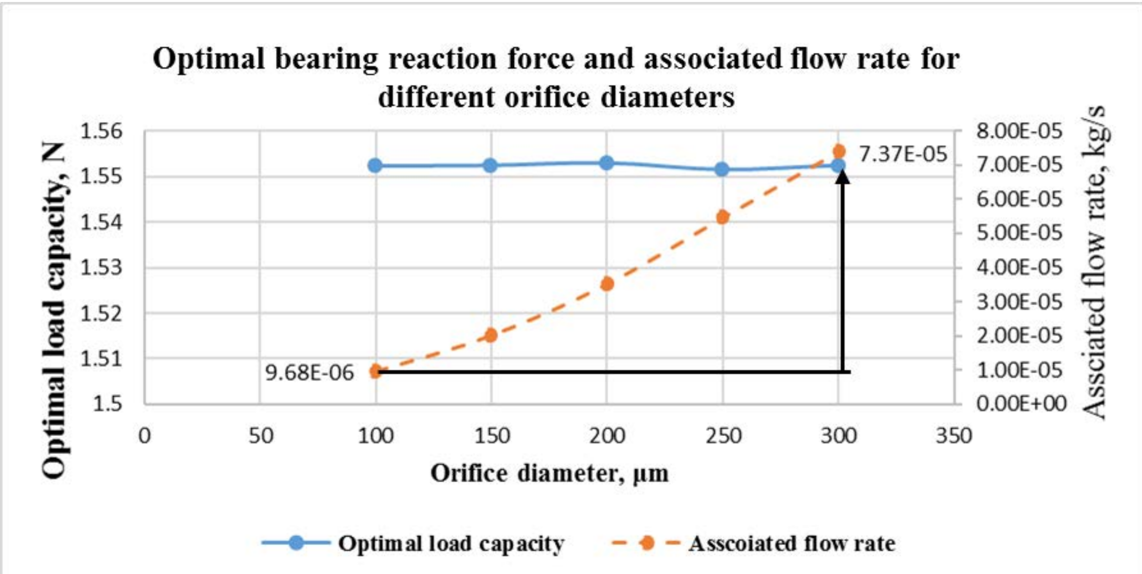

Figure 4.10 Optimal bearing reaction forces to static load and associated flow rate for different orifice diameters

4.4 Theoretical studies on rotational performance of hydrostatic journal air bearings

This section focuses on theoretical studies on the rotational performance of hydrostatic journal air bearings from three aspects using the linear perturbation analysis approach proposed in Chapter 3. Firstly, the static equilibrium analysis is performed at varies configurations. Secondly, bearing forces are represented by stiffness and damping coefficients with respect to the static equilibrium configurations. Thirdly, the stability and natural frequencies are analysed for rotor-bearing system using linear bearing models.

4.4.1 Static equilibrium analysis of hydrostatic journal air bearings at rotational condition

At a given static load and rotational speed, the static equilibrium configuration of a hydrostatic journal air bearing largely depends on the compressibility number Λ and the restrictor setup. The hydrodynamic effect increases with the compressibility number. From its definition in Equation 3.3, it can be increased by either increasing the radius of the journal or reducing radial clearance. For a rotor with a given dimension, a small radial clearance is preferred to achieve a high compressibility number and therefore a high dynamic flow effect. Figure 4.11 shows the pressure distribution of a hydrostatic journal air bearing when Λ is 0 and 1.86. There is a significant pressure build up at the convergent zone of the air film because of the journal rotation. Figure 4.12 gives the pressure profiles at the symmetry plane of the two cases respectively.

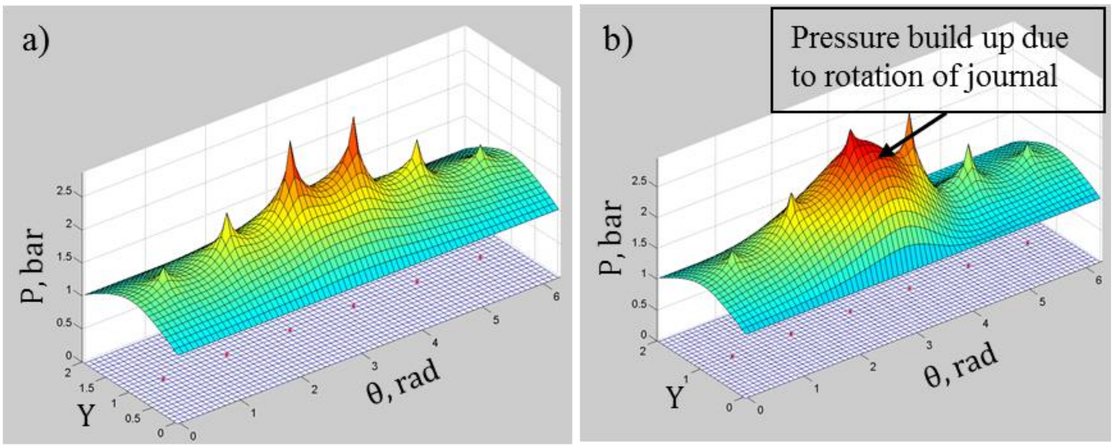

Figure 4.11 Pressure distribution for journal bearings, $r_0 = 4$ mm; $l = 8$ mm; $d_0 = 150$ µm; $c = 14$ µm; a) $\omega = 0,\ \Lambda = 0$, b) $\omega = 200000$ rpm, $\Lambda = 1.86$

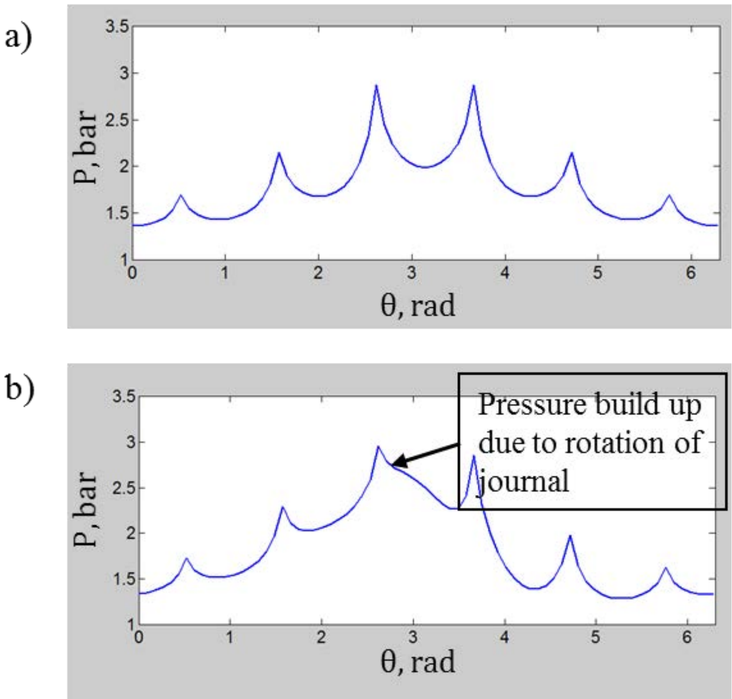

Figure 4.12 Pressure profile at symmetry plane, $r_0 = 4$ mm; $l = 8$ mm; $d_0 = 150$ µm; $c = 14$ µm; a) $\omega = 0, \Lambda = 0$, b) $\omega = 200000$ rpm, $\Lambda = 1.86$

The relationship between bearing reaction forces and eccentricity at various compressibility numbers is presented in Figure 4.13. The results are calculated for bearings with 8mm diameter and 8 mm length. The solid line represents 11 µm radial clearance, while the dashed line represents 8μm radial clearance. In the both cases, the rotational speeds are adjusted to achieve the same values for Λ. There are slight differences for the two cases with the same Λ and the difference becomes smaller with a higher Λ.

Using low radial clearance is a preferable method to enhance the rotational performance of hydrostatic journal air bearings. Table 4.5 lists the maximum percentage difference on bearing forces with respect to compressibility number. Although bearings with the shown geometry achieve maximum bearing forces with 11μm radial clearance at non-rotational condition in Figure 4.9, the rotation speed must be much higher to maintain the same bearing reaction forces compared to bearings with an 8 μm radial clearance at rotational condition.

Table 4.5 Rotational speed to achieve same Λ for different radial clearances and percentage differences of bearing forces

	Bearing Geometry:		**r**: 4mm	**l**: 8mm,	$\boldsymbol{d_0}$:100**μm**	$\boldsymbol{P_s}$: 3bar
	Λ	0.75	1.51	2.56	4.84	7.12
Rotation speed, rpm	C = 8μm	26450	52895	89920	170000	250190
	C = 11μm	50000	100000	170000	321500	473000
Percentage difference		9.80%	4.60%	1.10%	1.60%	3.70%
r - radius, ***l*** - length, ***C*** - radius clearance, $\boldsymbol{d_0}$ – orifice diameter						

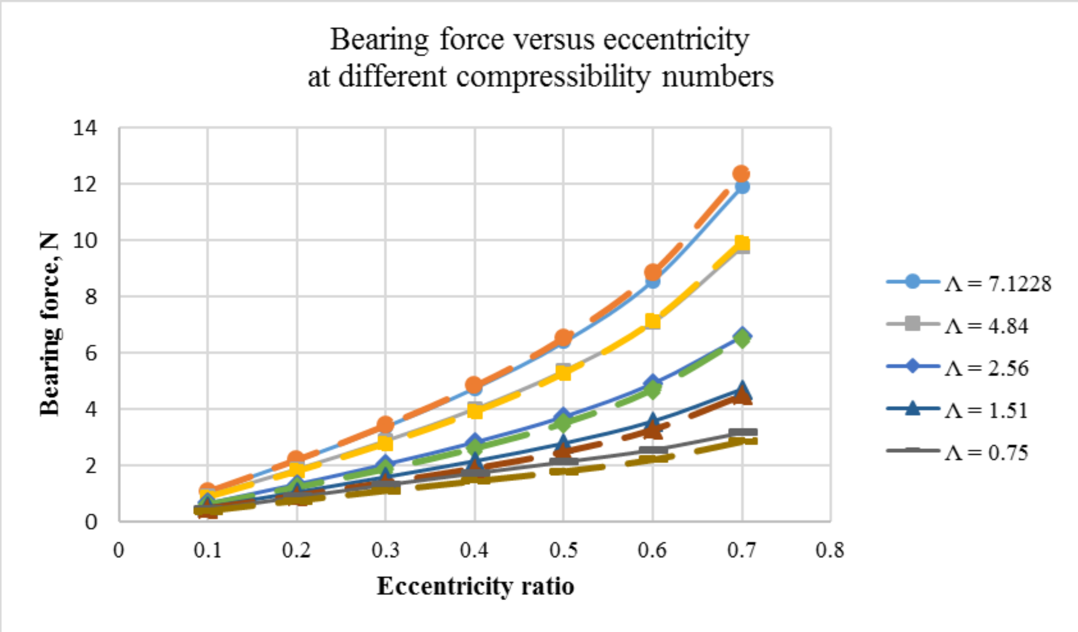

Figure 4.13 Relation of bearing reaction forces and eccentricity at different compressibility numbers, solid line for c = 11 μm and dashed line for c = 8 μm

Because of the rotation of the journal, the pressure in air film is no longer distributed symmetrically on the surface of the bearing. The angle between the line of centres of the journal and bearing sleeve to bearing reaction force at a static equilibrium position is called the attitude angle. The static equilibrium position varies with compressibility numbers and restrictor setup. The track of these equilibrium positions at different eccentricity ratios forms a static equilibrium locus curve. When the static load applied to an air bearing changes, the static equilibrium position moves along this curve. It can be used as an indicator of attitude angles. Also, the rotational performance of air bearings is often studied according to the static equilibrium positions. In Figure 4.14, the static equilibrium locus curves are plotted for the cases shown in Table 4.5.

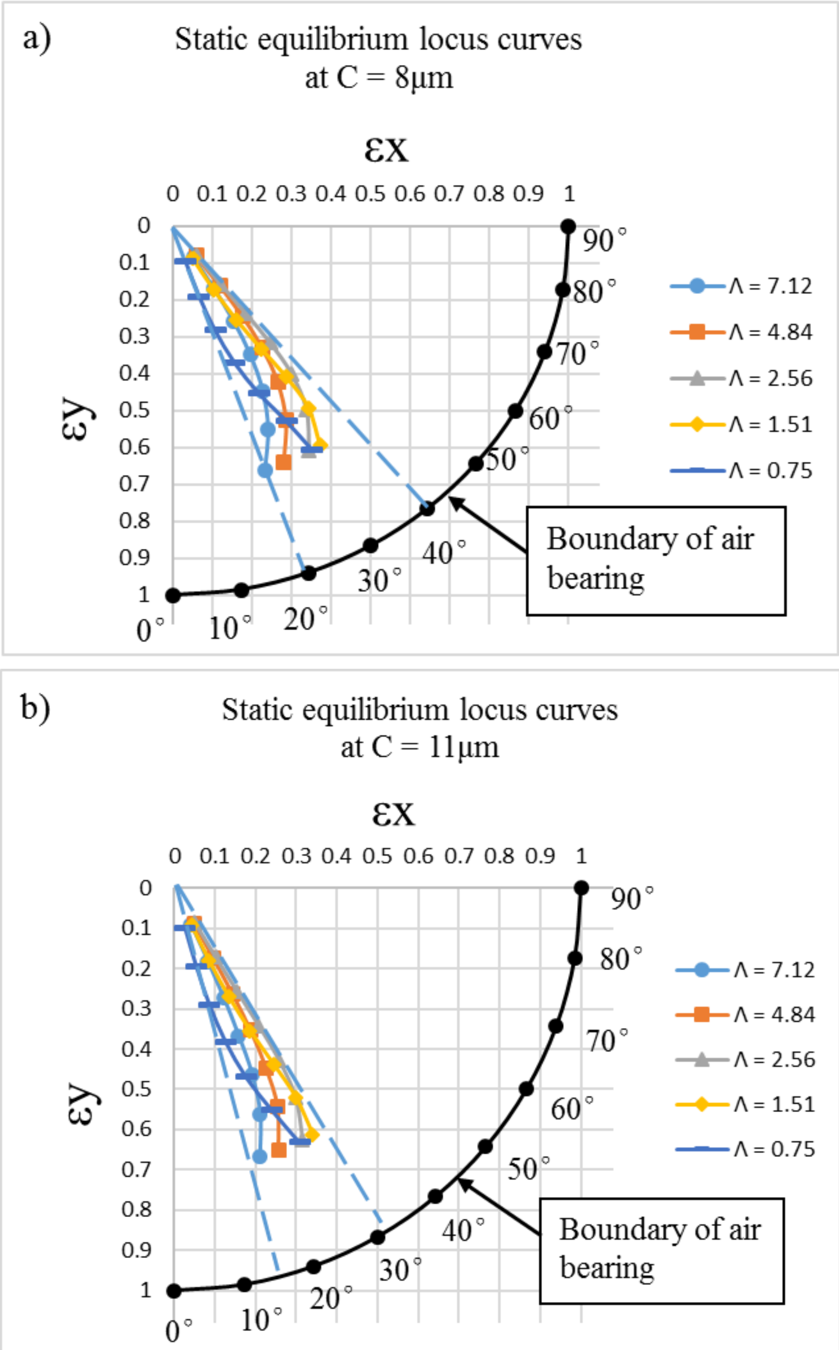

Figure 4.14 Attitude angles for different compressibility numbers. a) Attitude angle for bearing with 8 μm radial clearance at various compressibility numbers. b) Attitude angle for bearing with 11 μm radial clearance at various compressibility numbers

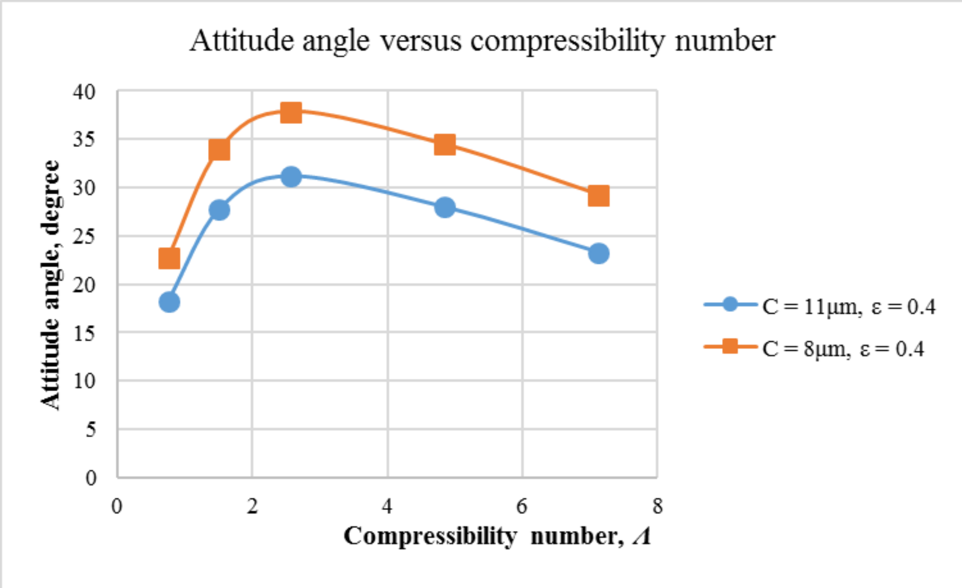

Figure 4.15 Attitude angle for different compressibility numbers. Eccentricity ratio is 0.4

In Figure 4.14 a), the attitude angle varies between 20° and 40° for an 8 μm radial clearance. While in Figure 4.14 b), the range is between 15° and 30°. This suggests that the attitude angle is greatly influenced by rotational speed. Figure 4.15 shows the prediction on the variation of attitude angle with Λ. As listed in Table 4.5, smaller radial clearance requires lower rotation speed to achieve the same values of Λ. It can be concluded that a combination of low radial clearance and rotation speed operation will lead to relatively high attitude angles.

4.4.2 Stiffness and damping coefficients of hydrostatic journal air bearings

Bearing forces can be represented by Equation 3.61 when a static equilibrium position and a rotational speed are given. The associate stiffness ($k_{i,j}$) and damping ($d_{i,j}$) coefficients can be calculated by means of assigning a whirling frequency (ω_w) of the journal centre and using Equations from 3.53 to 3.60. It is convenient to represent the whirling frequency as a ratio to rotational speed. This ratio is noted as the whirling frequency ratio (Ω), or perturbation frequency ratio.

Figure 4.16 gives the variation of $k_{i,j}$ and $d_{i,j}$ of a hydrostatic journal air bearing with whirling frequency ratio at the concentric journal position. Note that the principal stiffness coefficients increase rapidly with whirling frequency showing a typical gas bearing hardening effect [0] . On the other hand, the direct damping coefficients decrease dramatically as the whirling frequency rises. Similar behaviour can be found on the cross-coupled stiffness coefficients. It indicates that hydrostatic journal air bearings become quite stiff with little or zero viscous damping coefficients at high perturbation frequencies.

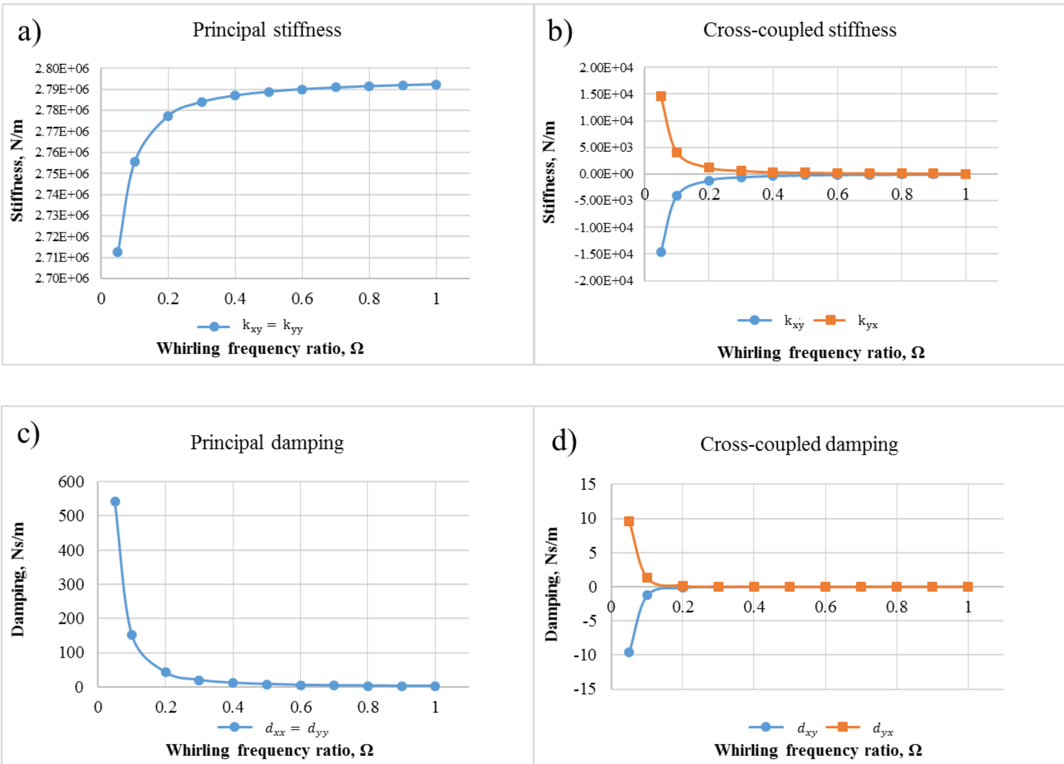

Figure 4.16 Stiffness and damping coefficients at concentric journal position, r = 4mm; l = 8 mm, when c = 6 μm; ω = 100,000 rpm; Λ = 5.06; d_0 = 100 μm; P_S= 3 bar

In this section, the variation of $k_{i,j}$ and $d_{i,j}$ at synchronic whirling frequency ($\Omega = 1$) will be investigated in several cases to reveal the effect of different design parameters and working conditions. The principal coefficients are plotted in solid lines and the cross coupled coefficients are plotted in dash lines.

Figure 4.1 shows the variation of these coefficients versus the eccentricity ratio. In this case, the compressibility number (Λ) is 7.9 with 4bar supply pressure at restrictors. The difference in the amplitude of two principal stiffness coefficients increases with the eccentricity ratios while the cross coupled stiffness coefficients are still very similar. The amplitude of all stiffness coefficients increases with eccentricity ratios. The damping coefficients have no significant change in this case.

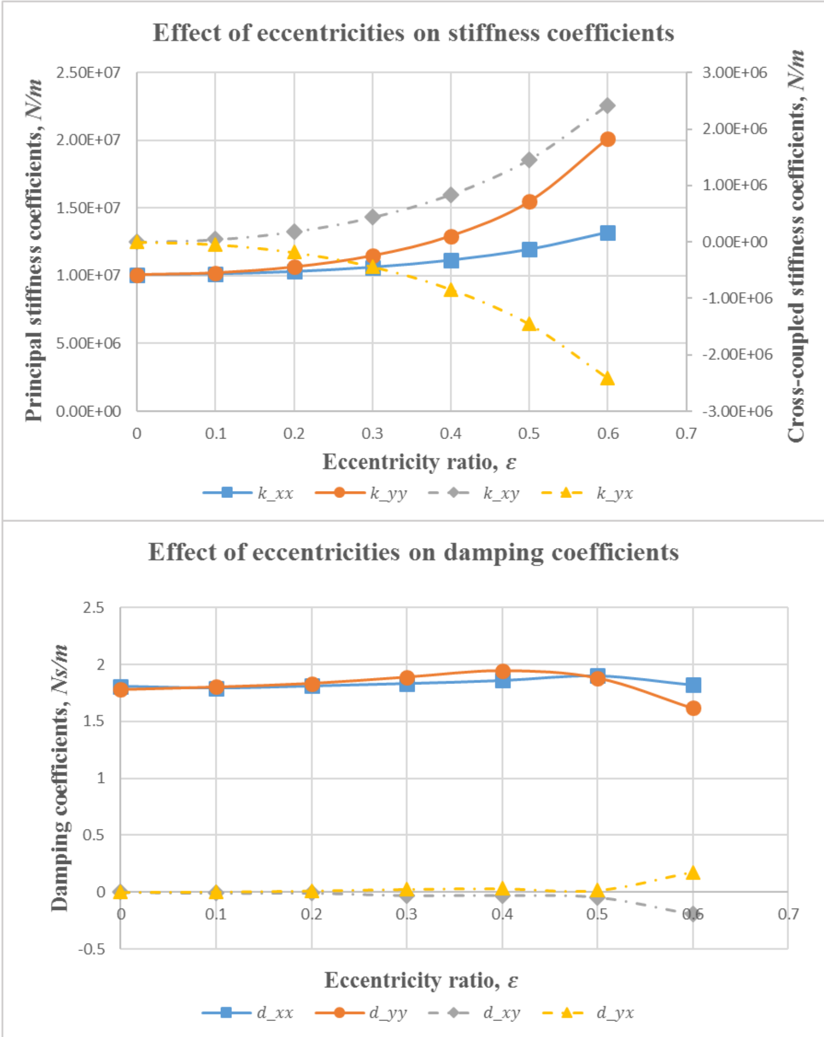

Figure 4.1 The effect of eccentricity ratio on the bearing stiffness and damping coefficients, where $d_0 = 0.25\, mm$, $r = \frac{l}{2} = 10\, mm$, $c = 10\, \mu m$, $\Lambda = 7.9$, $P_s = 4\, bar$

The variation of bearing radius (r), radial clearance (C) and rotational speed (ω) will change the compressibility number (Λ). Their effects on $k_{i,j}$ and $d_{i,j}$ are similar and studied as the effect of Λ. Figure 4.18 gives the values of $k_{i,j}$ and $d_{i,j}$ at various Λ. The amplitude of the stiffness coefficients increases significantly with Λ while the damping coefficients show slightly variation. The figure shows hardening effect of hydrostatic journal air bearings introduced by high compressibility number.

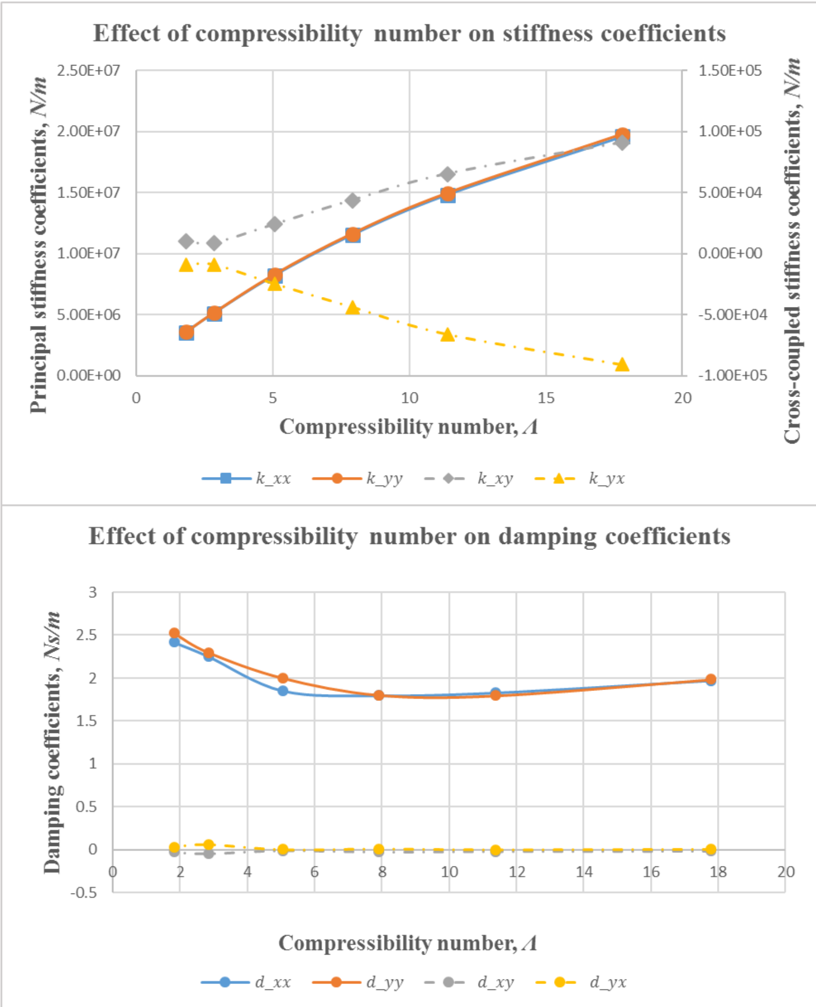

Figure 4.18 The effect of compressibility number on bearing stiffness and damping coefficients, where $d_0 = 0.25mm$, $r = l/2 = \ 10mm$, $c = 10\mu m$, $P_s = 4bar$

The influence of design parameters investigated in this section is analysed based on the static equilibrium configuration at 0.1 eccentricity ratio from Figure 4.1 . The design parameters being studied are the orifice restrictor diameters (d_o), supply pressure (P_s) and length to diameter ratio ($\zeta = l/2r_0$).

Figure 4.19 presents the effect of the orifice restrictor diameters on $k_{i,j}$ and $d_{i,j}$. The stiffness coefficients increase gradually with orifice diameter (d_o) from 0.15mm to 0.35mm. When d_o is larger than 0.35mm, there is no further increase on the stiffness coefficients. If the orifice diameter is larger than 0.85mm for this bearing configuration, the orifices lose their function as restrictors and introduces sharp decreasing of stiffness. The damping coefficients show a similar trend. In general, the variation of orifice diameters has limited effects on $k_{i,j}$ and $d_{i,j}$.

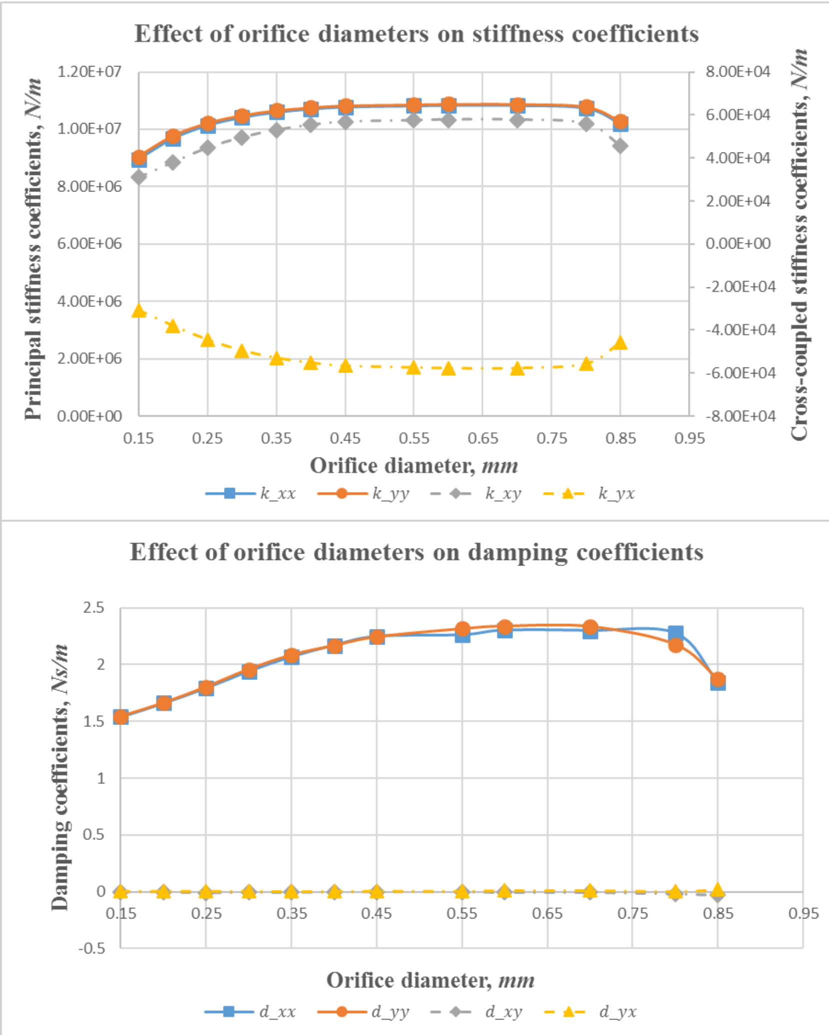

Figure 4.19 Effect of orifice diameter on bearing stiffness and damping coefficients, where $r = l/2 = 10mm$, $c = 10\mu m$, $P_s = 4bar$

Figure 4.20 shows the variation of stiffness and damping coefficients at different supply pressures (P_s). The eccentricity ratio is 0.1 and the orifice diameter is 250μm. The principal stiffness coefficients increase linearly with the supply pressure. On the other hand, the cross coupled stiffness coefficients reach the maximum amplitude when P_s about 3bar. It is found that the supply pressure has no effect on the damping coefficients of a hydrostatic journal bearings.

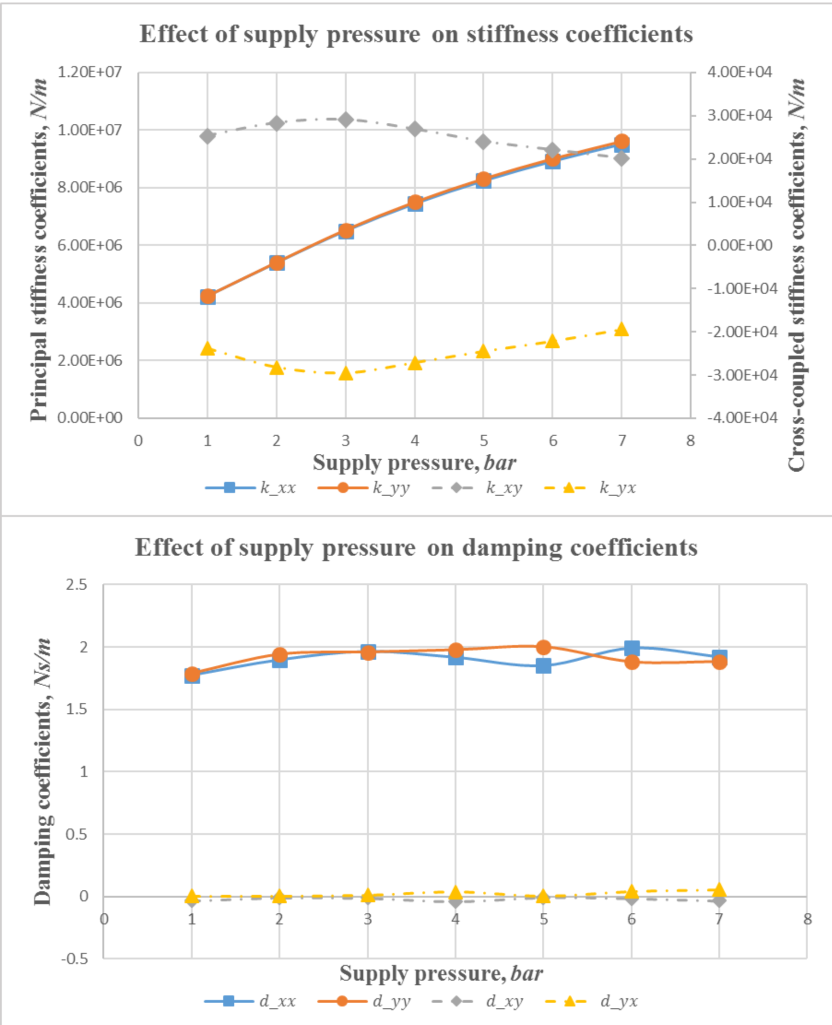

Figure 4.20 The effect of supply pressure on bearing stiffness and damping coefficients, where $d_0 = 0.25mm$, $r = l/2 = 10mm$, $c = 10\mu m$

Figure 4.21 shows the variation of stiffness and damping coefficients with the length to bearing diameter ratios ζ. The stiffness coefficients increase significantly with ζ. This is because the bearing surface area has been increased with large ζ. Although the principal damping coefficients increase with ζ, the amplitude of this improvement is very limited. In this analysis, the maximum value of ζ is within 2.

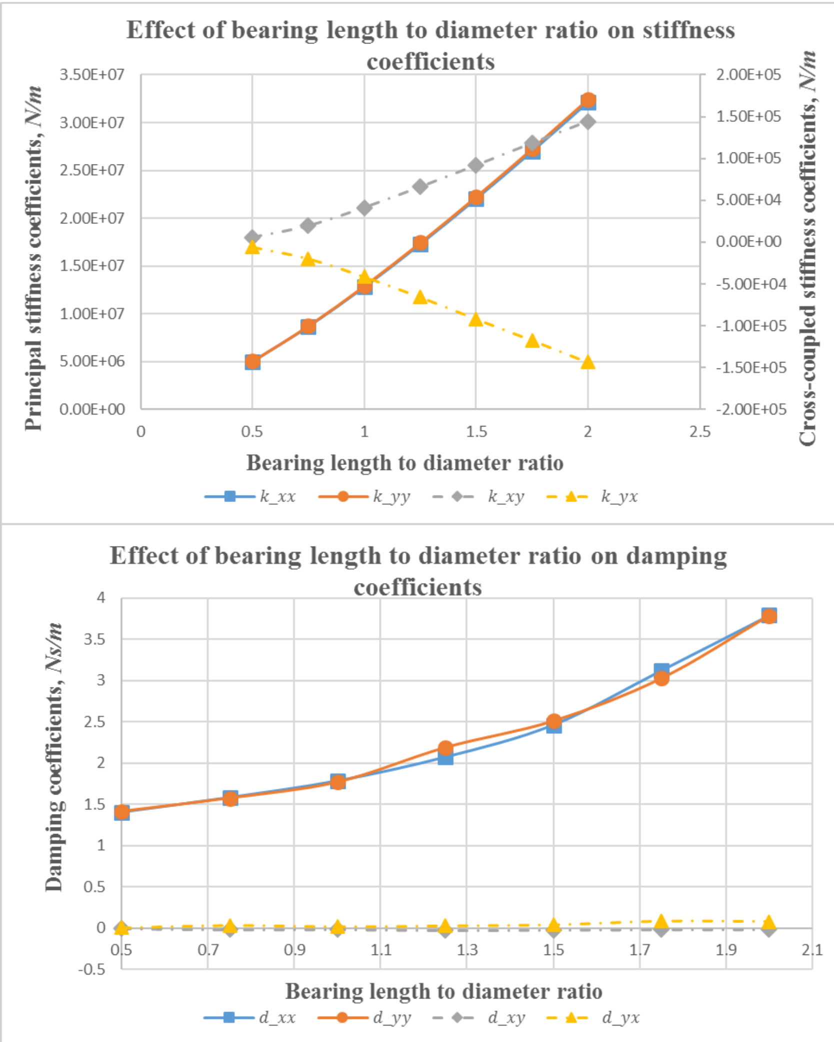

Figure 4.21 The effect of bearing length to diameter ratio on bearing stiffness and damping coefficients, where $d_0 = 0.25mm$, $r = 10mm$, $c = 10\mu m$, $\Lambda = 7.9$, $P_s = 4bar$

From the above analysis on the stiffness and damping coefficients, it can be found that the compressibility number (Λ), eccentricity ratio (ε), supply pressure (P_s) and bearing length to diameter ratio (ζ) have direct influences on the stiffness coefficients. By means of adopting a large orifice diameter (d_o), the stiffness coefficients can be improved in a limited margin at the cost of high compressed air consumption. The damping coefficients of a hydrostatic journal air bearings are mainly influenced by the journal whirling frequency (ω_w) or the excitation frequency. They cannot be improved by means of adjusting bearing design parameters.

The analysis on the stiffness and damping coefficients of hydrostatic journal air bearings can assist the bearing design and provide useful information for stability and natural frequencies predictions of a rotor bearing system.

4.4.3 Analysis of stability and natural frequencies of a rotor bearing system using linear bearing model

In this section, the stability and natural frequencies of a rotor bearing system supported by hydrostatic journal air bearings are investigated. Rotor R-1 is supported by two identical journal bearings and two thrust bearings to constrain the axial movement. The major dimensions of the journal bearings are listed in Table 4.6.

Table 4.6 Dimensions of the hydrostatic journal air bearings used in analysis

Radius of the bearings, r_0 (mm)	Length to diameter ratio, $l/2r_0$	Radial clearance, c µm	Orifice diameter, d_0 (µm)	Supply Pressure, P_s (bar)	Number of orifices, N_{ori}
10	1	13	250	7	6

The hydrostatic journal air bearings under study here are represented as linear bearing units with stiffness and damping coefficients extracted from the perturbation analysis in Section 4.4.2. The bearing models are added into the rotor dynamic model to predict stability and critical speeds of the rotor bearing system.

The finite element rotor dynamic model of R-1 is adopted with the hydrostatic bearing model to form a linear time invariant (LTI) system. The stability of this system can be analysed using the static equilibrium stability analysis (SESA) proposed in Chapter 3.

Two cases are studied in this section:

Case I: R-1 with linear journal bearings only. The system is illustrated in Figure 4.22. The bearings support is taken to be rigid. The characteristic matrix of the system equations of motion is expressed in Equation 4.17. The stiffness and damping matrix of the journal bearings are added into the global matrices following the process from [84] as shown in Appendix C.

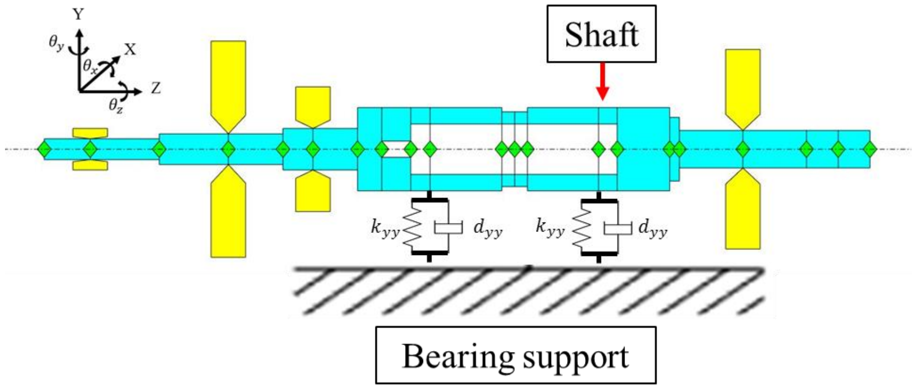

a) R-1 supported by linearized journal bearings

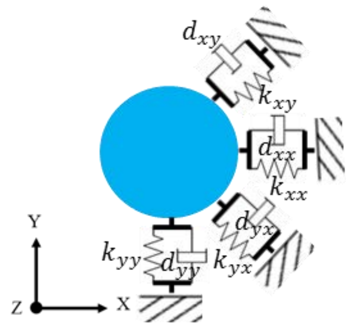

b) Linearized journal bearing – view in Z axis

Figure 4.22 Schematic views of R-1 with linearized journal bearing

$$J_1 = \begin{bmatrix} [0] & [1] \\ -[\boldsymbol{M_s}]^{-1}[\boldsymbol{K_{sys\_1}}] & -[\boldsymbol{M_s}]^{-1}[\boldsymbol{CG_{sys\_1}}] \end{bmatrix}$$

$$[\boldsymbol{K_{sys\_1}}] = [[\boldsymbol{K_s}] + [\boldsymbol{K_b}]]$$

Equation 4.17

$$[\boldsymbol{CG_{sys\_1}}] = [[\boldsymbol{C_s}] + [\boldsymbol{C_b}] + [\boldsymbol{G}]]$$

where $[\boldsymbol{M_s}]$ is the shaft structure mass and inertia matrix, $[\boldsymbol{K_{sys\_1}}]$ the system stiffness matrix, $[\boldsymbol{K_s}]$ the shaft structure stiffness matrix, $[\boldsymbol{K_b}]$ the bearings' stiffness matrix, $[\boldsymbol{CG_{sys\_1}}]$ the system damping and gyroscopic matrix, $[\boldsymbol{C_s}]$ the shaft structure damping coefficients, $[\boldsymbol{C_b}]$ the bearing's damping matrix, and $[\boldsymbol{G}]$ the shaft structure gyroscopic matrix.

Case II: R-1 is supported by linear journal bearings with linear viscoelasticity. The system is illustrated in Figure 4.23. The bearing sleeve is supported by a viscoelastic support made from 4 O-rings in parallel. The whole system is connected to a rigid body. The dynamic properties of the O-rings can be calculated using the empirical Equations 4.19 [43]. The characteristic matrix of the system equation of motion is expressed as Equation 4.18. In addition to the conditions as given in **Case I**, the mass and inertia matrix, stiffness and damping matrix of the viscoelastic support are also assembled into the global matrices following the process introduced in [84]. Since the bearing sleeve supported by the O-rings are not rotating, there is no need to use the gyroscopic matrix of it.

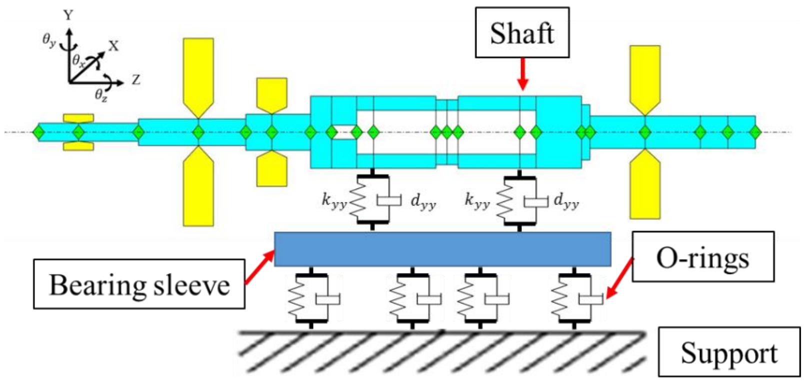

a) R-1 supported by linearized journal bearings with bearing sleeve supported by O-rings

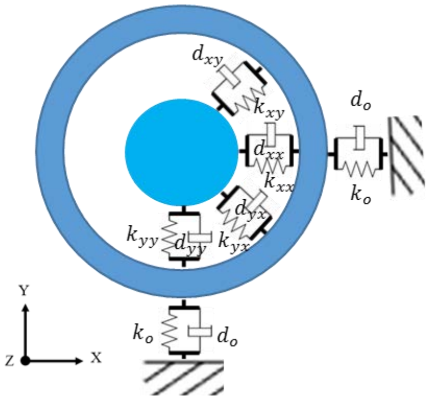

b) Axial view of the rotor bearing system

Figure 4.23 Schematic views of the R-1 with linearized journal bearing and viscoelastic support. a) The R-1 supported by linearized journal bearings with bearing sleeve supported by O-rings; b) A linearized journal bearing with bearing sleeve supported by O-rings – view in Z axis

$$J_2 = \begin{bmatrix} [0] & [1] \\ -[\boldsymbol{M_2}]^{-1}[\boldsymbol{K_{sys\_2}}] & -[\boldsymbol{M_2}]^{-\boldsymbol{1}}[\boldsymbol{CG_{sys\_2}}] \end{bmatrix}$$

$$[\boldsymbol{M_2}] = \begin{bmatrix} [\boldsymbol{M_s}] & [\boldsymbol{0}] \\ [\boldsymbol{0}] & [\boldsymbol{M_v}] \end{bmatrix}$$

Equation 4.18

$$[\boldsymbol{K_{sys\_2}}] = \begin{bmatrix} [\boldsymbol{K_s}] + [\boldsymbol{K_b}] & -[\boldsymbol{K_b}{}'] \\ -[\boldsymbol{K_b}{}']^T & [\boldsymbol{K_v}] \end{bmatrix}$$

$$[\boldsymbol{CG_{sys\_2}}] = \begin{bmatrix} [\boldsymbol{C_s}] + [\boldsymbol{C_b}] + [\boldsymbol{G}] & -[\boldsymbol{C_b}] \\ -[\boldsymbol{C_b}] & [\boldsymbol{C_v}] \end{bmatrix}$$

where $[\boldsymbol{M_s}]$ is the shaft structure mass and inertia matrix, $[\boldsymbol{K_{sys\_2}}]$ the system stiffness matrix, $[\boldsymbol{K_s}]$ the shaft structure stiffness matrix, $[\boldsymbol{K_b}]$ the bearings' stiffness matrix, $[\boldsymbol{CG_{sys\_2}}]$ the system damping and gyroscopic matrix, $[\boldsymbol{C_s}]$ the shaft structure damping coefficients, $[\boldsymbol{C_b}]$ the bearing's damping matrix, $[\boldsymbol{G}]$ the shaft structure gyroscopic matrix, $[\boldsymbol{M_v}]$ the bearing sleeve mass and inertia matrix, and $[\boldsymbol{K_v}]$ and $[\boldsymbol{C_v}]$ the stiffness and damping matrix of the bearing sleeve respectively.

$$k_o = (5.57\gamma - 0.636) \cdot \exp((0.754\gamma - 0.0111) \cdot f_p)$$
$$c_o = (0.483\gamma - 0.074) + 1/\exp((-33.3\gamma + 11.8) \cdot f_p)$$
Equation 4.19

where γ is the deformation ratio of the O-ring and f_p the excitation frequency in kHz.

The natural frequencies of the two cases identified from theoretical analysis are presented as Campbell diagrams in Figure 4.24 a) and b), with the speed up to 150k rpm. The first two modes are rigid modes and the third one is bending mode. It can be found that the natural frequencies of all three modes drops significantly because of viscoelastic support. For example, the natural frequency of mode 1 drops from 1680Hz to 383Hz. The differences in forward and backward whirl is also reduced for mode 2 and 3. This implies the system in **Case II** is a much 'soft' system in comparison with **Case I**. Figure 4.24 c) is a Campbell diagram of the bearing sleeve supported by O-rings. It is part of the system in **Case II** and has its own natural frequencies. Because it is not rotating and there is no gyroscopic effect, the natural frequencies of all three modes stay as constants throughout the rotor speed range. It also worth noting that, for this system, natural frequencies of the first two rigid modes are quite close to each other, 470Hz and 657Hz respectively, while the bending mode occurs at 27900Hz.

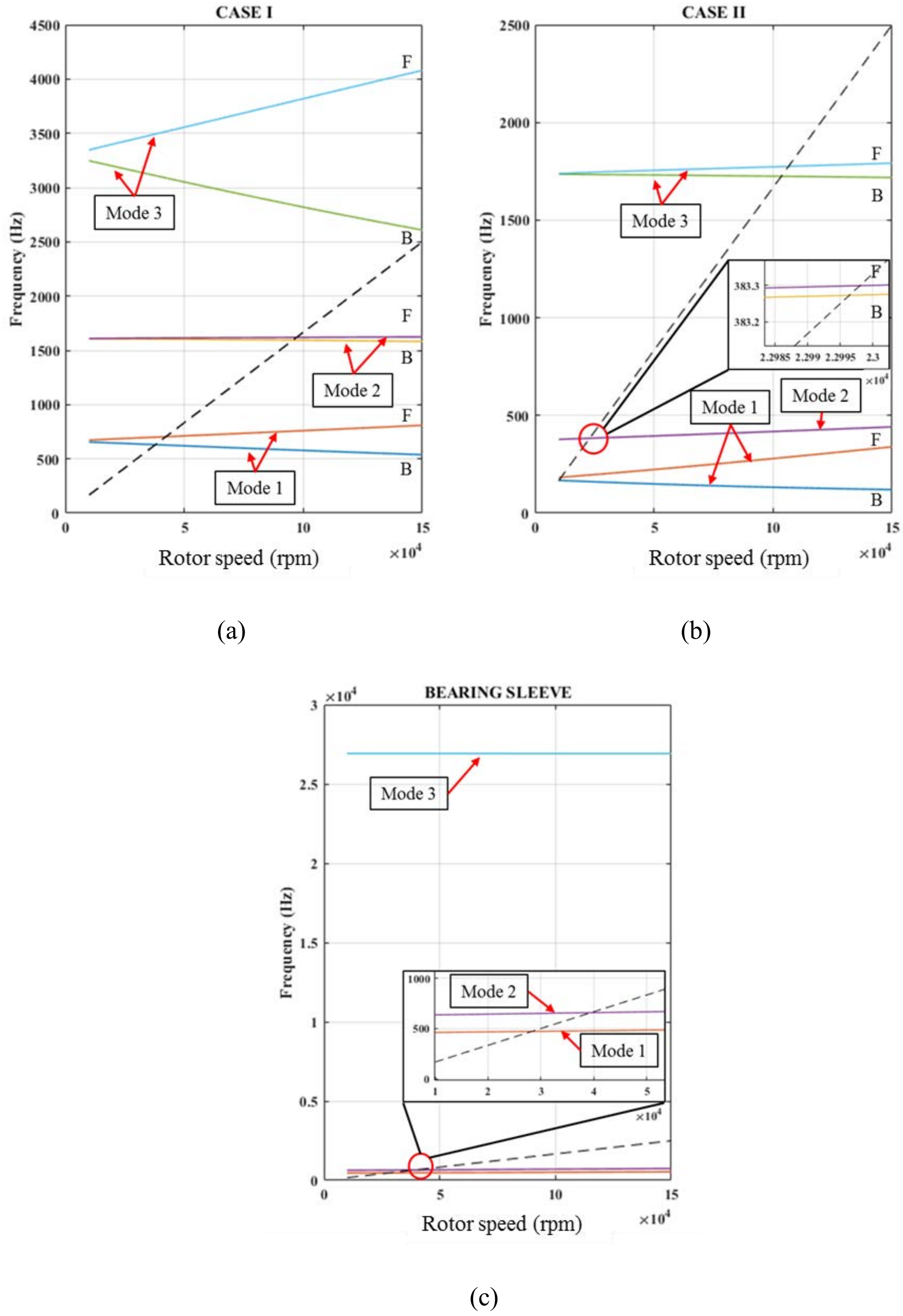

Figure 4.24 The Campbell diagrams for **Case I & II** and the bearing sleeve with linear dampers. The dash line is the synchronous line. '**F**' denotes forward whirl and '**B**' denotes backward whirl. a) **Case I:** linear rotor with linear bearings. b) **Case II:** linear rotor with linear bearings and linear dampers. c) Bearing sleeve with linear dampers.

The results of the two cases in stability analysis are shown in Figure 4.25 a) and b). In the stability maps, the real part of the leading eigenvalue of the system characteristic matrix is plotted against rotational speeds from 100k to 200k rpm. The system in **CASE I** become unstable when rotation speed slightly goes over 110k rpm and remains for the rest of the speed range. By means of introducing the viscoelastic support in **CASE II**, the stability of the system is greatly improved throughout the speed range. Figure 4.26 shows the predicted dominant whirling frequency ratio for **CASE I** after the system became unstable.

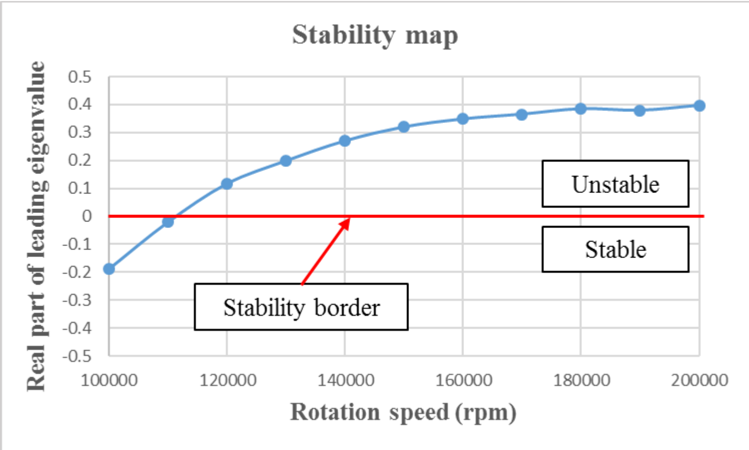

a) Stability map of **CASE I**

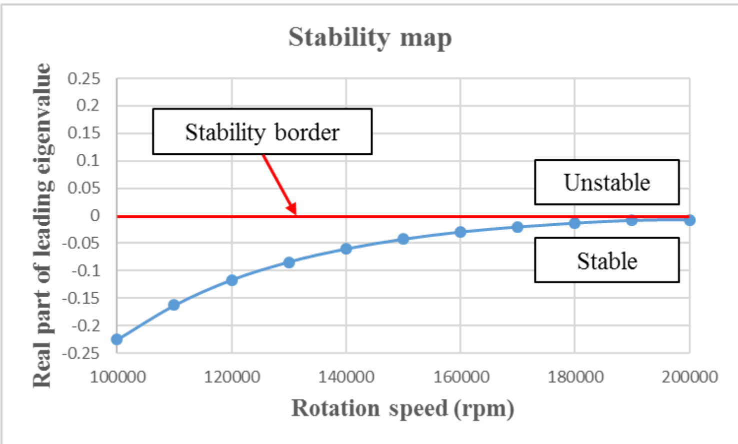

b) Stability map of **CASE II**, $\gamma = 0.2$

Figure 4.25 Stability maps based on SESA a) stability map of **CASE I**. b) stability map of **CASE II**

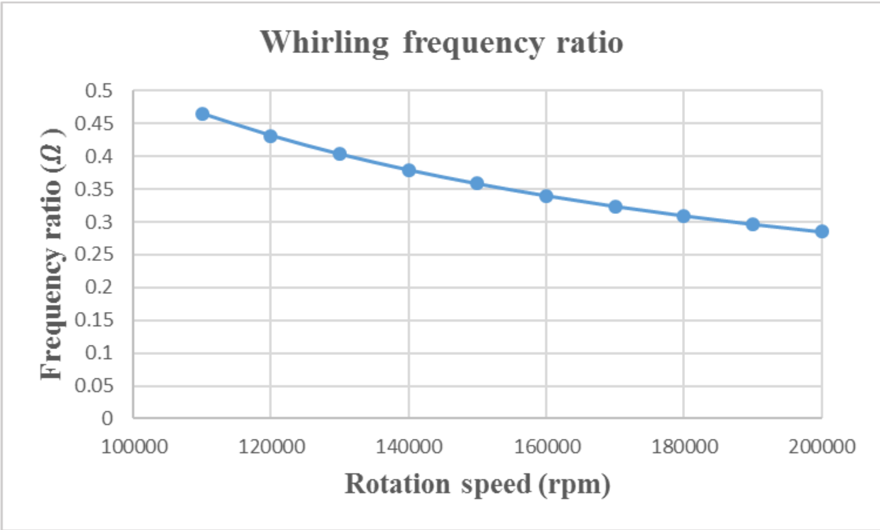

Figure 4.26 Frequency ratio of self-excited whirl to rotation speed for **CASE I**

The above analysis shows that viscoelastic support has the capability of improving the system stability. However, this will rely on careful selections of its dynamic properties as reported in [43]. From Equation 4.19, the dynamic properties of O-rings used in this project depend on both excitation frequencies and the O-ring deformation ratio, γ. The improper deformation of O-rings will introduce instability rather than stabilize the system. For example, Figure 4. 2 shows the stability map of **CASE II** when γ is 0.153. In comparison with Figure 4.25 a), the system becomes unstable at just over 50k rpm.

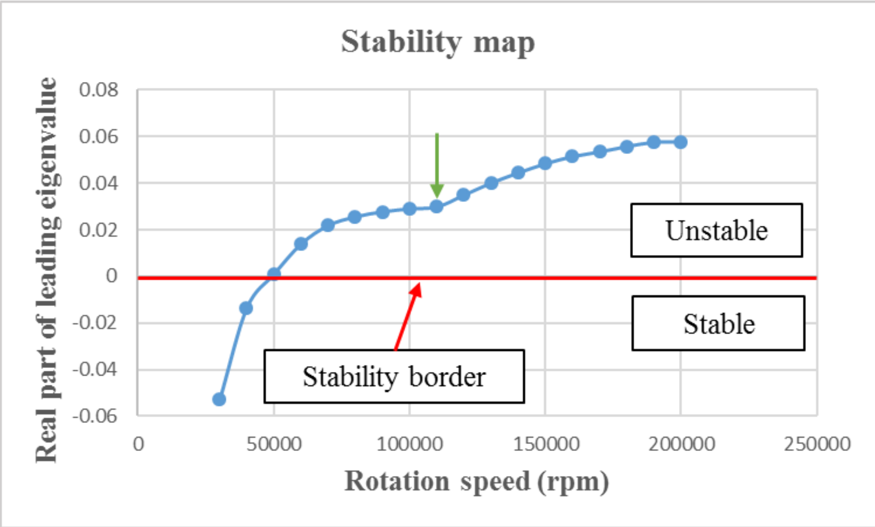

Figure 4. 2 Stability map of **CASE II**, γ = 0.153

It is interesting to note that there is a kink in the plot of leading eigenvalues in Figure 4. 2 , pointed by a green arrow. This effect has been reported in other research works, e.g. [60, 96]. It happens when one of the n_{state} eigenvalues supersedes another to become the leading eigenvalue [60]. There will also be a shift in the whirling frequency whenever the change in leading eigenvalue occurs. To extend the study on this effect, an analysis was performed on **CASE I** with a lower supply pressure at 5bar and speed up to 250k rpm. The results are presented in Figure 4.28. From the stability map, the change of leading eigenvalue happens around 170k rpm. An abrupt whirling frequency shift can also be observed at the same speed.

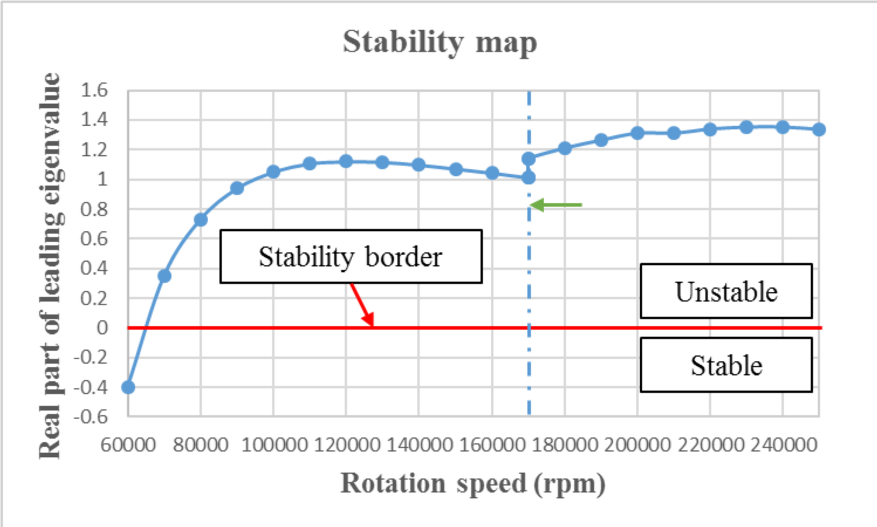

a)

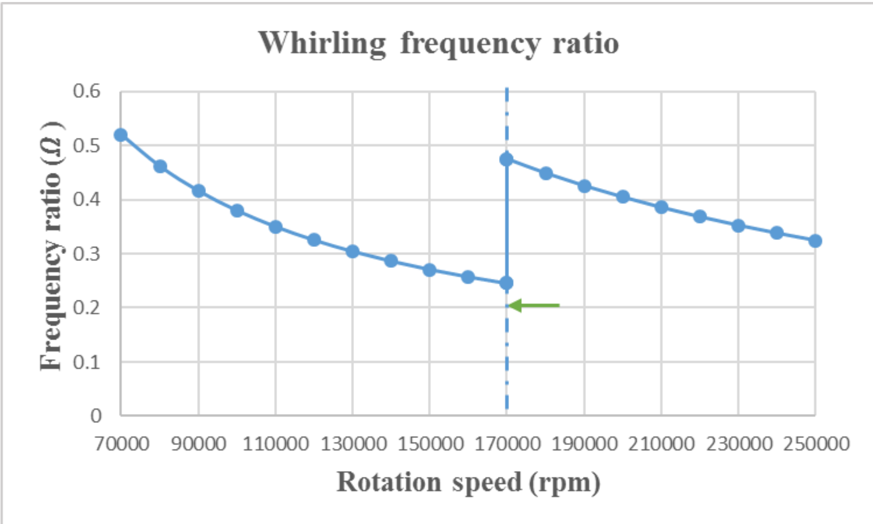

b)

Figure 4.28 Stability map and predictions of whirling frequency ratio of the rotor bearing system in **CASE I**, $P_s = 5bar$ a) stability map b) predicted whirling frequency ratio

4.5 Non-linear transient analysis and experimental verification

The performed analysis using linear bearing models in previous section provided useful information on the system's natural frequencies and stability in frequency domain. It can serve as a useful tool to assist the design of rotor bearing system supported by air bearings. A limitation of this approach is that it cannot give predictions on the steady state amplitude of self-excited whirl, which can only be calculated using a nonlinear model. In [94], it is also reported that the use of linear bearing models in predicting synchronous unbalance responses has limitations. To overcome the limitations, a non-linear transient analysis approach is applied here and then verified with experiments in the unbalance responses.

Experiments in this section were performed with a prototype manufactured based on the rotor bearing configuration shown in Figure 4.23, **CASE II**. The viscoelastic support can not only improve stability but also reduce the amplitude when the rotor speed passes the system natural frequencies. The rotor was balanced to achieve G1 standard for a service speed at 100k rpm. The unbalance responses of this device were measured up to the service speed and compared with predictions using non-linear bearing model.

4.5.1 Non-linear transient analysis of hydrostatic journal air bearings

The non-linear transient analysis follows the non-simultaneous routine described in Chapter 3. The air-film ODEs were uncoupled from the system ODE and treated as algebraic rather than state equations [60]. In the case that the bearing sleeve is supported by O-rings (**CASE II**), its equations of motion needs to be solved with that of the rotor at the same time.

In the analysis of **CASE II**, the mechanical structure of the bearing sleeve is modelled using Timoshenko beam theory with no gyroscopic effect. The O-rings to support it are still modelled as linear with equivalent stiffness and damping coefficient from [97] to avoid the reliance on the excitation frequency in Equation 4.19.

The governing equations of motion for the bearing sleeve is:

$$[M_v]\{\ddot{q_v}\} + [K_v]\{q_v\} + [C_v]\{\dot{q}\} = [-F_{brg}] \qquad \textit{Equation 4.20}$$

where $\{q_v\}$ is the states vector of bearing sleeve. The number of states is $4(N_v + 1)$ and N_v is the number of nodes used to model the structure. $[\boldsymbol{M_v}]$ and $[\boldsymbol{K_v}]$ are the structure mass/inertia matrix and stiffness matrix respectively. $[\boldsymbol{K_v}]$ also has the stiffness coefficients of O-rings added to their locations. $[\boldsymbol{C_v}]$ is the damping matrix. $[\boldsymbol{C_v}]$ only contains the damping coefficients of O-rings. $[-\boldsymbol{F_{brg}}]$ is the bearing force vector. The negative sign indicates that the direction of bearing forces applied on the bearing sleeve and its viscoelastic support is opposite to that on the rotor.

The governing equation of motion, Equation 3.42, is related to Equation 4.20 by the bearing forces vector and they are solved together using the ODE solvers provided in Matlab. In addition, the left-hand side of both equations is in the standard form required by the state space method. They can be assembled together and form global state equations that contains all the states from the rotor and the bearing sleeve.

The nonlinear transient analysis was first applied on **CASE I** and **CASE II** with perfectly balanced rotors. Figure 4.29 presents the responses of bearing journal at turbine side to free perturbation at 120k rpm. The red arrows in the figures indicate the position of journal centre at time zero in simulations. From SESA, the system in **CASE I** is unstable at this speed and can be stabilized by using viscoelastic supports as in **CASE II**. Figure 4.29 a) shows the trajectory of the journal centre at turbine side in **CASE I**. It forms a limit cycle which has a whirling frequency at 769Hz. It implies the system is unstable. Figure 4.29 b) shows the journal orbit in **CASE I** but with unbalance excitations. It can be found that the added unbalance has no effect on the self-excited orbit (as far as the fundamental frequency and steady state amplitude of the limit cycle is concerned). It also can be found the whirl ratio predicted by non-linear transient analysis is 0.38, which is quite close to the prediction from SESA (0.42).

At the meantime, trajectory of the same point in **CASE II** only shows a decaying free vibration and eventually converged to the static equilibrium position of the bearing at this speed, Figure 4.29 c). That is to say the system is stable.

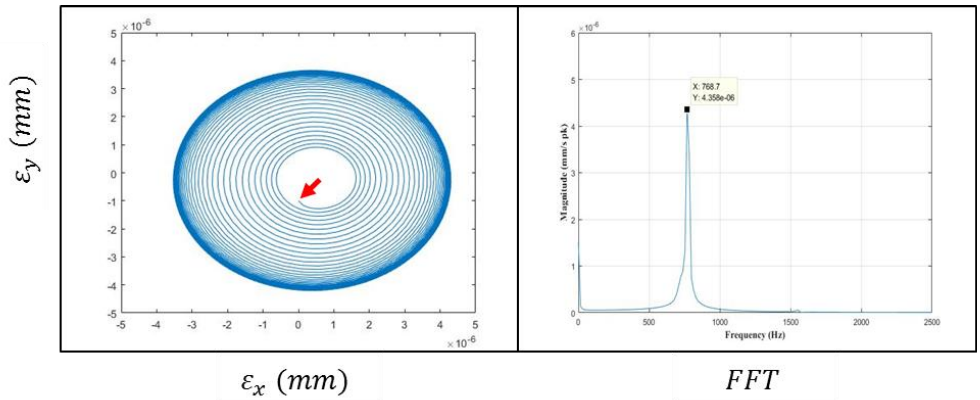

a) Limit cycle of journal bearing at turbine side of perfect balanced rotor R-1 in **CASE I** at 120k rpm rotor speed.

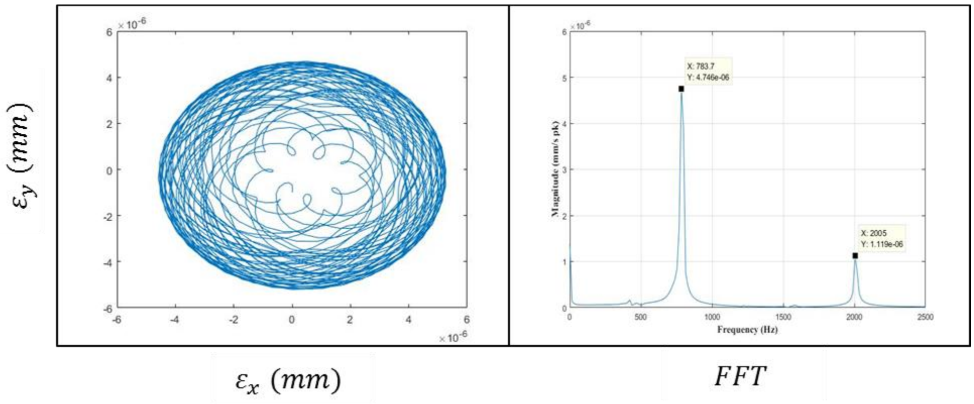

b) Limit cycle of the bearing journal at turbine side of rotor R-1 in **CASE I** at 120k rpm rotor speed with unbalance excitation.

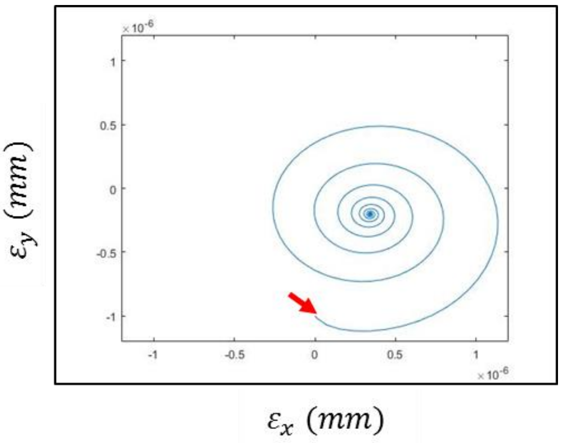

c) Converging orbit of journal bearing at turbine side of perfect balanced rotor R-1 in **CASE II**

Figure 4.29 Trajectory of the journal centre at 120k rotor speed of rotor R-1 in **CASE I** and **II**

The unbalance responses predicted by the non-linear transient analysis are demonstrated with the experimental results in Section 4.5.3. The bearing forces are calculated using the actual bearing geometry measured from manufactured components. The unbalance on the rotor is calculated using the information provided by the balancing service provider.

4.5.2 Hydrostatic journal air bearing test rig and experiment configuration

A test rig was designed for experiments on the hydrostatic journal air bearings. Figure 4.30 shows a cross section view of the test rig. The flow channel of compressed air in the hydrostatic journal air bearings is indicated by blue arrows. The measurements on dimensions of the bearing components are listed in Table 4.7 and compared with their design values.

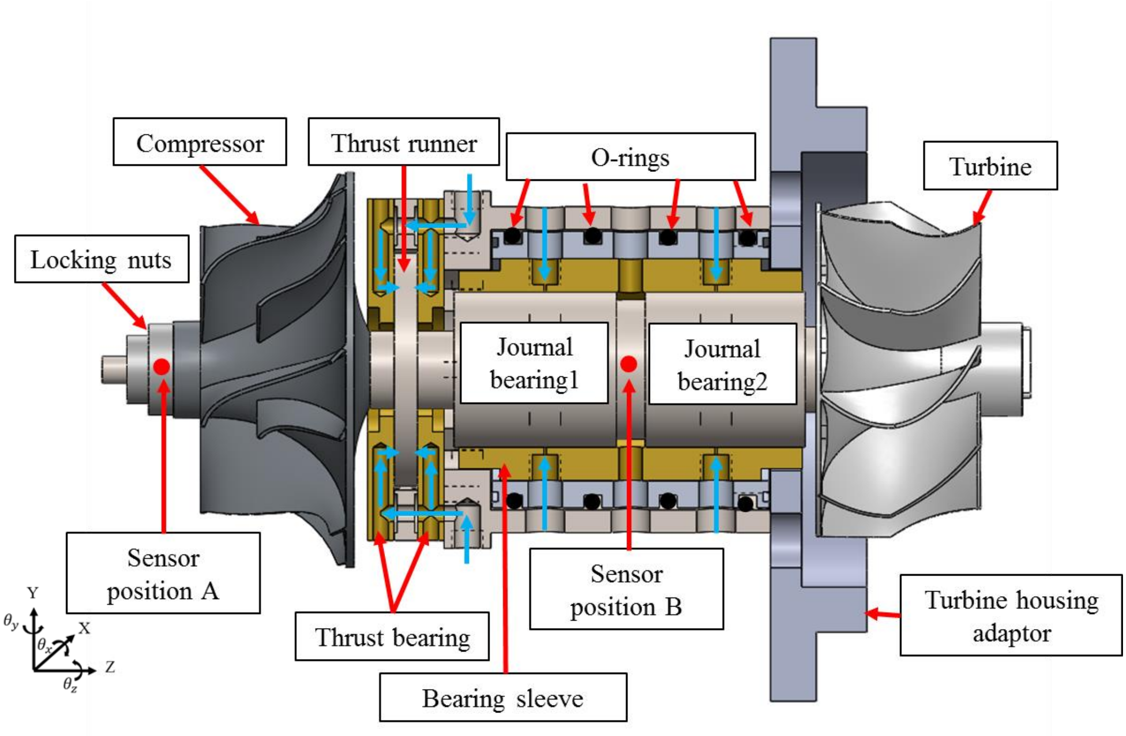

Figure 4.30 Cross-section view of prototype hydrostatic bearing test rig

Table 4. Dimensions of hydrostatic journal bearings used in the test rig

Bearing dimensions	Design value	Manufactured value
Radius, $\boldsymbol{r_0}$ (mm)	10.00	10.03
Length, $\boldsymbol{l}$ (mm)	20.00	20.15
Radial clearance, $\boldsymbol{c}$ (μm)	10.00	13.00
Orifice diameter, $\boldsymbol{d_0}$ (mm)	0.25	0.27
Supply pressure (Gauge, bar)	7.00	7.00+/-0.5

The test rig is mounted on a VSR balancing system supplied by Turbotechnic, which is used as a test bench as shown in Figure 4.31. The bench is connected to a compressed air reservoir and can supply massive air flow in a short time to drive the turbine wheel. The speed of the rotor can be controlled using a speed control valve manually, which adjusts the air flow during the turbine wheel.

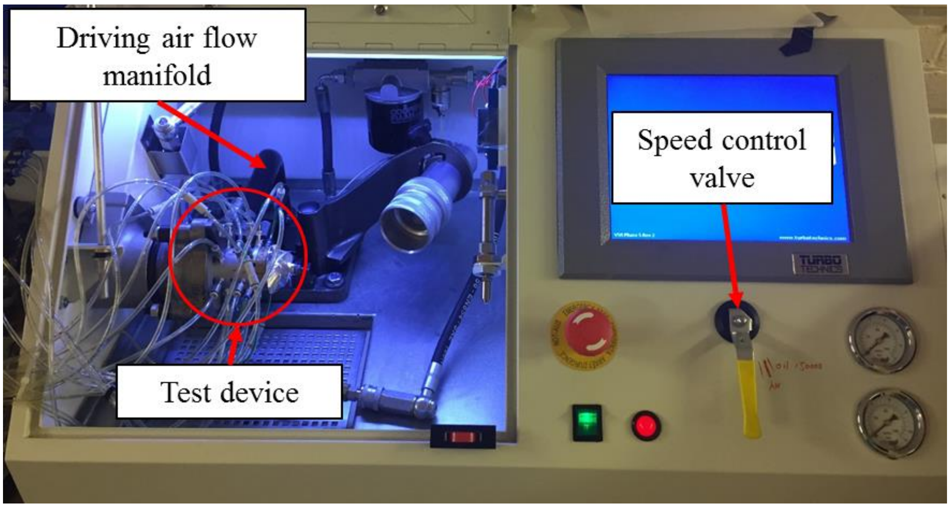

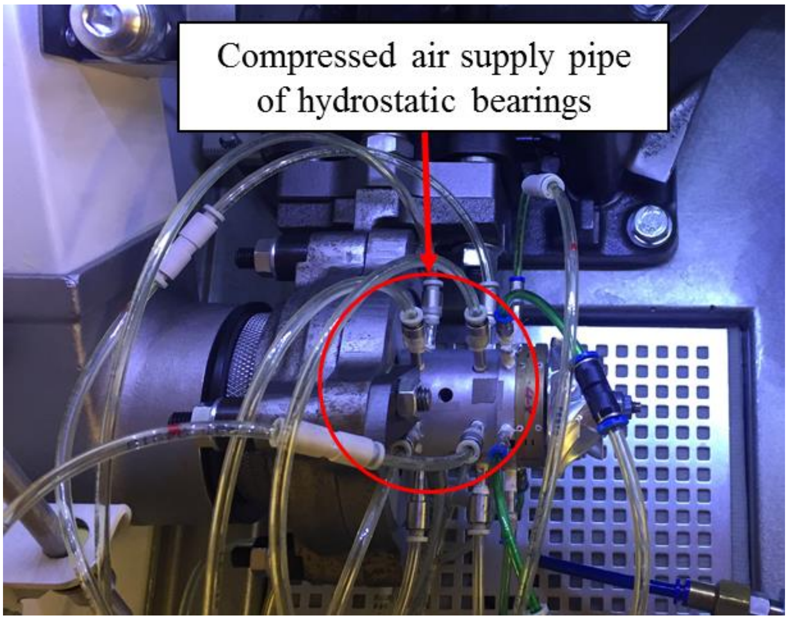

Figure 4.31 High speed air bearing test bench

The unbalance responses of the rotor were measured at two sensor positions marked in Figure 4.30 and both match with a node in the shaft rotor dynamic model (See Figure 3.12). Sensor position A matches with Node 2 and sensor position B matches with Node 12. The vibration of the rotor was measured at constant speed in horizontal and vertical direction (X & Y) using a laser vibrometer. The direct measurements of the vibrometer are the velocities of the vibration.

They are compared with predictions on the velocity states of the nodes from non-linear transient analysis.

In the measurements, the laser vibrometer is placed on the floor with the test bench. The measured vibration velocities are therefore relative to ground. However, in the simulation, the vibration velocities are relative to the casing of the device. A pre-measurement on the casing was first performed. It was found the amplitude of vibration from the casing is no more than 10% percent of the measurement from the rotor. In this case, the casing is considered as fixed and its vibration is neglected. The measurements on the rotor are used directly to compare with simulation results.

Rotor R-1 used in the hydrostatic bearing experiments was balanced to G1 standard for a service speed at 100k rpm. The rotor was balanced using two-plane dynamic balancing approach. The equivalent unbalance residuals are concentrated on two planes and listed in Table 4.8.

Table 4.8 Unbalance information of R-1

	Left hand correction plane	Right hand correction plane
Unbalance residual (g*mm)	0.020	0.022
Unbalance phase angle	45°	60°
Positions on Rotor	Compressor disc	Turbine disc
Position on Rotor model	Node 4	Node 18

4.5.3 Experiments on unbalance responses

The experimental study on unbalance responses of the rotor is presented in this section and compared with simulation results. Because of the limitation of using a manual speed control valve, it is almost impossible for the rotor to be tested consistently and repeatedly at a target speed below 50k rpm. As the unbalance responses at a high-speed region are the main interest of this study, the responses of the rotor were measured at speeds of 50k rpm, 60k rpm, 0k rpm, 80k rpm, 90k rpm and 100k rpm respectively. A 5% difference in the provide power of drive was allowed in each test.

From the analysis shown by Figure 4.24 b) of Section 4.4.3, the system has no natural frequency within the test speed range from 50k to 100k rpm. In experiments, the bearing sleeve is a non-rotating component which was excited by bearing forces. Therefore, a resonance should be observed at 660Hz. Figure 4.32 are the event time waterfall plots [98] in a run-up test to 100k rpm. Plot (a) was measured from the rotor directly, while Plot (b) was measured from the bearing sleeve. It shows relatively good agreement with the predictions on the natural frequencies from the linear analysis approach. Both plots present a synchronous component (1x) only. This indicates the system is stable within the speed range as predicted from the SESA. Figure 4.32 also shows the acceleration using the compressed air driven mechanism is not uniform and might be different in each individual test.

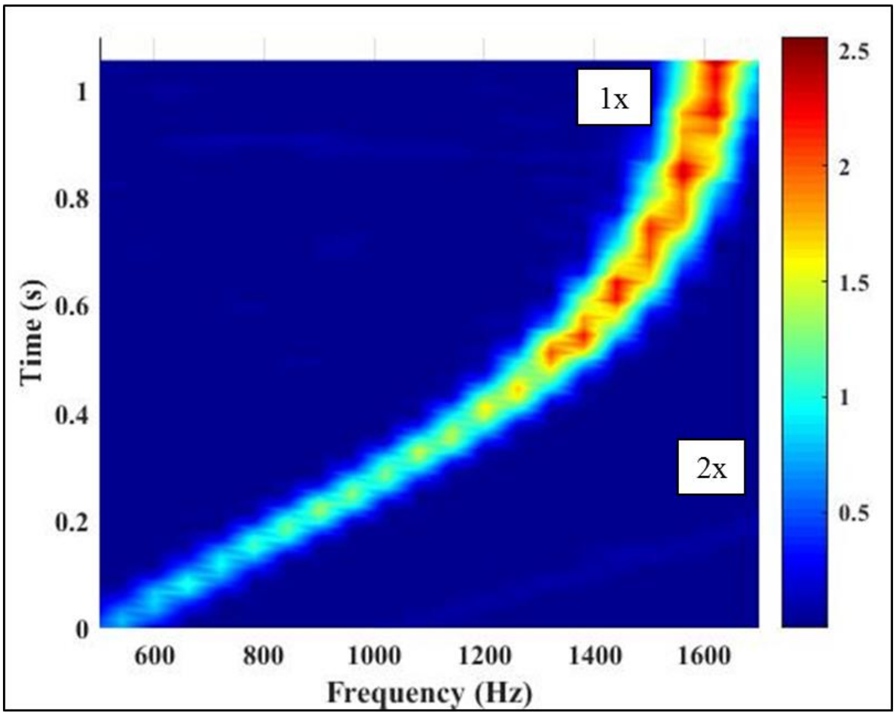

a)

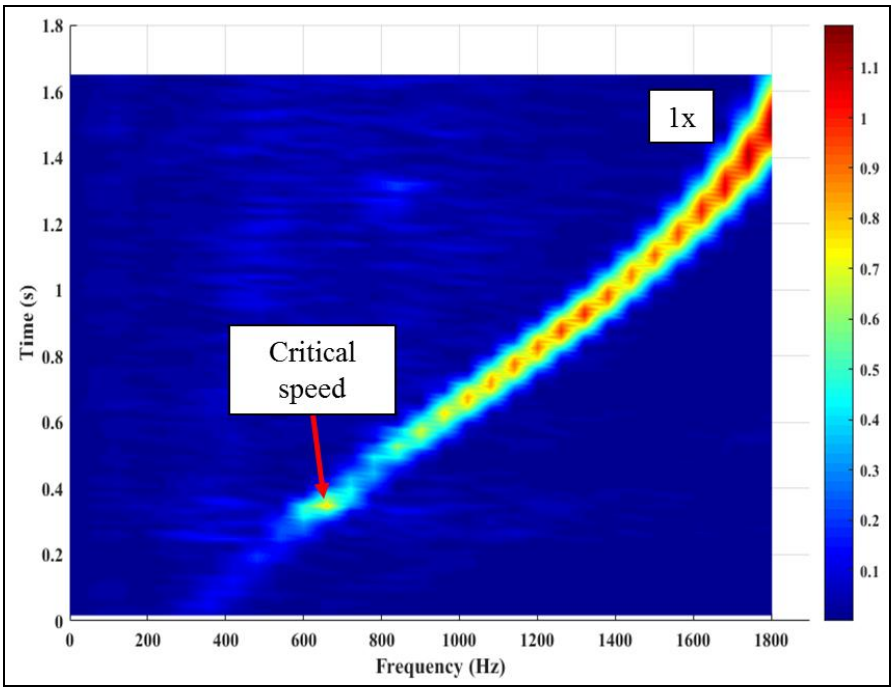

b)

Figure 4.32 Top views of waterfall plots in a run-up test at sensor position B to 100k rpm. a) vibration velocity measured from rotor and b) vibration velocity measured from bearing sleeve

The experimental unbalance responses and related simulation results are shown Appendix D. In each group of the figures, the dominating vibration frequency and the peak vibration amplitude are marked on the FFT plot. The simulations were produced using the actual rotation speed (1x component in frequency spectrum) acquired from experiments. At each speed, the rotor responses were calculated for the first 0 0 shaft revolutions and a steady state was assumed to be achieved at the last 100 revolutions. The response data were collected for the last 100 revolutions and analysed using FFT. Figure 4.33 shows a case of these measurements and predictions at 100k rpm rotor speed for both sensor positions.

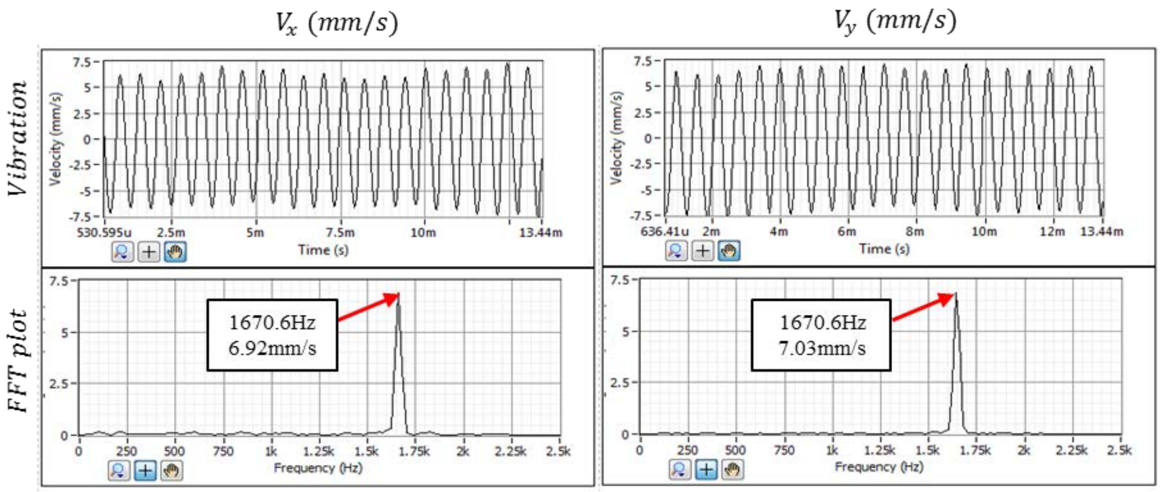

a) Measurements at sensor position A

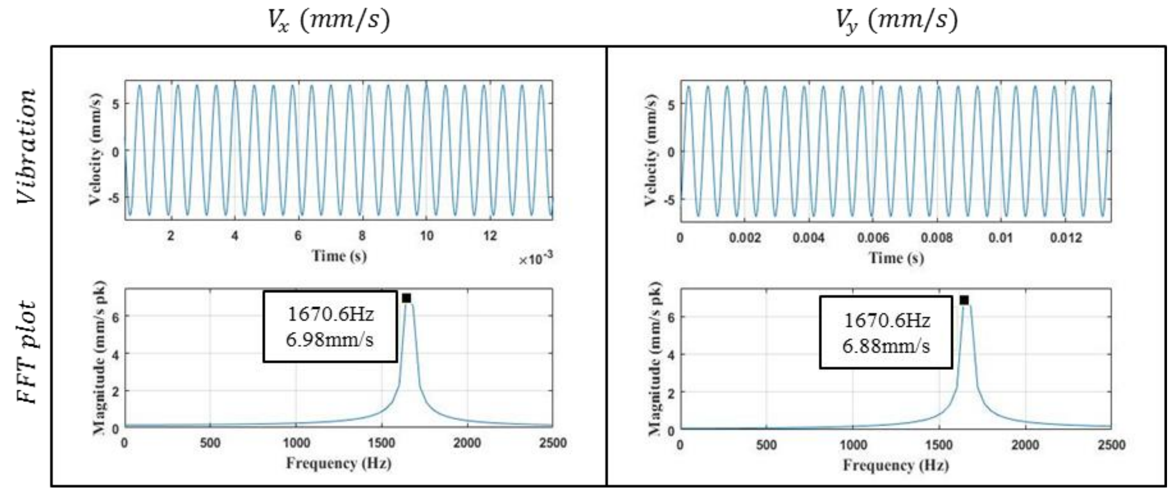

b) Predictions at sensor position A

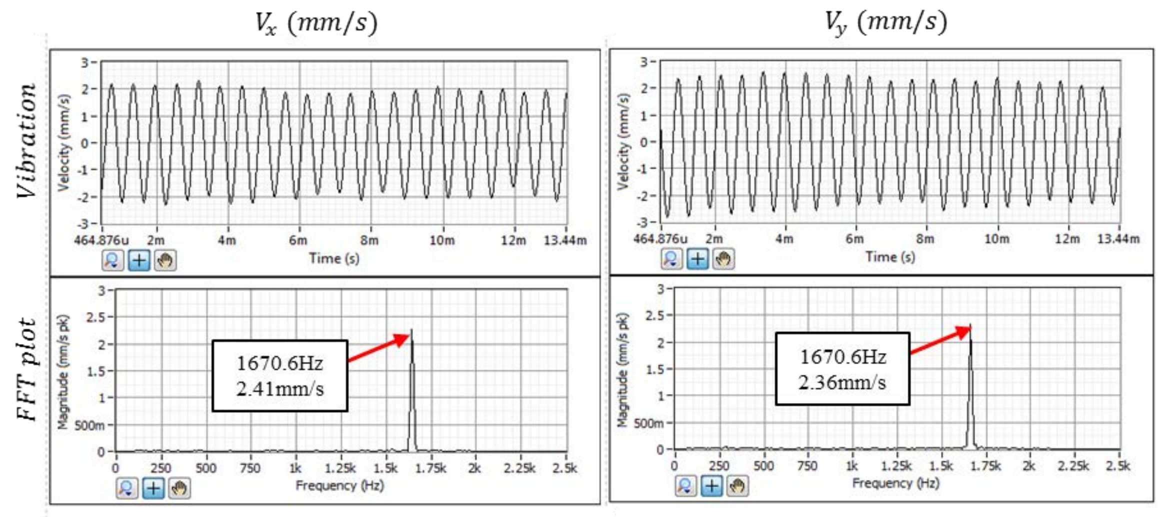

c) Measurements at sensor position B

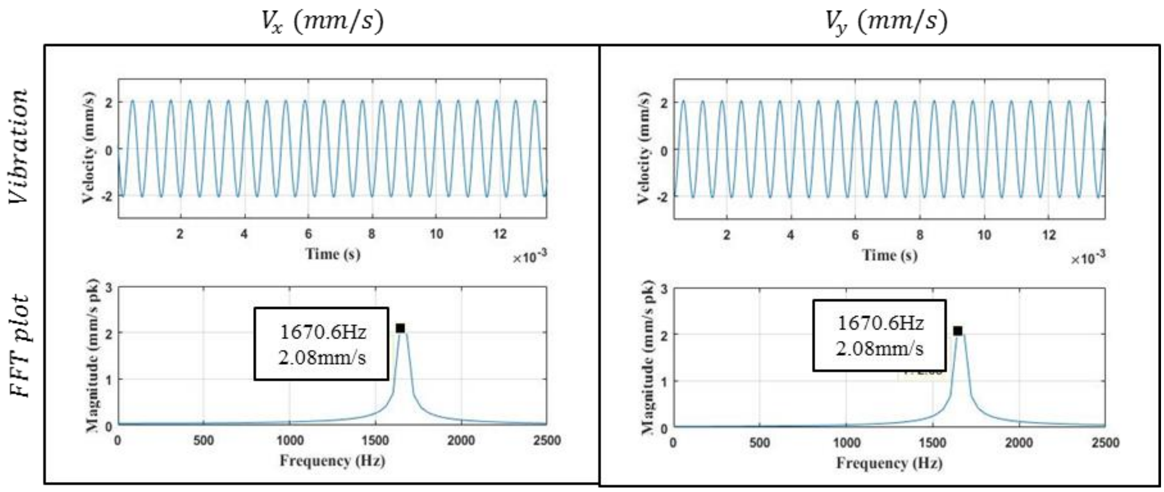

d) Predictions at sensor position B

Figure 4.33 Unbalance responses of sensor position *A & B* obtained at 100k rpm in speed

The presented results, also the results in Appendix D, have a relatively good agreement between experimental and prediction results. They show that the vibrations of the system are dominated by synchronous component and no self-excited whirl has been spotted. The amplitudes of the unbalance responses from experiments and simulations are very similar, as shown in Figure 4.34. However, the predicted amplitudes of vibrations at the both sensor positions are smaller than those observed. This can be caused by two reasons: first, the rotor was slightly altered at both journal positions during balancing as marked in Figure 4.35. Second, the rotor was balanced alone and then reassembled back into the device. Extra imbalance can be expected in the process without further field balancing. There was a significant increasing on vibration level at sensor position A when the speed was close to 100k rpm (1.6 k Hz). This is likely to imply that the system is running towards the 1st bending natural frequency as shown in Figure 4.24 b).

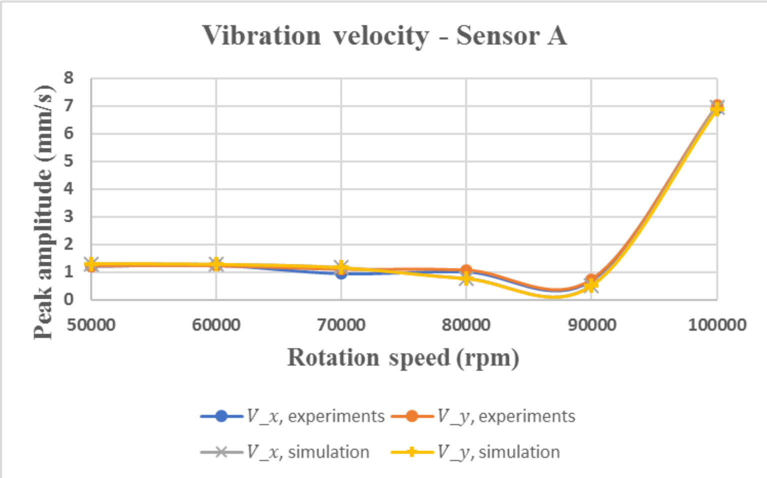

a) Sensor position A

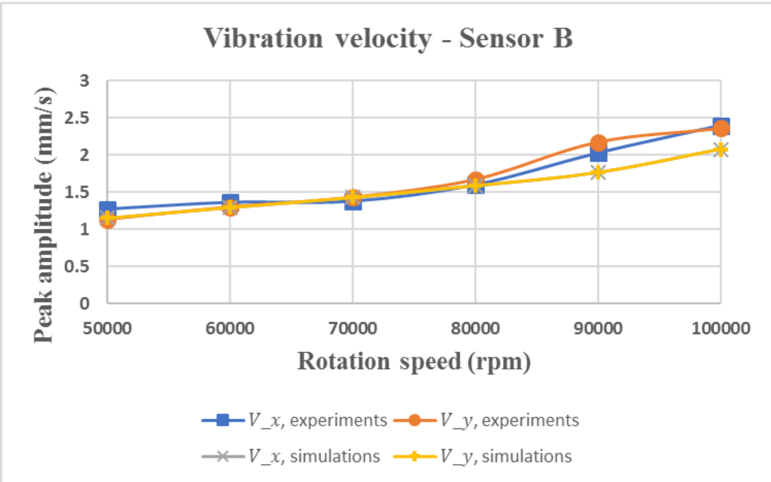

b) Sensor position B

Figure 4.34 Peak vibration velocities at sensor positions

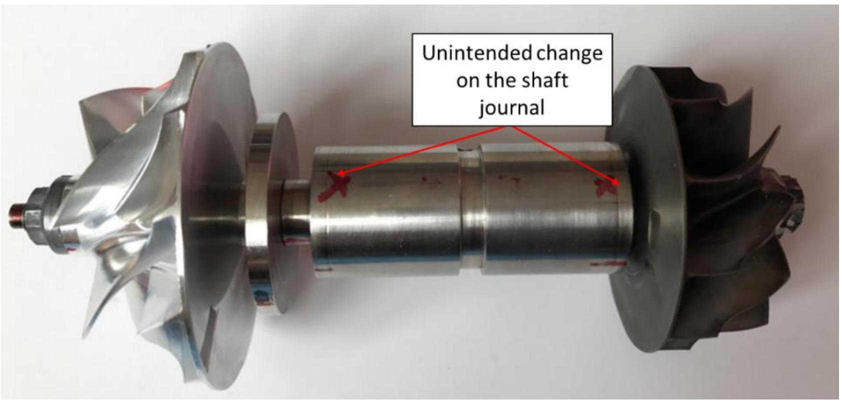

Figure 4.35 Unintended change on the shaft journal during a balancing process

There are also marginal differences between the simulation and experimental results. Some of the measurements also have a small portion of low frequency vibration around 100Hz to 120Hz, referring to Figure D-3 c) in Appendix D for example. This was introduced by excitations from the mounting bench, which has a motor running at the same frequency as long as the bench is switched on. The *X & Y* vibration velocities from a simulation for hydrostatic bearings are identical. However, the difference between them is slightly larger in reality, Figure 4.34. This is because the bearing components, the assembly and the mounting are not isotropic in the two directions which are not considered in the simulation.

4.5.4 Limitations of experiments

The experiments in this section are designed to verify the non-linear transient analysis of hydrostatic journal air bearings. The test rig was designed to simulate a system in **CASE II**. However, the rig only provided limited access for measurements of vibrations on the rotor. Most of the shaft sections, including the turbine wheel were sealed or covered due to the mounting and driving mechanism (like a turbocharger) to achieve high speed operations. This limited gaining sufficient information to identify the mode shape of the rotor, e.g. cylindrical, conical, bending or mixed. This can only be done by gathering vibration information, including the phase angle on multiple points of the rotor. Accessing such information would involve redesign of the test rig, manufacture, balancing, assembly, and repeated tests, which would require much more time than currently allowed for this PhD study. However, this work is likely to be arranged in the follow up investigation.

Another limitation is the use of laser vibrometer to measure vibrations. The single point laser vibrometer only provided accurate measurements of absolute vibrational velocities. It cannot give relative positions of the shaft centre at the two sensor positions in rotating condition. That is to say the trajectory of the shaft centre relative to ground (or casing) cannot be detected. As the tests show that the vibration amplitude of the stand (excitation from mounting) is negligible, the vibration velocities of the rotor measured are reasonable to be used to compare with the simulation results. The latter does not simulate excitations from the mounting and consider the system is mounted on a fixed rigid body.

4.6 Summary

This chapter provides a comprehensive study on hydrostatic journal air bearings and the rotor dynamic structure they support. A novel orifice model was adopted to improve the accuracy of bearing model for predictions of bearing reaction forces at a static equilibrium configuration. The non-rotational performance was then investigated with a focus on the optimization of bearings to achieve the maximum bearing forces while reducing compressed air consumption rate. The rotational performance was studied using the linear perturbation analysis. Bearing forces were represented by equivalent stiffness and damping coefficients with given static equilibrium configurations. The effects of different design parameters on these dynamic coefficients were investigated. The research shows a 'hardening' effect at high rotation speeds. It results in a lack of damping which cannot be improved effectively by adjusting bearing design parameters, but can be done by introducing dampers, such as O-rings as shown in CASE II. The bearing stiffness and damping coefficients were also used in the rotor dynamic models for two cases (**CASE I & II**) to predict the stability and natural frequencies of the rotor dynamic system supported by hydrostatic journal air bearings. In the end, non-linear transient analysis was performed together with experimental verifications on unbalance responses. The analysis and experiments were focused on the rotor bearing system in **CASE II** and they have good agreement on the synchronous unbalance responses. No self-excited whirl was observed at this stage for the tested speed range from 50k to 100k rpm. The limitations of the experiments were also discussed.

CHAPTER 5: HYBRID JOURNAL AIR BEARINGS

5.1. Introduction

In this chapter, rotational performance of hybrid journal air bearings is investigated using the numerical approach developed in Chapter 3. The proposed hybrid journal air bearing consists of orifice restrictors located on a stationary bearing sleeve and herringbone grooved journal, as shown in Figure 5.1. This combination allows the bearing to lift at zero speed with external compressed air supply and self-suspending without the supply of compressed air when the rotational speed is sufficiently high.

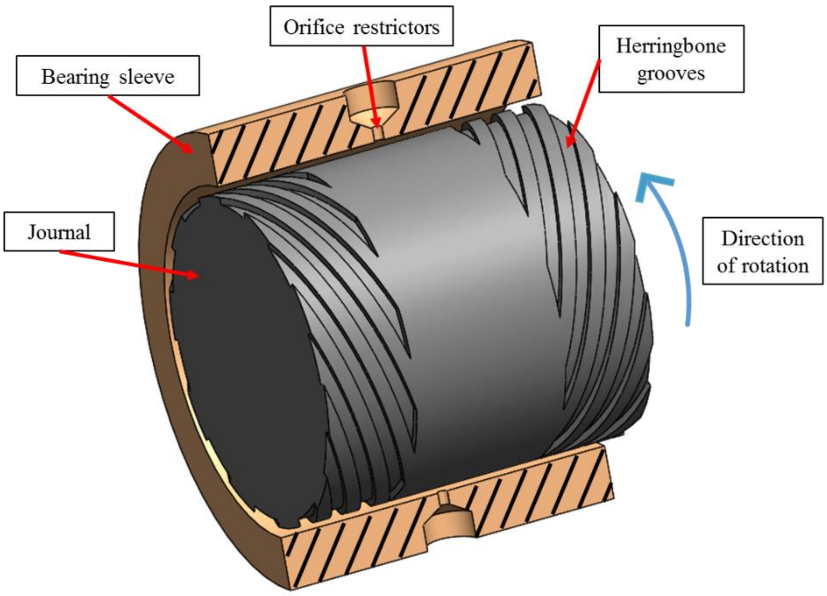

Figure 5.1 A proposed hybrid journal air bearing. The stationary bearing sleeve is presented in cross section view to show orifice restrictors, which are used to supply compressed air when rotational speed is zero or low.

The research in this area is presented in five sections. After the introduction above, Section 5.2 presents the modelling of hybrid journal air bearings. The FVM approach proposed in Chapter 3 has advantages in simulating air bearings with herringbone grooves and is adopted here. The validity of this approach was first tested on hydrodynamic air bearings with the same configuration. The predicted bearing reaction forces at a given static equilibrium position are compared with those in published references. A novel herringbone groove geometry is also introduced in this section. The design can help increase bearing reaction forces to a static load and is applied to the hybrid bearings in this project.

Section 5.3 presents theoretical study on the rotational performance of hybrid journal air bearings using linear perturbation analysis. The influence of bearing design parameters on equivalent bearing stiffness and damping coefficients is investigated. The analysed coefficients are then used to build up linear bearing model and combined with the rotor model (R-1) to give predictions on the stability and natural frequencies of the system.

In section 5.4, the non-linear transient analysis (NTA) is used to study rotational performance of rotor-bearing systems described in Section 5.3 with a focus on stability and unbalance responses. NTA is adopted to give predictions on unbalance responses of the rotor in the test rig developed in Chapter 4. The journal bearings in the test rig are replaced by hybrid air bearings. The predicted unbalance responses are then presented and compared with experimental results.

For the convenience of writing, nomenclature of design parameters of hybrid journal air bearings are presented below. Table 5. 1 lists the range of these parameters used in this chapter.

- r_0, radius of the bearing, mm
- l, length of the bearing, mm
- ζ, bearing length to diameter ratio
- c, radial clearance, μm
- P_s, supply pressure (absolute), bar
- d_0, orifice diameter, mm
- N_{ori}, number of orifices
- G_{num}, number of herringbone grooves
- β_g, angle of herringbone grooves, degree
- h_g, maximum depth of herringbone grooves, μm
- H_g, maximum groove depth ratio, h_g/c
- α_g, ratio of groove width to total width (groove plus ridge)
- γ_g, fraction of bearing length occupied by grooves

Table 5. 1 Dimensions of hybrid journal air bearings studied

a) Dimensions of hybrid journal air bearings

Radius of the bearings, $\boldsymbol{r_0}$ (mm)	Length to diameter ratio, $\boldsymbol{\zeta}$	Radial clearance, $\boldsymbol{c}$ μm	Orifice diameter, $\boldsymbol{d_0}$ (mm)	Supply Pressure, $\boldsymbol{P_s}$ (bar)	Number of orifices, $\boldsymbol{N_{ori}}$
10	0.5 to 2	8 to 13	0.25	1 to 7.5	6

b) Dimensions of hybrid journal air bearings - continued

Number of grooves, G_{num}	Angle of grooves, β_g (degree)	Maximum depth of groove, h_g µm	Ratio of groove width to total width, α_g	Fraction of bearing length occupied by grooves, γ_g
10	0.5 to 2	10 to 13	0.25	0 to 1

5.2 Modelling of hybrid journal air bearings

In this project, models of hydrostatic journal air bearings are based on the method proposed in Chapter 3. The Reynold's Equation is solved numerically using finite volume method (FVM). Similar to the hydrostatic journal air bearing model, the hybrid bearing is symmetric and open to atmosphere at both ends. Calculation only need to be performed on half of the bearing axial length. Orifices are applied as boundary conditions with flow model proposed in Chapter 4. The centre of each orifice coincides with a node on the axial symmetry plane of FVM grid.

5.2.1 Finite volume model of hybrid journal air bearings

In Figure 5.2 a), the FVM grid of a hybrid journal air bearing is presented with the circular surface of bearing sleeve spread flat. The total volume to perform numerical calculation is enlarged (not in scale) and presented as empty volume between the surfaces of the journal and the bearing sleeve. Herringbone grooves are modelled in a way that all groove edges pass through a node on FVM grid. To simplify computations, the groove edge can also be aligned to the diagonal line of the controlled volume around a node, as shown in Figure 5.2 b) and c). If this is adopted, the groove angle, β_g, determines the grid aspect ratio, $\frac{\Delta Z}{\Delta\theta}$, and they follow the relation: $tan\beta_g = \frac{\Delta Z}{\Delta\theta}$.

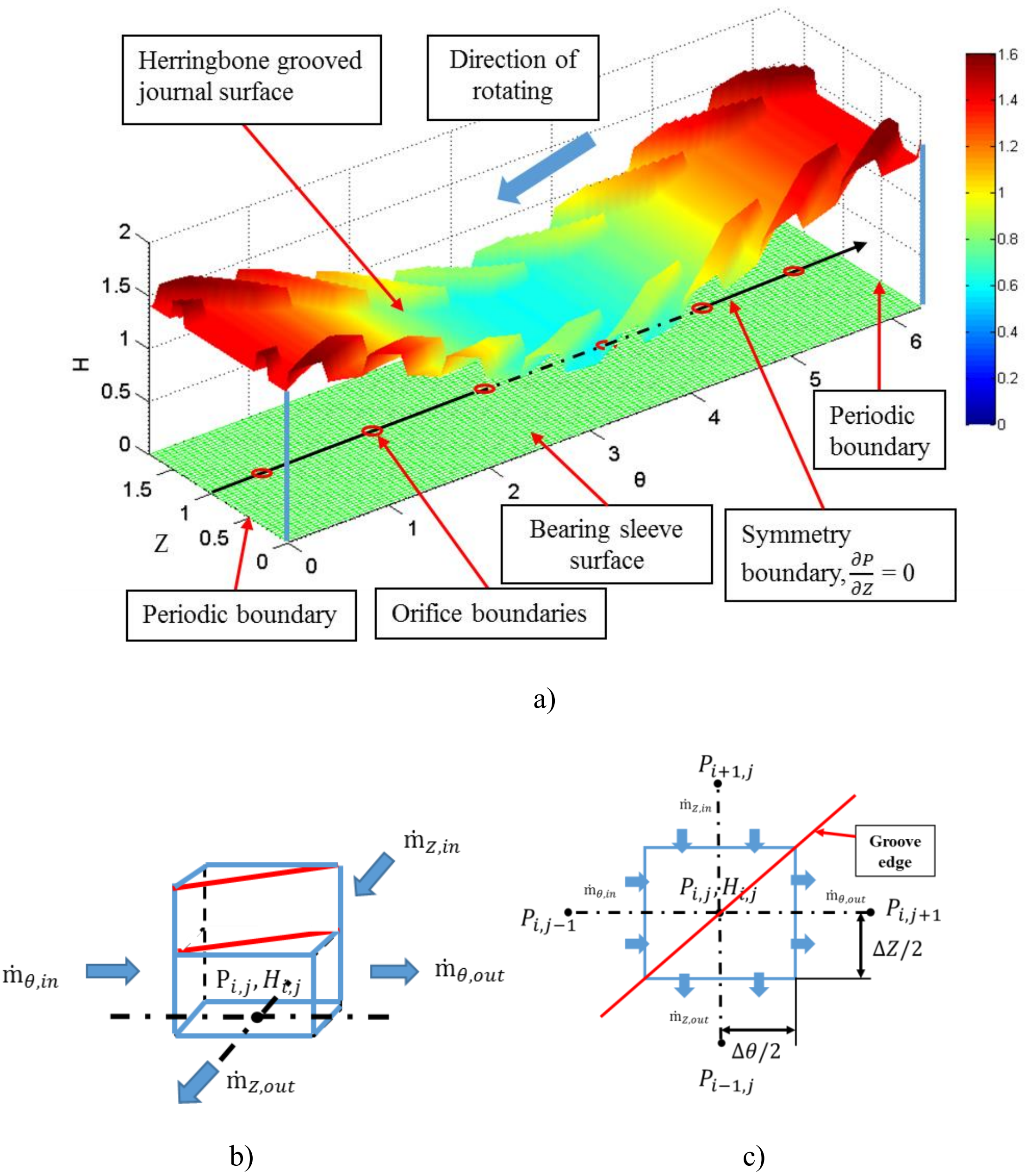

Figure 5.2 The Model of a hybrid journal air bearing. a) FVM grid and boundary conditions, b) The controlled volume around a node coinciding with a groove edge, and c) A top view of the controlled volume when the groove edge is aligned to the diagonal line.

In modelling air bearings with herringbone grooves, particularly hydrodynamic bearings, a conventional approach is based on the narrow groove theory [99], which assumes the bearing has infinite grooves with infinitesimal width. This approach is valid for bearing with large groove numbers, for example 20 grooves [42]. Other numerical approaches involve the use of neutral coordinate system for the surface of the bearing, in which one of the axes coincides with the groove edges [36] and finite element method [100].

Before moving on to investigating the performance of hybrid air bearings, the model of hydrodynamic air bearings with herringbone grooves was tested by means of removing the orifice boundaries from the model. Predictions on bearing reaction forces at a given static equilibrium configuration were compared with the method proposed in [36], in which the Reynold's Equation was solved on a neutral coordinate system. The reference also provided experimental data from [93]. Figure 5.3 shows the comparisons. The method in [36] overestimated the bearing force when compressibility number is below 8.6 and changes to underestimating when compressibility is higher. The proposed FVM model agrees well with experiments with less than 5% difference in the compressibility number (Λ) range. Only one exception occurs at $\Lambda = 26.8$ and eccentricity ratio is greater than 0.3. However, this is not the condition for the air bearings in this project to operate at. The FVM model can serve as an adequate approach to model air bearings with herringbone grooves.

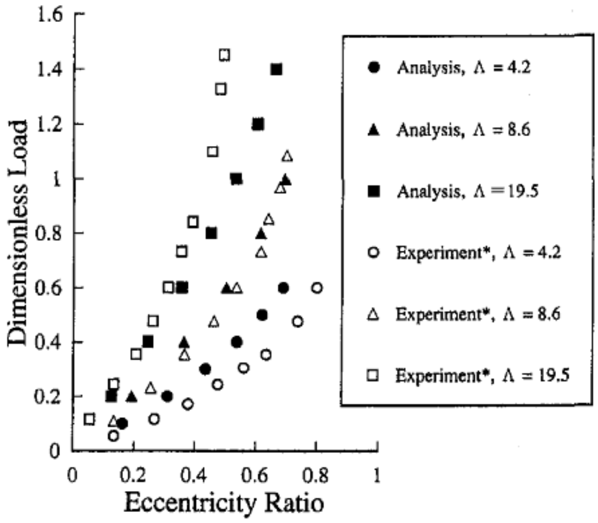

a) Predictions of bearing reaction forces based on the numerical model in [36]

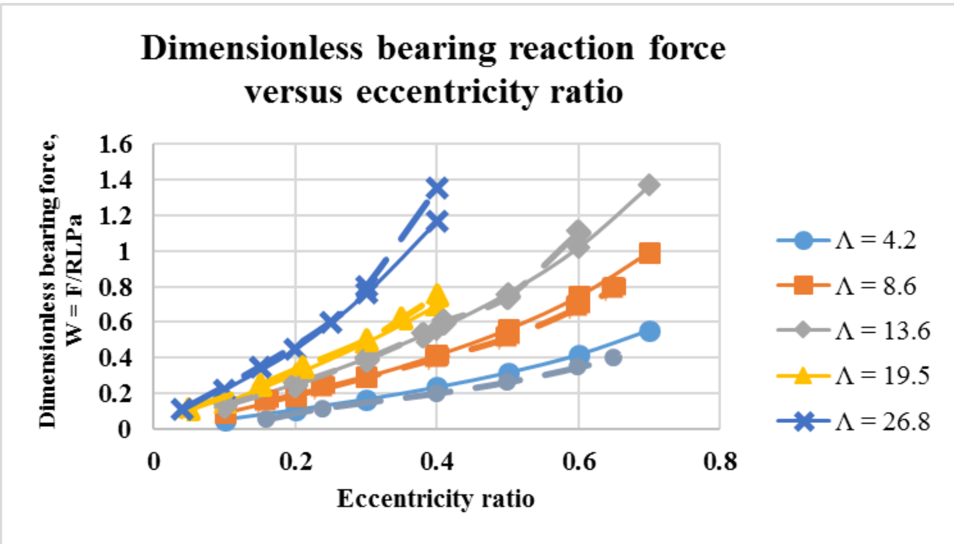

b) Predictions of bearing reaction forces using the proposed numerical approach

Figure 5.3 Dimensionless bearing reaction forces versus eccentricity ratio at various compressibility numbers: the dashed line is experimental data and the solid line is the predictions from the proposed model. a) Results from [36] b) Predictions using the proposed bearing model.

5.2.2 A novel herringbone groove geometry

In Figure 5.4, pressure distribution of a hybrid air bearing is predicted at a given static equilibrium position for two cases: one with compressed air supply at 2.5bar, and the other without compressed air supply. It can be found that when compressed air is cut-off, the orifice restrictors will introduce leakage in the air film and disturb the pressure build-up around them and result in reduction of bearing reaction forces. To compromise this issue, a novel groove profile is proposed.

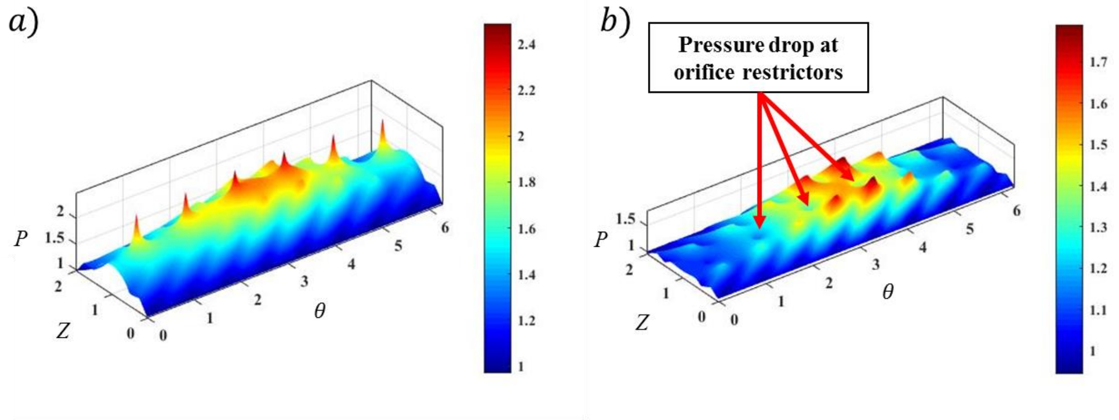

Figure 5.4 Pressure distribution of hybrid journal air bearings at a given static equilibrium configuration. a) Compressed air supply at 2.5bar. b) No external compressed air supply

Unlike conventional rectangular profile, the novel herringbone groove is constructed on a curved profile formed by cosine spline. This unique design can enhance bearing reaction forces at a static equilibrium position. Figure 5.5 shows a comparison between the conventional design and proposed design. The edges of the grooves in herringbone bearings can be divided into the leading edges and the trailing edges. At the leading edge, the air film forms a convergent zone, while at the trailing edge, the air film is divergent. With reference to [4] , the flow passage at the trailing edge of a rectangular groove is suddenly enlarged which results in vortex and pressure loss, as shown in Figure 5.5 a). In theory, this can be avoided by means of modifying the trailing edge with a spline as shown in Figure 5.5 b). The gradually enlarged air film can avoid pressure loss and improve the bearing reaction forces. The spline used in this thesis is cosine spline and can be described using Equation 5.1.

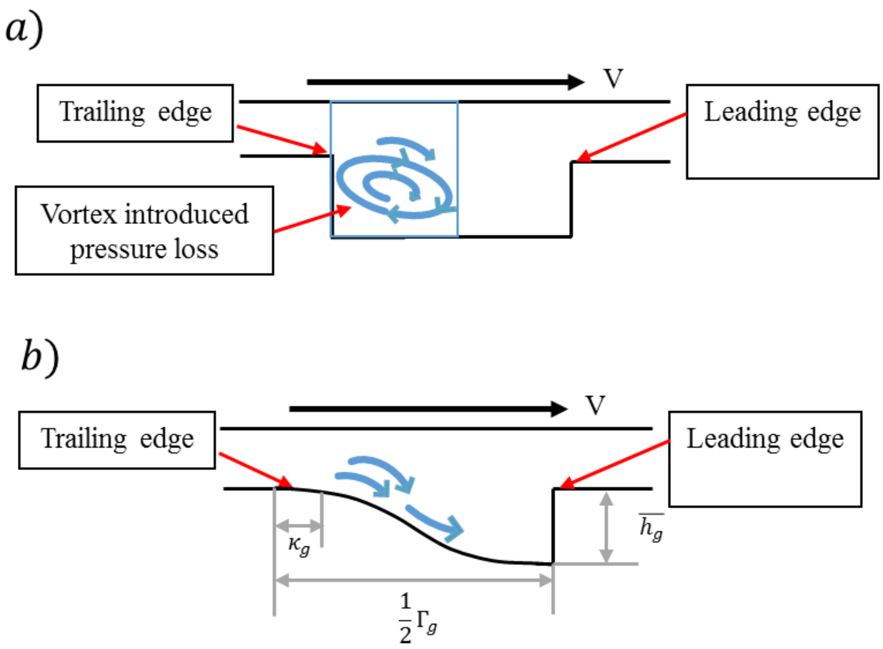

Figure 5.5 Air flow over the groove. a) conventional rectangular groove profile. b) Spline groove profile

$$h_g = \frac{1}{2}\overline{h_g} * \left(1 + \cos\left(\frac{2\pi}{\Gamma_g} * \kappa_g\right)\right) \qquad \textit{Equation 5.1}$$

where h_g is the groove depth, $\overline{h_g}$ the maximum groove depth, Γ_g the period of cosine spline, and κ_g the distance of any point on spline relative to the start point of a tailing edge.

To verify the improvement of using the curved groove profile, numerical simulation was performed on two hybrid air bearings with dimensions shown in Table 5.2 and no supply of compressed air. One of the bearing has adopted curved grooves and the other one uses conventional rectangular ones. The groove profiles of the two journals are spread flat and presented in Figure 5.6 a). Pressure distributions at a quarter bearing length are compared in Figure 5.6 b). The bearing with curved groove profile shows the pressure recovery at the trailing edge as predicted. Figure 5.6 c) compares bearing reaction forces at a given static equilibrium position with various compressibility numbers for the two bearings. The comparison shows that the proposed groove profile has improved the bearing reaction forces 16%.

The proposed groove profile will be applied to the hybrid air bearings and all related analysis on hybrid air bearing from here onwards in this thesis is based on this novel herringbone design.

Table 5.2 Dimensions of hybrid journal air bearings used in simulation

Dimensions	
Radius (mm)	10
Length (mm)	20
Radial clearance (μm)	10
Groove depth (μm)	10
Groove angle (°)	30
Groove number	8
Groove to ridge width ratio	1
Groove length ratio	0.5

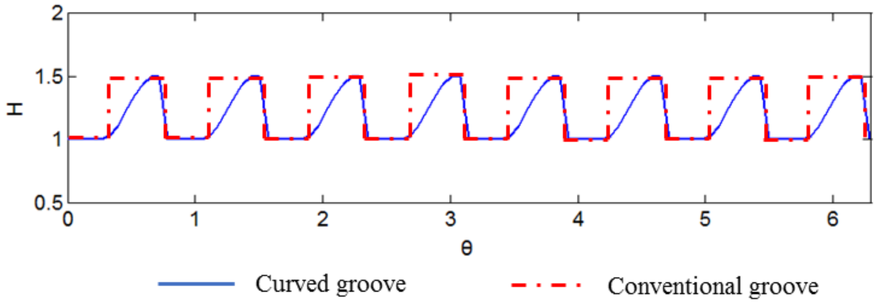

a)

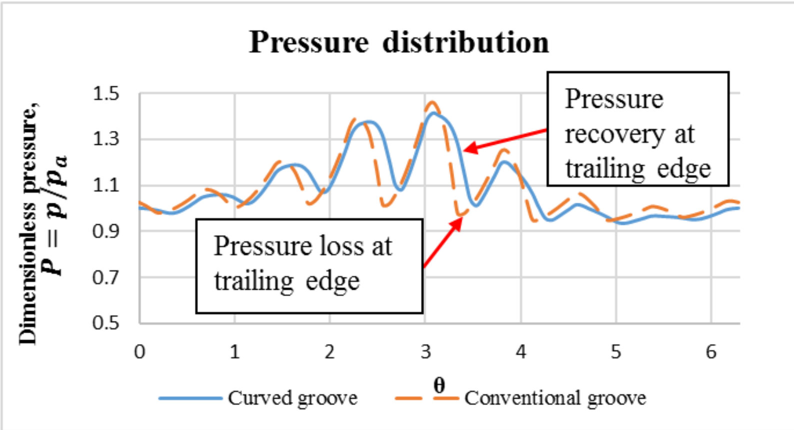

b)

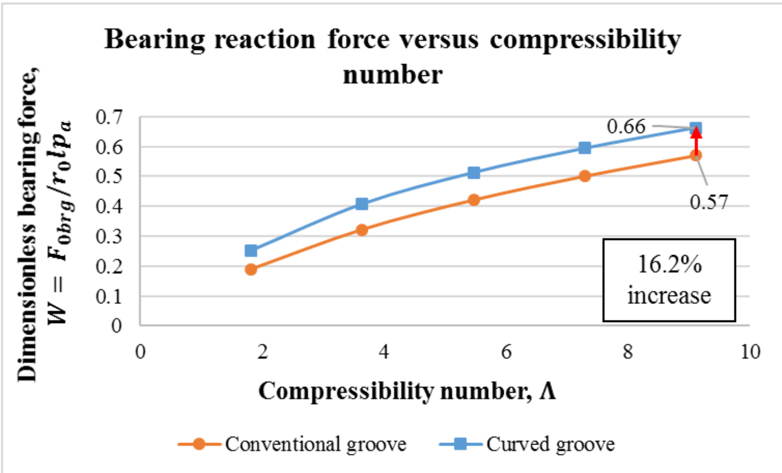

c)

Figure 5.6 Comparisons between herringbone grooves and their effects. a) Curved groove profile, H is dimensionless film thickness; θ is circumferential coordinate; b) Comparison of pressure distribution at the same location of conventional and curved groove. c) Bearing reaction forces at the same static equilibrium position with various compressibility number.

5.3 Theoretical studies on rotational performance of hybrid journal air bearings

This section focuses on theoretical studies on the rotational performance of hybrid journal air bearings. The bearings investigated in this section adopt the novel groove profile proposed in Section 5.2.2. First, bearing reaction forces at given static equilibrium configurations are investigated. Second, bearing forces are represented by stiffness and damping coefficients with respect to the static equilibrium configurations using linear perturbation analysis. Third, the stability and natural frequencies are analysed for rotor-bearing system using linear bearing models.

5.3.1 Analysis of bearing reaction forces at given equilibrium positions

In this section, numerical calculations were performed on hybrid journal air bearings to investigate the influence of design parameters on bearing reaction forces at given static equilibrium positions. The effects of compressibility number and restrictor setup are very similar to that of hydrostatic bearings and will not be discussed here again. Instead, the influences of groove number (G_{num}), maximum groove depth ratio ($H_g = h_g/c$) and groove angle (β_g) are studied. The dimensions of the hybrid air bearings being studied in this section are given in Table 5.3. The bearing reaction forces of hydrostatic journal air bearings with the same dimensions are also analysed for comparisons. The static equilibrium position (SEP) is chosen at eccentricity ratio of 0.4. The attitude angle is adjusted in each case to ensure the bearing reaction force is in vertical direction only.

Table 5.3 Design parameters and restrictor setup of hybrid air bearings to be studied

Design parameters	Value
Radius (mm), $\boldsymbol{r_0}$	4
Length (mm), $\boldsymbol{l}$	8
Radial clearance ($\mathbf{\mu m}$), $\boldsymbol{c}$	6
Orifice diameter ($\mathbf{\mu m}$), $\boldsymbol{d_0}$	300
Supply pressure (bar), $\boldsymbol{P_s}$	3
ratio of groove width to total width (groove plus ridge), $\boldsymbol{\alpha_g}$	0.6
fraction of bearing length occupied by grooves, $\boldsymbol{\gamma_g}$	0.6

Figure 5. shows bearing reaction forces at the chosen SEP for multiple groove number (G_{num}) and maximum groove depth ratio (H_g) of the hybrid bearing. The red dash line in the plots is the result calculated from hydrostatic bearings at the same condition. It is found that bearing reaction forces change with compressibility number (Λ) more rapidly in hybrid bearings than in hydrostatic bearings. When Λ goes over a threshold (pointed by a black arrow in plots), hybrid bearings can provide higher reaction forces than hydrostatic bearings. This threshold of Λ can be reduced by means of increasing H_g or G_{num}. Figure 5.8 presents the change on threshold of Λ when G_{num} is increased. One interesting fact observed from the figures is that there is a point at which bearing reaction forces calculated at different H_g merged together. The value of Λ at this point is regarded as a 'stagnation value'. At this compressibility number, if the same static load is applied, hybrid air bearings with different H_g will operate at the same SEP. However, their dynamic performance can be quite different. For example, in the case that the bearing forces are represented by stiffness and damping coefficients, the coefficients will change with H_g. This effect has been further investigated and explained in Section 5.3.2.

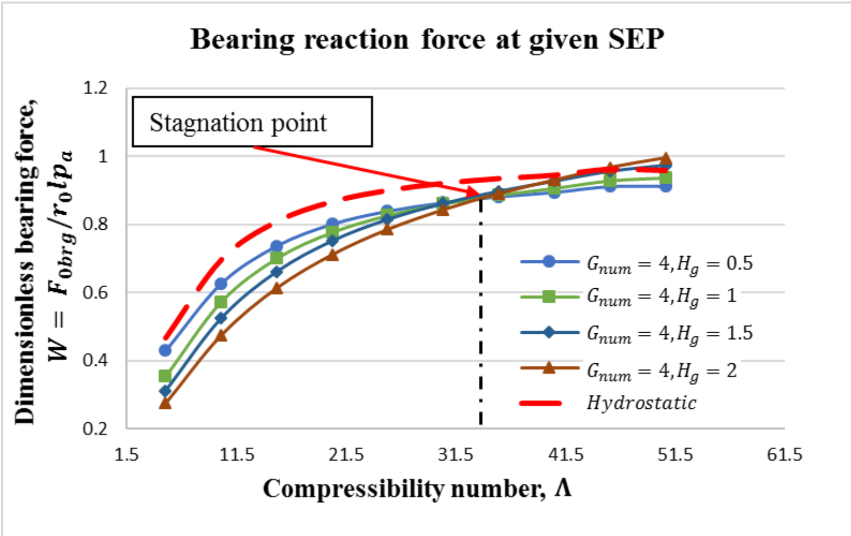

Bearing reaction force at given SEP
Stagnation point
Dimensionless bearing force, $W = F_{0brg}/r_0 l p_a$
Compressibility number, Λ
1.2
1
0.8
0.6
0.4
0.2
1.5
11.5
21.5
31.5
41.5
51.5
61.5
$G_{num} = 4, H_g = 0.5$
$G_{num} = 4, H_g = 1$
$G_{num} = 4, H_g = 1.5$
$G_{num} = 4, H_g = 2$
$Hydrostatic$

a)

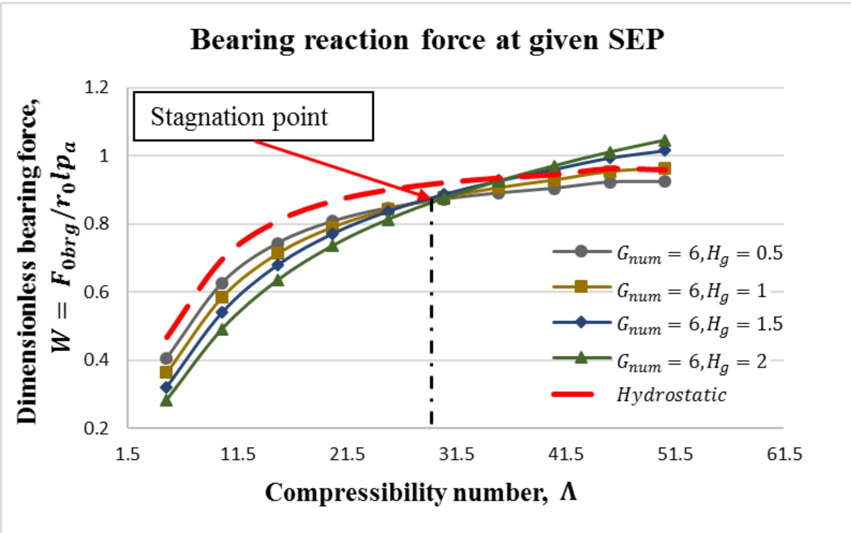

Bearing reaction force at given SEP
Stagnation point
Dimensionless bearing force, $W = F_{0brg}/r_0 l p_a$
Compressibility number, Λ
1.2
1
0.8
0.6
0.4
0.2
1.5
11.5
21.5
31.5
41.5
51.5
61.5
$G_{num} = 6, H_g = 0.5$
$G_{num} = 6, H_g = 1$
$G_{num} = 6, H_g = 1.5$
$G_{num} = 6, H_g = 2$
$Hydrostatic$

b)

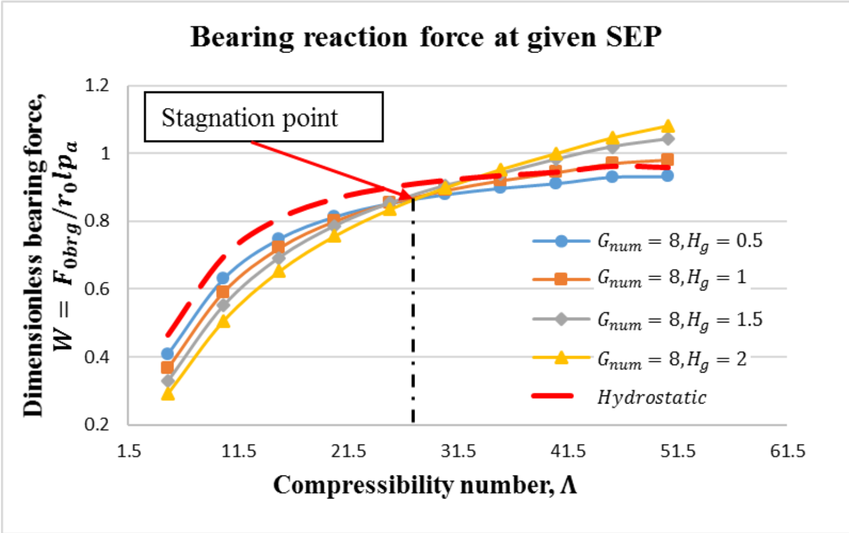

c)

Figure 5. Bearing reaction forces at the given SEP of multiple groove number G_{num} and maximum groove depth ratio (H_g) combinations. Groove angle (β_g) is 30 degrees. H_g increases from 0.5 to 2 in all plots. a) $G_{num} = 4$; b) $G_{num} = 6$; and c) $G_{num} = 8$.

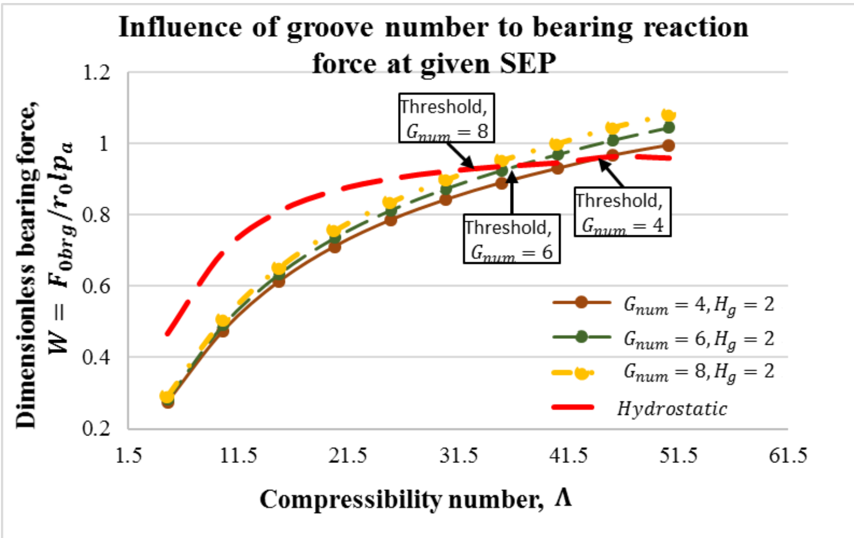

Figure 5.8 The influence of groove number to bearing reaction forces at the given SEP. Threshold Λ of each case is marked in the figure.

Figure 5.9 is an enlarged view of the cases in Figure 5. c) when H_g equals to 1 and 2, and Λ is between 30 and 50. An additional case that $H_g = 3$ is plotted together. It shows bearing reaction forces do not always increase with H_g. In this particular case, maximum bearing reaction forces are achieved when $H_g = 2$.

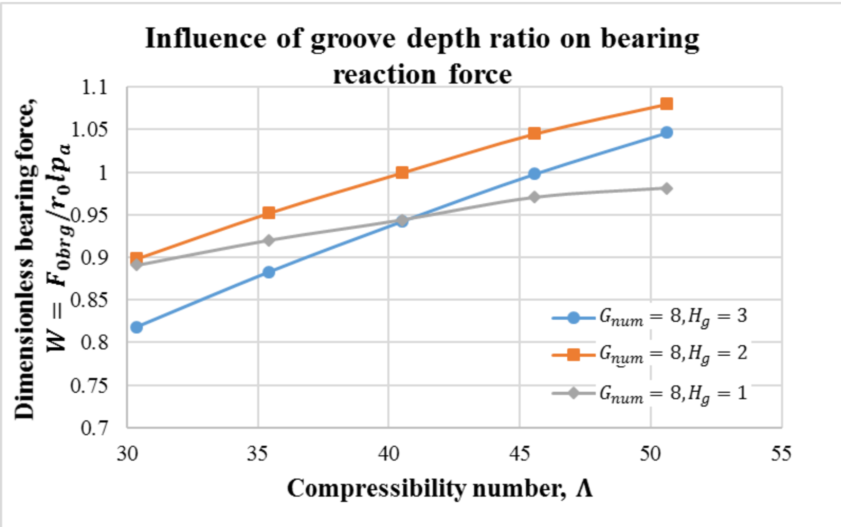

Figure 5.9 Influence of maximum groove depth ratio on bearing reaction forces.

The influence of groove angle to bearing reaction forces is presented in Figure 5.10. The angle of herringbone grooves (β_g) is changed from 20° to 30° for one of the cases in Figure 5. c) ($G_{num} = 8, H_g = 2, \Lambda = 31$). The maximum bearing reaction force is achieved when $\beta_g = 24°$.

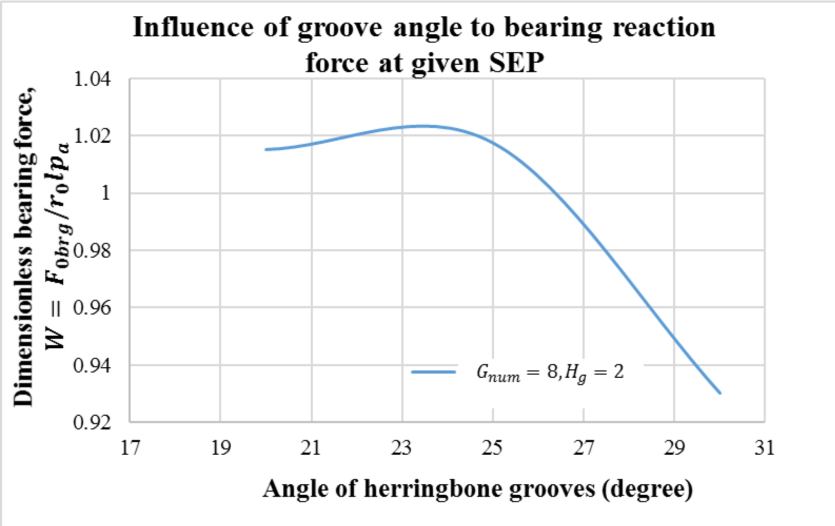

Figure 5.10 Influence of groove angle to bearing reaction force at given SEP

5.3.2 Stiffness and damping coefficients of hybrid journal air bearings

In this section, the influence of herringbone groove configurations on equivalent stiffness ($k_{i,j}$) and damping ($d_{i,j}$) coefficients is investigated. Bearing forces of the proposed hybrid journal air bearings are represented using Equation 3.61 regarding a static equilibrium position at a given rotational speed. The equivalent stiffness ($k_{i,j}$) and damping coefficients ($d_{i,j}$) are calculated by means of assigning a whirling frequency (ω_w) of the journal centre and using Equations from 3.53 to 3.60. In the analysis, the whirling frequency ratio ($\Omega = \omega_w/\omega$) was defined as the ratio of whirl frequency (ω_w) to rotational speed (ω). Dimensions and restrictor setup of the hybrid journal air bearings investigated in this section are listed in Table 5.4.

Table 5.4 Design parameters and restrictor setup of hybrid journal air bearings to be studied

Design parameters	Value
Radius (mm), $\boldsymbol{r_0}$	10
Length (mm), $\boldsymbol{l}$	20
Radial clearance ($\mathbf{\mu m}$), $\boldsymbol{c}$	10
Orifice diameter ($\mathbf{\mu m}$), $\boldsymbol{d_0}$	250
Supply pressure, $\boldsymbol{P_s}$	1 to 6.5

For the convenience of writing, the principal stiffness and damping coefficients are noted as $k_{i,i}$ and $d_{i,i}$ respectively. The cross-coupled stiffness and damping coefficients are noted as $k_{i,j}$ and $d_{i,j}$ respectively.

Similar to the analysis performed on hydrostatic journal air bearings, the variation of stiffness and damping coefficients of the hybrid journal air bearings with whirling frequency ratio (Ω) at the concentric journal position are studied and the results are presented in Figure 5. 11. The change of all coefficients with Ω is the same as those of hydrostatic bearings. However, the amplitude of the principal stiffness coefficients is smaller. For example, under synchronous excitation, k_{yy} is $8.90e^6$ N/m for the hybrid bearings and is $1.15e^7$ N/m for hydrostatic bearings with the same dimension and rotational speed. On the other hand, the hybrid air bearing shows improvement with principal damping coefficients. For example, at synchronous excitation, d_{yy} is $8.50\mathrm{Ns/m}$ for the hybrid bearing while it is only $1.74\ \mathrm{Ns/m}$ for a hydrostatic bearing at the same configuration.

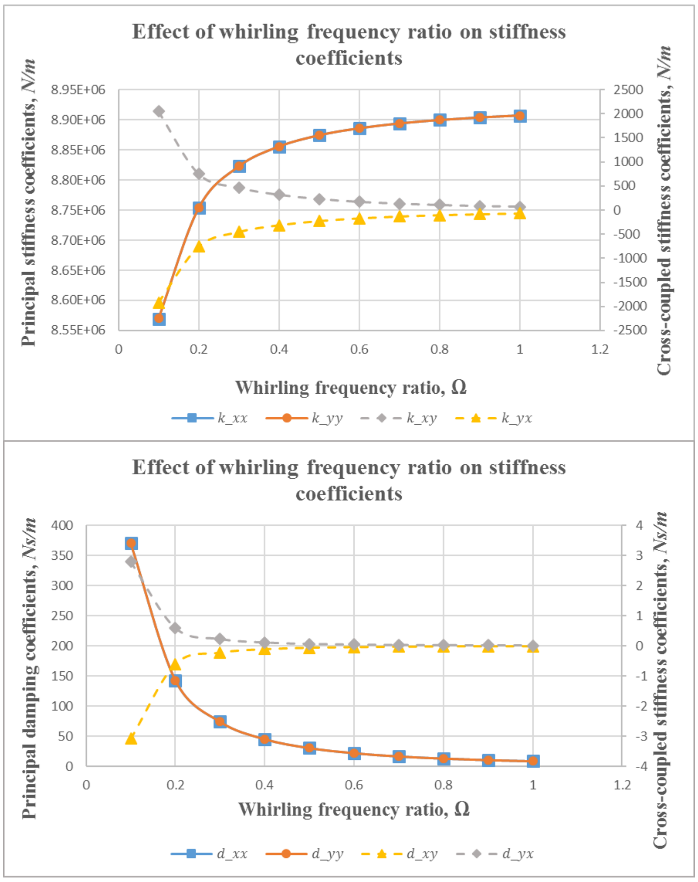

Figure 5. 11 The effect of whirling frequency ratio on the stiffness and damping coefficients of hybrid journal air bearings at concentric journal position. The coefficients are calculated at $\omega = 100k\ rpm, P_s = 3.5bar, c = 10\mu m, h_g = 13\mu m,\ \beta_g = 30°, G_{num} = 18, \alpha_g = \gamma_g = 0.6$

Figure 5.12 presents the variation of synchronous stiffness and damping coefficients with compressibility number (Λ) at the given static equilibrium position (eccentricity ratio, $\varepsilon = 0.1$). The plots indicate a combination effect of bearing radius (r), radial clearance (c) and rotational speed (ω). The figure shows the hardening effect as what was observed in hydrostatic journal air bearings. It is interesting to note that the cross-coupled stiffness of hybrid bearings will reach their maximum value when Λ is around 10. In comparison, the cross-coupled stiffness of hydrostatic bearings increases with Λ.

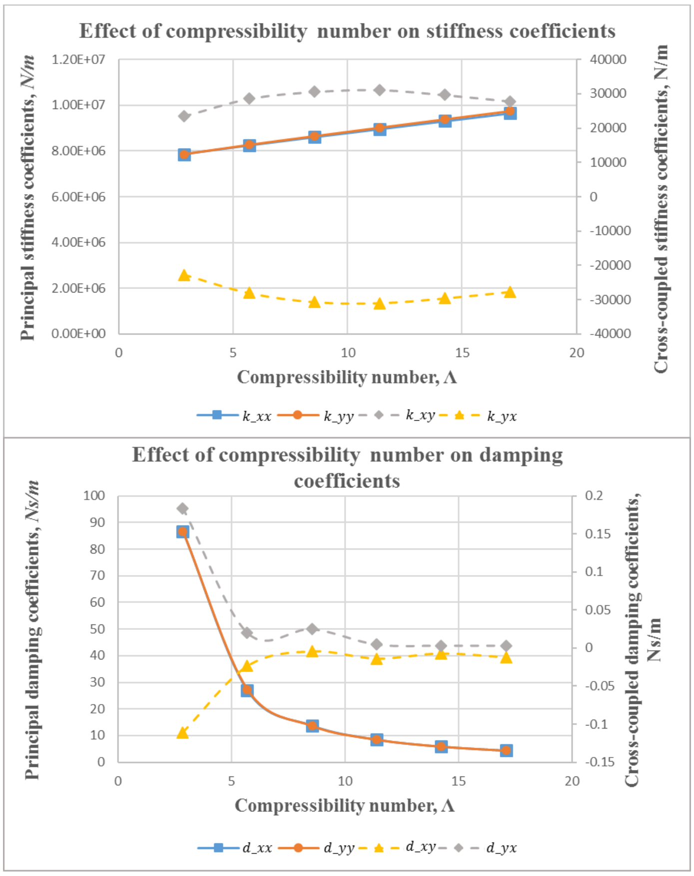

Figure 5.12 The effect of compressibility number on the synchronous stiffness and damping coefficients of hybrid journal air bearings. The coefficients are calculated at $\varepsilon = 0.1, \omega = 150k\ rpm, c = 10\mu m, h_g = 13\mu m,\ \beta_g = 30°, G_{num} = 18, \alpha_g = \gamma_g = 0.6$

The effect of restrictor setup is very like what have been investigated on hydrostatic bearings except supply pressure (P_s), as shown in Figure 5.13. In hybrid air bearings, herringbone grooves enable the principal damping coefficients to be increased with P_s. In hydrostatic air bearings, the damping coefficients are not influenced by P_s. The cross-coupled damping coefficients are very small (almost zero). When P_s is 1 bar, i.e. under ambient pressure, the results represent the coefficients of hybrid air bearing operating with no external compressed air supply.

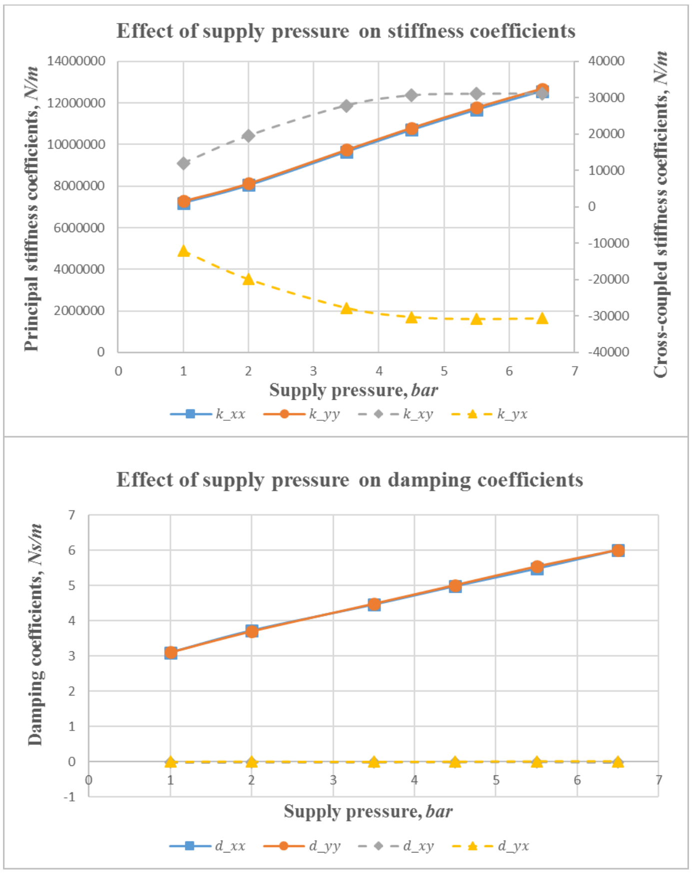

Figure 5.13 The effect of supply pressure on the synchronous stiffness and damping coefficients of hybrid journal air bearings. The coefficients are calculated at $\varepsilon = 0.1, \omega = 150k\ rpm, c = 10\mu m, h_g = 13\mu m,\ \beta_g = 30°, G_{num} = 18, \alpha_g = \gamma_g = 0.6$

The influence of herringbone groove configurations on the stiffness and damping coefficients are investigated using the static equilibrium position at 0.1 eccentricity ratio. The herringbone groove structure parameters being studied are maximum groove depth (h_g), groove angle (β_g), groove number (G_{num}), groove width ratio (α_g) and the fraction of grooved area to bearing length (γ_g). The simulation results are summarized and plotted from Figure 5.14 to Figure 5.18. The coefficients in the figures are calculated at the synchronous whirl frequency.

The effect of maximum groove depth (h_g) on principal stiffness coefficients and damping coefficients is presented in Figure 5.14. In the plot, $h_g = 0\mu\text{m}$ implies there is no herringbone grooves (hydrostatic bearings). The principal stiffness coefficients have a maximum value when $h_g = 10\mu\text{m}$. Increasing h_g over $15\mu\text{m}$ considerably reduces the principal stiffness (reduced over 12% when $h_g = 30\mu\text{m}$). It is interesting to note that the cross-coupled stiffness coefficients also reach their minimum at a groove depth h_g close to $8\mu\text{m}$. Meanwhile, the principal damping coefficients increase significantly with h_g and reaches the maximum at $h_g = 20\mu\text{m}$. In comparison with hydrostatic bearings ($h_g = 0\mu\text{m}$), the principal damping coefficients are increased from 0.9Ns/m to 5.9Ns/m. By means of comparing the effect of h_g on the principal stiffness and damping coefficients, it can be found that the increased damping property is at the cost of reduced bearing stiffness. It also worth noting, when $h_g = 10\mu\text{m}$, principal stiffness coefficients of hybrid air bearings are the same as hydrostatic bearings ($h_g = 10\mu\text{m}$). However, the cross coupled stiffness coefficients are reduced 20% and the damping coefficients are increased to 4Ns/m from 0.9Ns/m

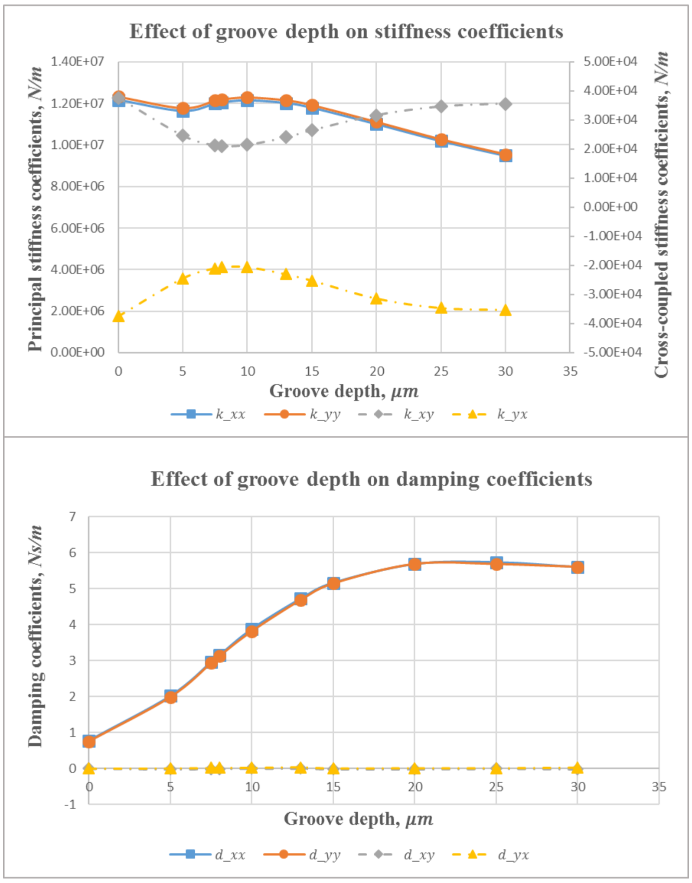

Figure 5.14 The effect of maximum groove depth on the stiffness and damping coefficients of hybrid journal air bearings. The coefficients are calculated at $\varepsilon = 0.1, \omega = 150k\ rpm, c = 8\mu m, P_s = 2.5bar, \beta_g = 30°, G_{num} = 18, \alpha_g = \gamma_g = 0.6$

Figure 5.15 shows the influence of groove angle (β_g). When β_g is between 16° and 30°, the change on principal stiffness coefficients is not significant (4% variation), although maximum stiffness is achieved $\beta_g = 25°$. Further increasing in β_g will cause the principal stiffness coefficients drop considerably. On the other hand, the cross-coupled stiffness coefficient (k_{xy}) present an ascending trend with β_g (descending for k_{yx}). For example, k_{xx} is reduced 12% at $\beta_g = 46°$ in comparison with k_{xx} at $\beta_g = 26°$. In the same process, k_{xy} is increased 38%. The damping coefficients decrease with β_g. However, the principal damping coefficients are only reduced from 5Ns/m to 3.5Ns/m when β_g increases from 16° to 48°. The groove angle only has marginal influence on the damping coefficients.

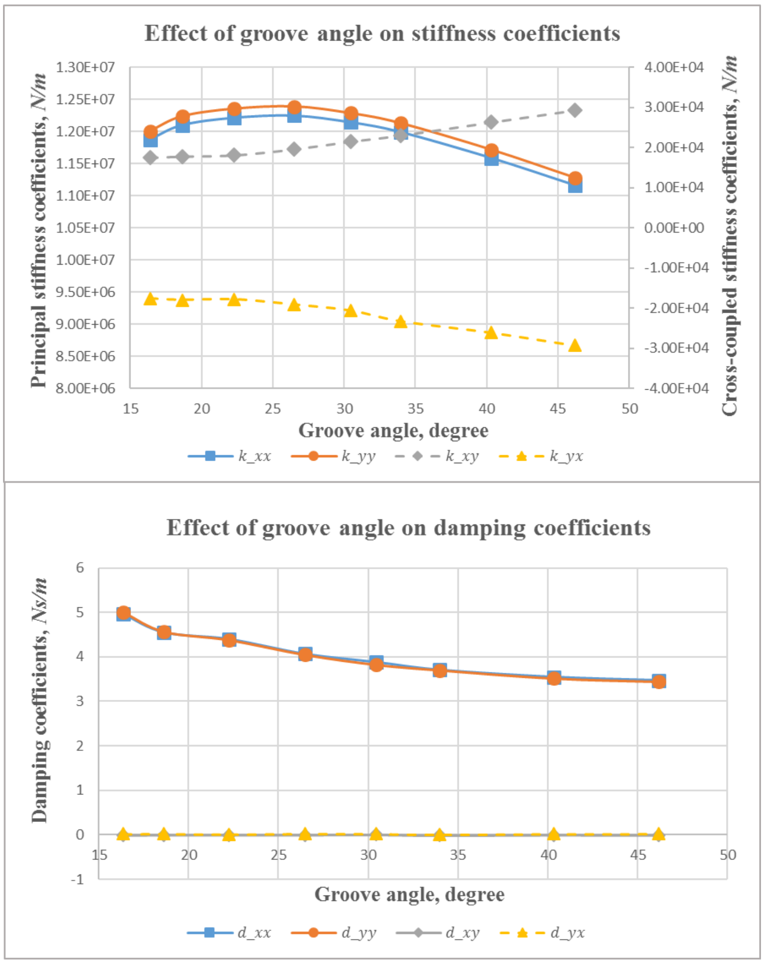

Figure 5.15 The effect of groove angle on the stiffness and damping coefficients of hybrid journal air bearings. The coefficients are calculated at $\varepsilon = 0.1, \omega = 150k\ rpm, c = 8\mu m, P_s = 2.5bar, h_g = 10\mu m, G_{num} = 18, \alpha_g = \gamma_g = 0.6$

Figure 5.16 shows the effect of groove number (G_{num}). It is found that G_{num} has very limited effect on the principal stiffness coefficients. The overall variation is less than 5% when G_{num} changes from 6 to 24. However, the amplitude of cross-coupled stiffness coefficients is reduced about 28%. On the other hand, the principal damping coefficients increase linearly with G_{num}. When G_{num} increases from 6 to 24, the principal damping coefficients are increased from 2Ns/m to 4.9Ns/m.

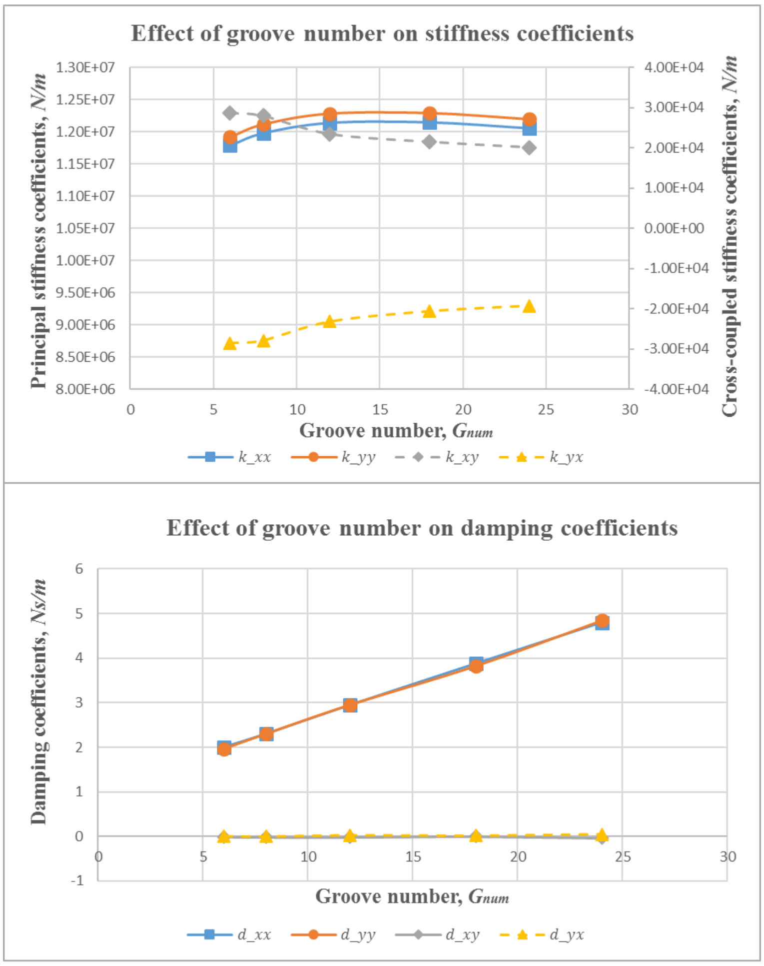

Figure 5.16 The effect of groove number on the stiffness and damping coefficients of hybrid journal air bearings. The coefficients are calculated at $\varepsilon = 0.1, \omega = 150k\ rpm, c = 8\mu m, P_s = 2.5bar, h_g = 10\mu m, \beta_g = 30°, \alpha_g = \gamma_g = 0.6$

In Figure 5.1 , the effect of groove width ratio (α_g) is presented. It is found that all principal and cross-coupled stiffness coefficients increase with α_g. At the same time, the principal damping coefficients only decrease with α_g slightly (drop from 3Ns/m to 2.5Ns/m). This indicated the influence of α_g is mainly on the stiffness coefficients.

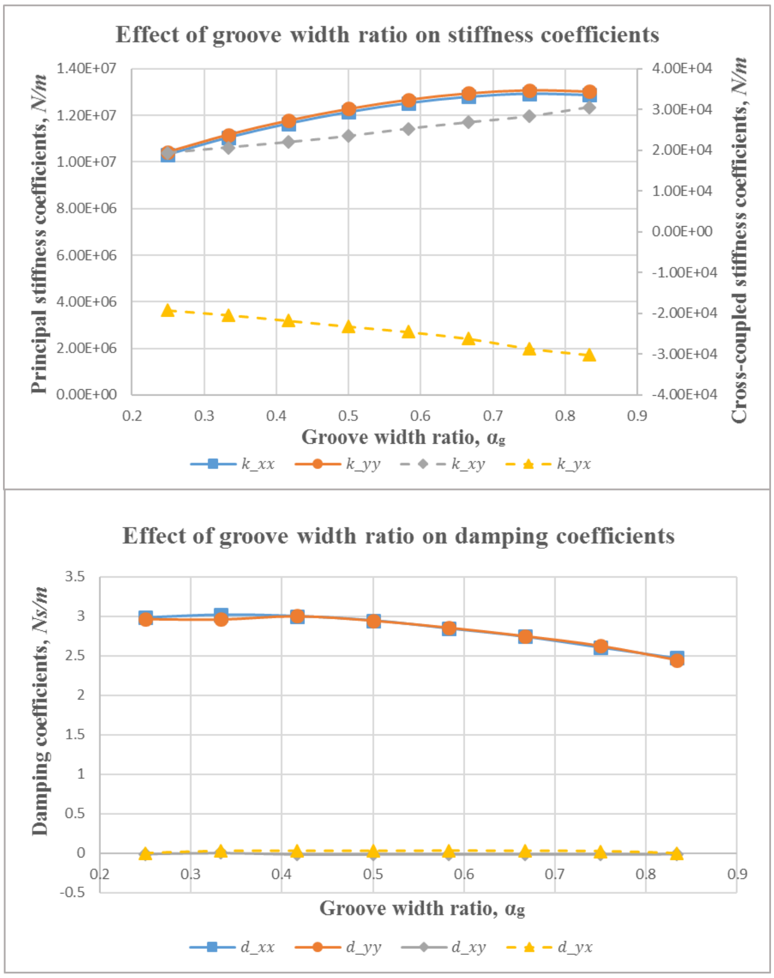

Figure 5.1 The effect of groove width ratio on the stiffness and damping coefficients of hybrid journal air bearings. The coefficients are calculated at $\varepsilon = 0.1, \omega = 150k\ rpm, c = 8\mu m, P_s = 2.5bar, h_g = 10\mu m, \beta_g = 30°, G_{num} = 18, \gamma_g = 0.6$

The effect of grooved area fraction (γ_g) is shown in Figure 5.18. $\gamma_g = 1$ implies the journal surface is fully grooved. It is found that the principal stiffness coefficients drop quickly with γ_g when it is greater than 0.6. However, the amplitude of cross-coupled stiffness coefficients is reduced with the increase of γ_g. The plot also indicates γ_g can improve principal damping coefficients significantly.

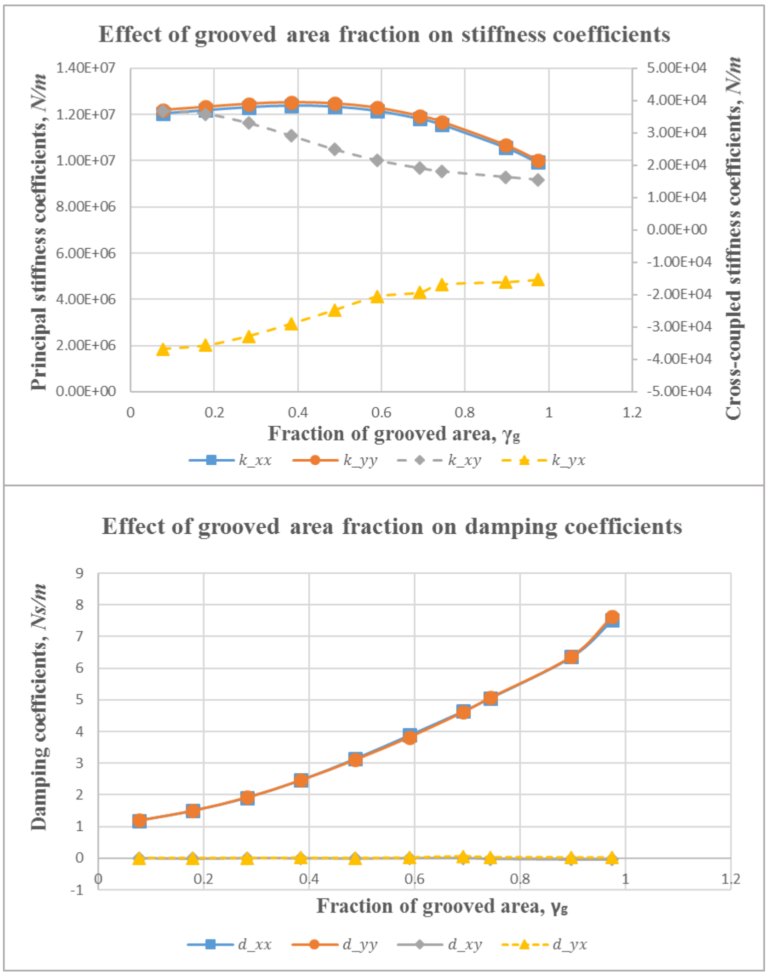

Figure 5.18 The effect of grooved area fraction on the stiffness and damping coefficients of hybrid journal air bearings. The coefficients are calculated at $\varepsilon = 0.1, \omega = 150k\ rpm, c = 8\mu m, P_s = 2.5bar, h_g = 10\mu m, \beta_g = 30°, G_{num} = 18, \alpha_g = 0.6$

Throughout the analysis from Figure 5.14 to Figure 5.18, the effect of herringbone groove configurations on the stiffness and damping coefficients of hybrid journal air bearing can be summarized as follows:

(a) The influence of herringbone groove parameters groove depth (h_g), groove width ratio (α_g) and grooved area fraction (γ_g) will influence the volume of air film. Other parameters will not.

(b) The principal damping coefficients can be improved by increasing h_g and $\gamma_g$at the cost of reduced principal bearing stiffness coefficients. By changing h_g, one can get the maximum principal and minimum cross-coupled stiffness coefficients with same value of h_g. However, α_g mainly has effect on the stiffness coefficients. The principal stiffness coefficients increase with α_g, which is different from h_g and γ_g.

(c) β_g mainly has effect on changing the stiffness coefficients, while G_{num} has more effect on changing the principal damping coefficients.

(d) With reference to [85, 94] and study on hydrostatic journal air bearing in Chapter 4, the cross-coupled stiffness in air bearings are the source to cause instability. In hybrid air bearings, the stability of the bearing can be improved by manipulating the groove configurations to reduce the cross-coupled stiffness coefficients and improve the damping coefficients.

One can also manipulate the groove configurations to achieve different bearing stiffness and damping coefficients to meet the requirement of rotor dynamic configuration supported by the bearings. For example, one can improve the bearing’s damping coefficients using larger h_g, γ_g and G_{num}, at the same time, selecting proper values of α_g and β_g to avoid too much compromise on reducing bearing stiffness.

5.3.3 Analysis on stability and natural frequencies of rotor bearing system using linear bearing model

In this section, the stability and natural frequencies of a rotor bearing system with hybrid air bearings are investigated. The configurations of the rotor bearing system under study here are the same as **CASES I & II**. The hybrid air bearings are represented as linear bearing units with stiffness and damping coefficients extracted from the linear perturbation analysis in Section 5.3.2. The dimensions and groove configurations of the bearings are listed in Table 5.5. Because there is no change in the mechanical configurations in both cases, only the characteristic matrices of the system governing equations of motion are presented as Equation 5.2 and Equation 5.3. The analytical method is the same as that performed on hydrostatic air bearings in Chapter 4.

Table 5.5 Design parameters and restrictor setup of hybrid air bearings to be studied

Design parameters	Value
Radius (mm), $\boldsymbol{r_0}$	10
Length (mm), $\boldsymbol{l}$	20
Radial clearance ($\boldsymbol{\mu m}$), $\boldsymbol{c}$	12.5
Orifice diameter ($\boldsymbol{\mu m}$), $\boldsymbol{d_0}$	250
Supply pressure (bar), $\boldsymbol{P_s}$	1 and 7
Maximum groove depth ($\boldsymbol{\mu m}$)	13
Groove angle (degree), $\boldsymbol{\beta_g}$	28.5
Number of grooves, $\boldsymbol{G_{num}}$	18
ratio of groove width to total width (groove plus ridge), $\boldsymbol{\alpha_g}$	0.6
fraction of bearing length occupied by grooves, $\boldsymbol{\gamma_g}$	0.6

Characteristic matrix of the governing equation of motion for the rotor bearing system presented in Chapter 4, **CASE I:**

$$J_1 = \begin{bmatrix} [0] & [1] \\ -[\boldsymbol{M_s}]^{-1}[\boldsymbol{K_{sys\_1}}] & -[\boldsymbol{M_s}]^{-\boldsymbol{1}}[\boldsymbol{CG_{sys\_1}}] \end{bmatrix}$$

$$[\boldsymbol{K_{sys\_1}}] = [[\boldsymbol{K_s}] + [\boldsymbol{K_b}]] \qquad \textit{Equation 5.2}$$

$$[\boldsymbol{CG_{sys\_1}}] = [[\boldsymbol{C_s}] + [\boldsymbol{C_b}] + [\boldsymbol{G}]]$$

where $[\boldsymbol{M_s}]$ is the shaft structure mass and inertia matrix, $[\boldsymbol{K_{sys\_1}}]$ the system stiffness matrix, $[\boldsymbol{K_s}]$ the shaft structure stiffness matrix, $[\boldsymbol{K_b}]$ the bearings' stiffness matrix, $[\boldsymbol{CG_{sys\_1}}]$ the system damping and gyroscopic matrix, $[\boldsymbol{C_s}]$ the shaft structure damping coefficients, $[\boldsymbol{C_b}]$ the bearing's damping matrix, and $[\boldsymbol{G}]$ the shaft structure gyroscopic matrix.

Characteristic matrix of the governing equation of motion for rotor bearing system presented in Chapter 4, **CASE II:**

$$J_2 = \begin{bmatrix} [0] & [1] \\ -[\boldsymbol{M_2}]^{-1}[\boldsymbol{K_{sys\_2}}] & -[\boldsymbol{M_2}]^{-\boldsymbol{1}}[\boldsymbol{CG_{sys\_2}}] \end{bmatrix}$$

$$[\boldsymbol{M_2}] = \begin{bmatrix} [\boldsymbol{M_s}] & [\boldsymbol{0}] \\ [\boldsymbol{0}] & [\boldsymbol{M_v}] \end{bmatrix}$$

$$[\boldsymbol{K_{sys\_2}}] = \begin{bmatrix} [\boldsymbol{K_s}] + [\boldsymbol{K_b}] & -[\boldsymbol{K_b}'] \\ -[\boldsymbol{K_b}']^T & [\boldsymbol{K_v}] \end{bmatrix} \qquad \textit{Equation 5.3}$$

$$[\boldsymbol{CG_{sys\_2}}] = \begin{bmatrix} [\boldsymbol{C_s}] + [\boldsymbol{C_b}] + [\boldsymbol{G}] & -[\boldsymbol{C_b}] \\ -[\boldsymbol{C_b}] & [\boldsymbol{C_v}] \end{bmatrix}$$

where $[\boldsymbol{M_s}]$ is the shaft structure mass and inertia matrix, $[\boldsymbol{K_{sys\_2}}]$ the system stiffness matrix, $[\boldsymbol{K_s}]$ the shaft structure stiffness matrix, $[\boldsymbol{K_b}]$ the bearings' stiffness matrix, $[\boldsymbol{CG_{sys\_2}}]$ the system damping and gyroscopic matrix, $[\boldsymbol{C_s}]$ the shaft structure damping coefficients, $[\boldsymbol{C_b}]$ the bearing's damping matrix, $[\boldsymbol{G}]$ the shaft structure gyroscopic matrix, $[\boldsymbol{M_v}]$ the bearing sleeve mass and inertia matrix, and $[\boldsymbol{K_v}]$ and $[\boldsymbol{C_v}]$ the stiffness and damping matrix of the bearing sleeve respectively.

The analysis on natural frequencies is performed at the working condition that external compressed air supply pressure (P_s) is maintained at bar. Figure 5.19 shows the natural frequencies of the two cases identified from theoretical analysis as Campbell diagrams, with the rotor speed up to 150k rpm. Mode shapes of the rotor are obtained at 1330Hz. In the plots, the first two modes are rigid modes and the third and fourth one (if it is shown) are bending modes. It can be seen that natural frequencies of all modes are reduced in comparison with systems running on hydrostatic air bearings, referring to Figure 4.24 in Chapter 4. For example, the natural frequency of mode 2 in **CASE I** is 1315 Hz, while it is 1680 Hz for hydrostatic air bearings; the natural frequency of mode 3 in **CASE II** is 1470 Hz, while it is 1790 Hz for hydrostatic air bearings. A forth mode also appears in the speed range of **CASE II**. They are the result of hybrid bearings with given geometry having lower stiffness than that of the hydrostatic bearings with similar geometry investigated in Chapter 4.

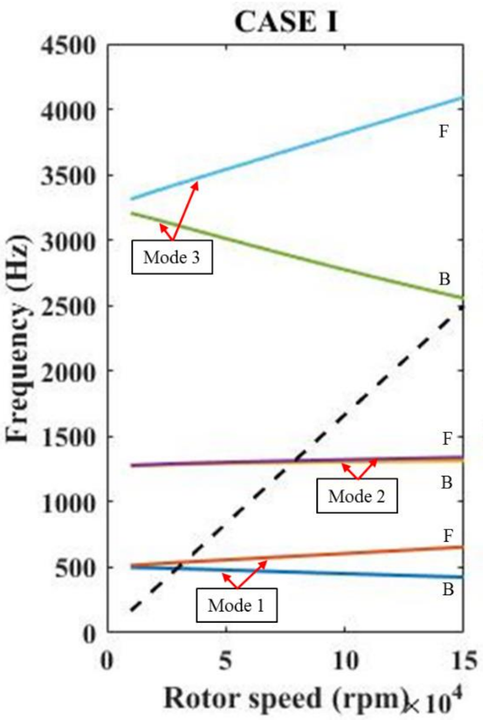
CASE I
Frequency (Hz)
Rotor speed (rpm)
× 10^4
0
500
1000
1500
2000
2500
3000
3500
4000
4500
0
5
10
15
Mode 3
Mode 2
Mode 1
F
B
F
B
F
B

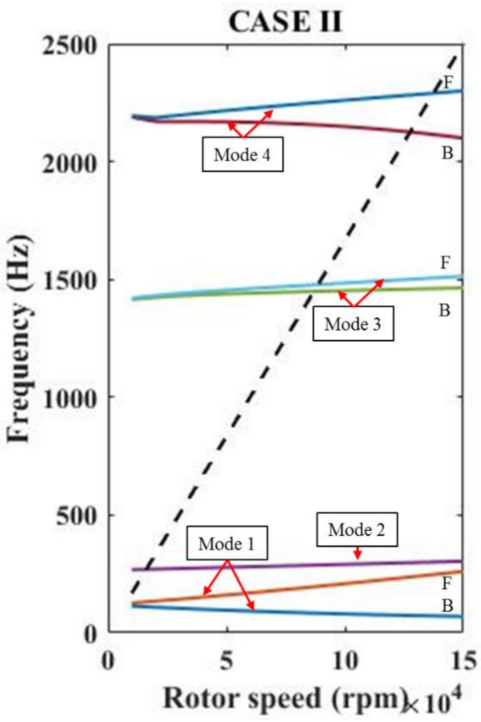
CASE II
Frequency (Hz)
Rotor speed (rpm)
× 10^4
0
500
1000
1500
2000
2500
0
5
10
15
Mode 4
Mode 3
Mode 1
Mode 2
F
B
F
B
F
B

a) b)

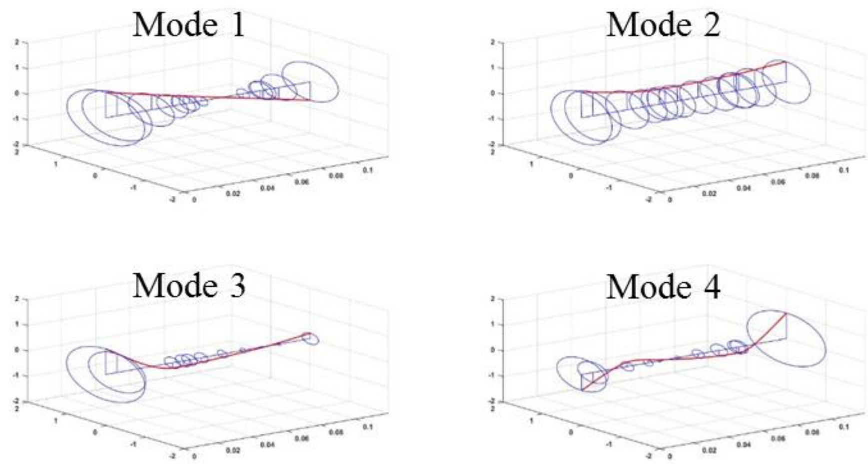
Mode 1
Mode 2
Mode 3
Mode 4

c)

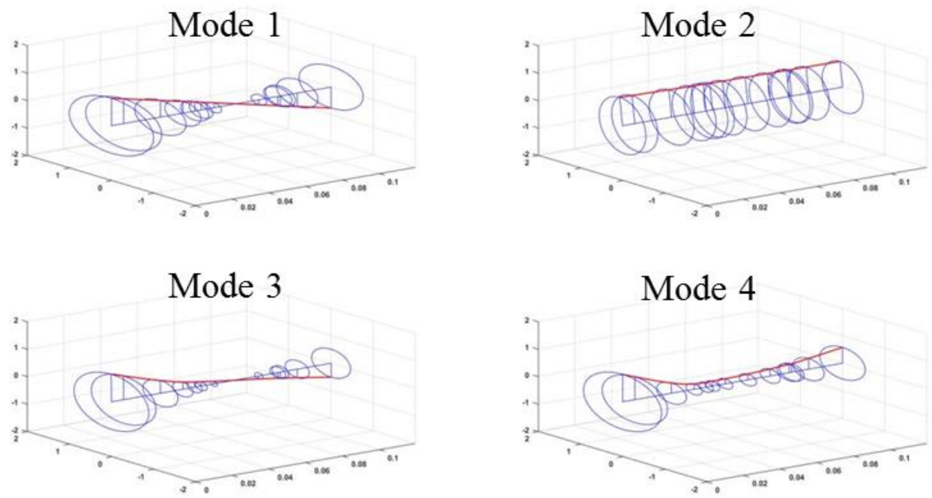

d)

Figure 5.19 Campbell diagrams for **Cases I & II**. The dash line is the synchronous line. '**F**' denotes forward whirl and '**B**' denotes backward whirl. a) **Case I:** linear rotor with linear bearings. b) **Case II:** linear rotor with linear bearings and linear dampers. c) Mode shape obtained at 1330Hz of the rotor in **CASE I**. d) Mode shape obtained at 1330Hz of the rotor in **CASE II**.

From the Campbell diagram, it is seen the frequency of the backward whirl of mode 2 in **CASE I**, mode 2 and 3 in **CASE II** gradually ascends with increasing rotor speed, which leads to a very small difference with the forward whirl of these modes. Similar effect was observed for the two cases with hydrostatic air bearings. This has also been reported in [85], in which the analysis was made on a turbocharger rotor supported by floating ring bearings.

The stability analysis is performed in two working conditions for both cases. In the first working condition, the compressed air supply pressure (P_s) is maintained at bar. In the second working condition, the bearings are fully self-acting with no external pressurized air (the supply pressure is ambient, $P_s = 1\text{bar}$).

The results of stability analysis are shown in Figure 5.20. In the stability maps, the real part of the leading eigenvalue of the system characteristic matrix is plotted against rotational speeds from 10k to 250k rpm. Plots a and b show the both cases are stable within the speed range when compressed air supply is maintained at 7bar. In comparison, the system of **CASE I** supported by hydrostatic air bearings becomes unstable at 110k rpm (See Figure 4.25 a). This proves the use of hybrid air bearings can greatly improve the stability of a rotor bearing system. Plots c and d are the stability maps when the bearings are working as hydrodynamic ones. At this condition, the bearings can lift the rotor only when its rotational speed is over 20k rpm. The system in **CASE I** is unstable within the speed range while the system in **CASE II** becomes stable once the rotational speed goes over 200k rpm. It indicates the viscoelastic support can be used to improve the stability. The whirl frequency ratio corresponding to stability map c and d are presented in Figure 5.20 e) and f) respectively. As discussed in Section 4.4.3, the abrupt whirling frequency shift is observed again in both cases when one leading eigenvalue supersedes another. The shift of whirling frequency and leading eigenvalue are marked with green arrows.

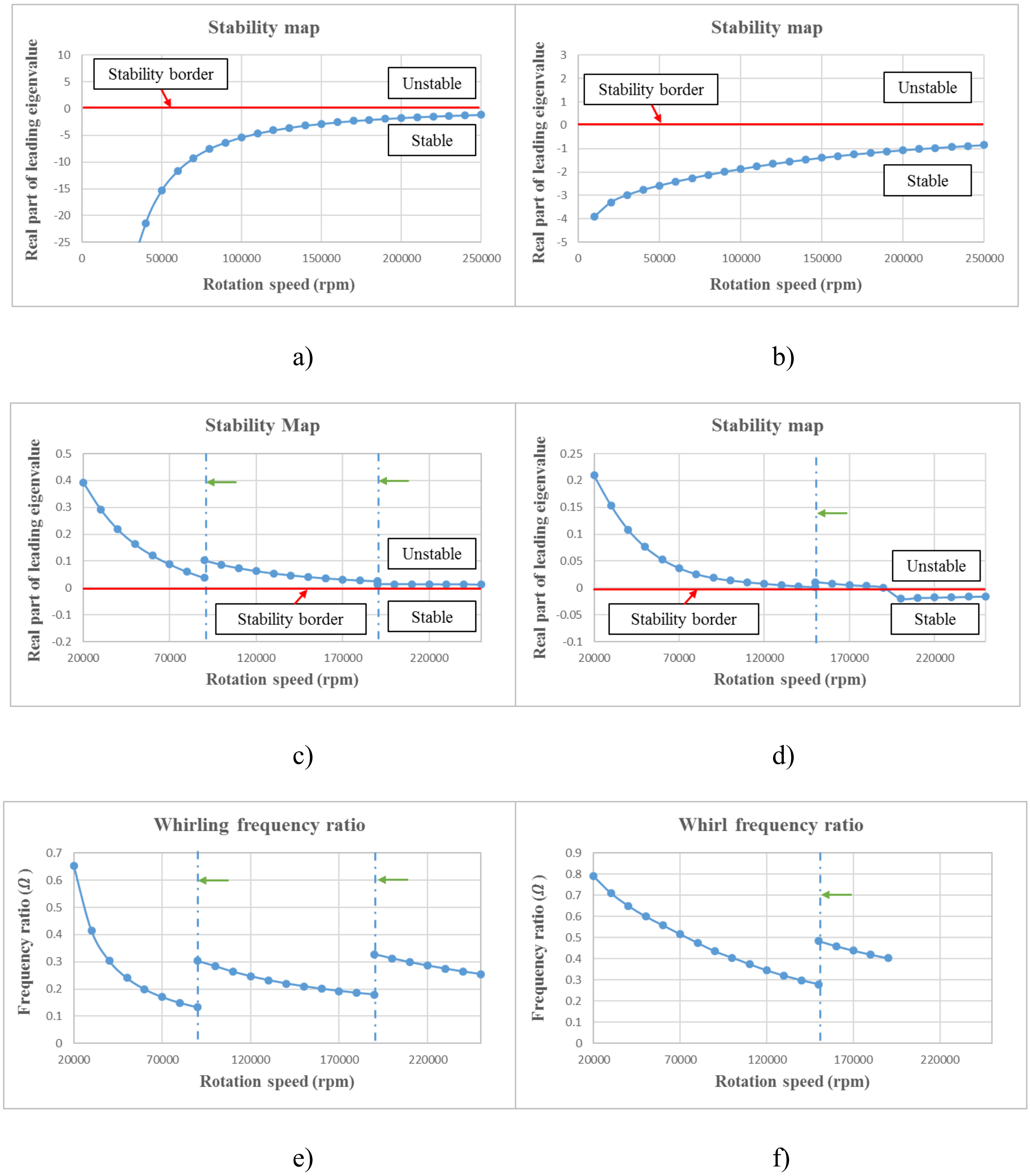

Figure 5.20 Stability maps and whirl frequency ratio based on SESA. a) stability map of **CASE I**, $P_s = 7$, b) stability map of **CASE II**, $P_s = 7$, c) stability map of **CASE I**, $P_s = 1$, d) stability map of **CASE II**, $P_s = 1$, $\gamma = 0.2$, e) whirl frequency ratio of **CASE I**, $P_s = 1$, f) whirl frequency ratio of **CASE II**, $P_s = 1$, $\gamma = 0.2$.

The above analysis shows that the viscoelastic support has the capability of improving the system stability when hybrid air bearing is operating with no supply of externally compressed air.

The deformation ratio (γ) of the O-rings under the current study is selected as 0.2. This is based on the actual O-ring deformation evaluated from the testing device used in experiments. Although the viscoelastic support with this configuration can improve the stability, it may not be ideal. For example, the rotor bearing system in **CASE II** is still unstable under 190k rpm. This is a speed range where the rotor in the size of R-1 typically working at. A further study on stability was performed by increasing γ to 0.25. The stability map is shown in Figure 5.21. It is found that the viscoelastic support with increased O-ring deformation ratio can stabilize the system when hybrid air bearings working with no compressed air supply.

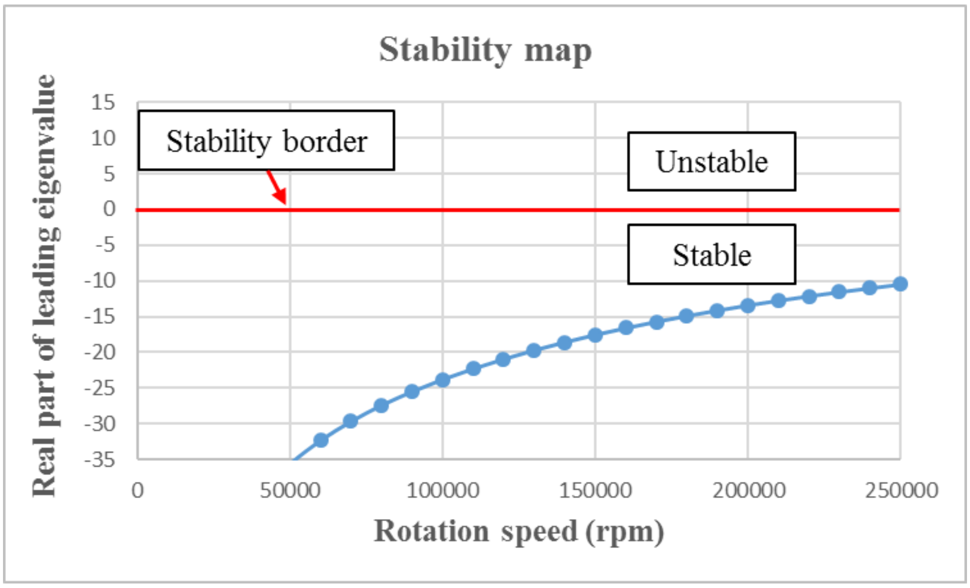

Figure 5.21 Stability map based on SESA of **CASE II**, $P_s = 1, \gamma = 0.25$

5.4 Non-linear transient analysis and experimental verification of hybrid air bearings

In this section, the non-linear transient analysis performed in Chapter 4 is applied to hybrid air bearings and the results are then verified by experiments in unbalance responses. The bearing test rig developed is also used here. The rotor is remanufactured with the novel herringbone grooves fabricated on two journals of the rotor to form the hybrid air bearings. In order to operating at a higher rotational speed, this rotor was balanced to achieve G1 standard for a service speed at 150k rpm. The unbalance responses of the rotor were measured up to 120k and compared with predictions from the non-linear transient analysis.

This section begins with an introduction to the manufacturing process of the novel herringbone groove with its geometry measured. The predicted unbalance responses of the test rig are then discussed under two occasions. In the first one, the rotor is running with hybrid air bearing using compressed air supply pressure (P_s) at bar and tested up to 120k rpm. The discussion is focused on the synchronous responses. In the second one, the rotor is initially lifted by hybrid air bearings with $P_s = 7\text{bar}$. Once the rotor accelerates to a speed between 50k and 60k rpm, compressed air supply to the hybrid journal bearings is cut off and the bearings are self-acting. The theoretically studies and experiments were performed from 0k rpm up to 120k rpm. The discussion is focused on the unbalance responses with sub-synchronous components (self-excited whirl).

5.4.1 Manufacturing of the novel herringbone groove

In the proposed hybrid air bearings, the novel herringbone grooves are the key feature and fabricated using the latest laser machining technology. Figure 5.22 a) shows the manufactured rotor. Some design parameters and the groove profile measuring place are indicated on an enlarged view of the grooved journal in Figure 5.22 b). The measured values of these parameters are given in Table 5.6. The groove profile is measured using Alicona microscope and presented in Figure 5.22 c). It is designed as a cosine weave spline with 13µm maximum depth and 1 40 µm span (half cycle). The measured dimensions of the grooves were used in the non-linear bearing model.

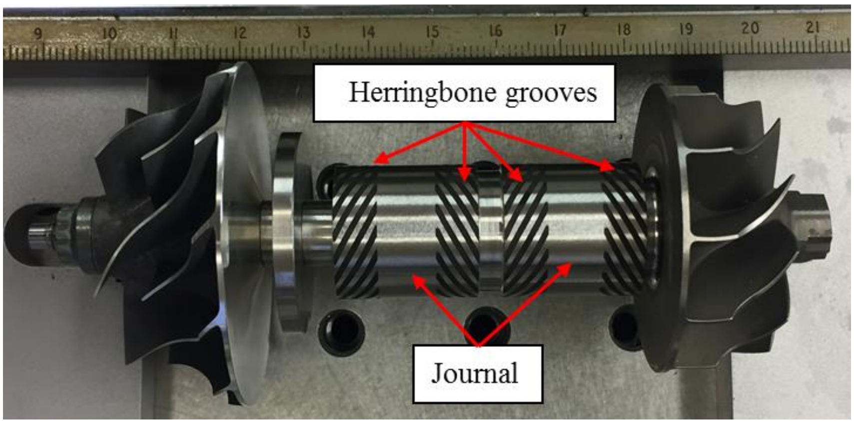

a) R-1 with herringbone grooved journal

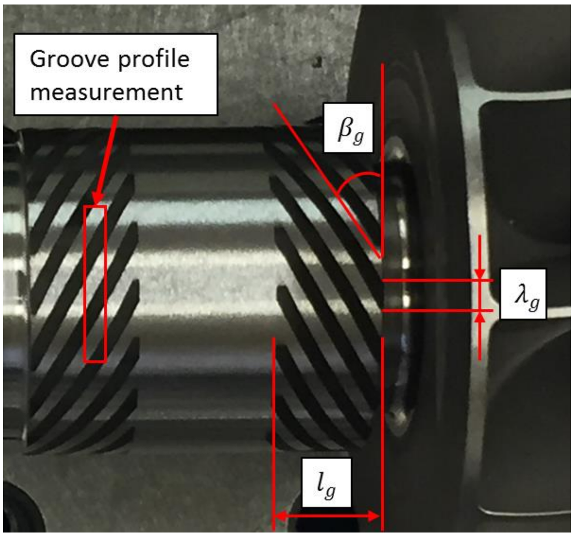

b) Enlarged view of the herringbone grooved journal

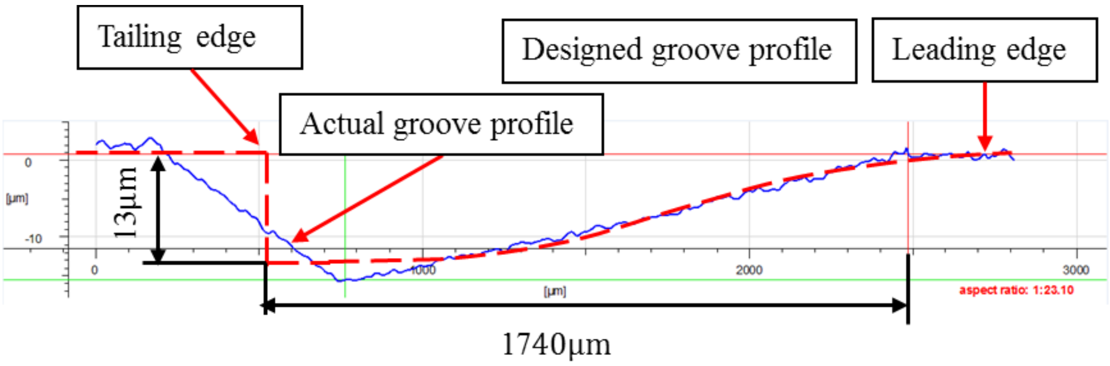

c) Measured groove profile

Figure 5.22 The rotor used in the hybrid air bearings and the novel herringbone grooves. a) The manufactured rotor, b) Enlarged view of the herringbone grooved journal, and c) Measured groove profile: the red dash line is the design profile; the blue curve is the measured profile.

Table 5.6 Design parameters of the novel herringbone groove

Design parameters	Value
Number of grooves, $\boldsymbol{G_{num}}$	18
Maximum groove depth ($\boldsymbol{\mu m}$)	13
Groove angle (degree), $\boldsymbol{\beta_g}$	28.5
Groove width (mm), $\boldsymbol{\lambda_g}$	1.74
Groove length (mm), $\boldsymbol{\gamma_g}$	6.3

5.4.2 Unbalance responses of hybrid journal air bearings with compressed air supply

In this section, the experimental studies on unbalance responses of the rotor were measured when compressed air was supplied to the hybrid air bearings at b ar. The test rig introduced in Chapter 4 was used. The responses of the rotor were measured at the same sensor positions and compared with simulation results. The bearing components had no significant changes in dimensions with that used in hydrostatic bearing tests. The responses of the rotor were measured at constant speeds 0k, 80k, 90k, 100k, 110k and 120k rpm respectively. A 5% difference in the power of the provide drive was allowed in each test.

Rotor R-1 used in hybrid air bearing tests has been presented in Figure 5.22 a). It was balanced to G1 standard for a service speed at 150k rpm. The rotor was balanced using two-plane dynamic balancing approach. The equivalent unbalance residuals are concentrated on two planes and listed in Table 5. .

Table 5. Unbalance information of R-1

	Left hand correction plane	Right hand correction plane
Unbalance residual (g*mm)	0.008	0.005
Unbalance phase angle	220°	78°
Positions on Rotor	Compressor disc	Turbine disc
Position on Rotor model	Node 4	Node 18

From the analysis shown by Figure 5.19 b) of Section 5.3.3, the system has a natural frequency at 14 0 Hz within the test speed range. Figure 5.23 is the event time waterfall plots in a run-up test to 120k rpm. It shows the vibrations of the rotor are dominated by the synchronous components (1x) and have a critical speed at 1400 Hz. The results have good agreement with the predictions on the natural frequencies. The rotor bearing system is stable at this working condition up 120k rpm rotor speed (no sub-synchronous vibration) as expected.

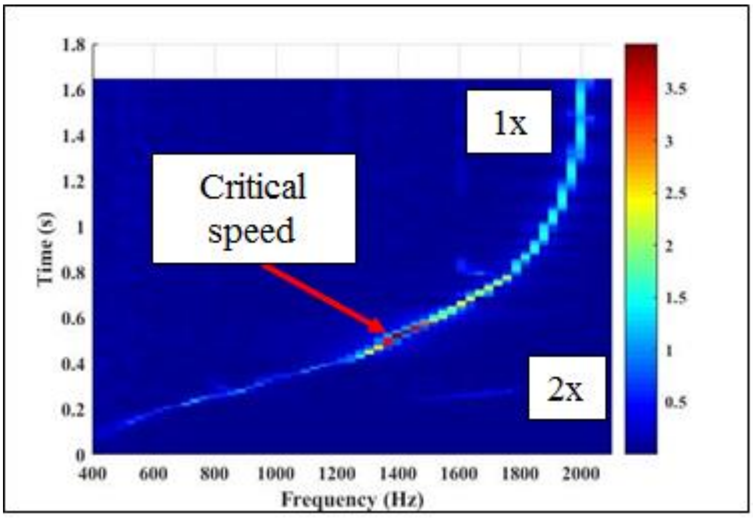

Figure 5.23 Top views of waterfall plots in a run-up test to 120k rpm. Measurements were made at sensor position A in horizontal direction.

The experimental unbalance responses and related simulation results from non-linear transient analysis at the given constant rotor speeds are shown in Appendix E for hybrid air bearings with ba r compressed air supply. In each group of the figures, the dominating vibration frequency and the peak vibration velocity amplitude are marked on the FFT plot. The simulations were produced using the actual rotor speed (1x component in frequency spectrum) acquired from experiments. At each speed, the rotor responses were calculated for the first 00 shaft revolutions and a steady state was assumed to be achieved at the last 100 revolutions. The response data were collected for the last 100 revolutions and analysed using FFT. Figure 5.24 shows a case of these measurements and predictions at 120.9k rpm rotor speed for both sensor positions. By comparing Figures 5.24 a & b, it can be found that the vibration frequencies and magnitudes of the measured and simulation results are very similar, and both peak at 2015Hz (unbalance excitations), but the peak amplitudes of the vibration velocities are 2.91mm/s measured from experiments, and 2.80mm/s acquired from simulation. The difference between them is 3%, which can be neglected. Figures 5.24 c & d show that the vibration frequencies and magnitudes of the measured and simulation results are very similar again, but the peak amplitudes of the speeds are too small to give meaningful readings.

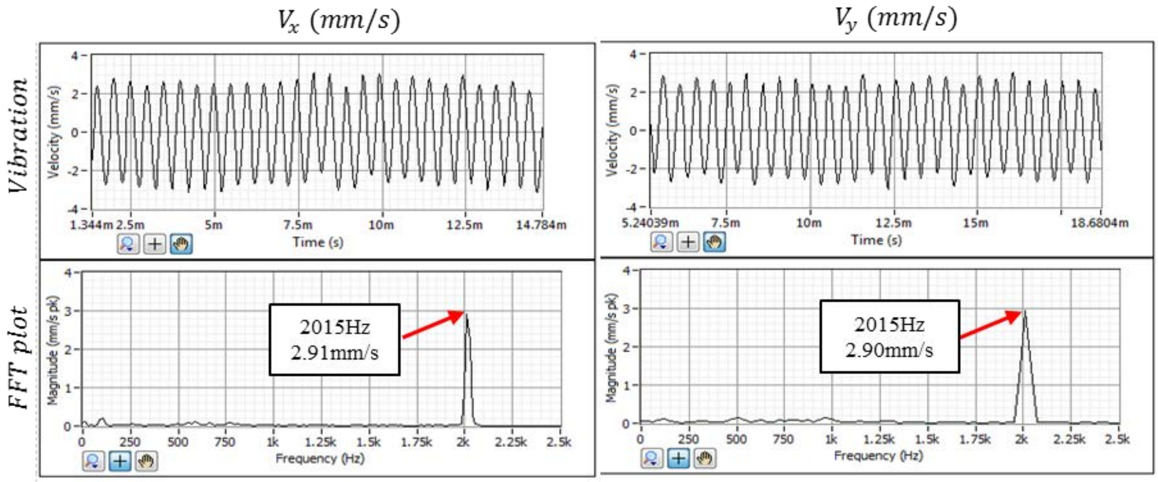

a) Measurements at sensor position A

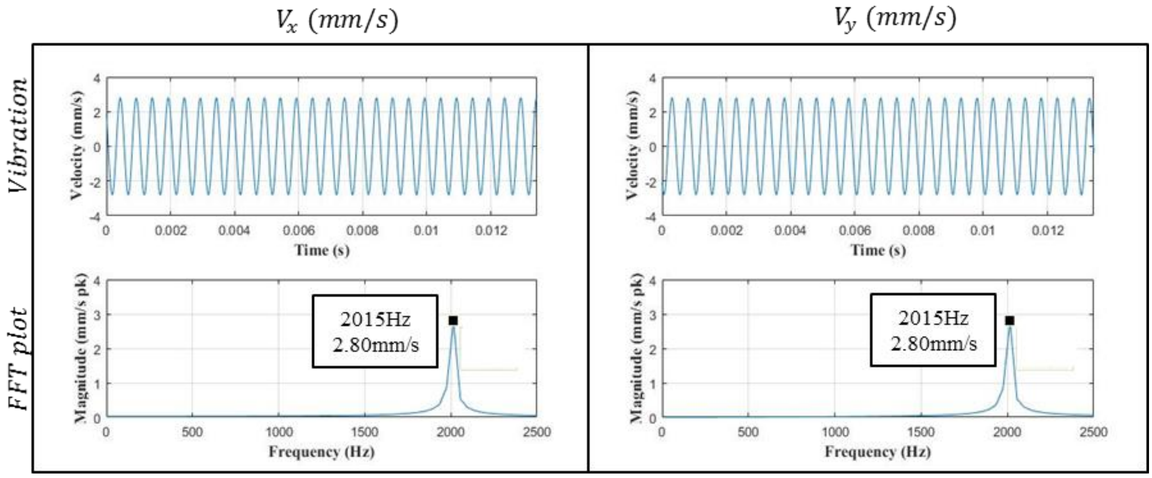

b) Predictions at sensor position A

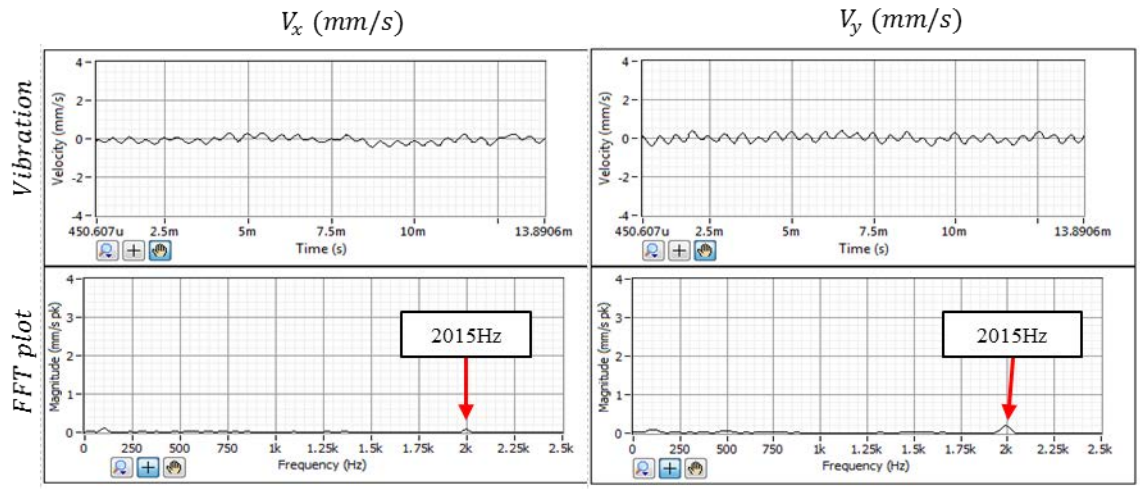

c) Measurements at sensor position B

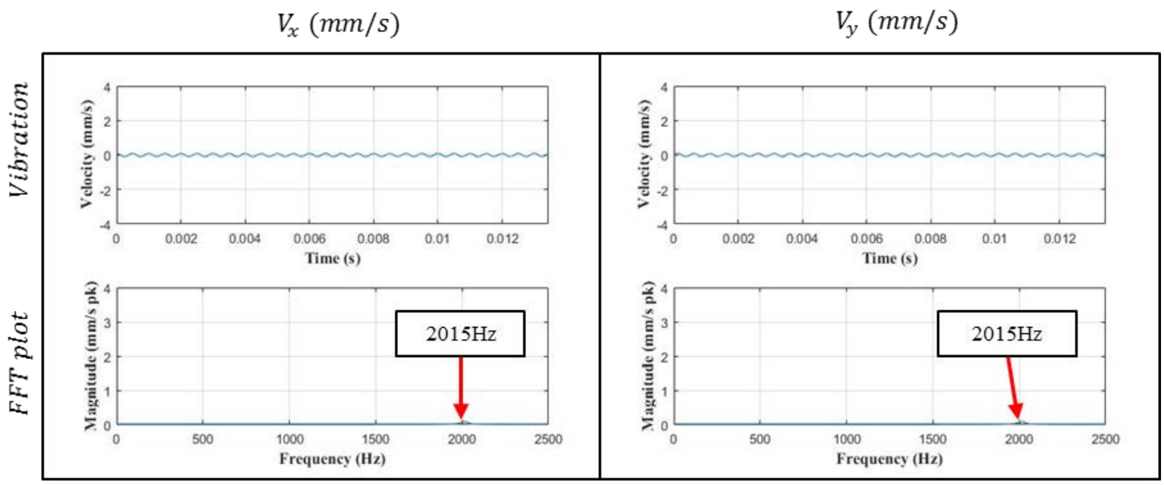

d) Predictions at sensor position B

Figure 5.24 Unbalance responses of sensor positions *A & B* obtained at 120.9k rpm in speed. Supply pressure maintained at ba r.

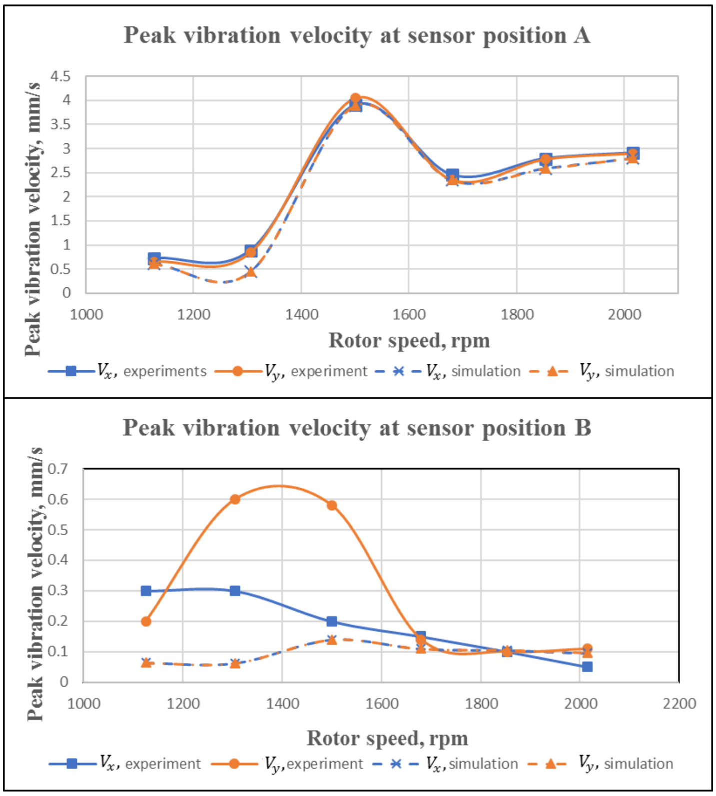

Figure 5.25 Peak synchronous vibration velocities of rotor at sensor position A and B of various rotor speeds

Figure 5.25 compares the sychronous vibration velocities of the rotor measured in experiments (solid lines) and predicted from non-linear transient analysis (dash lines) at the two sensor positions for the test speeds. The presented results, also the results in Appendix E, have a reasonable agreement between experiments and predictions. Both of them show that the vibrations of the rotor are dominated by synchronous component and no self-excited whirl has been spotted. The results also show that there is an increasing on the amplitude of vibration when the rotor speed is close to the critical speed of the system (1400Hz). This could also be found from the watfall plot in Figure 5.23. It is found that the unbalance responses at sensor position B have exceedingly small amplitudes in comparison with that from sensor position A. This can be explained using the shaft responses to out of phase unbalance from non-linear transient analysis shown in Figure 5.26. Figure 5.26 a) illustrates the shaft responses at 0k rpm. The sensor position B is placed at the waist of the conical orbits. When the system work at the rotor speed higher than 1400Hz, for example at 120k rpm, the shaft is likely to working at a bending mode as illustrated in Figure 5.26 b). The maximum displacement of the shaft centre happens at the position close to sensor position A. The shaft responses at sensor position B are still very small. The disparancy between experimental and prediction results is also significant than that of sensor position A. This is because the vibration velocities at this position are low and close to reaching the lower sensiticity limit of the vibrometer. The vibration signals are merged with sensor noise and difficult to be filtered out. From the above analysis, it can be said that, for the tested speeds, the numerical model developed are dynamically equivalent to the rotor bearings system at both sensor positions when compressed air are supplied to the bearings at bar.

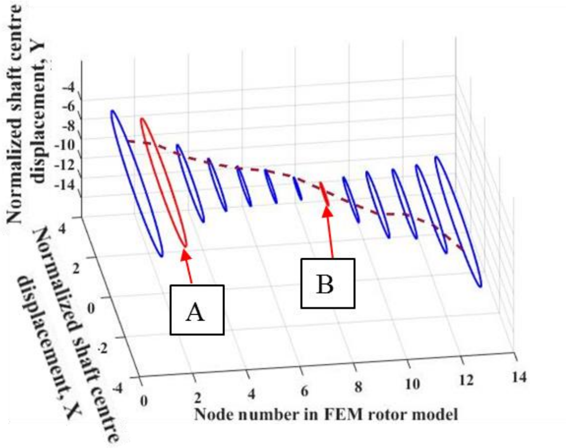

a)

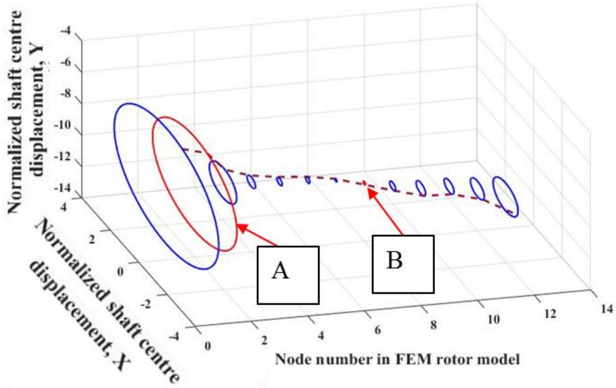

b)

Figure 5.26 The theoretical shaft response of R-1 in **CASE II** with hybrid air bearings in response to out of phase unbalance. The orbits of each node are obtained using the last 50 shaft revolutions in simulation. The dash line indicates positions of the shaft centre at each node at the last simulation time step. Shaft responses at two sensor positions are marked in red. a) rotor speed at 0k rpm. b) rotor speed at 120k rpm

5.4.3 Unbalance responses of hybrid air bearings without supply of compressed air

This section presents the experimental and theoretical studies on unbalance responses of the rotor with hybrid journal air bearings operating without the supply of compressed air. The compressed air supply was manually switched off during the experiments when rotor speed went over 50k rpm. The responses of the rotor were measured at constant speeds of 0k, 80k, 90k, 100k, 110k and 120k rpm respectively.

Figure 5.2 shows the waterfall plot to indicates the responses of the rotor before and after the compressed air supply to hybrid air bearings was switched off. Besides the synchronous component, it is found that a sub-synchronous component quickly builds up when there is no compressed air supply. The frequency of this sub-synchronous component is locked around 820Hz. However, its ratio to the synchronous frequency descends with the rotational speed as shown in Figure 5.28. The appearance of sub-synchronous vibrations indicates the system is unstable as the analysis shown by Figure 5.20 d). The descending whirl frequency ratio was also predicted in Figure 5.20 f).

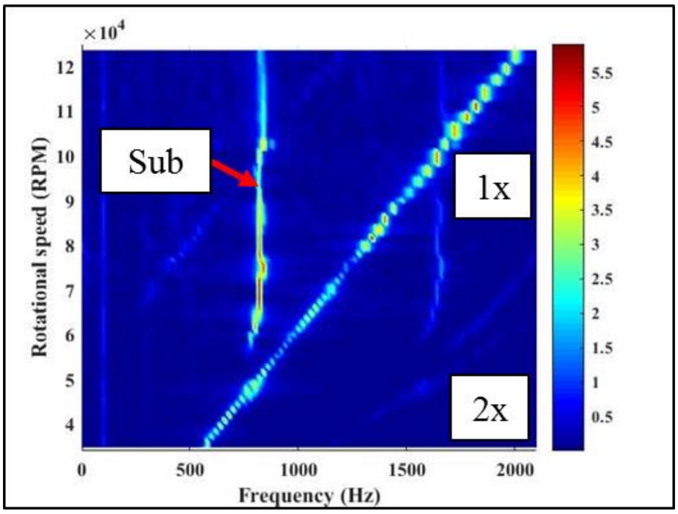

Figure 5.2 Top views of waterfall plots generated from experimental data. Measurements were made at sensor position A in horizontal direction.

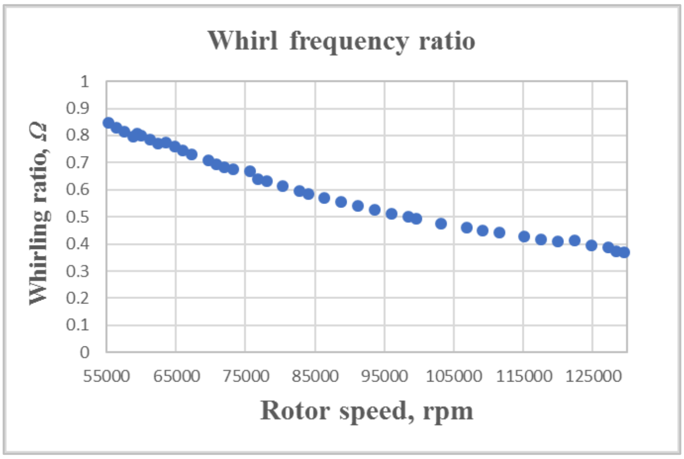

Figure 5.28 Frequency ratio of sub-synchronous vibration to rotational speed at various speeds using the experimental data from Figure 5.2 .

The unbalance responses measured from experiments and ralated simulation results from non-linear transient analysis at the given constant rotor speeds are provided in Appendix F for hybrid air bearings with no compressed air supply. In each group of the figures, the sub- and synchronous vibration frequencies and their peak vibration velocity amplitude are marked on the FFT plot. The simulations were conducted using the actual rotor speed (1x component in frequency spectrum) acquired from experiments. At each speed, the rotor responses were calculated for the first 0 0 shaft revolutions and a steady state was assumed to be achieved at the last 100 revolutions. The response data were collected for the last 100 revolutions and analysed using FFT.

Figure 5.29 shows a case of these measurements and predictions at 98.4k rpm rotor speed for both sensor positions. The results illustrate the instability corresponds to a case of 'half-frequency whirl' (as far as the fundamental frequency to speed ratio is concerned) in both simulation and experiment.

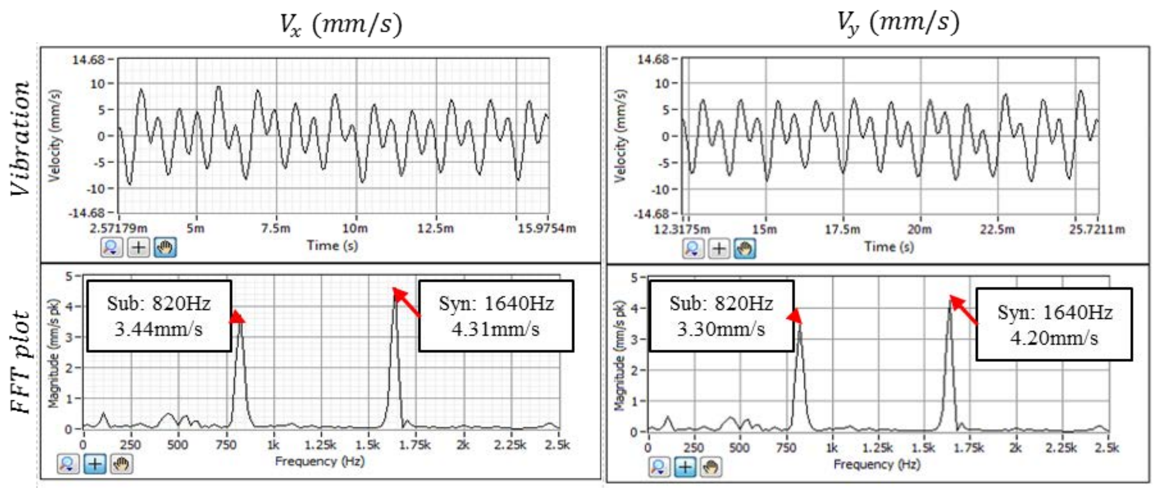

a) Measurements at sensor position A

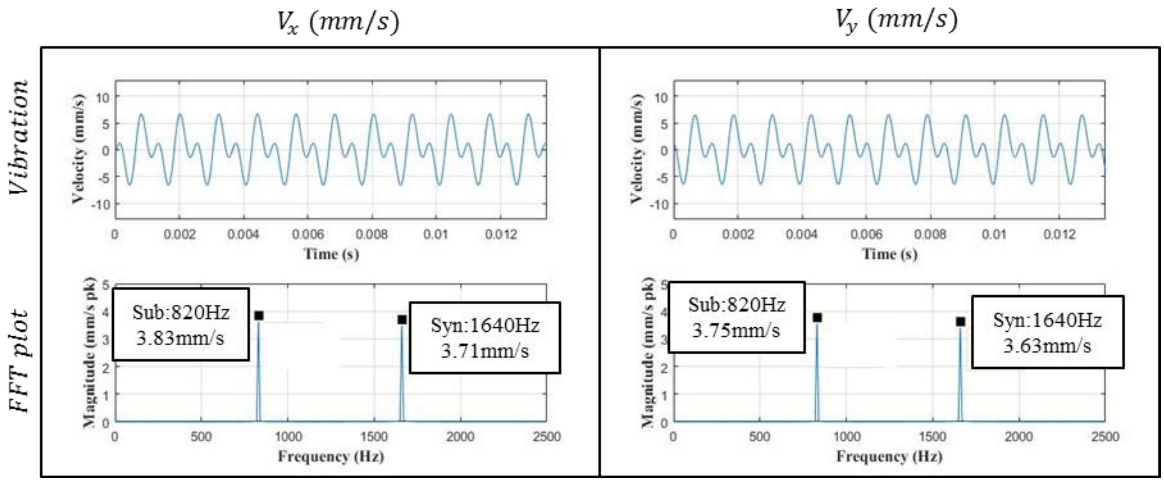

b) Predictions at sensor position A

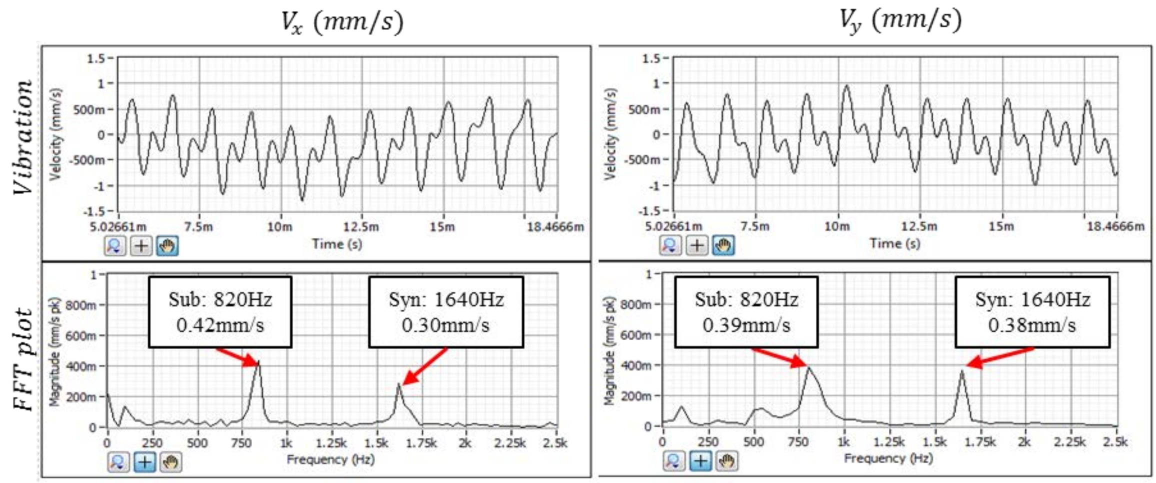

c) Measurements at sensor position B

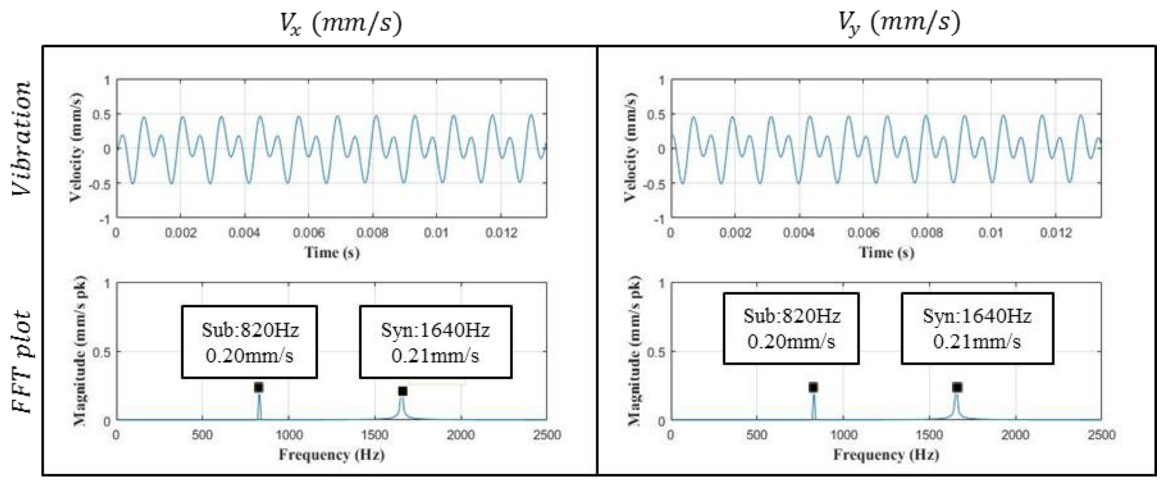

d) Predictions at sensor position B

Figure 5.29 Unbalance responses of sensor positions *A & B* obtained at 98.4k rpm in speed

In Figure 5.30, the peak amplitude of vibration velocities (both sub- and synchronous components) and sub-sychronous whirl frequency ratio are summarized and compared at the constant rotor speeds between experimental and prediction results at the two sensor positions.

Figure 5.30 a) shows the peak amplitude of vibration velocities at sensor position A in horizontal directions. The experimental results are marked as solid lines at various rotor speeds. The blue line is the amplitude of sub-synchronous vibration velocites while the orange line represents the amplitude of syhchronous vibration velocites. The prediction results are marked as discrete points at the rotor speeds at which the simulations were performed (triangle for sub-sychronous and diamond for synchronous). The responses at sensor position B are ploted in Figure 5.30 b) following the same rule. The whirl frequency ratio of sub-synchronous vibrations to rotor speeds are presented in Figure 5.30 c) with prediciton from SESA added. It can be seen that there are good agreement between the simulations and experiments at most test speeds.

At sensor position A, the prediction results clearly reflect the change on amplitude of the vibration velocities, especially the steady state amplitude of sub-synchronous vibration (self-excited whirl). The differences between experimental and predicted synchronous vibration are mainly the result of the extra imbalance introduced by reassembly of a balanced rotor to the test rig. There are only marginal discrepancies at sensor position B. However, this is the result of the vibration velocity at this position being close to the lower sensiticity limit of the vibrometer. The experimental measurements may not be as accurate as that at sensor positon A.

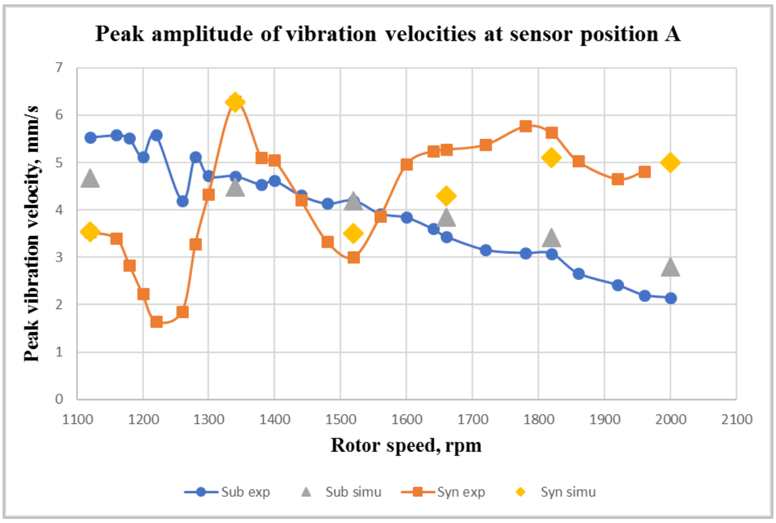

a) Comparisions on the amplitude of peak vibrations velocities at sensor position A.
Blue dots are the amplitude of sub-sychronous vibration velocity measured in experiments.
Orange squares are the amplitude of sychronous vibration velocity measured in experiments
Grey triangles are the predicted amplitude of sub-sychronous vibration velocity.
Yellow diamonds are the predicted amplitude of sub-sychronous vibration velocity.

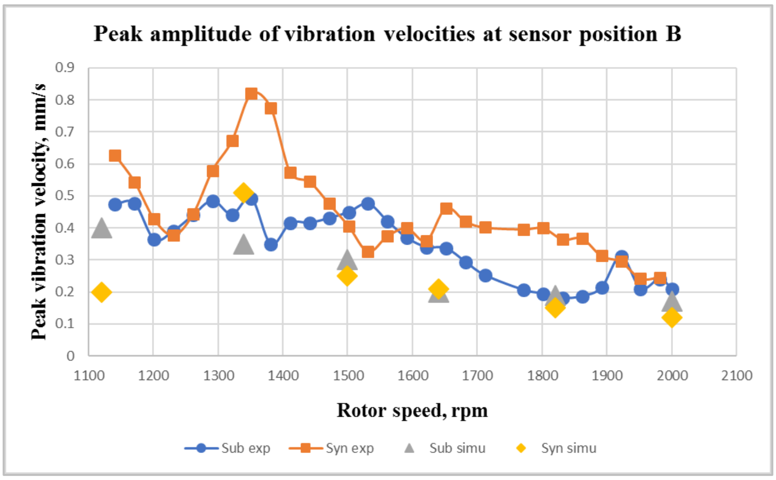

b) Comparisions on the amplitude of peak vibrations velocities at sensor position B.
Blue dots are the amplitude of sub-sychronous vibration velocity measured in experiments.
Orange squares are the amplitude of sychronous vibration velocity measured in experiments
Grey triangles are the predicted amplitude of sub-sychronous vibration velocity.
Yellow diamonds are the predicted amplitude of sub-sychronous vibration velocity.

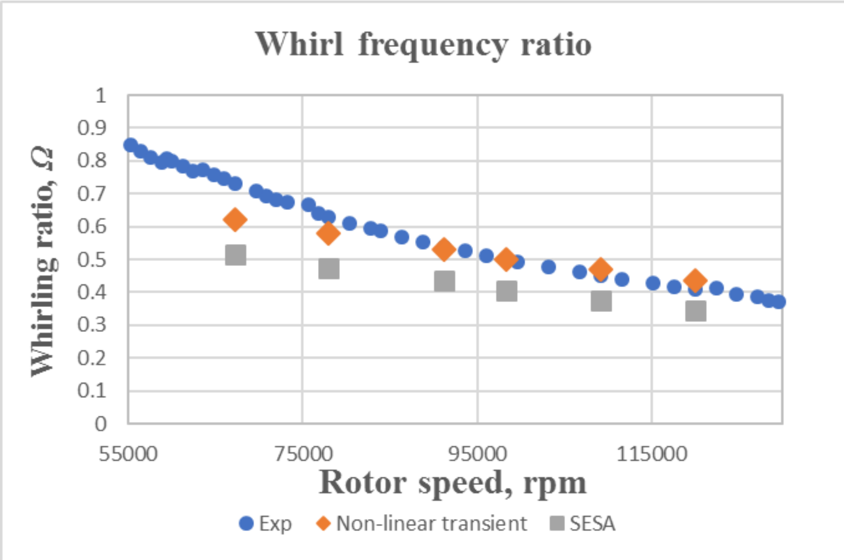

c) The blue dots are experimental observations. Prediction results from non-linear transient analysis are represented by diamonds. Prediction results from SESA are represented by squares

Figure 5.30 Comparisons of prediction results with experimental results. The amplitude of peak vibration velocities of the sub- and sychrounous vibration components at the two sensor positions are compared in a) and b) respectivelly. Plot c) compares the frequency ratio of sub-sychronous vibration components to rotatinal speed.

Meanwhile, predicitons on the whirling frequency ratios of self-excited whirl from non-linear transient analysis have a good agreement with experimental observations, as shown in Figure 5.30 c). The differences between experimental and prediction results for rotor speed from 8k rpm to 120k rpm is less than 9%. The main discrepancy on the whirl frequency ratio occurs at a rotor speed of 6 .2k rpm. At this speed, the sub-sychronous frequency is predicted to be 696Hz while it is observed at 810Hz in experiments, i.e. 14. % in difference. In experiments, the frequency of sub-synchronous vibration is quickly locked at 820Hz. While in the simulations, this frequency ascends with the rotor speed slightly from 696Hz and is locked at 855Hz when the rotor speed goes over 100k rpm. On the other hand, it is found that the whirl frequency ratio varies with speed in the same way between the SESA and non-linear approach, but the whirl ratio predicted by SESA is lower. Althought the whirl frequency ratio observed in experiments is higher than predictions and descends slightly more rapidly, predictions from non-linear transient and SESA have an adequate agrement with experimental results.

The simulations and experiments performed in this section both prove that the proposed hybrid air bearings work well without the supply of compressed air from 60k rpm up to 120k rpm. The non-linear transient analysis performed successfully predicted the frequency and steady state amplitude of self-excited whirl at several test speeds. Predictions on frequency ratio of self-excited whirl from SESA are also acceptable in comparisons with experimental results. It can be said that the numerical analysis proposed (both linear and non-linear analysis) are dynamicaly equivalent to the actural rotor bearing system at the two sensor positions within the given test rotor speed range. Although instability of the rotor bearing system appears when compressed air is switched off, both simulation and experimental results show that is contained within a limited cycle by the bearings and no contacts between rotor and bearings were observed in experiments.

Based on the discussions of unbalnace responses in Section 5.4.2 and 5.4.3, it can be stated that the numerical analysis performed shows the portential to predict rotational performance of a rotor bearing system supported by the proposed hybrid journal air bearings. In general, the linear approach will give predictions in frequency domain, including natural frequenices and frequency ratio of self-excited whirl. The non-linear transient analyis on the other hand can predict the shaft orbits in time domian and is capable of predicting the steady state amplitude of self-excited whirl. Further improvement can be made on the non-linear transient analysis as part of the follow up investigations by considering mounting excitations and non-constant rotation speed (run-up or run down simulations) as discussed in [85].

5.5 Summary

This chapter provides a comprehensive study on hybrid journal air bearings and the rotor structure they support. The finite volume model of hybrid air bearings is presented. The validity of using FVM to model air bearings with herringbone grooves was examined and compared with references. A novel herringbone groove design was adopted to increase the bearing reaction forces of hybrid air bearings at a given equilibrium configuration. The rotational performance was studied using the linear perturbation analysis. The effects of herringbone groove configurations on the equivalent stiffness and damping coefficients of bearing forces at given static equilibrium configurations were investigated. The theoretical studies showed hybrid air bearings had better damping properties in comparison with hydrostatic air bearings. The stability and natural frequencies were analysed for the system in **CASE I & II** with a rotor supported by hybrid air bearings. Non-linear transient analysis was performed with experimental verifications on unbalance responses at two working conditions of hybrid air bearings. In the first working condition, compressed air was supplied to the hybrid air bearings at ba r. Both experimental and prediction results showed that the system was stable and there was no self-excited whirl. In the second working condition, compressed air was supplied initially to lift the rotor at ba r and was switched off once the rotor speed went over 50k rpm. Self-excited whirl was observed in both simulations and experiments when the hybrid air bearings were running without supply of compressed air. The experimental and prediction results were compared and discussed.

CHAPTER 6: CONCLUSIONS AND FUTURE WORK

This chapter summarises the research work of this thesis, highlights important findings, and draw conclusions of the research. It also recommends future work to extend this study.

6.1 Summary

This PhD project was set up to provide a deeper insight into hybrid journal air bearings and explore their possible applications in high speed and mobile micro turbo machinery, such as turbochargers and micro-gas turbine engines. Two main challenges need to be resolved in order to achieve the project aims. One is to develop a valid model to predict the dynamics performance of the hybrid air bearings and the rotor dynamic structure and help the design of hybrid air bearings. The other is to apply the proposed hybrid journal air bearings on a micro turbomachine and verify both the proposed hybrid air bearings and the modelling method through experiments. This PhD thesis presents the research to reach the project's targets.

The research scope covers hydrostatic and hybrid journal air bearings with non-compliant boundaries. The approach adopted combines numerical analysis based on CFD and methodologies in rotor dynamic analysis with experimental verifications of the designs. The stability and natural frequencies of the system are predicted using a linear approach. The unbalance responses are predicted using non-linear transient analysis. Repeated experiments were carried out on a test rig. A rotor taken from a turbocharger was modified to accommodate the required size of hybrid air bearings. The experiments were performed in ambient temperature and no thermal effects were involved at this stage. The experimental and simulation results have an adequate agreement in a rotor speed range from 50k rpm to 120k rpm in the design specifications. The idea to eliminate the reliance on compressed air supply to the bearings at high speeds has been proven working by both simulation and experiments. Air supply to the bearings was switched off at speed of 50k to 60k rpm and the bearings can fully self-suspended and support the rotor to maintain the speed and accelerate up to 120k rpm.

6.2 Conclusions

Through the theoretical and experimental investigation of the hybrid journal air bearings, the objectives of the project have been implemented and the aims have been met. The following conclusions can be drawn from the research:

1. In the theoretical studies on hydrostatic journal air bearings, it is found the bearing reaction forces to static load is determined by the supply pressure. The orifices' diameter and radial clearance have a combined effect on the optimal design. The optimal orifice diameter decreases with the radial clearances. When orifice restrictors with a 100 μm diameter are used, the bearing reaction forces to static load varies sharply with the radial clearance. Orifice restrictors with larger diameters provide a smooth change instead.

2. The linear perturbation analysis on the rotational performance of hydrostatic journal air bearings shows a 'hardening effect' at high rotor speed results in very weak damping. The damping property (indicated by the equivalent damping coefficients) of hydrostatic journal

air bearings with plain orifices cannot be improved effectively by adjusting bearing design parameters such as radial clearance (c), supply pressure (P_s) or orifice diameter (d_0), except increasing the bearing length to diameter ratio (ζ).

3. The numerical modelling approach proposed in this research is valid in predicting natural frequencies and stability of a rotor bearing system with hydrostatic journal air bearings and viscoelastic damp. The unbalance responses of the same system are predicted using non-linear transient analysis from 50k rpm to 100k rpm rotor speed. The experimental and prediction results have a good agreement at the sensor positions where the system responses were measured.

4. In the theoretical studies on hybrid journal air bearings, a novel herringbone groove configuration is proposed and proven effective in improving bearing reaction forces at a given static equilibrium position investigated. The herringbone groove configuration is novel in a way that a cosine spline is used to form the profile of it. The theoretical study shows a maximum 16% increasing on bearing reaction forces in comparison with conventional herringbone groove design. The study also shows the hybrid journal air bearings with different herringbone groove configurations can achieve same bearing reaction forces to static load at the same static equilibrium position and rotational speed. However, their dynamic properties are significantly different with each other.

5. The linear perturbation analysis on the rotational performance of hybrid journal air bearings also shows a 'hardening effect' at high rotor speed. However, the damping property (indicated by the equivalent damping coefficients) of hybrid journal air bearings can be

improved by adjusting multiple herringbone groove configurations with compromise on the stiffness. Increasing supply pressure (P_s) of hybrid journal air bearings can also improve the damping property, which is quite different from hydrostatic journal air bearings. In summary, the damping properties of hybrid journal air bearing can be improved by increasing the maximum groove depth (h_g), grooved area fraction (γ_g) and groove number (G_{num}). At the same time, one can select proper values of groove width ratio (α_g) and groove angle (β_g) to increase the stiffness of the bearing.

6. In the case that no compressed air is supplied to hybrid air bearings, the stability analysis using the linear approach shows the system will be unstable from 20k rpm up to 200k rpm and would be stable afterwards. In experiments, the compressed air supply is switched off when rotor speed goes over 50k rpm. The responses of the system measured at the sensor positions from 0k rpm up to 120k rpm show a synchronous component (from unbalance excitation) and a clear sub-synchronous component around 820Hz (from self-excited whirl). This indicated the system is unstable. The stability predictions from the linear approach within this speed range is valid. Tests at higher speeds are unavailable at this stage, as 120k rpm (or a slight higher speed, e.g.125k rpm) is the limit by means of driving the turbo rotor with compressed air using available facilities. Predictions of stability from 120k rpm onwards need further investigation or proof.

7. Based on the theoretical and experimental work presented in this thesis, the analytical methods (both linear and non-linear) adopted can be used as adequate tools to analyse the rotational performance of a rotor bearing system supported by the hybrid air bearings. The experiments also prove the reliance on compressed air supply of the proposed hybrid journal

air bearings can be reduced at high speeds. With the specifications of the hybrid journal air bearings and the rotor dynamic structure designed in this project, the suggested speeds when compressed air supply can be switched off should be no less than 50k rpm.

6.3 Suggestions for future work

This thesis presents a research effort to explore a type of hybrid air bearings for high speed and portable turbo machinery applications. The results obtained in the research can be regarded as a solid foundation for future work. Future effort is required to extend the related research and to complete the works initiated in this PhD thesis which still need further investigation.

The following is a list of proposed further research topics:

1. Non-linear transient analysis with non-constant rotor speed.

   The current non-linear transient analysis is only valid with constant rotor speed. The responses of the rotor bearing system during run-up and run-down is not fully clear. This can be done by improving the rotor bearing system model and perform further theoretical studies. Similar studies were found in [85] which could be a starting point.

2. Investigations on the performance of the rotor bearing system with thermal effect being considered.

   The current theoretical and experimental study are all based on constant temperature, more specifically the lab temperature ($20°C$ to $25°C$). This is an important limitation on apply the proposed hybrid air bearings on realistic micro turbomachinery, which normally work in environment that involves high temperature. This could be further investigated theoretically by considering the shaft expansion in the numerical model. Experiments are also possible, for example, tests could be performed by means of driving the turbo rotor using heated air.

3. Investigations on the stability of the rotor bearing system supported by hybrid air bearings at higher speeds (from 130k rpm and upwards).

   In the static equilibrium stability analysis of the rotor bearing system, it is found there would be shift in the self-excited whirl frequency. This should also be observed in experiments if proper condition applies. The stability analysis on the rotor bearing system with hybrid air bearings in a case study presented in the thesis (**CASE II**) also shows the system can be stabilized even with compressed air switched off if the rotor speed goes over 200k rpm. This prediction can be validated if tests at higher speeds are available. In current experiments, the maximum rotor speed is limited by the size of compressed air reservoir (350 Litres), which stores compressed air to drive the turbo rotor in the test rig. Increasing the size of the reservoir to 900 Litres could remove this limit.

4. Investigations on the mode of rotor bearing system supported by hybrid air bearings.

   The mode shape of a rotor bearing system could be identified by measuring the rotor responses at multiple shaft locations. This could be beneficial to further verify/improve the current numerical model used in the non-linear transient analysis.

APPENDIX A

In this project, numerical model of hydrostatic journal air bearings is based on the finite difference method introduced in Chapter 3. The finite difference transformation of the Reynolds Equation is linearized using Newton's method to improve the numerical stability and converge rate. Equation 3.28 is the resulting system after applying Newton's method. Its coefficients are given here:

$$a_{i,j} = \frac{-2P_{i,j}{H_{i,j}}^3}{\Delta\theta^2} + {H_{i,j}}^3 (\frac{\partial^2 P}{\partial\theta^2})_{i,j} + 3{H_{i,j}}^2 \left(\frac{\partial H}{\partial\theta}\right)_{i,j} (\frac{\partial P}{\partial\theta})_{i,j} - \frac{2P_{i,j}{H_{i,j}}^2}{\Delta Z^2} + {H_{i,j}}^3 \left(\frac{\partial^2 P}{\partial Z^2}\right)_{i,j} - 6\left(\frac{\partial H}{\partial\theta}\right)_{i,j} \qquad A\text{-}1$$

$$b_{i,j} = \frac{P_{i,j}{H_{i,j}}^3}{\Delta Z^2} - \frac{{H_{i,j}}^3 (\frac{\partial P}{\partial\theta})_{i,j}}{\Delta Z} \qquad A\text{-}2$$

$$c_{i,j} = \frac{P_{i,j}{H_{i,j}}^3}{\Delta Z^2} + \frac{{H_{i,j}}^3 (\frac{\partial P}{\partial\theta})_{i,j}}{\Delta Z} \qquad A\text{-}3$$

$$d_{i,j} = \frac{P_{i,j}{H_{i,j}}^3}{\Delta\theta^2} - \frac{{H_{i,j}}^3 \left(\frac{\partial P}{\partial\theta}\right)_{i,j}}{\Delta\theta} - \frac{3{H_{i,j}}^2 P_{i,j} \left(\frac{\partial H}{\partial\theta}\right)_{i,j}}{2\Delta\theta} + \frac{6H_{i,j}}{2\Delta\theta} \qquad A\text{-}4$$

$$d_{i,j} = \frac{P_{i,j}{H_{i,j}}^3}{\Delta\theta^2} - \frac{{H_{i,j}}^3\left(\frac{\partial P}{\partial\theta}\right)_{i,j}}{\Delta\theta} - \frac{3{H_{i,j}}^2 P_{i,j}\left(\frac{\partial H}{\partial\theta}\right)_{i,j}}{2\Delta\theta} + \frac{6H_{i,j}}{2\Delta\theta} \tag{A-5}$$

$$e_{i,j} = \frac{P_{i,j}{H_{i,j}}^3}{\Delta\theta^2} + \frac{{H_{i,j}}^3\left(\frac{\partial P}{\partial\theta}\right)_{i,j}}{\Delta\theta} + \frac{3{H_{i,j}}^2 P_{i,j}\left(\frac{\partial H}{\partial\theta}\right)_{i,j}}{2\Delta\theta} - \frac{6H_{i,j}}{2\Delta\theta} \tag{A-6}$$

$$Con_{i,j} = P_{i,j}{H_{i,j}}^3\left[\left(\frac{\partial^2 P}{\partial\theta^2}\right)_{i,j} + \left(\frac{\partial^2 P}{\partial Z^2}\right)_{i,j}\right] + {H_{i,j}}^3\left[\left(\frac{\partial P}{\partial\theta}\right)_{i,j}^2 + \left(\frac{\partial P}{\partial Z}\right)_{i,j}^2\right]$$
$$+ 3{H_{i,j}}^2 P_{i,j}\left(\frac{\partial H}{\partial\theta}\right)_{i,j}\left(\frac{\partial P}{\partial\theta}\right)_{i,j} - 6H_{i,j}\left(\frac{\partial P}{\partial\theta}\right)_{i,j} - 6P_{i,j}\left(\frac{\partial H}{\partial\theta}\right)_{i,j} \tag{A-7}$$

where i and j denotes the point at i^{th} row and j^{th} column in a finite difference mesh.

The partial differential terms in A - 1 to A - a re expressed below using the second order central finite difference formulae.

$$\left(\frac{\partial H}{\partial\theta}\right)_{i,j} = \frac{H_{i,j+1} - H_{i,j-1}}{2\Delta\theta} \tag{A-8}$$

$$\left(\frac{\partial P}{\partial\theta}\right)_{i,j} = \frac{P_{i,j+1} - P_{i,j-1}}{2\Delta\theta} \tag{A-9}$$

$$\left(\frac{\partial P}{\partial Z}\right)_{i,j} = \frac{P_{i+1,j} - P_{i-1,j}}{2\Delta Z} \qquad \textit{A-10}$$

$$\left(\frac{\partial^2 P}{\partial \theta^2}\right)_{i,j} = \frac{P_{i,j+1} + P_{i,j-1} - 2P_{i,j}}{\Delta \theta^2} \qquad \textit{A-11}$$

$$\left(\frac{\partial^2 P}{\partial Z^2}\right)_{i,j} = \frac{P_{i+1,j} + P_{i-1,j} - 2P_{i,j}}{\Delta Z^2} \qquad \textit{A-12}$$

APPENDIX B

In this project, numerical model of hybrid journal air bearings is based on the finite volume method (FVM) introduced in Chapter 3. To perform the finite volume transformation, the Reynolds Equation was integrated using Green's theorem along the boundaries of the controlled volume surrounding a node on the meshed surface.

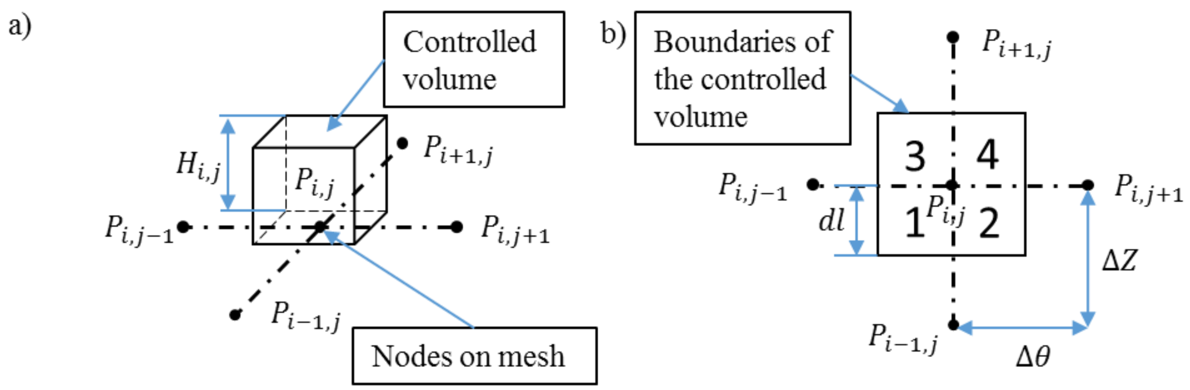

Figure B.1 a) Controlled volume surrounding a node in FVM approach b) Projected view of the controlled volume on a meshed surface

The finite volume was divided into four cells, as shown in Figure B.1 b). $\overline{Q_{\theta i}}$ and $\overline{Q_{Zi}}$ ($i =$ 1,2,3,4) are integrals of the Reynold equation along the boundaries of the controlled volume in θ and Z direction.

Expressions of $\overline{Q_{\theta i}}$ and $\overline{Q_{Zi}}$ (I = 1,2,3,4) are given here:

$$\overline{Q_{\theta 1}} = [-P_{i,j-1/2}H_{i-,j-1/2}{}^{3}\frac{P_{i,j} - P_{i,j-1}}{\Delta\theta} + \Lambda P_{i,j-\frac{1}{2}}H_{i-,j-\frac{1}{2}}]\frac{\Delta Z}{2}$$ *B-1*

$$\overline{Q_{Z1}} = -P_{i-1/2,j}H_{i-,j-1/2}{}^{3}\frac{P_{i,j} - P_{i-1,j}}{\Delta Z}\frac{\Delta\theta}{2}$$ *B-2*

$$\overline{Q_{\theta 2}} = [-P_{i,j+1/2}H_{i-,j+1/2}{}^{3}\frac{P_{i,j+1} - P_{i,j}}{\Delta\theta} + \Lambda P_{i,j+\frac{1}{2}}H_{i-,j+\frac{1}{2}}]\frac{\Delta Z}{2}$$ *B-3*

$$\overline{Q_{Z2}} = -P_{i-1/2,j}H_{i-,j+1/2}{}^{3}\frac{P_{i,j+1} - P_{i,j}}{\Delta Z}\frac{\Delta\theta}{2}$$ *B-4*

$$\overline{Q_{\theta 3}} = [-P_{i,j-1/2}H_{i-,j-1/2}{}^{3}\frac{P_{i,j} - P_{i,j-1}}{\Delta\theta} + \Lambda P_{i,j-\frac{1}{2}}H_{i+,j-\frac{1}{2}}]\frac{\Delta Z}{2}$$ *B-5*

$$\overline{Q_{Z3}} = -P_{i+1/2,j}H_{i+,j-1/2}{}^{3}\frac{P_{i+1,j} - P_{i,j}}{\Delta Z}\frac{\Delta\theta}{2}$$ *B-6*

$$\overline{Q_{\theta 4}} = [-P_{i,j+1/2}H_{i-,j+1/2}{}^{3}\frac{P_{i,j+1} - P_{i,j}}{\Delta\theta} + \Lambda P_{i,j+\frac{1}{2}}H_{i+,j+\frac{1}{2}}]\frac{\Delta Z}{2}$$ *B-7*

$$\overline{Q_{Z4}} = -P_{i+1/2,j}H_{i+,j+1/2}{}^{3}\frac{P_{i+1,j} - P_{i,j}}{\Delta Z}\frac{\Delta\theta}{2}$$ *B-8*

Equation 3.34 is the finite volume transformation of the Reynolds Equation. Its coefficients are expressed below:

$$A_{i,j} = \frac{{H_{i-,j-1/2}}^3}{4\Delta\theta}\Delta Z + \frac{{H_{i-,j+1/2}}^3}{4\Delta\theta}\Delta Z + \frac{{H_{i+,j-1/2}}^3}{4\Delta\theta}\Delta Z + \frac{{H_{i+,j+1/2}}^3}{4\Delta\theta}\Delta Z$$
$$+ \frac{{H_{i-,j-1/2}}^3}{4\Delta Z}\Delta\theta + \frac{{H_{i-,j+1/2}}^3}{4\Delta Z}\Delta\theta + \frac{{H_{i+,j-1/2}}^3}{4\Delta Z}\Delta\theta \qquad B\text{-}9$$
$$+ \frac{{H_{i+,j+1/2}}^3}{4\Delta Z}\Delta\theta$$

$$B_{i,j} = \Lambda\left(-\frac{{H_{i-,j-\frac{1}{2}}}^3}{4}\Delta Z - \frac{{H_{i+,j-\frac{1}{2}}}^3}{4}\Delta Z + \frac{{H_{i+,j-\frac{1}{2}}}^3}{4}\Delta Z + \frac{{H_{i+,j+1/2}}^3}{4}\Delta Z\right) \qquad B\text{-}10$$

$$C1_{i,j} = -\left(\frac{{H_{i-,j-\frac{1}{2}}}^3}{4\Delta\theta}\Delta Z + \frac{{H_{i-,j+\frac{1}{2}}}^3}{4\Delta\theta}\Delta Z\right) \qquad B\text{-}11$$

$$C2_{i,j} = -\left(\frac{{H_{i+,j-\frac{1}{2}}}^3}{4\Delta\theta}\Delta Z + \frac{{H_{i+,j+\frac{1}{2}}}^3}{4\Delta\theta}\Delta Z\right) \qquad B\text{-}12$$

$$D1_{i,j} = -\left(\frac{{H_{i-,j-\frac{1}{2}}}^3}{4\Delta Z}\Delta\theta + \frac{{H_{i-,j+1/2}}^3}{4\Delta Z}\Delta\theta\right) \qquad B\text{-}13$$

$$D2_{i,j} = -\left(\frac{{H_{i+,j-\frac{1}{2}}}^3}{4\Delta Z}\Delta\theta + \frac{{H_{i+,j+1/2}}^3}{4\Delta Z}\Delta\theta\right) \qquad B\text{-}14$$

$$E1_{i,j} = \Lambda\left(-\frac{{H_{i-,j-1/2}}^3}{4}\Delta Z - \frac{{H_{i+,j-1/2}}^3}{4}\Delta Z\right) \qquad B\text{-}15$$

$$E2_{i,j} = \Lambda(\frac{{H_{i+,j-\frac{1}{2}}}^3}{4}\Delta Z + \frac{{H_{i+,j+1/2}}^3}{4}\Delta Z) \quad B\text{-}16$$

APPENDIX C

Timenshenko Beam Element in FEM

The Timoshenko finite element matrices for homogeneous beam elements are listed here. By assuming with thin element, the diametral moment of inertia $I_d = \rho A_b ({D_o}^2 + {D_i}^2)/16$ and polar moment of inertia $I_p = 2I_d$

Shape factor:

$$\kappa = \frac{6(1+\nu)\left(1+(D_i/D_o)^2\right)^2}{(7+6\nu)\left(1+(D_i/D_o)^2\right)^2+(20+12\nu)(D_i/D_o)^2}$$

where ν is the Poission ratio, D_i is element inner diameter and D_o is element outer diameter.

Transverse shear factor:

$$\emptyset = \frac{12EI}{\kappa A_b G {L_b}^2}$$

where E is Young's modulus, G the shear modulus, I the polar moment of inertia, A_b the cross-section area and L_b the element length.

Element translational mass matrix, $\boldsymbol{M_e}^{\boldsymbol{t}}$

$\boldsymbol{M_{e0}^t} =$

$$\frac{\rho A_b L_b}{420(1+\emptyset)^2}\begin{bmatrix} 156 & 0 & 0 & 22L_b & 54 & 0 & 0 & -13L_b \\ 0 & 156 & -22L_b & 0 & 0 & 54 & 13L_b & 0 \\ 0 & -22L_b & 4L_b^2 & 0 & 0 & -13L_b & -3L_b^2 & 0 \\ 22L_b & 0 & 0 & 4L_b^2 & 13L_b & 0 & 0 & -3L_b^2 \\ 54 & 0 & 0 & 13L_b & 156 & 0 & 0 & -22L_b \\ 0 & 54 & -13L_b & 0 & 0 & 156 & 22L_b & 0 \\ 0 & 13L_b & -3L_b^2 & 0 & 0 & 22L_b & 4L_b^2 & 0 \\ -13L_b & 0 & 0 & -3L_b^2 & -22L_b & 0 & 0 & 4L_b^2 \end{bmatrix}$$

$\boldsymbol{M_{e1}^t} = \dfrac{\rho A_b L_b}{420(1+\emptyset)^2} *$

$$\begin{bmatrix} 394 & 0 & 0 & 38.5L_b & 126 & 0 & 0 & -31.5L_b \\ 0 & 294 & -38.5L_b & 0 & 0 & 126 & 31.5L_b & 0 \\ 0 & -38.5L_b & 7L_b^2 & 0 & 0 & -31.5L_b & -7L_b^2 & 0 \\ 38.5L_b & 0 & 0 & 7L_b^2 & 31.5L_b & 0 & 0 & -7L_b^2 \\ 126 & 0 & 0 & 31.5L_b & 294 & 0 & 0 & -38.5L_b \\ 0 & 126 & -31.5L_b & 0 & 0 & 294 & 38.5L_b & 0 \\ 0 & 31.5L_b & -7L_b^2 & 0 & 0 & 38.5L_b & 7L_b^2 & 0 \\ -31.5L_b & 0 & 0 & -7L_b^2 & -38.5L_b & 0 & 0 & 7L_b^2 \end{bmatrix}$$

$\boldsymbol{M_{e2}^t} = \dfrac{\rho A_b L_b}{420(1+\emptyset)^2} *$

$$\begin{bmatrix} 140 & 0 & 0 & 17.5L_b & 70 & 0 & 0 & -17.5L_b \\ 0 & 140 & -17.5L_b & 0 & 0 & 70 & 17.5L_b & 0 \\ 0 & -17.5L_b & 3.5L_b^2 & 0 & 0 & -17.5L_b & -3.5L_b^2 & 0 \\ 17.5L_b & 0 & 0 & 3.5L_b^2 & 17.5L_b & 0 & 0 & -3.5L_b^2 \\ 70 & 0 & 0 & 17.5L_b & 140 & 0 & 0 & -17.5L_b \\ 0 & 70 & -17.5L_b & 0 & 0 & 140 & 17.5L_b & 0 \\ 0 & 17.5L_b & -3.5L_b^2 & 0 & 0 & 17.5L_b & 3.5L_b^2 & 0 \\ -17.5L_b & 0 & 0 & -3.5L_b^2 & -17.5L_b & 0 & 0 & 3.5L_b^2 \end{bmatrix}$$

$$\boldsymbol{M_e}^{\boldsymbol{t}} = \boldsymbol{M_{e0}^t} + \emptyset \boldsymbol{M_{e1}^t} + \emptyset^2 \boldsymbol{M_{e2}^t}$$

Element rotational mass matrix, $\boldsymbol{M_e}^r$

$\boldsymbol{M^r_{e0}} =$

$$\frac{I_d}{30L_b(1+\emptyset)^2}\begin{bmatrix} 36 & 0 & 0 & 3L_b & -36 & 0 & 0 & 3L_b \\ 0 & 36 & -3L_b & 0 & 0 & -36 & -3L_b & 0 \\ 0 & -3L_b & 4L_b^2 & 0 & 0 & 3L_b & -L_b^2 & 0 \\ 3L_b & 0 & 0 & 4L_b^2 & -3L_b & 0 & 0 & -L_b^2 \\ -36 & 0 & 0 & -3L_b & 36 & 0 & 0 & -3L_b \\ 0 & -36 & 3L_b & 0 & 0 & 36 & 3L_b & 0 \\ 0 & -3L_b & -L_b^2 & 0 & 0 & 3L_b & 4L_b^2 & 0 \\ 3L_b & 0 & 0 & -L_b^2 & -3L_b & 0 & 0 & 4L_b^2 \end{bmatrix}$$

$\boldsymbol{M^r_{e1}} =$

$$\frac{I_d}{30L_b(1+\emptyset)^2}\begin{bmatrix} 0 & 0 & 0 & -15L_b & 0 & 0 & 0 & -15L_b \\ 0 & 0 & 15L_b & 0 & 0 & 0 & 15L_b & 0 \\ 0 & 15L_b & 5L_b^2 & 0 & 0 & -15L_b & -5L_b^2 & 0 \\ -15L_b & 0 & 0 & 5L_b^2 & 15L_b & 0 & 0 & -5L_b^2 \\ 0 & 0 & 0 & 15L_b & 0 & 0 & 0 & -15L_b \\ 0 & 0 & -15L_b & 0 & 0 & 0 & -15L_b & 0 \\ 0 & 15L_b & -5L_b^2 & 0 & 0 & -15L_b & 5L_b^2 & 0 \\ -15L_b & 0 & 0 & -5L_b^2 & -15L_b & 0 & 0 & 5L_b^2 \end{bmatrix}$$

$\boldsymbol{M^r_{e2}} =$

$$\frac{I_d}{30L_b(1+\emptyset)^2}\begin{bmatrix} 0 & 0 & 0 & 0 & 0 & 0 & 0 & 0 \\ 0 & 0 & 0 & 0 & 0 & 0 & 0 & 0 \\ 0 & 0 & 10L_b^2 & 0 & 0 & 0 & 5L_b^2 & 0 \\ 0 & 0 & 0 & 10L_b^2 & 0 & 0 & 0 & 5L_b^2 \\ 0 & 0 & 0 & 0 & 0 & 0 & 0 & 0 \\ 0 & 0 & 0 & 0 & 0 & 0 & 0 & 0 \\ 0 & 0 & 5L_b^2 & 0 & 0 & 0 & 10L_b^2 & 0 \\ 0 & 0 & 0 & 5L_b^2 & 0 & 0 & 0 & 10L_b^2 \end{bmatrix}$$

$$\boldsymbol{M_e}^r = \boldsymbol{M^r_{e0}} + \emptyset\boldsymbol{M^r_{e1}} + \emptyset^2\boldsymbol{M^r_{e2}}$$

Element gyroscopic matrix, $\boldsymbol{G_e}$

$\boldsymbol{G_{e0}} =$

$$\frac{I_p}{30L_b}\begin{bmatrix} 0 & -36 & 3L_b & 0 & 0 & 36 & 3L_b & 0 \\ 36 & 0 & 0 & 3L_b & -36 & 0 & 0 & 3L_b \\ -3L_b & 0 & 0 & -4L_b^2 & 3L_b & 0 & 0 & L_b^2 \\ 0 & -3L_b & 4L_b^2 & 0 & 0 & 3L_b & -L_b^2 & 0 \\ 0 & 36 & -3L_b & 0 & 0 & -36 & -3L_b & 0 \\ -36 & 0 & 0 & -3L_b & 36 & 0 & 0 & 3L_b \\ -3L_b & 0 & 0 & L_b^2 & 3L_b & 0 & 0 & -4L_b^2 \\ 0 & -3L_b & -L_b^2 & 0 & 0 & 3L_b & 4L_b^2 & 0 \end{bmatrix}$$

$\boldsymbol{G_{e1}} =$

$$\frac{I_p}{30L_b}\begin{bmatrix} 0 & 0 & -15L_b & 0 & 0 & 0 & -15L_b & 0 \\ 0 & 0 & 0 & -15L_b & 0 & 0 & 0 & -15L_b \\ 15L_b & 0 & 0 & -5L_b^2 & -15L_b & 0 & 0 & 5L_b^2 \\ 0 & 15L_b & 5L_b^2 & 0 & 0 & -15L_b & -5L_b^2 & 0 \\ 0 & 0 & 15L_b & 0 & 0 & 0 & 15L_b & 0 \\ 0 & 0 & 0 & 15L_b & 0 & 0 & 0 & 15L_b \\ 15L_b & 0 & 0 & 5L_b^2 & -15L_b & 0 & 0 & -5L_b^2 \\ 0 & 15L_b & -5L_b^2 & 0 & 0 & -15L_b & 5L_b^2 & 0 \end{bmatrix}$$

$\boldsymbol{G_{e2}} =$

$$\frac{I_p}{30L_b}\begin{bmatrix} 0 & 0 & 0 & 0 & 0 & 0 & 0 & 0 \\ 0 & 0 & 0 & 0 & 0 & 0 & 0 & 0 \\ 0 & 0 & 0 & 10L_b^2 & 0 & 0 & 0 & -5L_b^2 \\ 0 & 0 & 10L_b^2 & 0 & 0 & 5L_b & 5L_b^2 & 0 \\ 0 & 0 & 0 & 0 & 0 & 0 & 0 & 0 \\ 0 & 0 & 0 & -5L_b & 0 & 0 & 0 & 0 \\ 0 & 0 & 0 & -5L_b^2 & 0 & 0 & 0 & -10L_b^2 \\ 0 & 0 & 5L_b^2 & 0 & 0 & 0 & 10L_b^2 & 0 \end{bmatrix}$$

$$\boldsymbol{G_e} = \boldsymbol{G_{e0}} + \emptyset \boldsymbol{G_{e1}} + \emptyset^2 \boldsymbol{G_{e2}}$$

Element stiffness matrix, $\boldsymbol{K_e}$

$\boldsymbol{K_{e0}} =$

$$\frac{EI}{L_b^3(1+\emptyset)}\begin{bmatrix} 12 & 0 & 0 & 6L_b & -12 & 0 & 0 & 6L_b \\ 0 & 12 & -6L_b & 0 & 0 & -12 & -6L_b & 0 \\ 0 & -6L_b & 4L_b^2 & 0 & 0 & 6L_b & 2L_b^2 & 0 \\ 6L_b & 0 & 0 & 4L_b^2 & -6L_b & 0 & 0 & 2L_b^2 \\ -12 & 0 & 0 & -6L_b & 12 & 0 & 0 & -6L_b \\ 0 & -12 & 6L_b & 0 & 0 & 12 & 6L_b & 0 \\ 0 & -6L_b & 2L_b^2 & 0 & 0 & 6L_b & 4L_b^2 & 0 \\ 6L_b & 0 & 0 & 2L_b^2 & -6L_b & 0 & 0 & 4L_b^2 \end{bmatrix}$$

$\boldsymbol{K_{e1}} =$

$$\frac{EI}{L_b^3(1+\emptyset)}\begin{bmatrix} 0 & 0 & 0 & 0 & 0 & 0 & 0 & 0 \\ 0 & 0 & 0 & 0 & 0 & 0 & 0 & 0 \\ 0 & 0 & L_b^2 & 0 & 0 & 0 & -L_b^2 & 0 \\ 0 & 0 & 0 & L_b^2 & 0 & 0 & 0 & -L_b^2 \\ 0 & 0 & 0 & 0 & 0 & 0 & 0 & 0 \\ 0 & 0 & 0 & 0 & 0 & 0 & 0 & 0 \\ 0 & 0 & -L_b^2 & 0 & 0 & 0 & L_b^2 & 0 \\ 0 & 0 & 0 & -L_b^2 & 0 & 0 & 0 & L_b^2 \end{bmatrix}$$

$$\boldsymbol{K_e} = \boldsymbol{K_{e0}} + \emptyset \boldsymbol{K_{e1}}$$

Assembly of the element matrices into global matrix

The element mass, stiffness and damping matrices are assembled into the global matrix following the routine introduced in [84]. The Matlab toolbox Rotor Software V1 are used as reference. Figure C-1 gives the schematic illustration of the assembling process on global stiffness matrix using a model with 4 elements (5 nodes) as an example. $[K_{ei}]$ (i = 1,2,3,4) is the element stiffness matrix as shown above. $[K_s]$ is the global stiffness matrix of the shaft model. The process is the same for other element matrices.

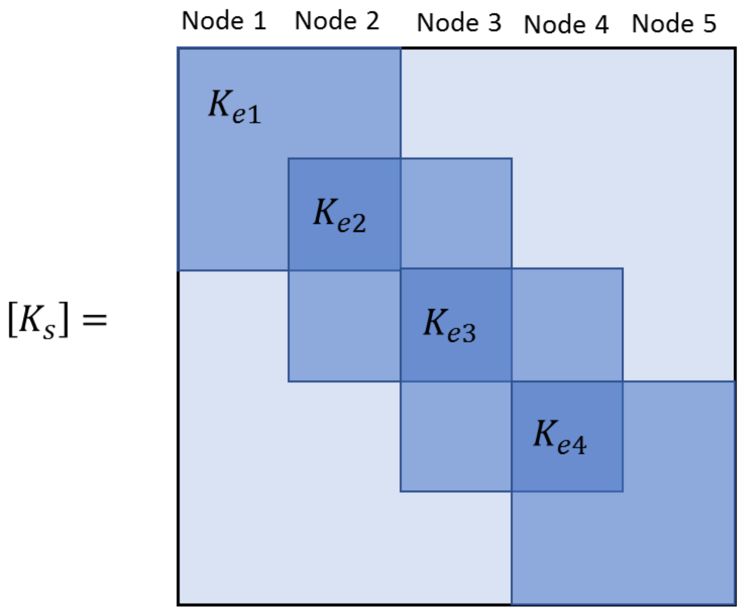

Figure C-1 Assembling the element stiffness matrix to the global stiffness matrix of the shaft model [84].

Assembling of the rotor bearing system:

CASE I: Linear rotor model with linear bearing model

The process of adding equivalent stiffness coefficients into the rotor bearing system of **CASE I** is demonstrated in Figure C-2 and C-3 using the aforementioned 4 elements rotor model. The linear bearing is assumed to be add to the location of Node 2 and Node 4 The process is the same to the system damping matrix $[C_{sys\_1}]$.

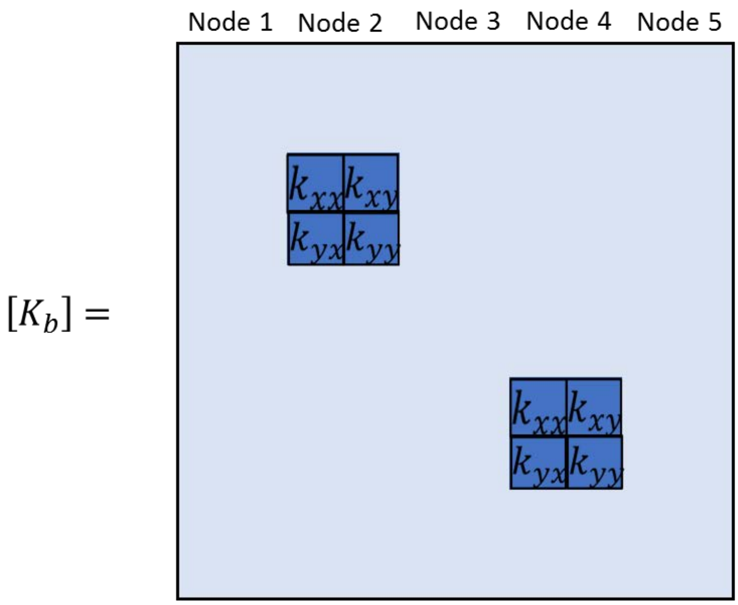

Figure C-2 Bearing stiffness matrix used in the assembling of the rotor bearing system in **CASE I** when linear bearing model is used

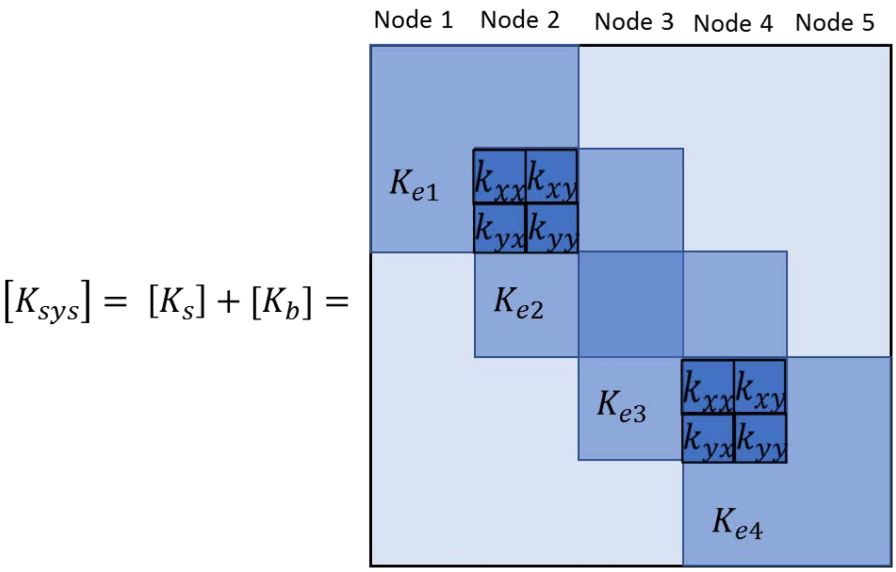

Figure C-3 The rotor bearing system stiffness matrix of **CASE I** after assembly the bearing stiffness matrix

CASE II: Linear rotor model with linear bearing and viscoelastic support

The assembly process of **CASE II** was introduced in [84]. The overall process is similar to **CASE I.** The bearing stiffness matrix (as well as the damping matrix) are first assembled into the two sub systems: Sub-system 1 is rotor with linear bearing model; Sub-system 2 is linear bearing model with model of bearing sleeve and linear O-ring model. The two sub-systems are then assembled together as shown in Section 4.4.3.

APPENDIX D

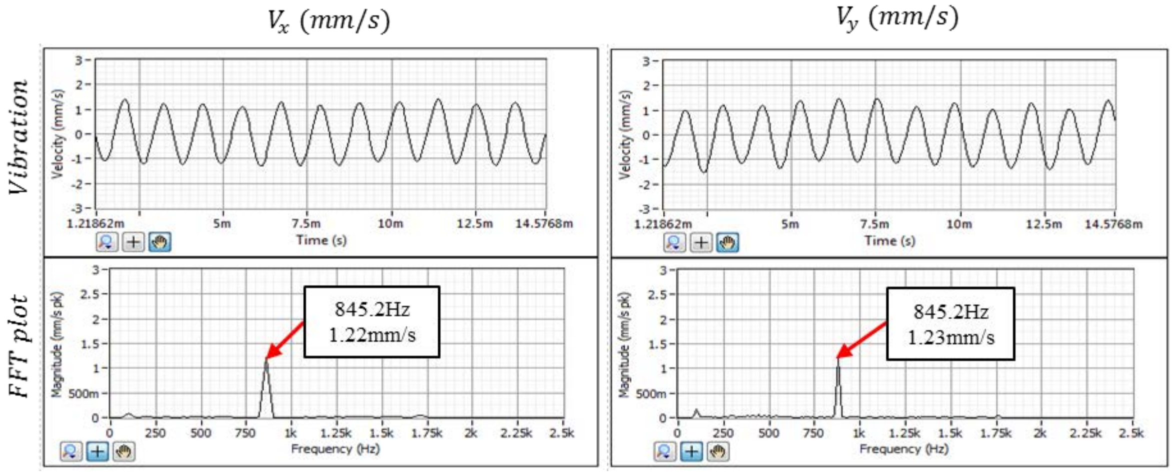

a) Measurements at sensor position A

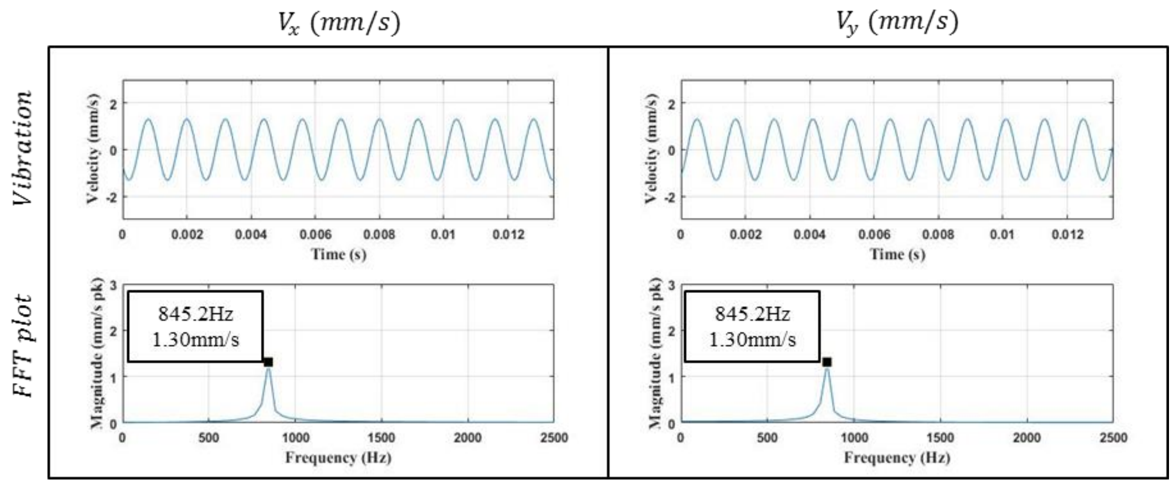

b) Predictions at sensor position A

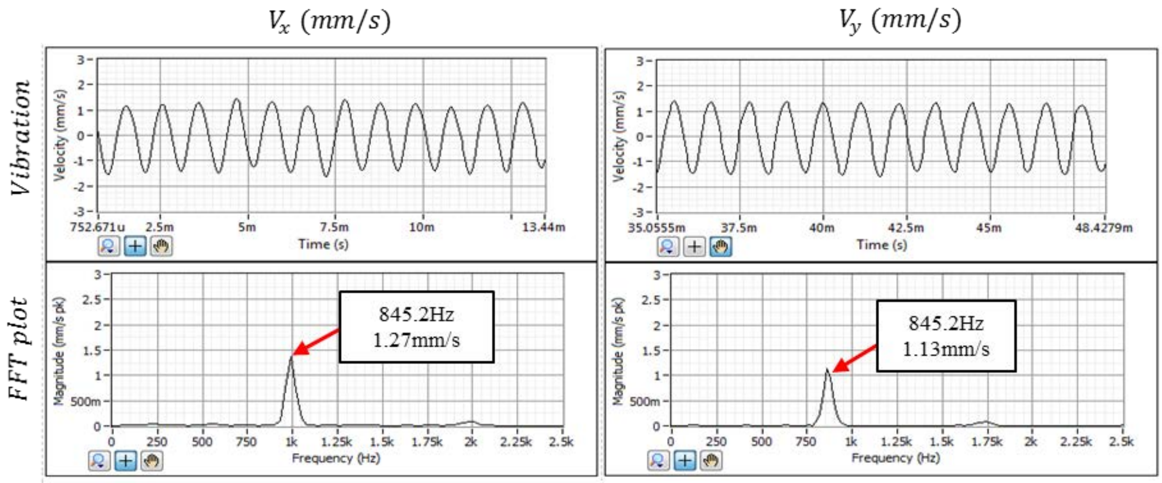

c) Measurements at sensor position B

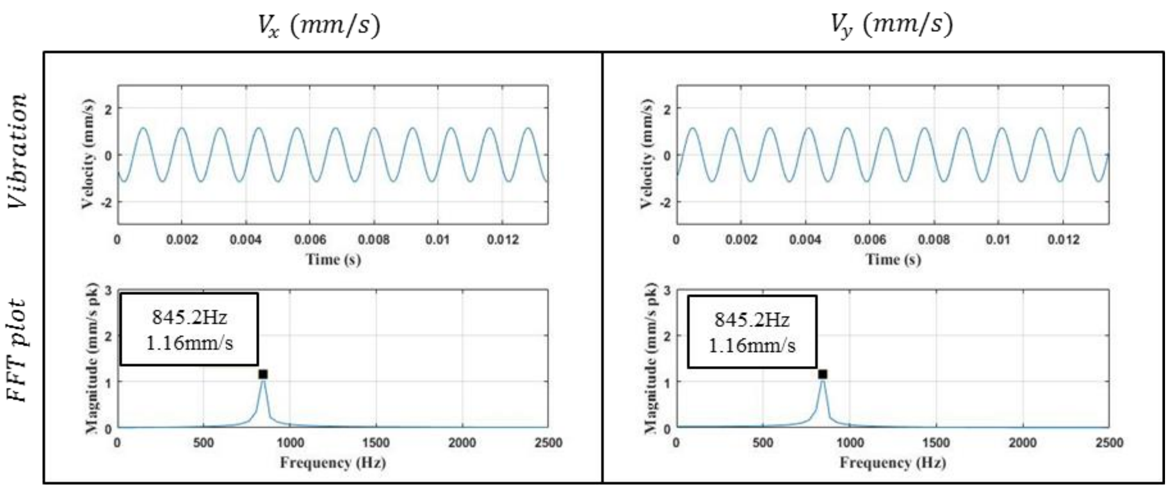

d) Prediction at sensor position B

Figure D-1 Unbalance responses of sensor positions *A & B* obtained at 50. k rp m in speed

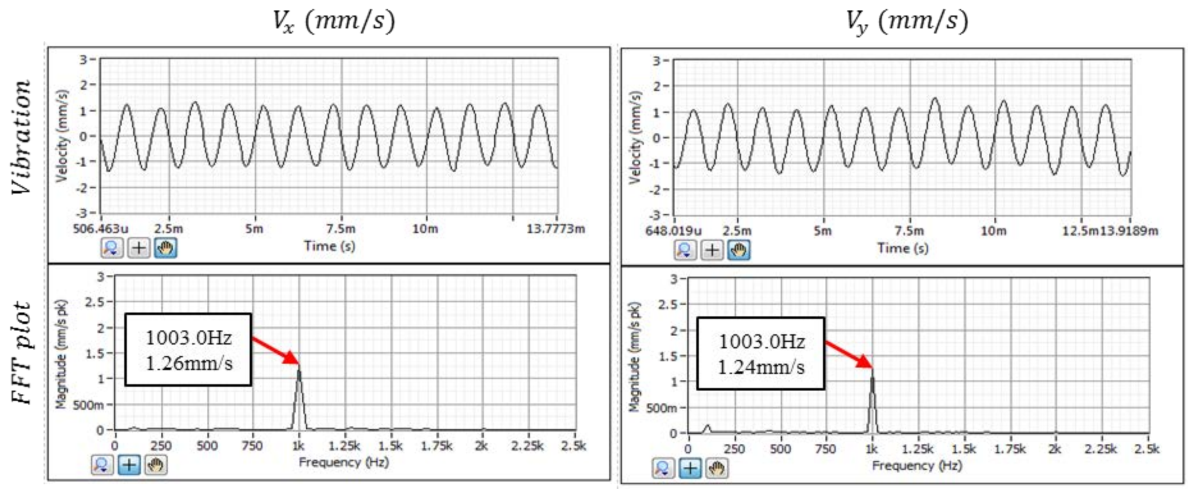

a) Measurements at sensor position A

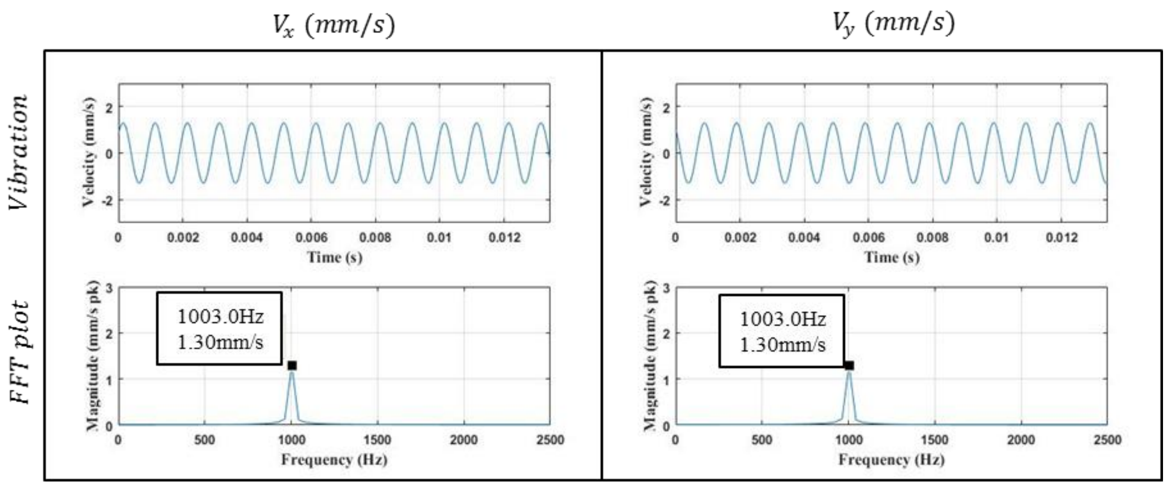

b) Predictions at sensor position A

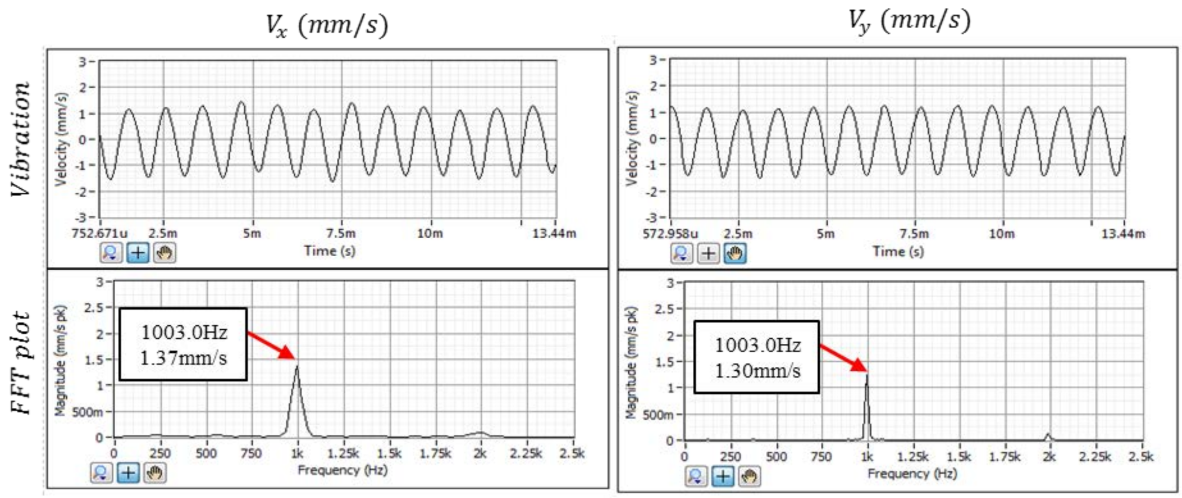

c) Measurements at sensor position B

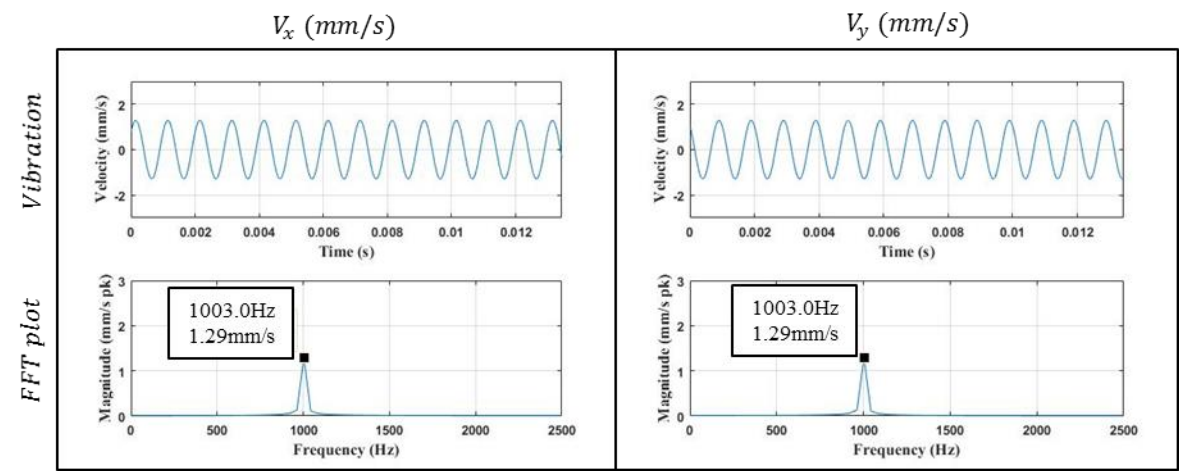

d) Predictions at sensor position B

Figure D-2 Unbalance responses of sensor positions *A & B* obtained at 60.2k rpm in speed

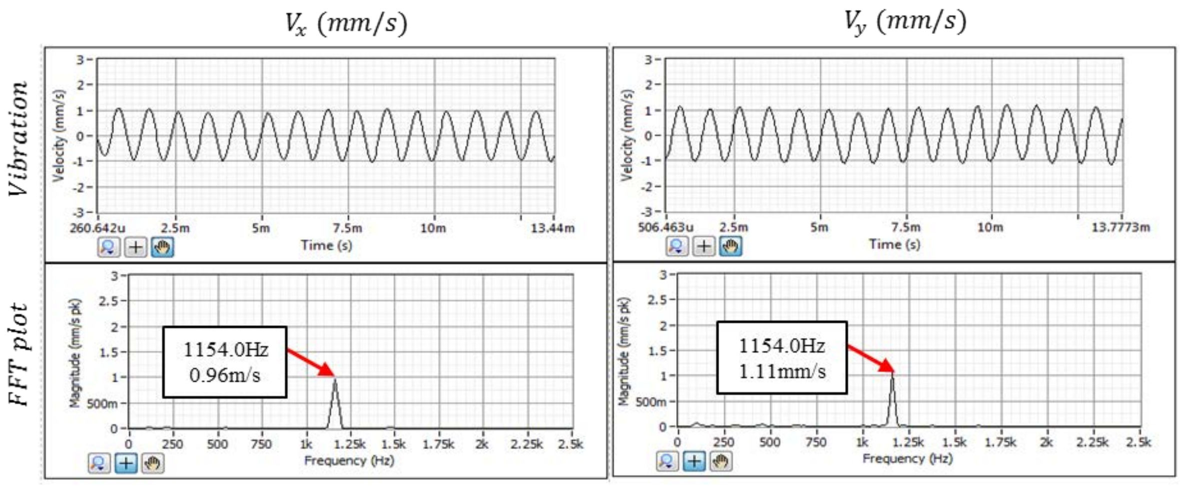

a) Measurements at sensor position A

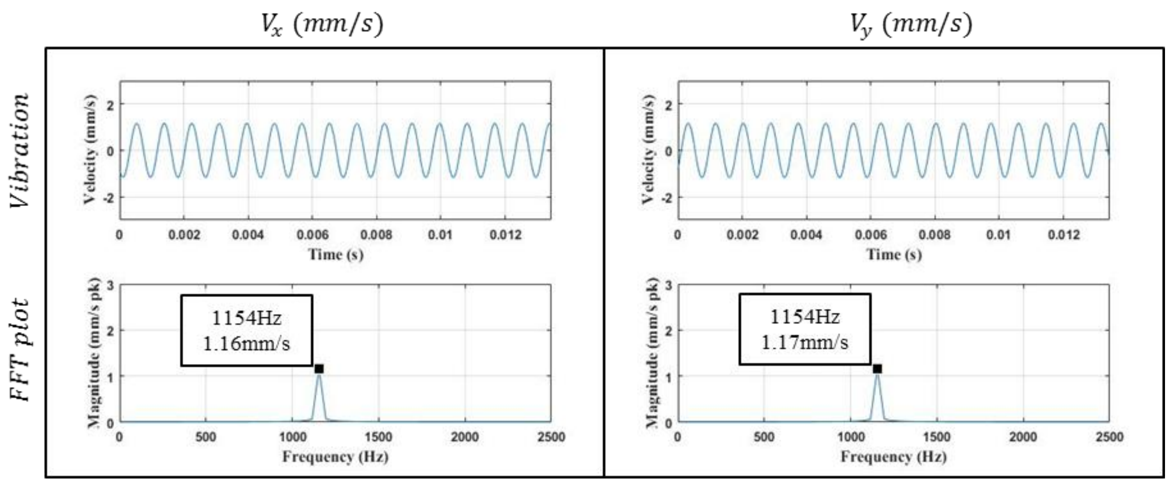

b) Predictions at sensor position A

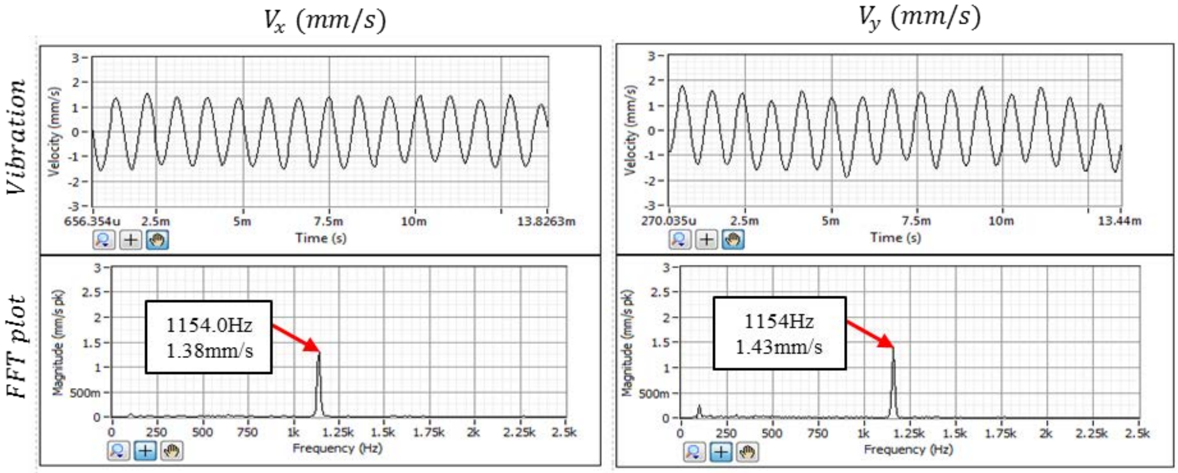

c) Measurements at sensor position B

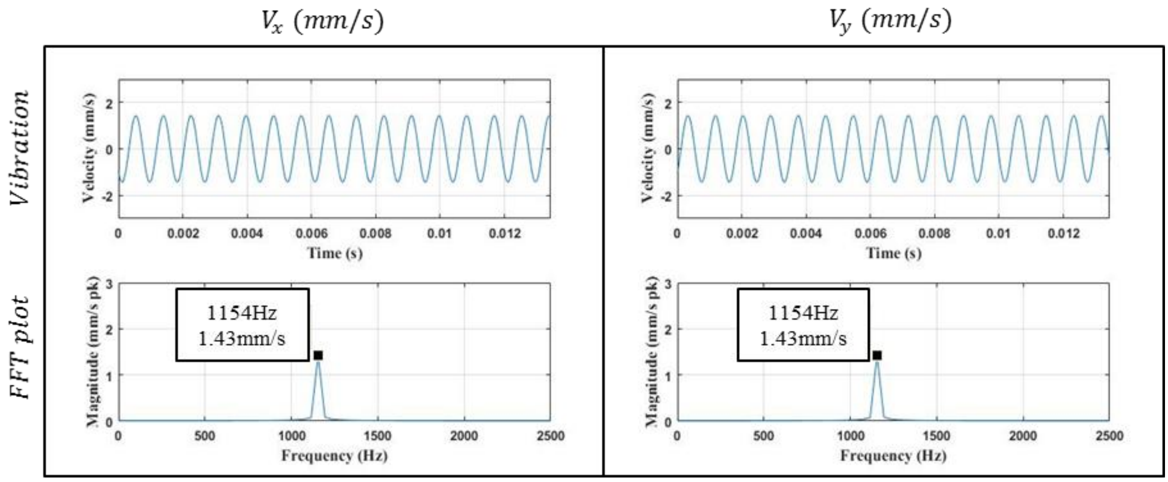

d) Predictions at sensor position B

Figure D-3 Unbalance responses of sensor positions *A & B* obtained at 69.2k rpm in speed

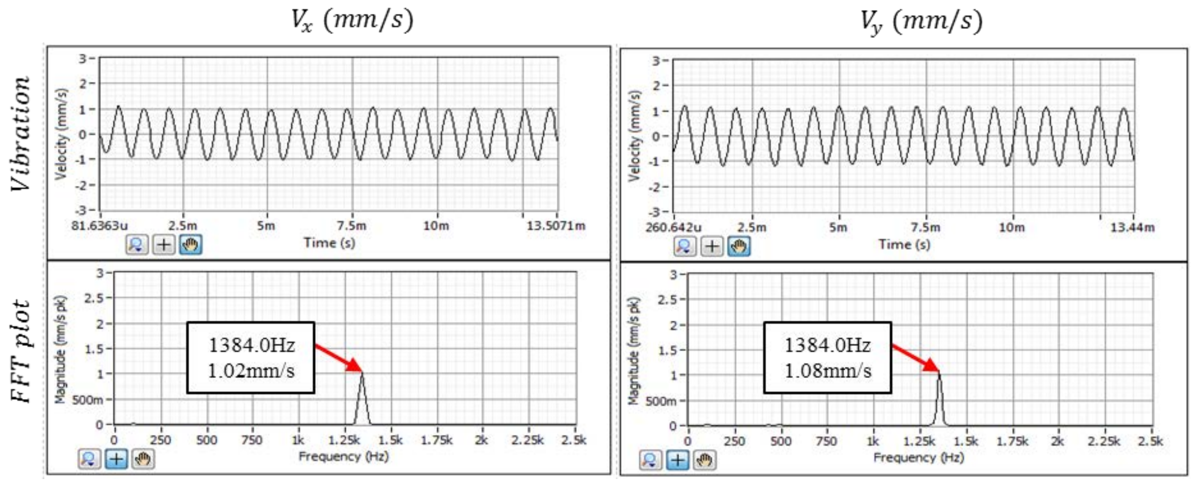

a) Measurements at sensor position A

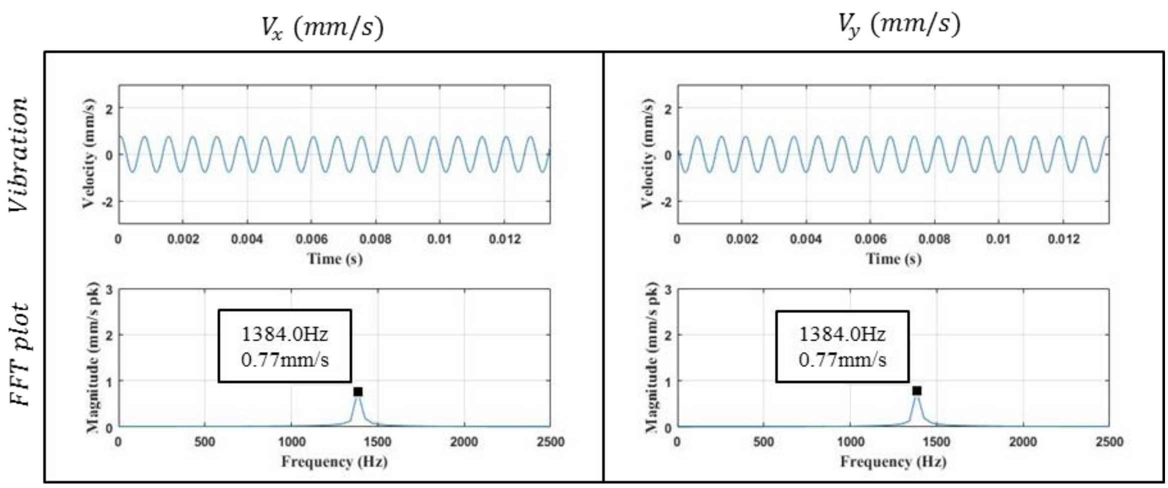

b) Predictions at sensor position A

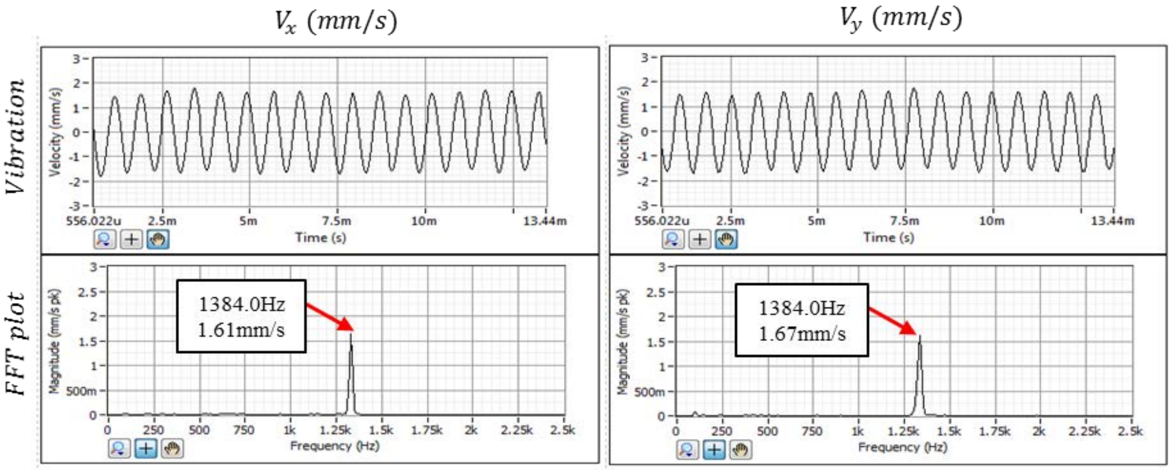

c) Measurements at sensor position B

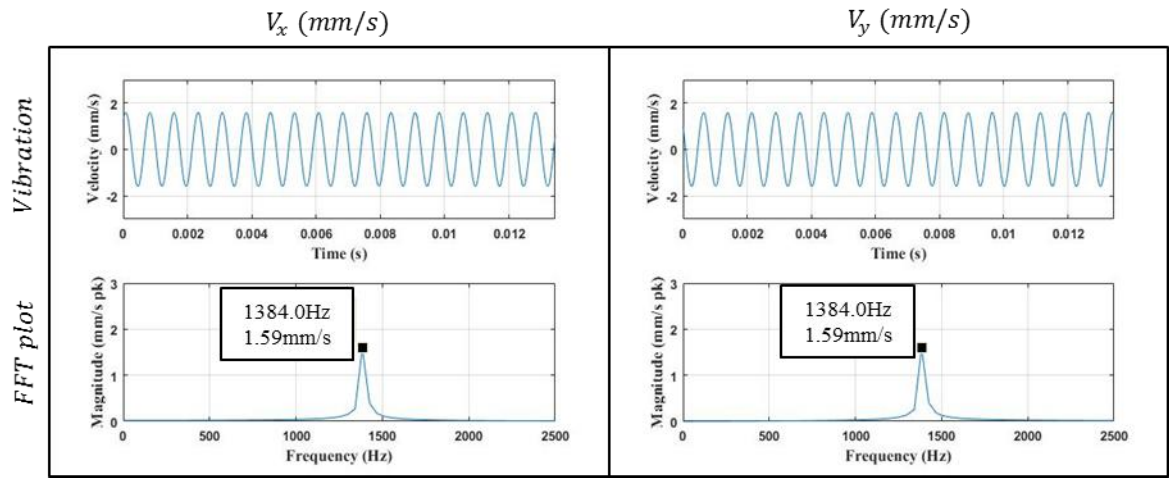

d) Predictions at sensor position B

Figure D-4 Unbalance response of sensor positions *A & B* obtained at 83.0k rpm in speed

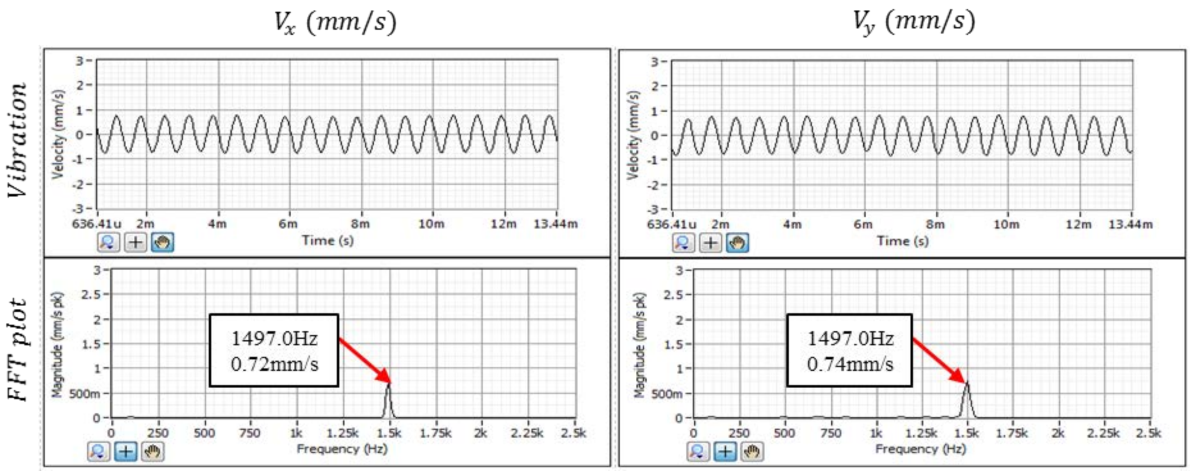

a) Measurements at sensor position A

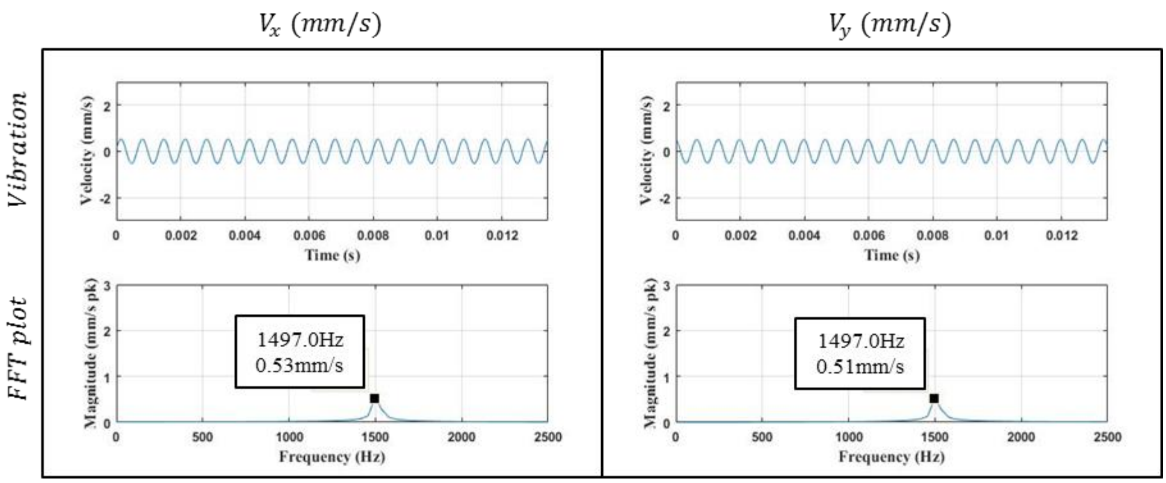

b) Predictions at sensor position A

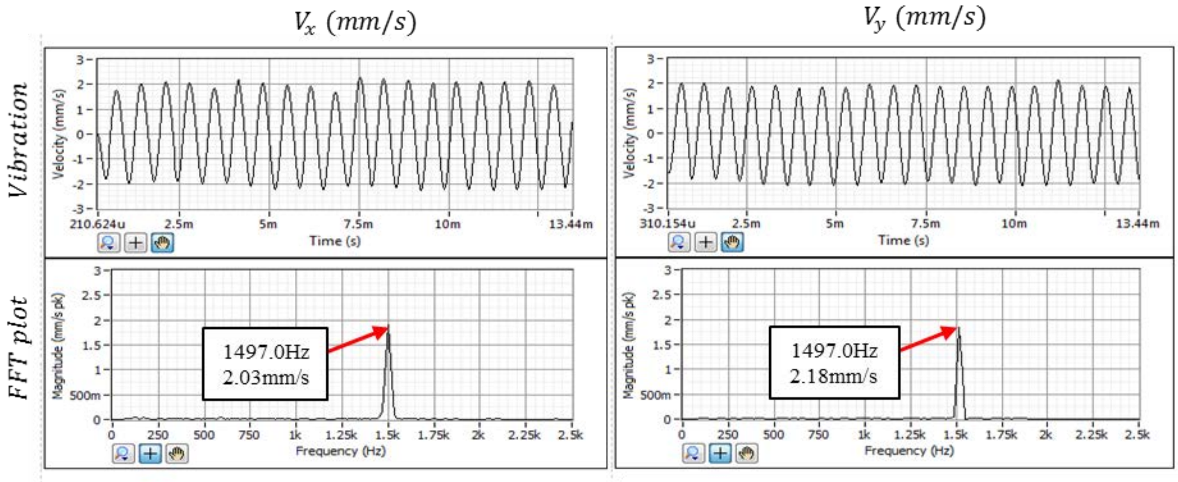

c) Measurements at sensor position B

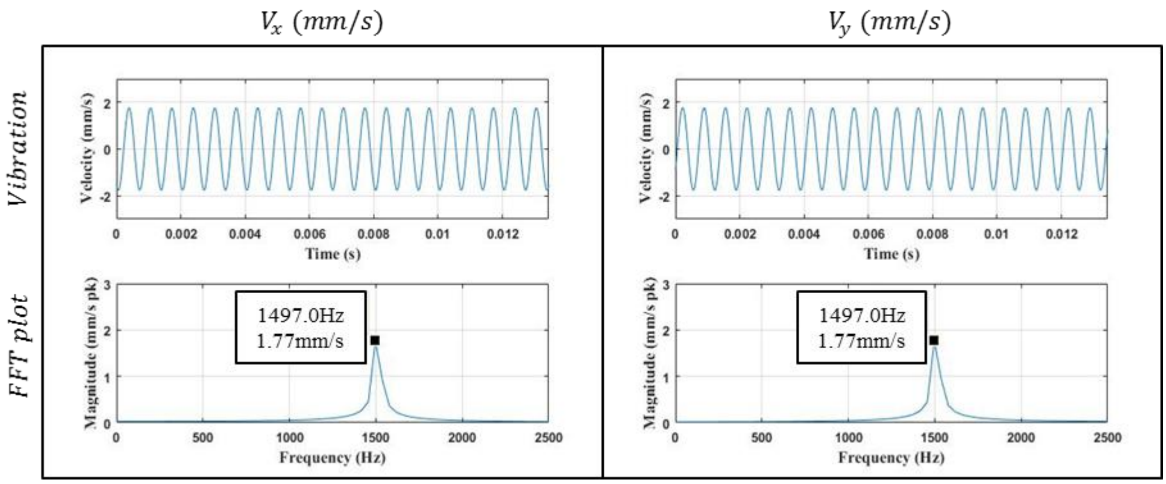

d) Predictions at sensor position B

Figure D-5 Unbalance responses of sensor positions *A & B* obtained at 89.8k rpm in speed

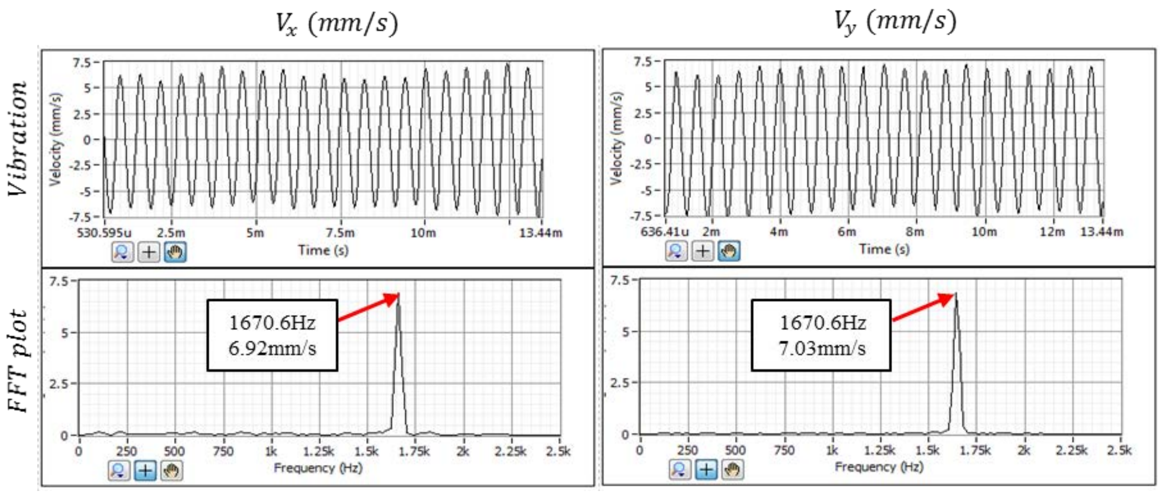

a) Measurements at sensor position A

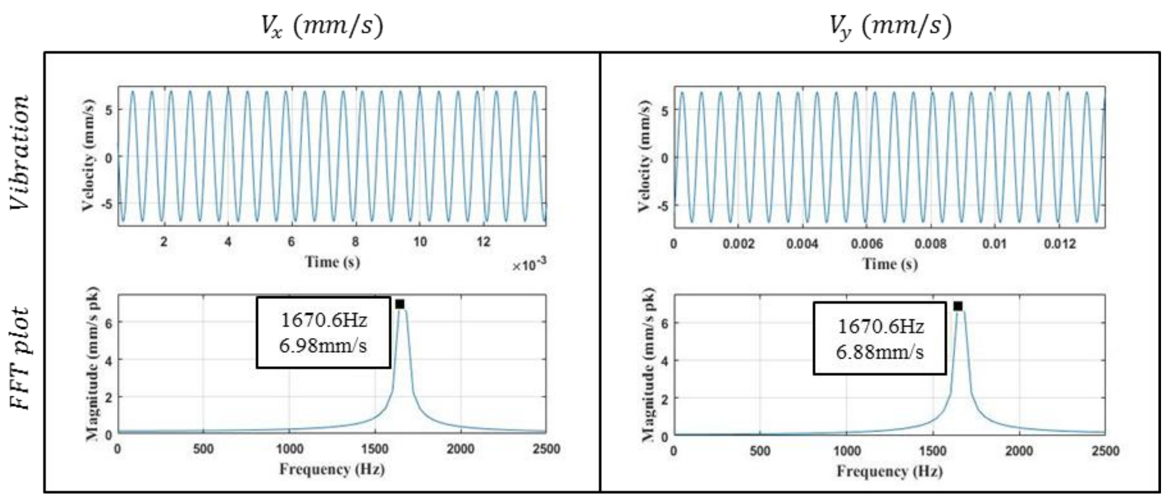

b) Predictions at sensor position A

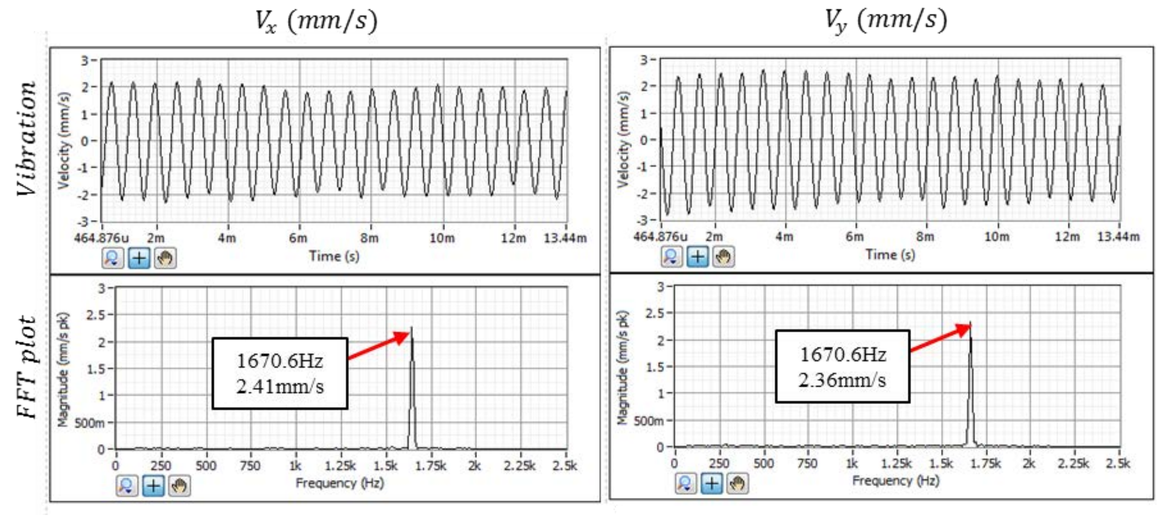

c) Measurements at sensor position B

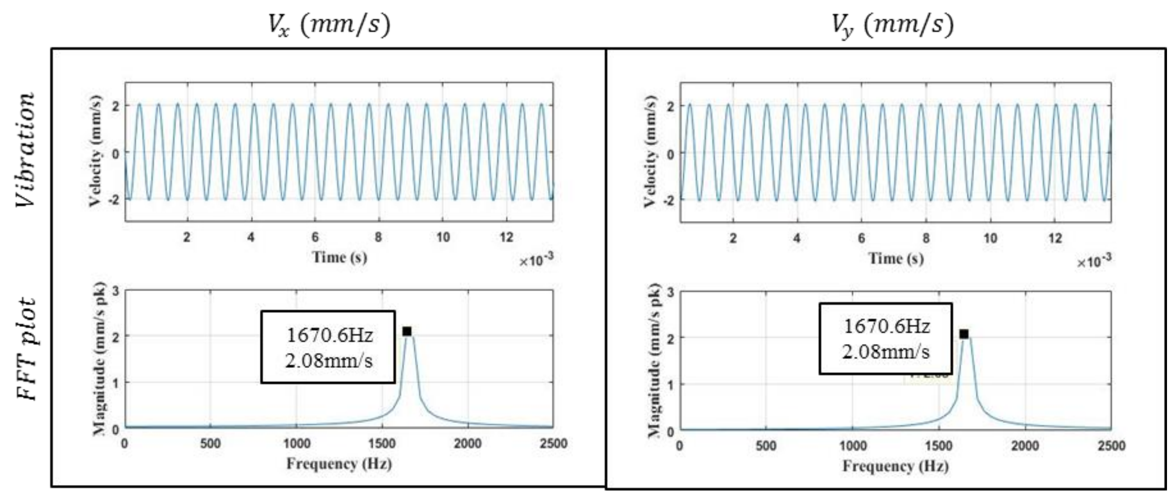

d) Predictions at sensor position B

Figure D-6 Unbalance responses of sensor position *A & B* obtained at 100k rpm in speed

APPENDIX E

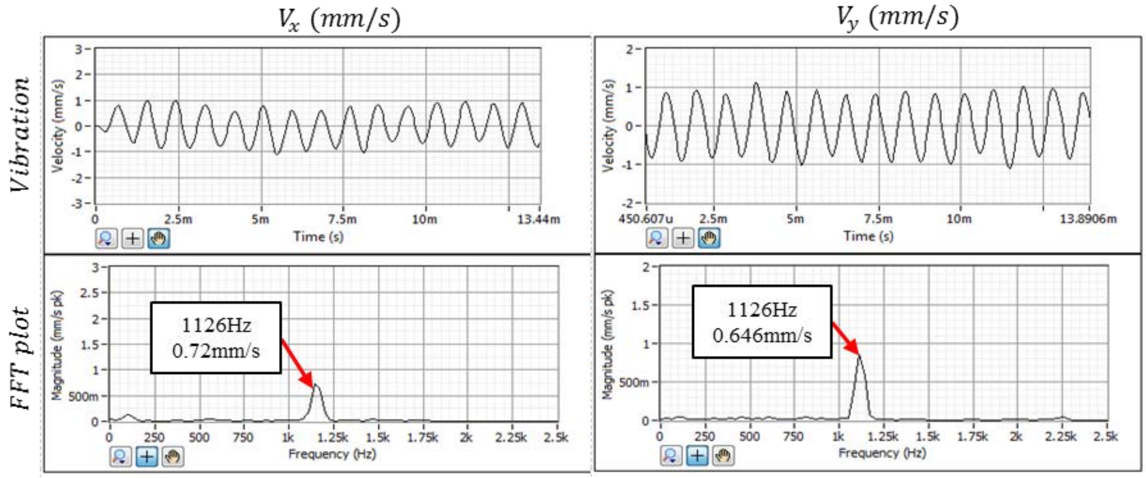

a) Measurements at sensor position A

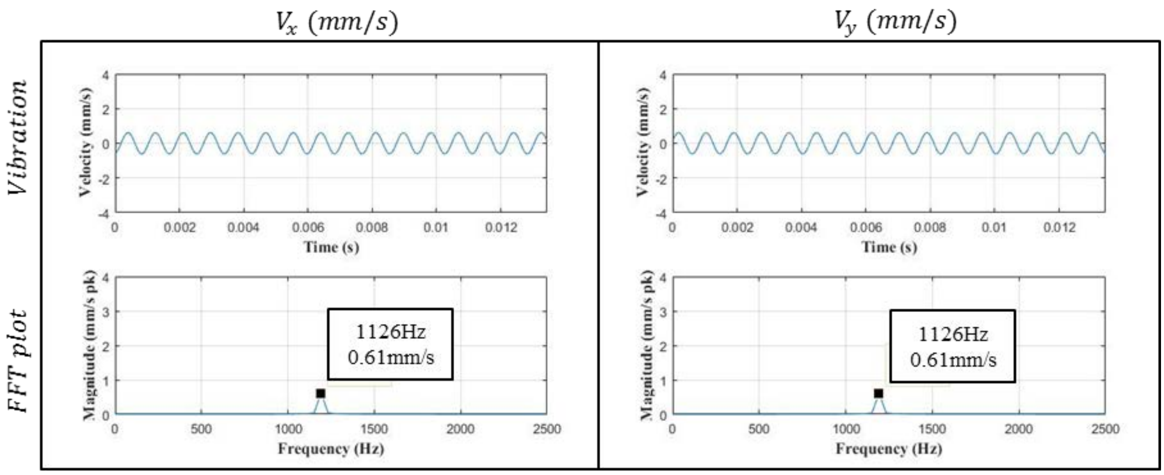

b) Predictions at sensor position A

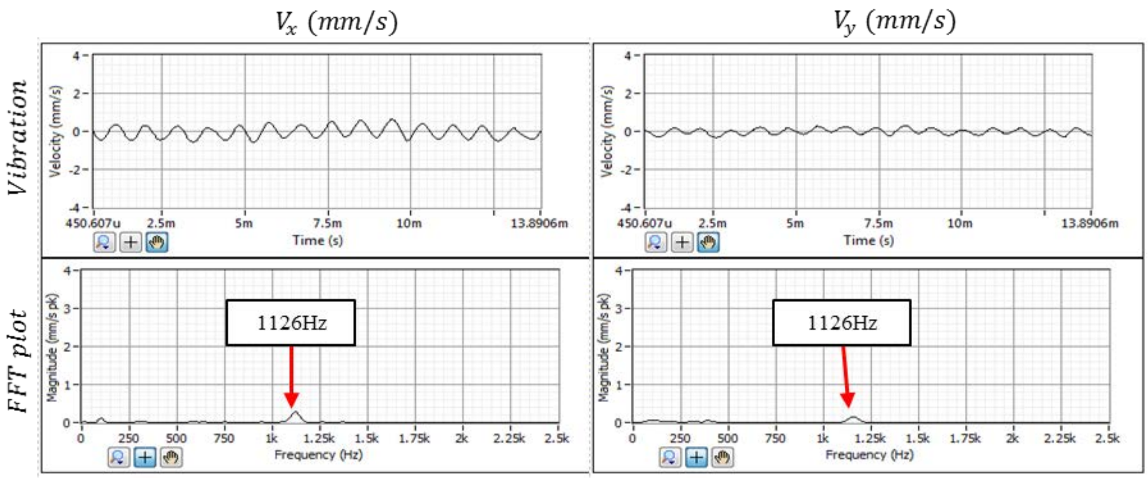

c) Measurement at sensor position B

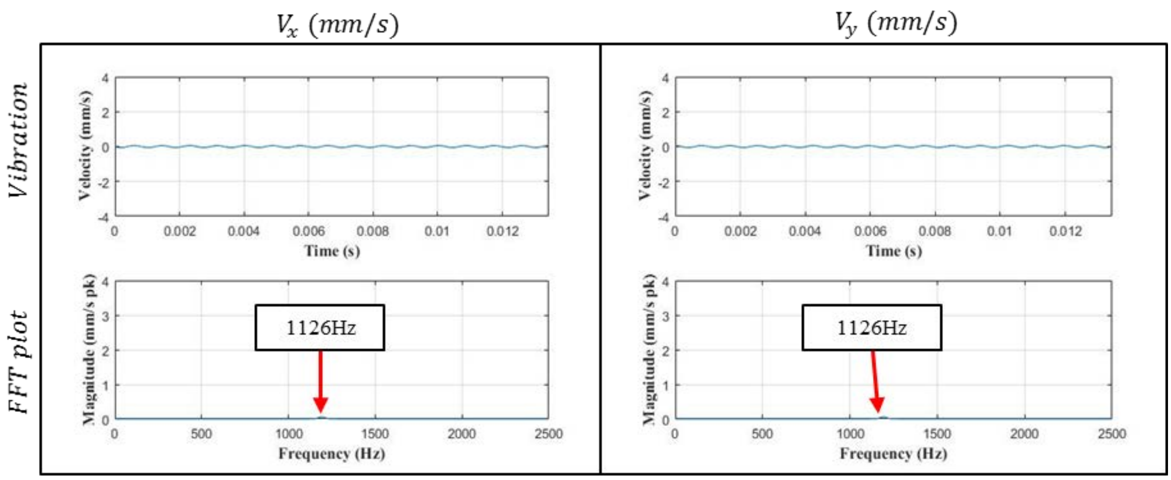

d) Predictions at sensor position B

Figure E-1 Unbalance responses of sensor positions *A & B* obtained at 6 . 5k rpm in speed. Supply pressure maintained at ba r.

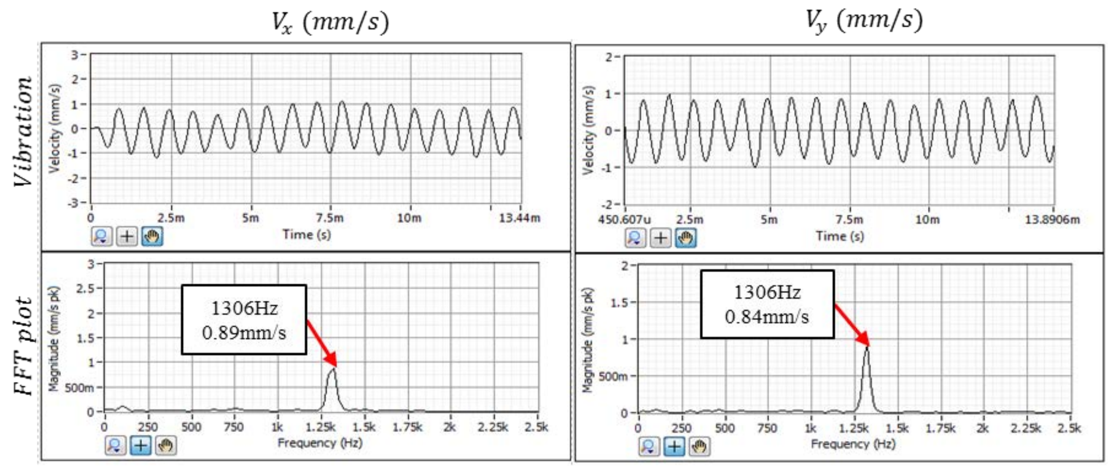

a) Measurements at sensor position A

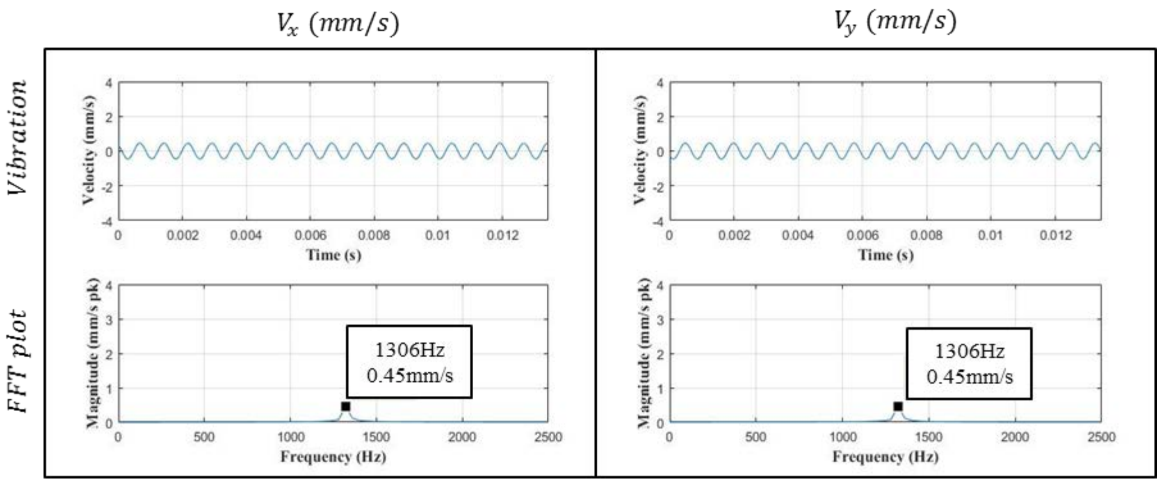

b) Predictions at sensor position A

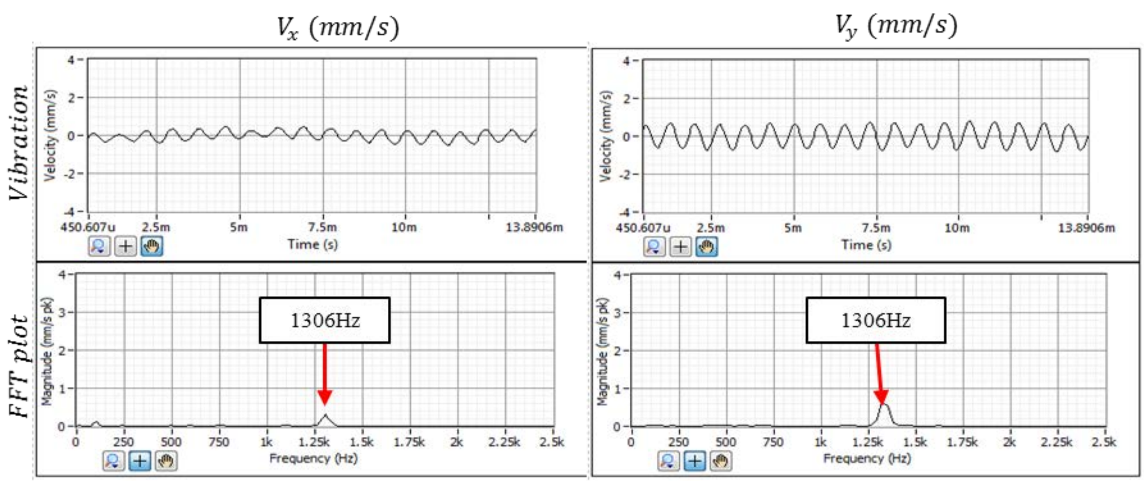

c) Measurements at sensor position B

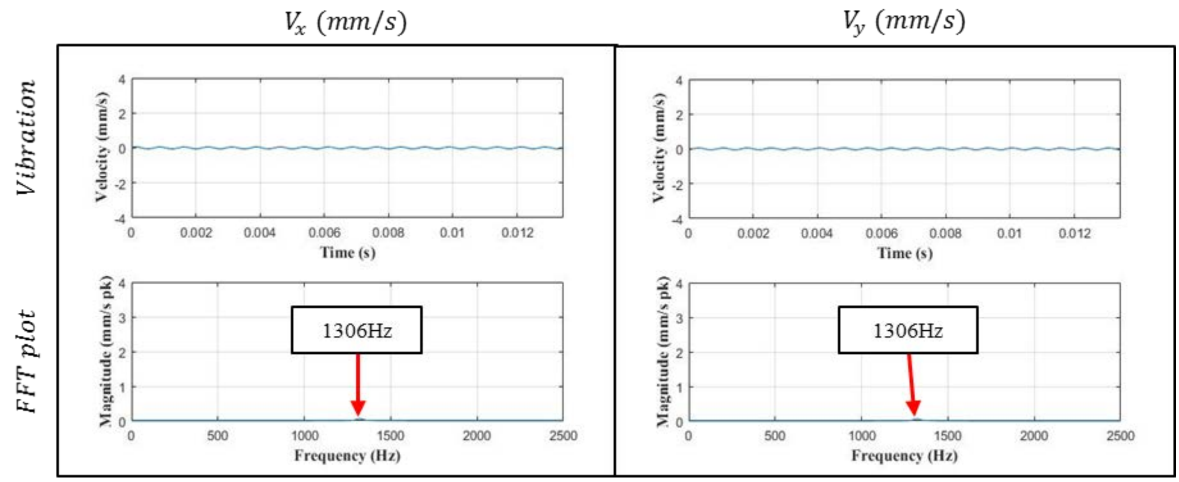

d) Predictions at sensor position B

Figure E-2 Unbalance responses of sensor positions *A & B* obtained at 8. 4k rpm in speed. Supply pressure maintained at ba r.

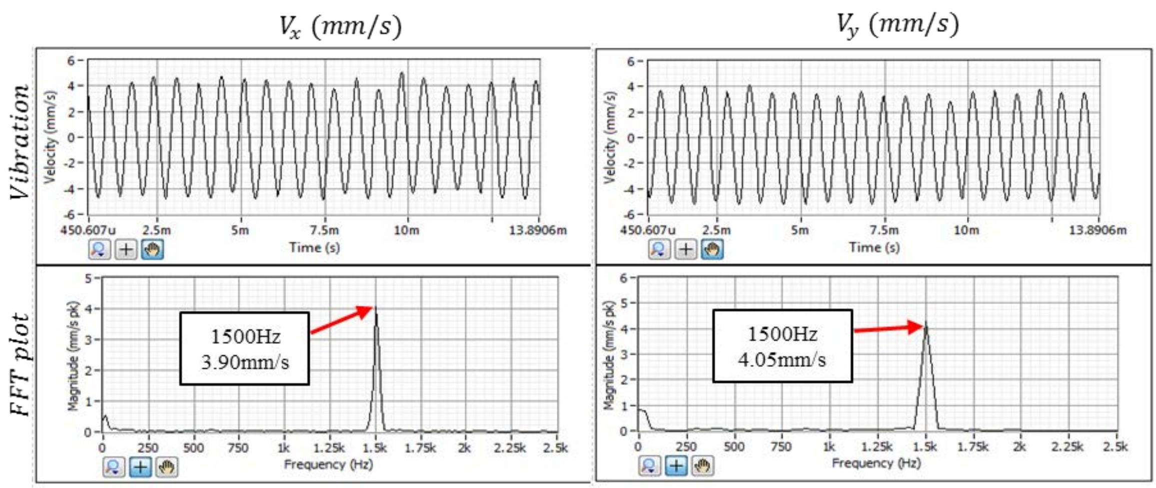

a) Measurements at sensor position A

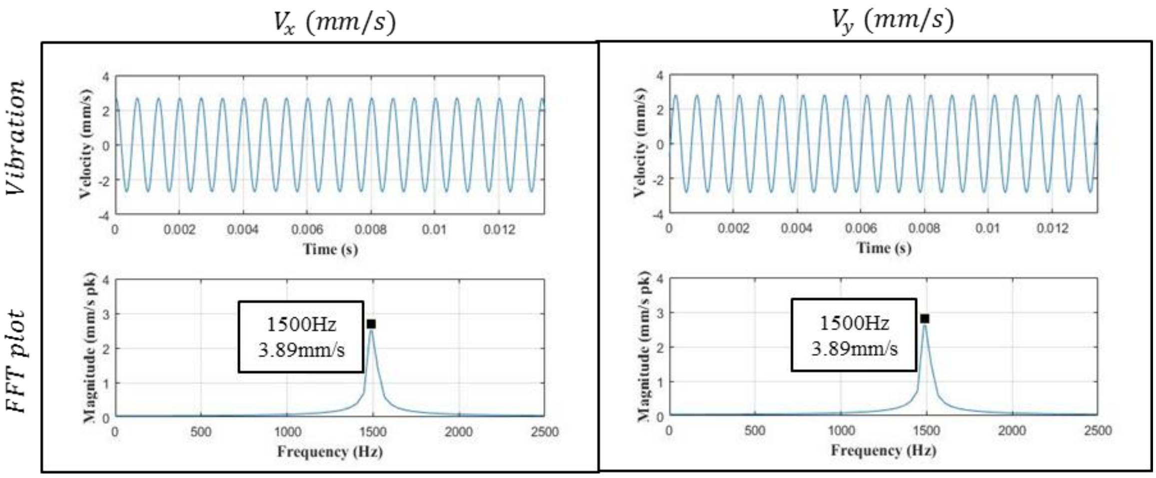

b) Predictions at sensor position A

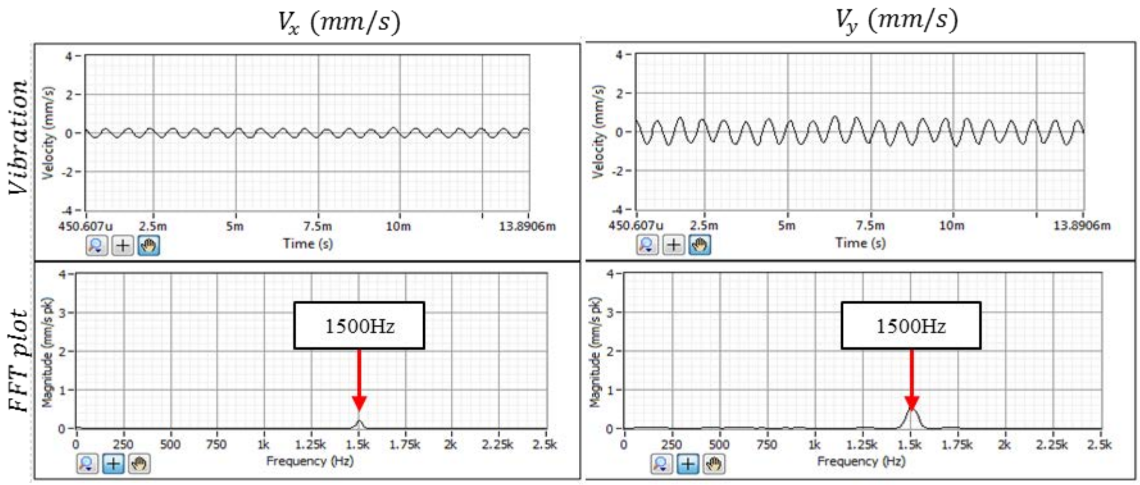

c) Measurements at sensor position B

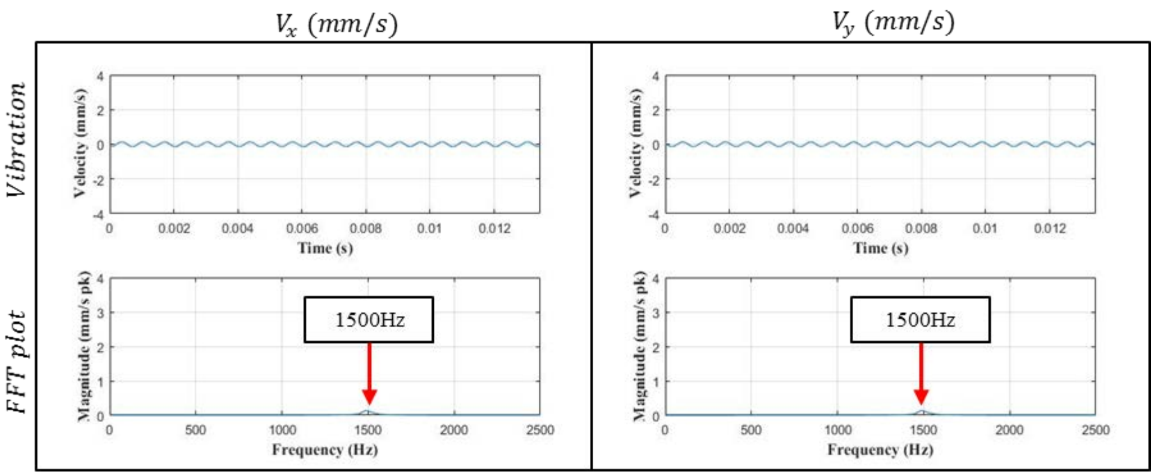

d) Predictions at sensor position B

Figure E-3 Unbalance responses of sensor positions *A & B* obtained at 90.0k rpm in speed. Supply pressure maintained at ba r.

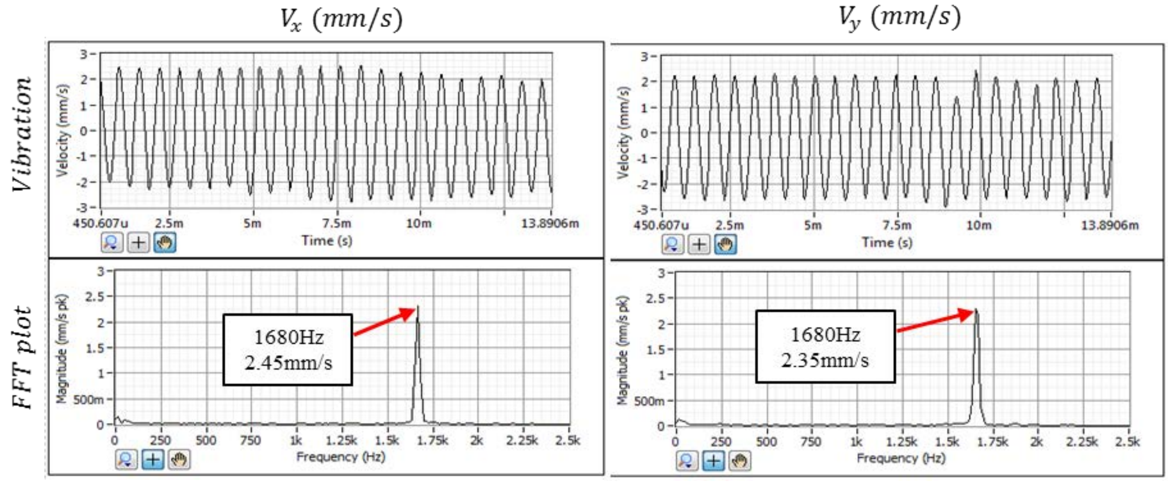

a) Measurements at sensor position A

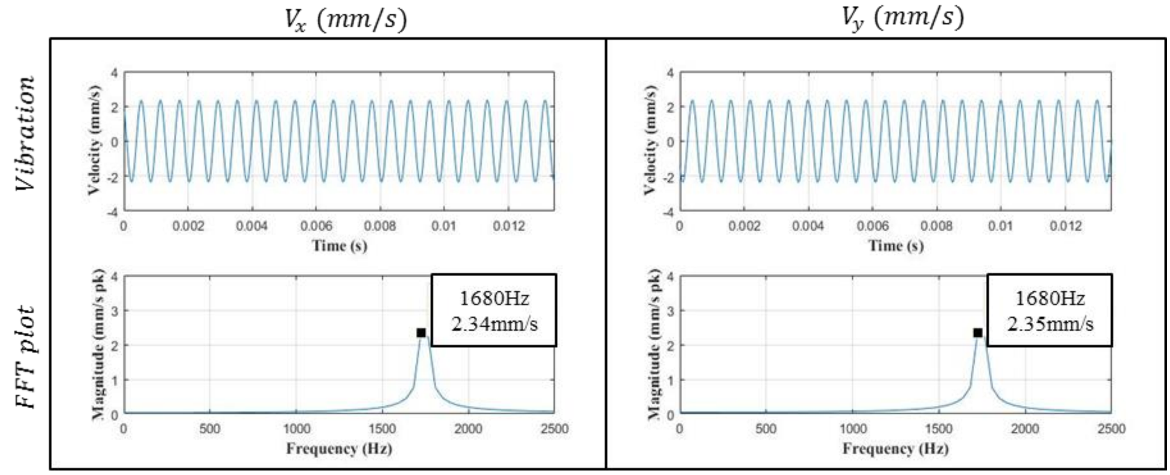

b) Predictions at sensor position A

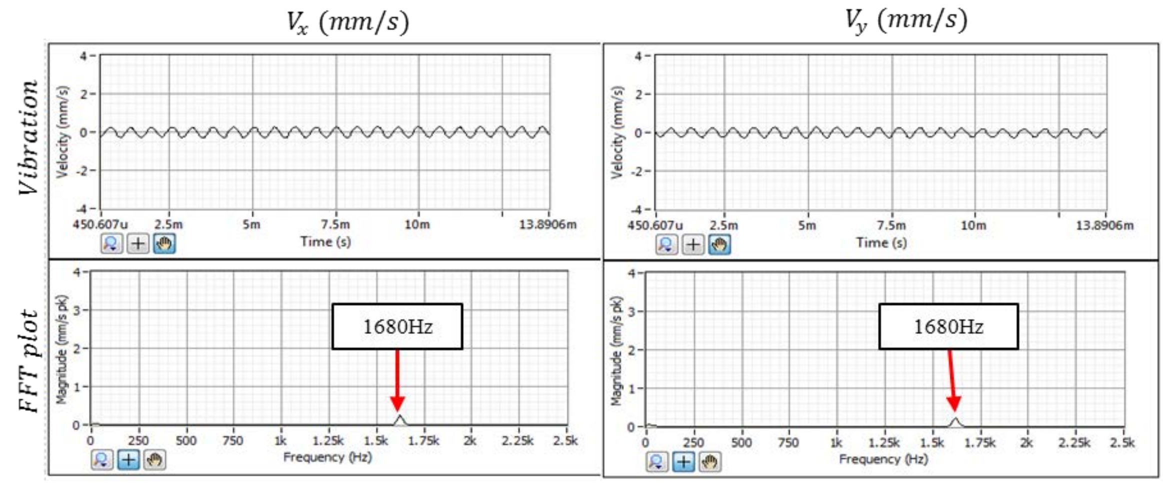

c) Measurements at sensor position B

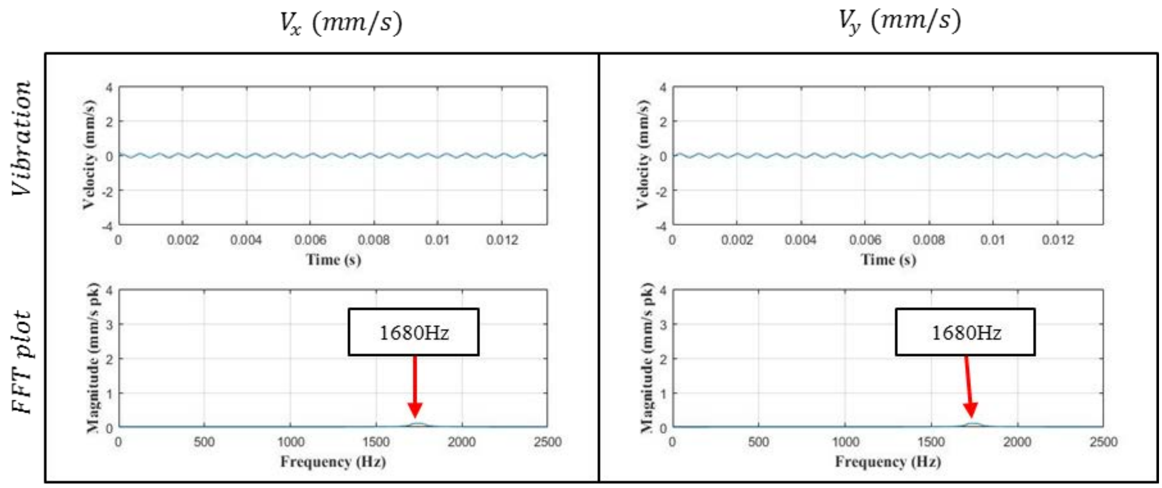

d) Predictions at sensor position B

Figure E-4 Unbalance responses of sensor positions *A & B* obtained at 100.8k rpm in speed. Supply pressure maintained at ba r.

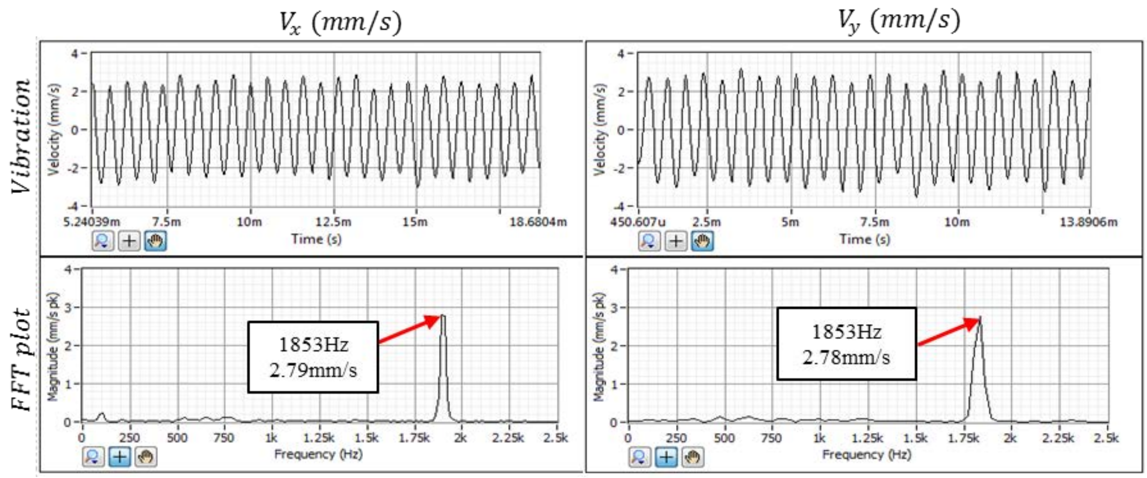

a) Measurements at sensor position A

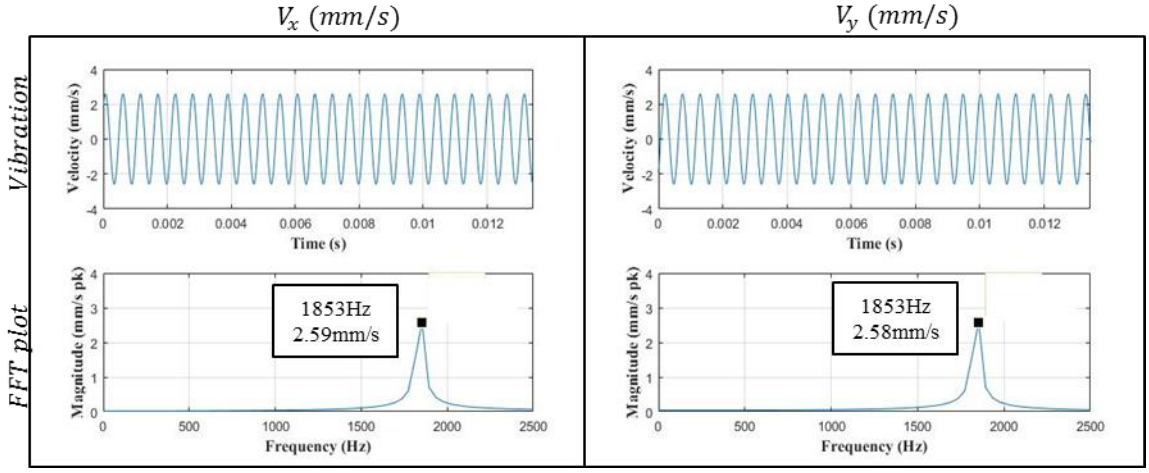

b) Predictions at sensor position A

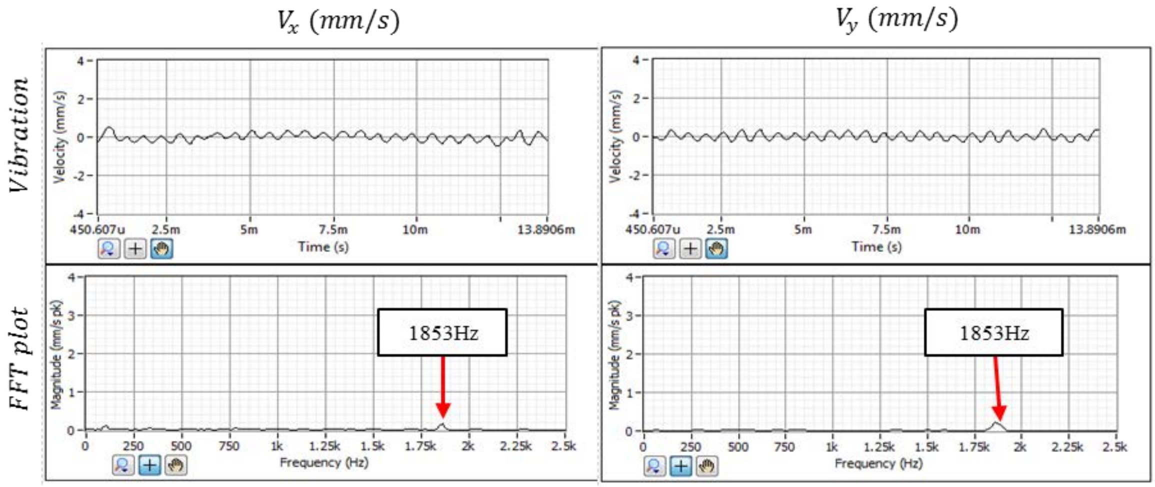

c) Measurements at sensor position B

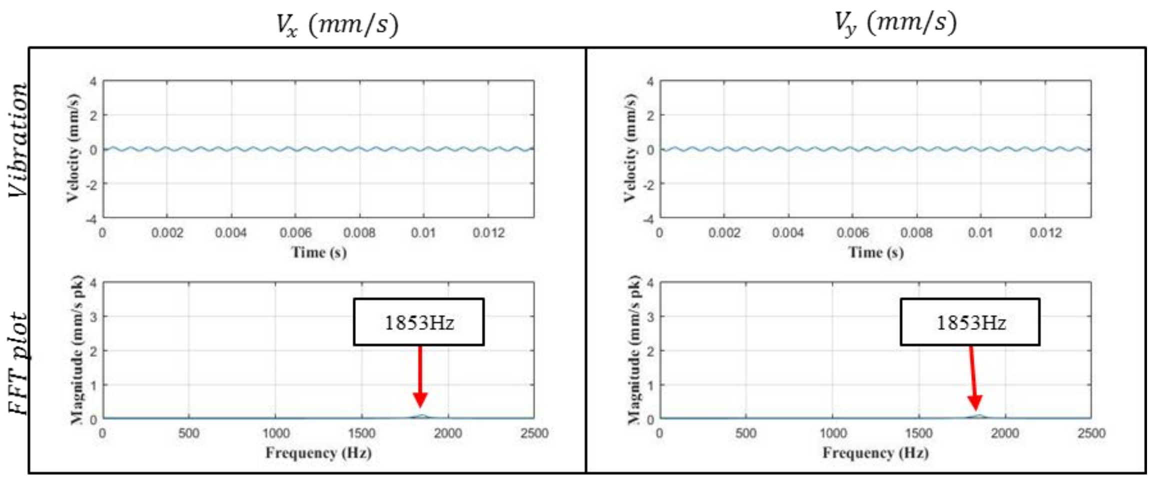

d) Predictions at sensor position B

Figure E-5 Unbalance responses of sensor positions *A & B* obtained at 111k rpm in speed. Supply pressure maintained at ba r.

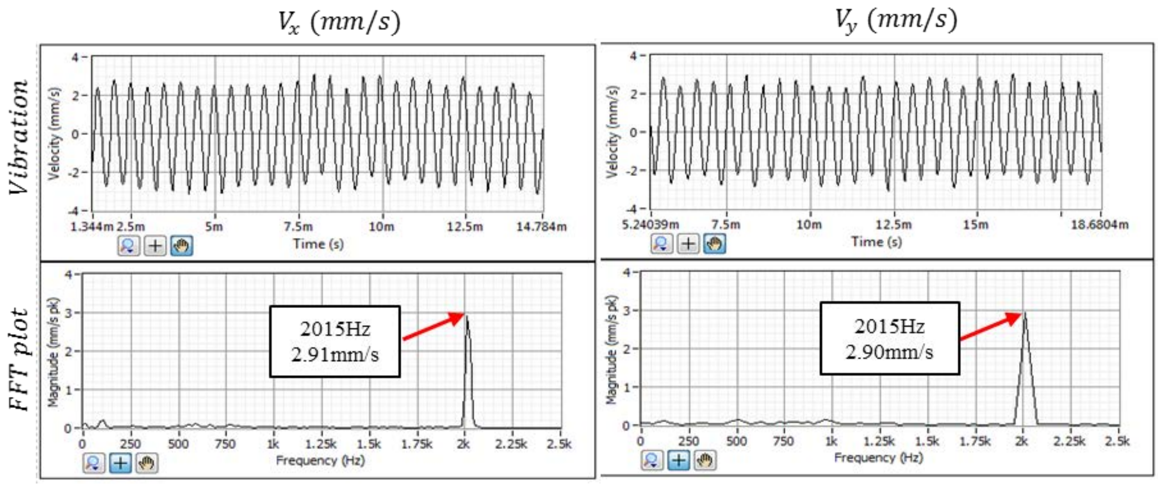

a) Measurements at sensor position A

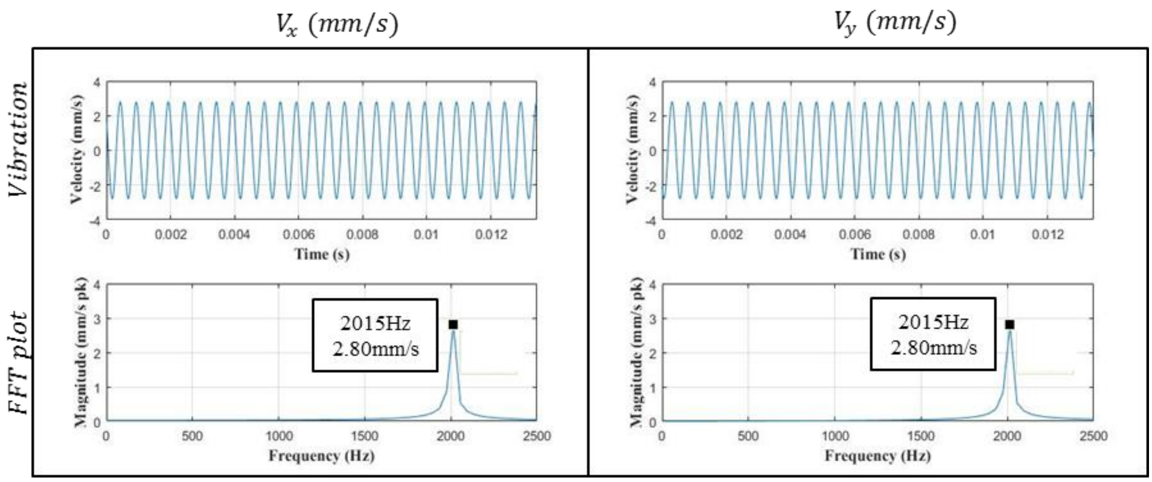

b) Predictions at sensor position A

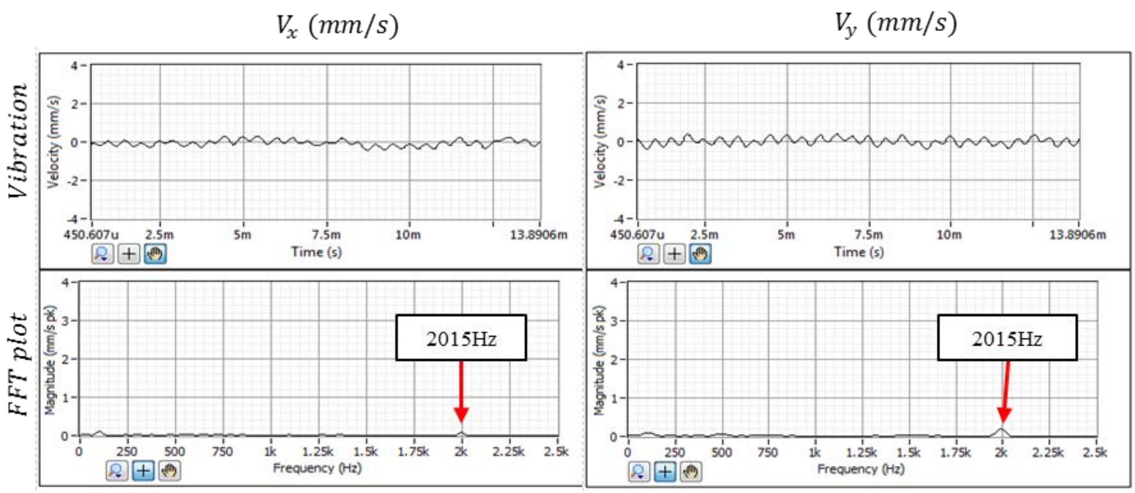

c) Measurements at sensor position B

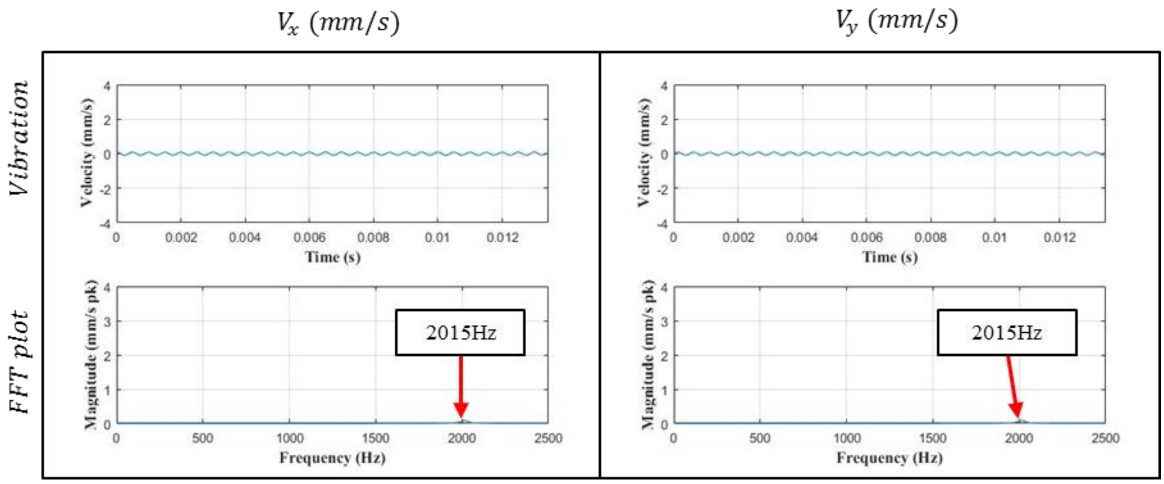

d) Predictions at sensor position B

Figure E-6 Unbalance responses of sensor positions *A & B* obtained at 120.9k rpm in speed. Supply pressure maintained at ba r.

APPENDIX F

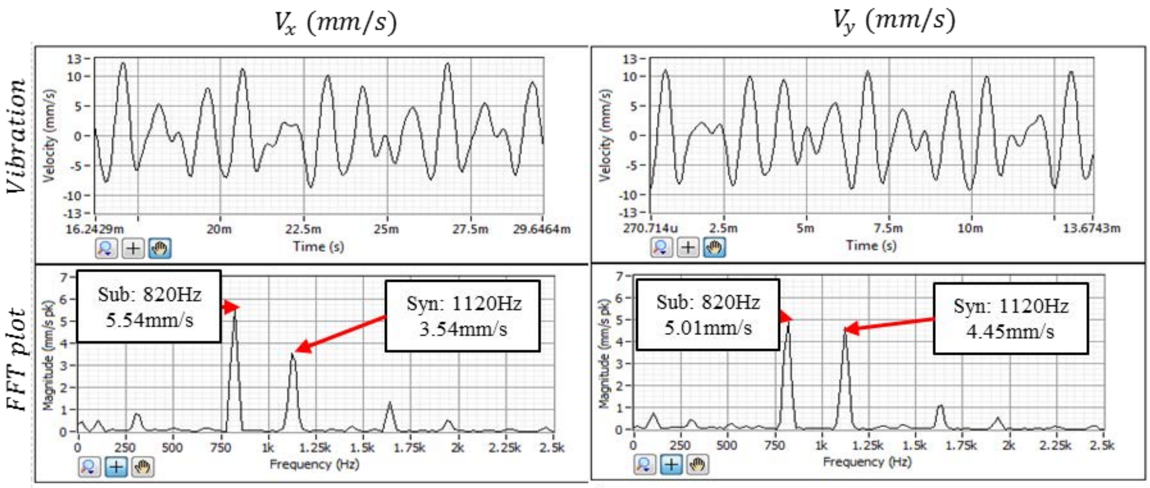

a) Measurements at sensor position A

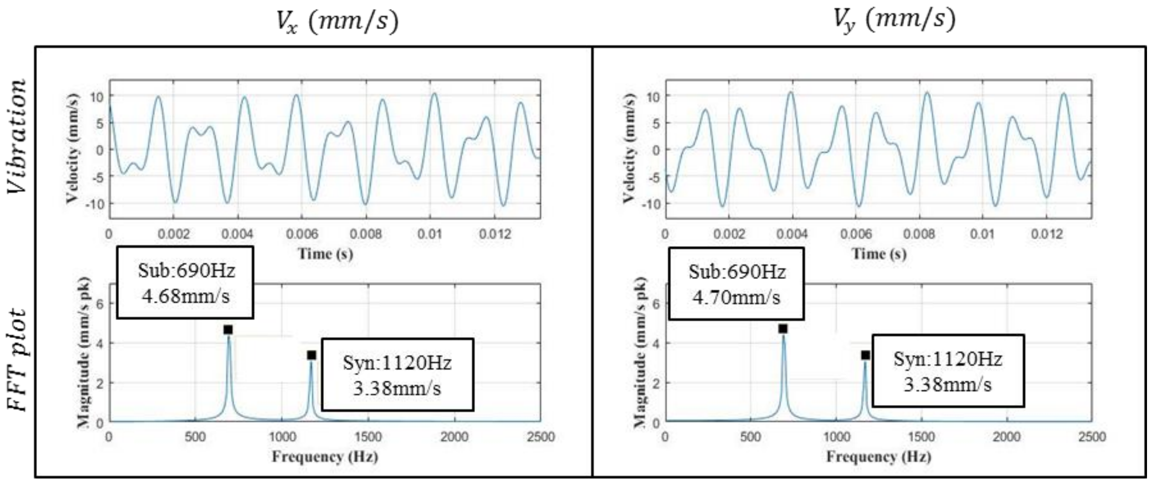

b) Predictions at sensor position A

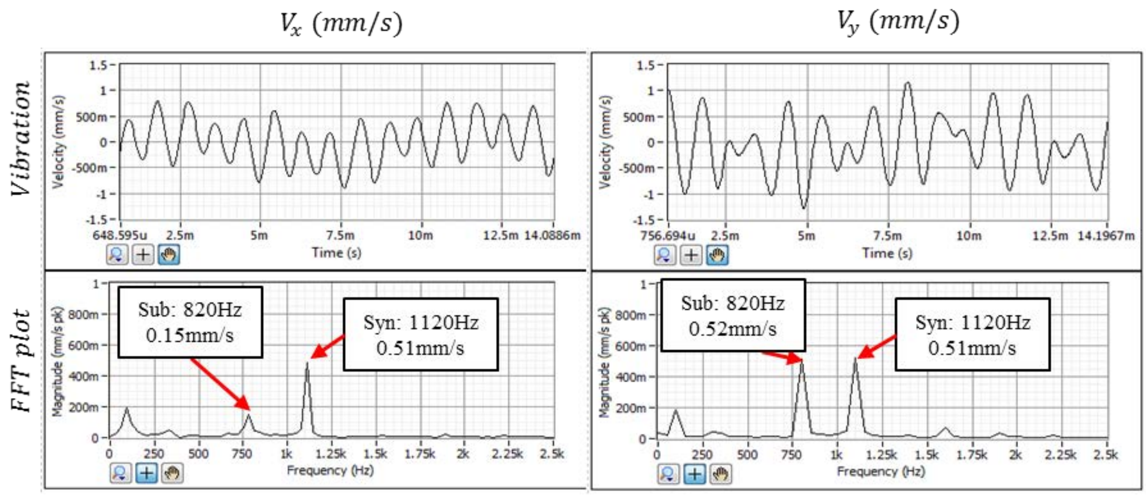

c) Measurements at sensor position B

Figure F-1 Unbalance responses of sensor positions *A & B* obtained at 6 .2 k rpm in speed

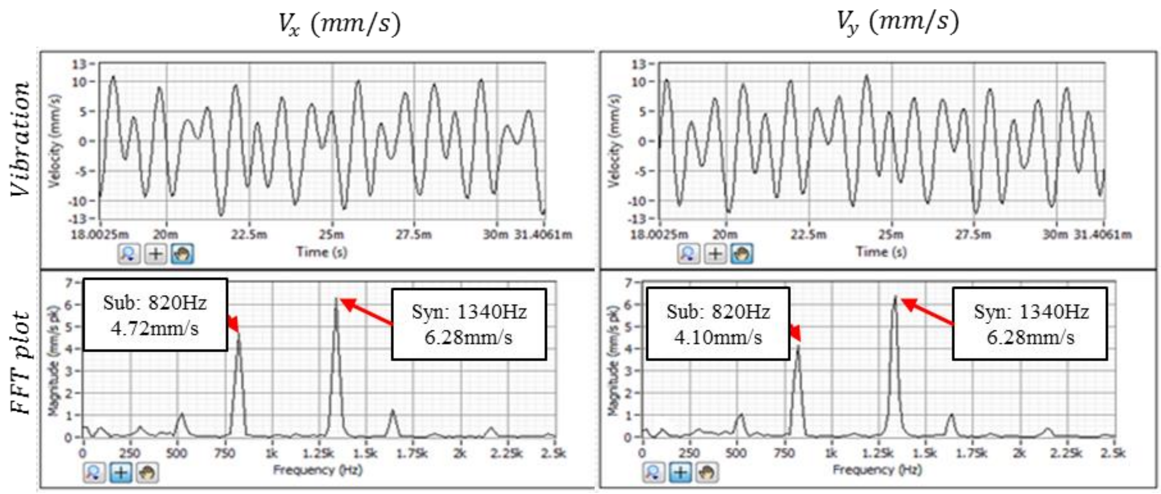

a) Measurements at sensor position A

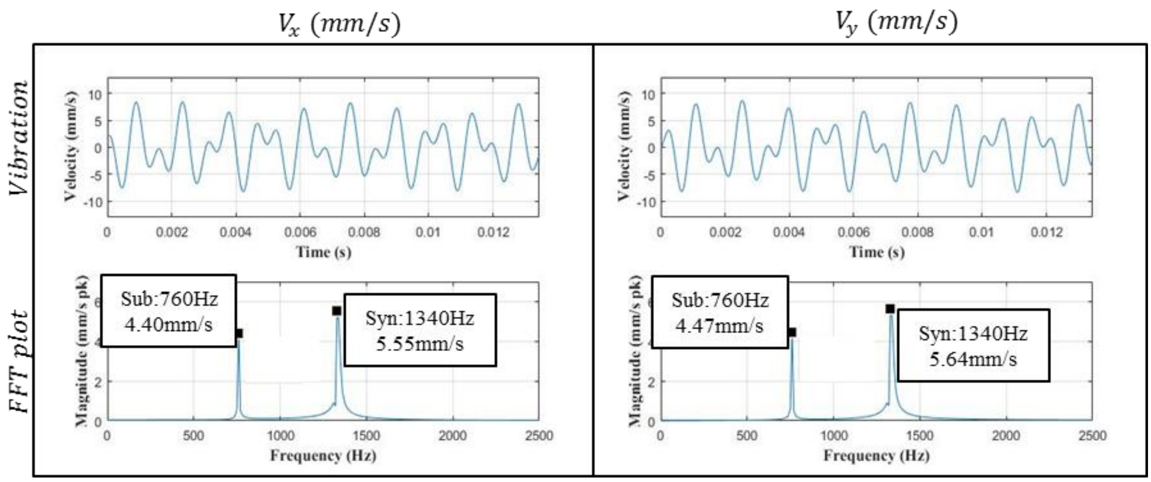

b) Predictions at sensor position A

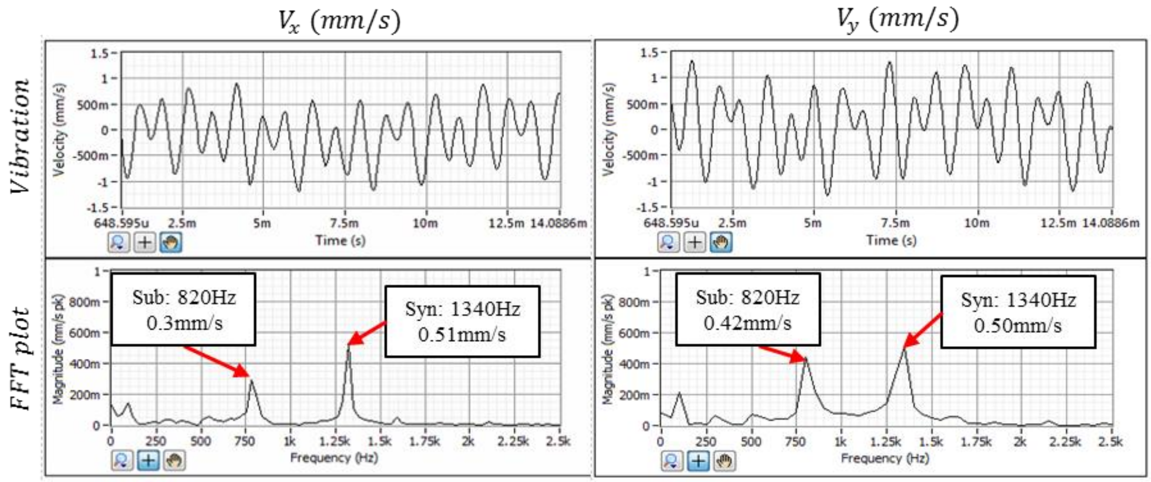

c) Measurements at sensor position B

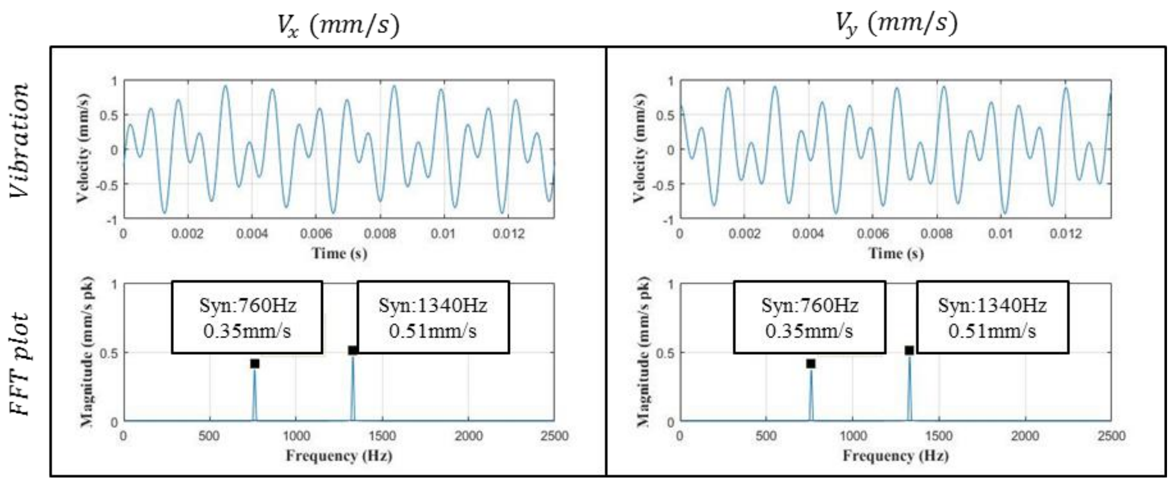

d) Predictions at sensor position B

Figure F-2 Unbalance responses of sensor positions *A & B* obtained at 80.4k rpm in speed

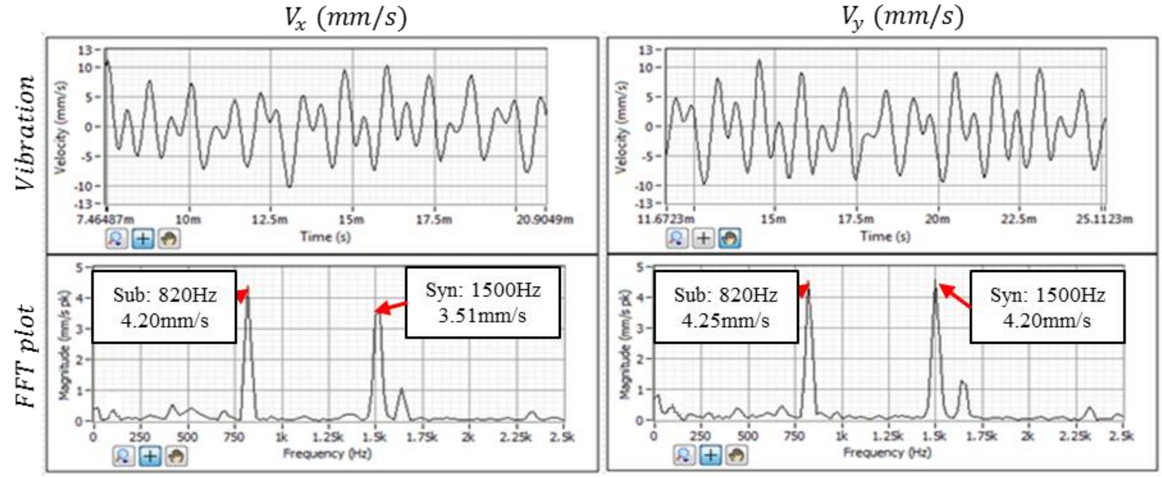

a) Measurements at sensor position A

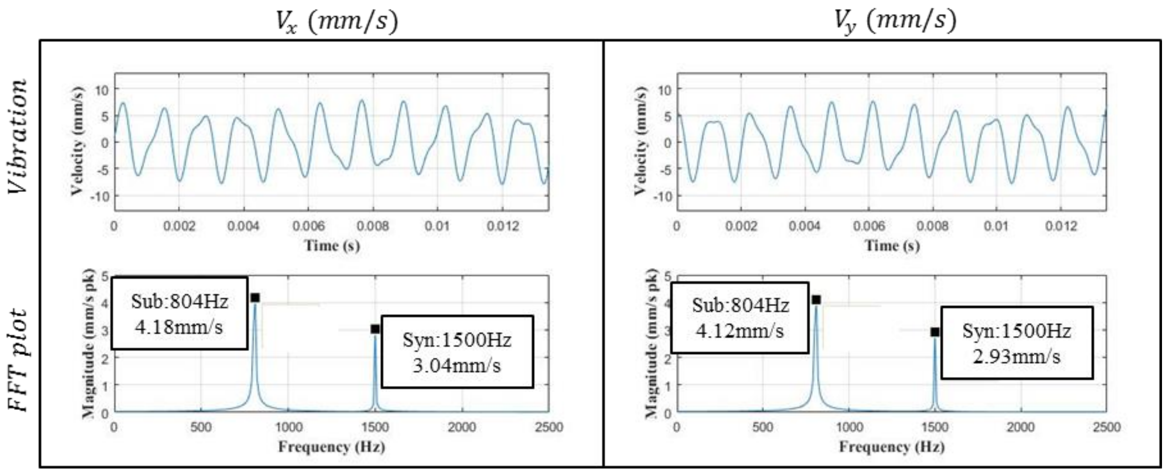

b) Predictions at sensor position A

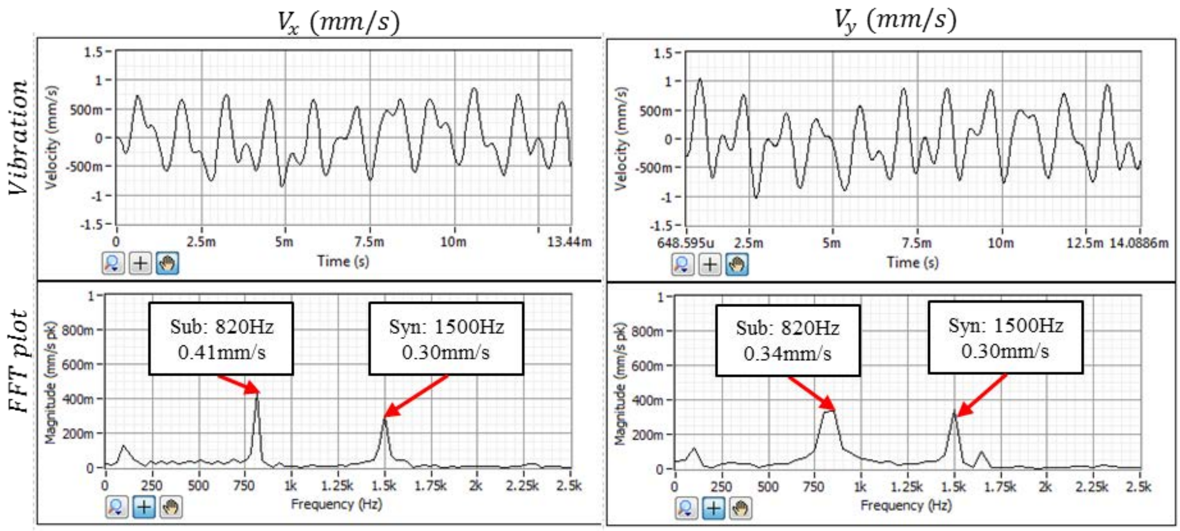

c) Measurements at sensor position B

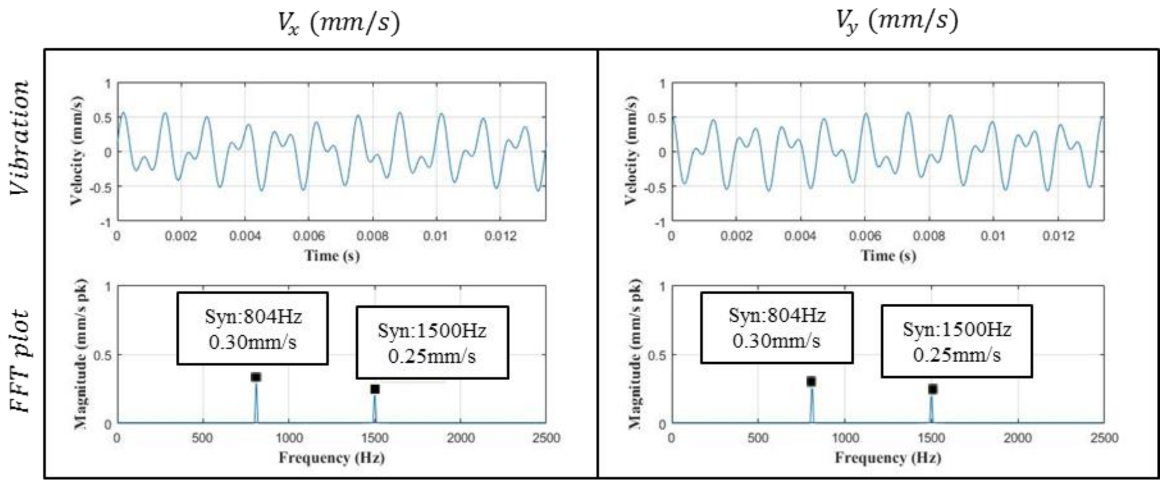

d) Predictions at sensor position B

Figure F-3 Unbalance responses of sensor positions *A & B* obtained at 90k rpm in speed

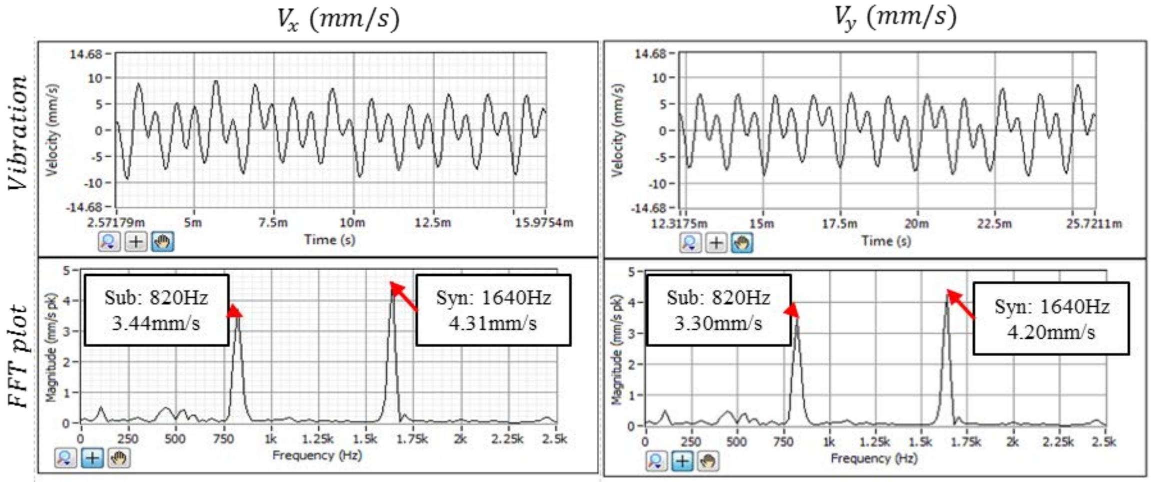

a) Measurements at sensor position A

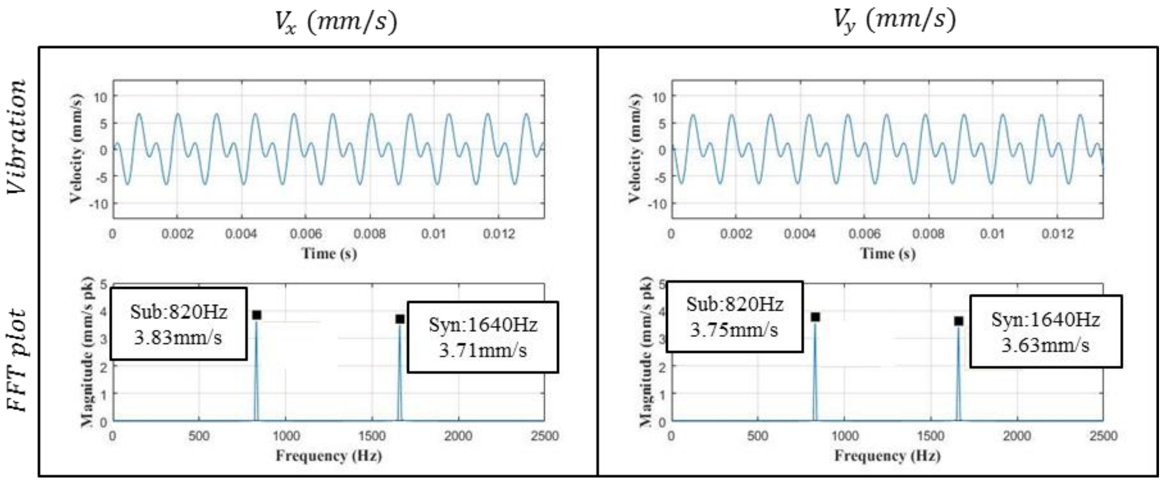

b) Predictions at sensor position A

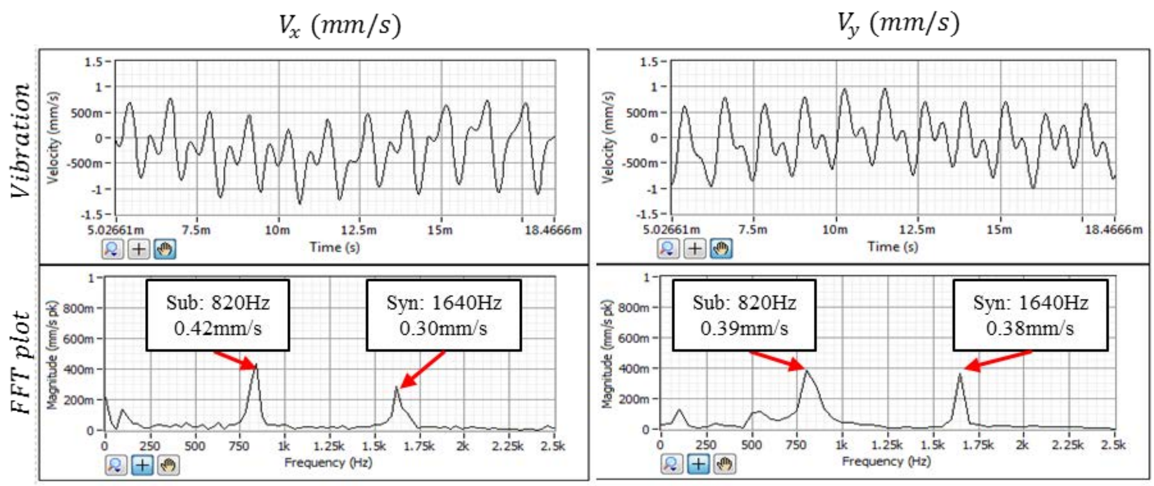

c) Measurements at sensor position B

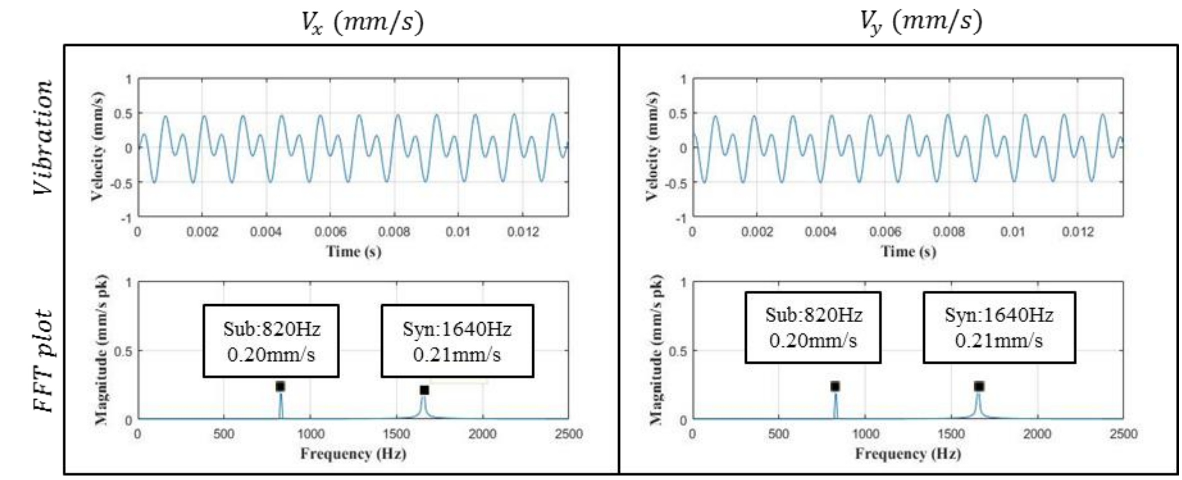

d) Predictions at sensor position B

Figure F-4 Unbalance responses of sensor positions *A & B* obtained at 98.4k rpm in speed

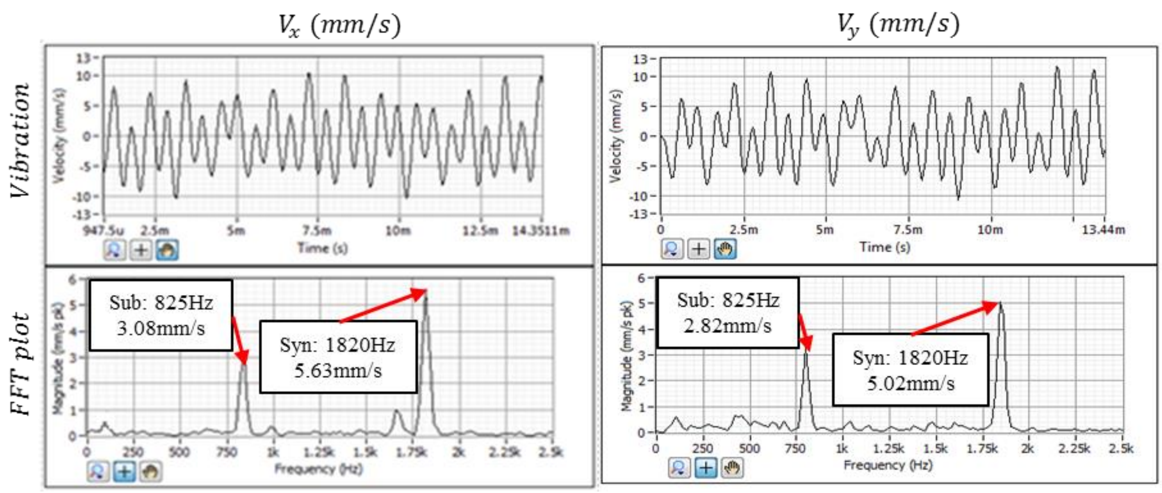

a) Measurements at sensor position A

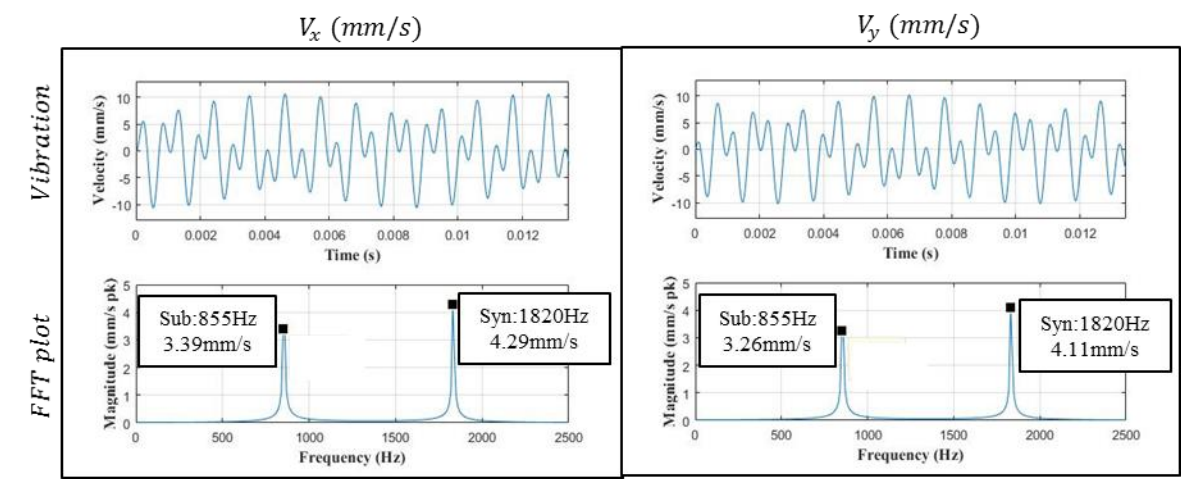

b) Predictions at sensor position A

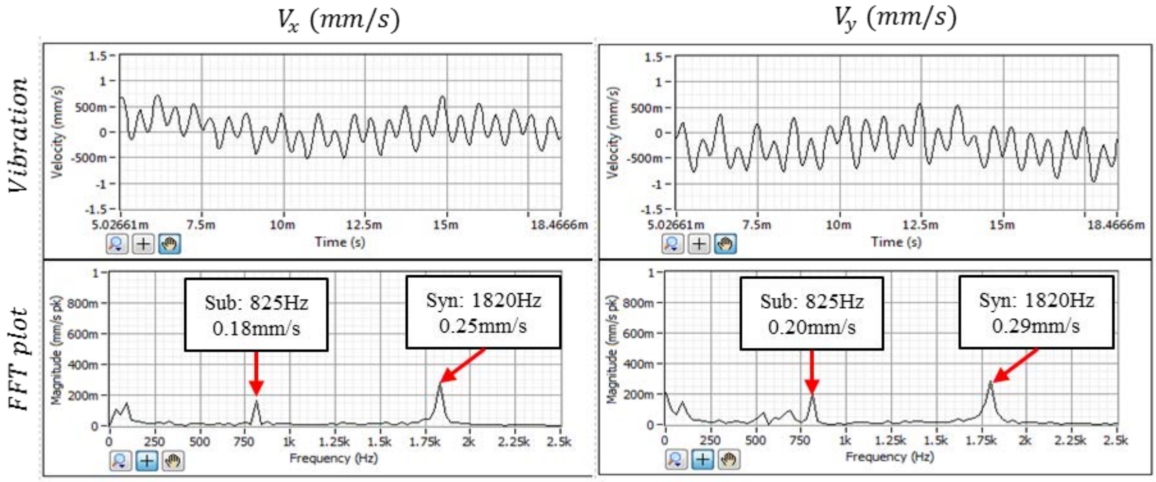

c) Measurements at sensor position B

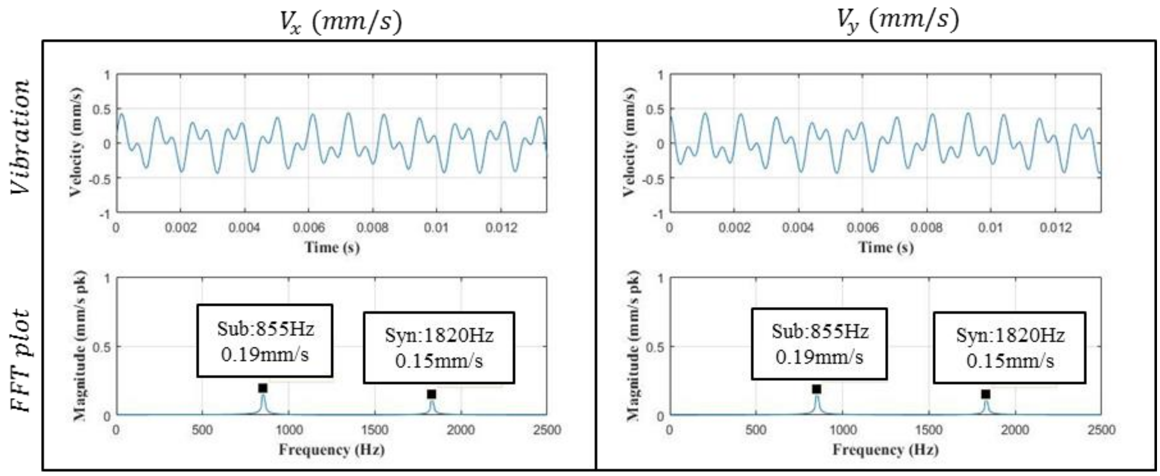

d) Predictions at sensor position B

Figure F-5 Unbalance responses of sensor positions *A & B* obtained at 109.2k rpm in speed

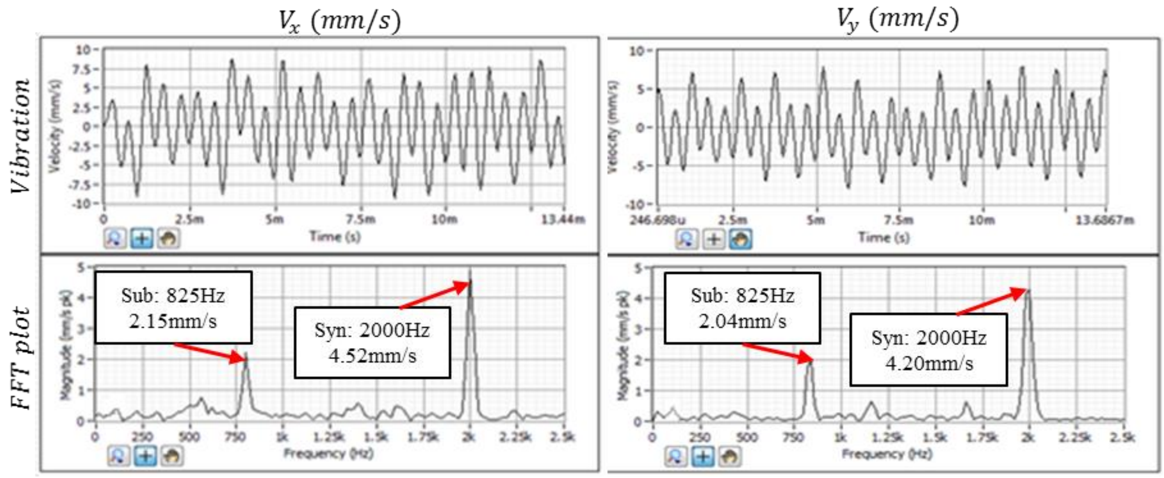

a) Measurements at sensor position A

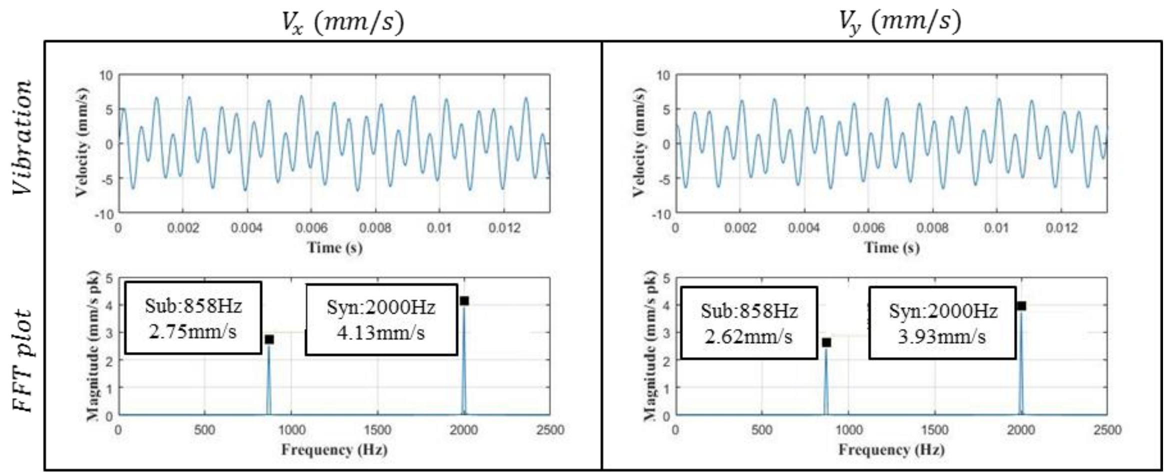

b) Predictions at sensor position A

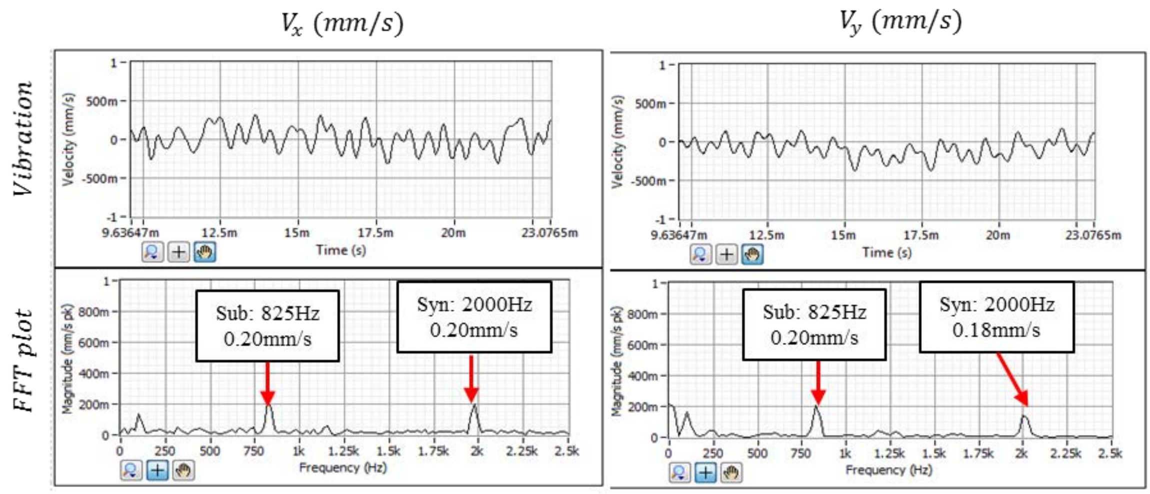

c) Measurements at sensor position B

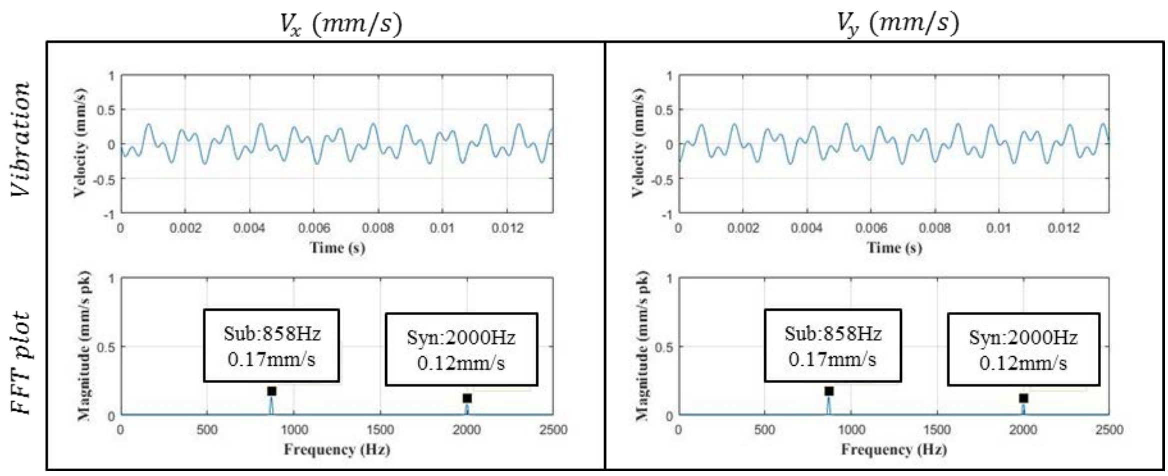

d) Predictions at sensor position B

Figure F-6 Unbalance responses of sensor positions *A & B* obtained at 120k rpm in speed

REFERENCES

[1] Pink E, Stout K. Design procedures for orifice compensated gas journal bearings based on experimental data. Tribology International. 19 8; 11(1):63- 5.

[2] Wilcock DF, Carbino J. Design of gas bearings. LA: Mechanical Technology Incorporated; 19 2 .

[3] Pink E, An experimental investigation of externally pressurised gas journal bearings and comparison with design method predictions. Proc. Gas Bear. Symp; 19 6.

[4] Ronze J, Weisstein EW. Separation of Variables: MathWorld--A Wolfram Web Resource. Available from: http://mathworld.wolfram.com/SeparationofVariables.html.

[5] Whitaker S. Flow in porous media I: A theoretical derivation of Darcy's law. Transport in porous media. 1986;1(1):3-25.

[6] Zhang X, Deeks LK, Bengough AG, Crawford JW, Young IM. Determination of soil hydraulic conductivity with the lattice Boltzmann method and soil thin-section technique. Journal of Hydrology. 2005;306(1):59- 0.

[ ] Pink E, Stout K. Orifice restrictor losses in journal bearings. Proceedings of the Institution of Mechanical Engineers. 19 9;193(1) :4 -52.

[8] Miyatake M, Yoshimoto S. Numerical investigation of static and dynamic characteristics of aerostatic thrust bearings with small feed holes. Tribology International. 2010;43(8):1353-9.

[9] Belforte G, Raparelli T, Trivella A, Viktorov V, Visconte C. CFD Analysis of a Simple Orifice-Type Feeding System for Aerostatic Bearings. Tribology Letters. 2015;58(2):1-8.

[10] Belforte G, Trivella A, Raparelli T, Viktorov V. Identification of discharge coefficients of orifice-type restrictors for aerostatic bearings and application examples: INTECH Open Access Publisher; 2011.

[11] Neves M, Schwarz V, Menon G. Discharge coefficient influence on the performance of aerostatic journal bearings. Tribology International. 2010;43(4): 46 -51.

[12] Wu D, Wang B, Luo X. Research on load characteristics of aerostatic journal bearing with pocketed orifice-type restrictor. Automation and Computing (ICAC), 2014 20th International Conference on; 2014: IEEE.

[13] Stout K, Pink E. Orifice compensated EP gas bearings: the significance of errors of manufacture. Tribology International. 1980;13(3):105-11.

[14] Sneck HJ. A survey of gas-lubricated porous bearings. Journal of tribology. 1968;90(4):804-9.

[15] Majumdar B. Gas-lubricated porous bearings: a bibliography. Wear. 19 6;36(3) :269- 3.

[16] Mori H, Yabe H, Ono T. Theory of externally pressurized circular thrust porous gas bearing. Journal of Fluids Engineering. 1965;8 (3) :613-20.

[1] Majumdar B. Analysis of externally pressurized porous gas journal bearings—I. Wear. 19 5;33(1) :25-35.

[18] Majumdar B. Analysis of externally pressurized porous gas journal bearings—II. Wear. 19 5;33(1) :3 -43.

[19] Rao N, Majumdar B. Dynamic characteristics of gas-lubricated externally pressurized porous bearings with journal rotation II. Wear. 19 8;50(2) :201-10.

[20] Rao N, Majumdar B. Dynamic characteristics of gas-lubricated externally pressurized porous bearings with journal rotation: I. Wear. 19 8;50(1) :59- 0.

[21] Rao N. Tilt stiffness and damping of externally pressurized porous gas journal bearings. Wear. 19 8;4 (1) :31-44.

[22] Singh K, Rao N, Majumdar B. Effects of velocity slip, anisotropy and tilt on the steady state performance of aerostatic porous annular thrust bearings. Wear. 1984;9 (1) :51-63.

[23] Kwan Y. Processing and fluid flow characteristics of hot isostatically pressed porous alumina for aerostatic bearing applications. 1996.

[24] Kwan Y, Corbett J. A simplified method for the correction of velocity slip and inertia effects in porous aerostatic thrust bearings. Tribology international. 1998;31(12): 9 -86.

[25] Fourka M, Bonis M. Comparison between externally pressurized gas thrust bearings with different orifice and porous feeding systems. Wear. 199 ;210(1) :311- .

[26] Belforte G, Raparelli T, Viktorov V, Trivella A. Feeding system of aerostatic bearings with porous media. ASME 8th Biennial Conference on Engineering Systems Design and Analysis; 2006: American Society of Mechanical Engineers.

[2] Togo S, Akiyama Y, Okano M. Experimental Study on Externally Pressurized Porous Gas Bearings. Journal of Japan Society of Lubrication Engineers. 19 2;1 (6):360-&.

[28] Yoshimoto S, Tozuka H, Dambara S. Static characteristics of aerostatic porous journal bearings with a surface-restricted layer. Proceedings of the Institution of Mechanical Engineers, Part J: Journal of Engineering Tribology. 2003;21 (2) :125-32.

[29] Miyatake M, Yoshimoto S, Sato J. Whirling instability of a rotor supported by aerostatic porous journal bearings with a surface-restricted layer. Proceedings of the Institution of Mechanical Engineers, Part J: Journal of Engineering Tribology. 2006;220(2):95-103.

[30] Yoshimoto S, Kohno K. Static and dynamic characteristics of aerostatic circular porous thrust bearings (effect of the shape of the air supply area). Journal of tribology. 2001;123(3):501-8.

[31] Otsu Y, Miyatake M, Yoshimoto S. Dynamic characteristics of aerostatic porous journal bearings with a surface-restricted layer. Journal of tribology. 2011;133(1):011 01.

[32] Vohr JH, Chow CY. Characteristics of herringbone-grooved, gas-lubricated journal bearings. Journal of Fluids Engineering. 1965;8 (3):568- 6.

[33] Malanoski S, Pan C. The static and dynamic characteristics of the spiral-grooved thrust bearing. Journal of Fluids Engineering. 1965;8 (3):54 -55.

[34] Cunningham RE, Fleming DP, Anderson WJ. Experiments on the steady state characteristics of herringbone-grooved air-lubricated journal bearings: National Aeronautics and Space Administration; 1969.

[35] Bonneau D, Absi J. Analysis of aerodynamic journal bearings with small number of herringbone grooves by finite element method. Journal of tribology. 1994;116(4):698- 04.

[36] Kobayashi T. Numerical analysis of herringbone-grooved gas-lubricated journal bearings using a multigrid technique. Journal of tribology. 1999;121(1):148-56.

[3] Srivastava V, Tamsir M. Crank-Nicolson semi implicit approach for numerical solutions of two-dimensional coupled nonlinear Burgers' equations. International Journal of Applied Mechanics andEngineering. 2012;1 (2) :5 1.

[38] Gad A, Nemat-Alla M, Khalil A, Nasr A. On the optimum groove geometry for herringbone grooved journal bearings. Journal of tribology. 2006;128(3):585-93.

[39] Ikeda S, Arakawa Y, Hishida N, Hirayama T, Matsuoka T, Yabe H. Herringbone - grooved bearing with non - uniform grooves for high - speed spindle. Lubrication Science. 2010;22(9):3 -92.

[40] Schiffmann J. Enhanced Groove Geometry for Herringbone Grooved Journal Bearings. Journal of Engineering for Gas Turbines and Power. 2013;135(10):102501.

[41] Tomioka J, Miyanaga N. Stability Threshold of Herringbone Grooved Aerodynamic Journal Bearings with External Stiffness and Damping Elements. Journal of Advanced Mechanical Design, Systems, and Manufacturing. 2013; (6) :8 6 -8 .

[42] Miyanaga N, Tomioka J. Effect of support stiffness and damping on stability characteristics of herringbone-grooved aerodynamic journal bearings mounted on viscoelastic supports. Tribology International. 2016;100:195-203.
[43] Miyanaga N, Tomioka J. Effect of Dynamic Properties of Support O-Rings on Stability of Herringbone-Grooved Aerodynamic Journal Bearings. Tribology Online. 2016;11(2):2 2 -80.
[44] Agrawal GL, Foil air/gas bearing technology—an overview. ASME 199 International Gas Turbine and Aeroengine Congress and Exhibition; 199 : American Society of Mechanical Engineers.
[45] Heshmat CA, Xu DS, Heshmat H. Analysis of gas lubricated foil thrust bearings using coupled finite element and finite difference methods. Journal of tribology. 2000;122(1):199-204.
[46] Peng Z, Khonsari M. Hydrodynamic analysis of compliant foil bearings with compressible air flow. Transactions-American Society of Mechanical Engineers Journal of Tribology. 2004;126(3):542-6.
[4] San Andrés L, Rubio D, Kim TH. Rotordynamic performance of a rotor supported on bump type foil gas bearings: experiments and predictions. Journal of Engineering for Gas Turbines and Power. 200 ;129 (3):850- .
[48] San Andrés L, Kim TH. Thermohydrodynamic analysis of bump type gas foil bearings: a model anchored to test data. Journal of Engineering for Gas Turbines and Power. 2010;132(4):042504.
[49] Wilkes JC, Wade J, Rimpel A, Moore J, Swanson E, Grieco J, et al. Impact of Bearing Clearance on Measured Stiffness and Damping Coefficients and Thermal Performance of a High-Stiffness Generation 3 Foil Journal Bearing. ASME Turbo Expo 2016: Turbomachinery Technical Conference and Exposition; 2016: American Society of Mechanical Engineers.
[50] San Andrés L, Chirathadam TA. A metal mesh foil bearing and a bump-type foil bearing: Comparison of performance for two similar size gas bearings. Journal of Engineering for Gas Turbines and Power. 2012;134(10):102501.
[51] Feng K, Zhao X, Huo C, Zhang Z. Analysis of novel hybrid bump-metal mesh foil bearings. Tribology International. 2016;103:529-39.
[52] Choe BS, Kim TH, Kim CH, Lee YB. Rotordynamic behavior of 225 kw (300 hp) class pms motor–generator system supported by gas foil bearings. Journal of Engineering for Gas Turbines and Power. 2015;13 (9) :092505.

[53] Lee Y-B, Kwon SB, Kim TH, Sim K. Feasibility study of an oil-free turbocharger supported on gas foil bearings via on-road tests of a two-liter class diesel vehicle. Journal of Engineering for Gas Turbines and Power. 2013;135(5):052 01.

[54] Lee Y-B, Park D-J, Sim K. Rotordynamic performance measurements of an oil-free turbocharger supported on gas foil bearings and their comparisons to floating ring bearings. International Journal of Fluid Machinery and Systems. 2015;8(1):23-35.

[55] Sim K, Lee Y-B, Kim TH. Effects of mechanical preload and bearing clearance on rotordynamic performance of lobed gas foil bearings for oil-free turbochargers. Tribology Transactions. 2013;56(2):224-35.

[56] Lee D-H, Kim Y-C, Kim K-W. The dynamic performance analysis of foil journal bearings considering coulomb friction: rotating unbalance response. Tribology Transactions. 2009;52(2):146-56.

[5] Bhore SP, Darpe AK. Nonlinear dynamics of flexible rotor supported on the gas foil journal bearings. Journal of Sound and Vibration. 2013;332(20):5135-50.

[58] Song J-h, Kim D. Foil gas bearing with compression springs: analyses and experiments. Journal of tribology. 200 ;129(3) :628-39.

[59] Bonello P, Pham H. The efficient computation of the nonlinear dynamic response of a foil–air bearing rotor system. Journal of Sound and Vibration. 2014;333(15):3459- 8.

[60] Bonello P, Pham H. Nonlinear dynamic analysis of high speed oil-free turbomachinery with focus on stability and self-excited vibration. Journal of Tribology. 2014;136(4):041 05.

[61] Simmons J, Advani S. Paper II (iii) Michell and the development of tilting pad bearings. Tribology Series. 198 ; 11:49-56.

[62] Dimond T, Younan A, Allaire P. A review of tilting pad bearing theory. International Journal of Rotating Machinery. 2011;2011.

[63] Wilkes JC. Measured and Predicted Transfer Functions Between Rotor Motion and Pad Motion for a Rocker-Back Tilting-Pad Bearing in LOP Configuration. ASME 2011 Turbo Expo: Turbine Technical Conference and Exposition; 2011: American Society of Mechanical Engineers.

[64] Lund J. On the Hybrid Gas Lubricated Journal Bearing. DTIC Document, 1962.

[65] Kim D, Park S. Hybrid air foil bearings with external pressurization. ASME 2006 International Mechanical Engineering Congress and Exposition; 2006: American Society of Mechanical Engineers.

[66] Wang YP, Kim D. Experimental Identification of Force Coefficients of Large Hybrid Air Foil Bearings. Journal of Engineering for Gas Turbines and Power. 2014;136(3):032503.

[6] Ives D, Rowe W. The performance of hybrid journal bearings in the superlaminar flow regimes. Tribology Transactions. 1992;35(4):62 -34.

[68] Osborne DA, San Andrés L. Experimental Response of Simple Gas Hybrid Bearings for Oil-Free Turbomachinery. Journal of Engineering for Gas Turbines and Power. 2006;128(3):626-33.

[69] Wilde DA, San Andrés L. Comparison of Rotordynamic Analysis Predictions with the test response of simple gas hybrid Bearings for oil free Turbomachinery. ASME Turbo Expo 2003, collocated with the 2003 International Joint Power Generation Conference; 2003: American Society of Mechanical Engineers.

[0] Zhu X, San Andrés L. Rotordynamic performance of flexure pivot hydrostatic gas bearings for oil-free turbomachinery. Journal of Engineering for Gas Turbines and Power. 200 ;129(4) :1020- .

[1] San Andrés L, Ryu K. Hybrid gas bearings with controlled supply pressure to eliminate rotor vibrations while crossing system critical speeds. Journal of Engineering for Gas Turbines and Power. 2008;130(6):062505.

[2] Stanev P, Wardle F, Corbett J. Investigation of grooved hybrid air bearing performance. Proceedings of the Institution of Mechanical Engineers, Part K: Journal of Multi-body Dynamics. 2004;218(2):95-106.

[3] Zhang X-Q, Wang X-L, Liu R, Zhang Y-Y. Modeling and Analysis of Micro Hybrid Gas Spiral-Grooved Thrust Bearing for Microengine. Journal of Engineering for Gas Turbines and Power. 2013;135(12):122508.

[4] Ertas BH. Compliant hybrid journal bearings using integral wire mesh dampers. Journal of Engineering for Gas Turbines and Power. 2009;131(2):022503.

[5] Delgado A. Experimental identification of dynamic force coefficients for a 110 MM compliantly damped hybrid gas bearing. Journal of Engineering for Gas Turbines and Power. 2015;13 ( ) :0 2502.

[6] Waumans T, Peirs J, Reynaerts D, Al-Bender F. On the dynamic stability of high-speed gas bearings: stability study and experimental validation. Sustainable Construction and Design. 2011;2(2):342.

[ ] Wang N, Chang C. An application of Newton's method to the lubrication analysis of air-lubricated bearings. Tribology Transactions. 1999;42(2):419-24.

[8] Wang N, Chang S-H, Huang H-C. Comparison of Iterative Methods for the Solution of Compressible-Fluid Reynolds Equation. Journal of tribology. 2011;133(2):021 02.

[9] Wang N, Chang S-H, Huang H-C. Stopping Criterion in Iterative Solution Methods for Reynolds Equations. Tribology Transactions. 2010;53(5): 39 -4 .

[80] Faria MTC. Performance Characteristics Curves for Gas Lubricated Herringbone Groove Journal Bearings. Proceedings of the COBEM 2005: 18 th International Congress of Mechanical Engineering; 2005.

[81] Arghir M, Alsayed A, Nicolas D. The finite volume solution of the Reynolds equation of lubrication with film discontinuities. International journal of mechanical sciences. 2002;44(10):2119-32.

[82] Bazoune A, Khulief Y, Stephen N. Shape functions of three-dimensional Timoshenko beam element. Journal of Sound and Vibration. 2003;259(2):4 3 -80.

[83] Chen W, Gunter E. Instruction to Dynamics of Rotor–Bearing System. Victoria, BA, Canada, Trafford Publishing. 2005.

[84] Cao J. Transient Analysis of Flexible Rotors with Nonlinear Bearings, Dampers and External Forces [Doctoral dissertation]: University of Virginia; 2012.

[85] Tian L, Wang W. Nonlinear dynamics of rotor bearing systems in automotive turbochargers: LAP LAMBERT Academic Publishing; 2013.

[86] Miyanaga N, Tomioka J. Stability Analysis of Herringbone-Grooved Aerodynamic Journal Bearings for Ultra High-Speed Rotations. International Journal of Materials, Mechanics and Manufacturing. 2016;4(3):156-61.

[8] Quarteroni A, Sacco R, Saleri F. Numerical mathematics: Springer Science & Business Media; 2010 Nov 30.

[88] Hamrock BJ, Schmid SR, Jacobson BO. Fundamentals of fluid film lubrication: CRC press; 2004.

[89] Lee Y-B, Kwak H-D, Kim C-H, Lee N-S. Numerical prediction of slip flow effect on gas-lubricated journal bearings for MEMS/MST-based micro-rotating machinery. Tribology international. 2005;38(2):89-96.

[90] Kincaid DR, Cheney EW. Numerical analysis: mathematics of scientific computing. 2 ed: American Mathematical Soc.; 2002.

[91] Simoncini V, Szyld DB. Recent computational developments in Krylov subspace methods for linear systems. Numerical Linear Algebra with Applications. 200 ; 14(1):1-59.

[92] Lo C-Y, Wang C-C, Lee Y-H. Performance analysis of high-speed spindle aerostatic bearings. Tribology International. 2005;38(1):5-14.

[93] Cunningham RE, Fleming DP, Anderson WJ. Experimental Load Capacity and Power Loss of Herringbone Grooved Gas Lubricated Journal Bearings. Journal of tribology. 19 1;93(3) :415-22.

[94] Lund J. Review of the concept of dynamic coefficients for fluid film journal bearings. ASME J Tribol. 198 ; 109(1):3 -41.

[95] Vohr J. A study of inherent restrictor characteristics for hydrostatic gas bearings. Proceedings of Fourth Gas Bearing Symposium: University of Southampton; 1969.

[96] Holmes R, Brennan M, Gottrand B. Vibration of an automotive turbocharger–a case study. Proceedings 8th International Conference on Vibrations in Rotating Machinery; 2004.

[9] Belforte G, Raparelli T, Viktorov V, Colombo F. A Theoretical Study of a High Speed Rotor Supported by Air Bearings Mounted on O-Rings. Fifth International Conference on Tribology, AITC-AIT 2006; 2006.

[98] Swanson E, Powell CD, Weissman S. A practical review of rotating machinery critical speeds and modes. Sound and vibration. 2005;39(5):16- .

[99] Chu L, Li W-L, Shen R, Tsai T. Dynamic characteristics of grooved air bearings in microsystems. Proceedings of the Institution of Mechanical Engineers, Part J: Journal of Engineering Tribology. 2009;223(6):895-908.

[100] Faria MTC. Some performance characteristics of high speed gas lubricated herringbone groove journal bearings. JSME International Journal Series C Mechanical Systems, Machine Elements and Manufacturing. 2001;44(3): 5 -81.